

Alma Mater Studiorum – Università di Bologna
in cotutela con Università di Groningen

DOTTORATO DI RICERCA IN
ASTROFISICA

Ciclo XXXII

Settore Concorsuale: 02/C1 – Astronomia, Astrofisica, Fisica della Terra e dei Pianeti

Settore Scientifico Disciplinare: FIS/05 – Astronomia e Astrofisica

STAR FORMATION LAWS AND GAS
TURBULENCE IN NEARBY GALAXIES

Presentata da: Cecilia Bacchini

Coordinatore Dottorato

**Chiar.mo Prof.
Francesco R. Ferraro**

Supervisore

**Chiar.mo Prof.
Filippo Fraternali**

Supervisore

**Chiar.mo Prof.
Carlo Nipoti**

Esame finale anno 2020



university of
 groningen



ALMA MATER STUDIORUM
 UNIVERSITÀ DI BOLOGNA

Star formation laws and gas turbulence in nearby galaxies

PhD thesis

to obtain the degree of PhD of the
 University of Groningen
 on the authority of the
 Rector Magnificus Prof. C. Wijmenga
 and in accordance with
 the decision by the College of Deans

and

to obtain the degree of PhD of the
 University of Bologna
 on the authority of the
 Rector Magnificus Prof. F. Ubertini

Double PhD degree

This thesis will be defended in public on
 Friday 25 September 2020 at hours 9.00

by

Cecilia Bacchini

born on 21 February 1992
 in Parma, Italy

Supervisors

Prof. dr. F. Fraternali

Prof. dr. C. Nipoti

Assessment Committee

Prof. dr. L. Ciotti

Prof. dr. A. Helmi

Prof. dr. R. C. Kennicutt, Jr.

Prof. dr. J. H. van Gorkom

Front cover: the image shows the spiral galaxy NGC 6503. The galaxy's arms and center are crossed by dark dust lanes. The red patches show the ionised gas and the blue regions indicate newly forming stars.

Back cover: the image shows the giant cluster of stars called Westerlund 2, which contains some of the hottest, brightest, and most massive stars in the Milky Way. Some of these stars emit strong ultraviolet radiation and powerful winds of charged particles, carving the surrounding gas cloud. The reddish-brown filaments are composed of gas and dust. The red dots are newly forming stars still wrapped in their gas-and-dust cocoons. The brilliant blue stars are mostly foreground stars. The red colors in the nebulosity represent hydrogen; the bluish colors are predominantly oxygen.

Credits: NASA, ESA, D. Calzetti (University of Massachusetts), H. Ford (Johns Hopkins University), the Hubble Heritage Team (STScI/AURA)-ESA/Hubble Collaboration, A. Nota (ESA/STScI), and the Westerlund 2 Science Team.

This thesis is printed by Gildeprint.

“Dobby likes work, but he wants to wear clothes and he wants to be paid, Harry Potter... Dobby likes being free!”

– Dobby, “Harry Potter and the Goblet of Fire” by Joanne Rowling.

Contents

1	Thesis introduction	1
1.1	Galaxy bimodality in the local Universe	3
1.1.1	Star-forming galaxies	3
1.2	Interstellar medium of star-forming galaxies	4
1.2.1	Atomic gas	4
1.2.2	Molecular gas	6
1.2.3	Other ISM components	8
1.3	Structure and kinematics of gas discs	9
1.3.1	The tilted-ring approach	9
1.3.2	Measuring the thickness of gaseous discs	12
1.3.3	Gas turbulence	14
1.4	Star formation in the nearby Universe	15
1.4.1	Star formation diagnostics	15
1.4.2	Empirical star formation laws	16
1.4.3	Theories of galactic-scale star formation	17
1.4.4	Stellar feedback	20
1.5	Thesis outline	21
2	Volumetric star formation laws of disc galaxies	23
2.1	Introduction	25
2.2	Volume densities from hydrostatic equilibrium	27
2.2.1	Hydrostatic equilibrium	27
2.2.2	Gravitational potential	28
2.2.3	Velocity dispersion	29
2.2.4	Scale height definition	30
2.2.5	From surface densities to volume densities	30

2.3	Sample description	32
2.3.1	Surface densities	32
2.3.2	Selection based on mass models	33
2.4	Gas disc thickness	35
2.4.1	Flaring HI disc	37
2.4.2	Flaring H ₂ disc	41
2.4.3	Star formation rate scale height	44
2.5	Volumetric star formation laws	44
2.5.1	Relation between total gas and star formation rate	45
2.5.2	Atomic gas versus star formation rate	47
2.5.3	Molecular gas versus star formation rate	48
2.6	Discussion	51
2.6.1	Comparison with other works on gas and star scale heights	51
2.6.2	Comparison with other works on volume-based SF laws	52
2.6.3	Physical interpretation	54
2.7	Summary and conclusions	56
	Appendix 2.A VSF law using the analytical approximation for the scale height	58
	Appendix 2.B ^{3D} BAROLO set-up	60
	Appendix 2.C Revisited mass model for NGC 7793	64
	Appendix 2.D NGC 2841, an example of the scale height imprint on the velocity dispersion field	78
	Appendix 2.E Uncertainties on scale heights and volume densities	79
	Appendix 2.F Likelihood and posterior distributions of Bayesian fittings	81
3	The volumetric star formation law in the Milky Way	85
3.1	Introduction	87
3.2	Volume densities	88
3.2.1	Distribution of gas in hydrostatic equilibrium	88
3.2.2	Definitions of volume densities	89
3.3	Observations in the Milky Way	90
3.3.1	Gas distribution and kinematics	90
3.3.2	SFR distribution	93
3.4	Results	95
3.4.1	Scale heights of classical Cepheids and gas in hydrostatic equilibrium	95
3.4.2	VSF laws in the Milky Way	96
3.5	Discussion	99
3.5.1	VSF law with alternative determinations from the literature	99
3.5.2	Previous works on star formation laws in the Milky Way and nearby disc galaxies	100
3.5.3	Physical interpretation of the VSF law	102
3.6	Summary and conclusions	104

Appendix 3.A	The Milky Way gas distribution compared with the literature	106
3.A.1	Gas surface densities	106
3.A.2	Gas scale height	106
3.A.3	Gas volume densities	108
Appendix 3.B	The Milky Way SFR distribution using different tracers	110
3.B.1	SFR surface density	110
3.B.2	SFR scale height	110
Appendix 3.C	Galactic rotation curve	111
4	The volumetric star formation law for nearby dwarf galaxies	113
4.1	Introduction	115
4.2	Method	117
4.2.1	3D distribution of the gas in hydrostatic equilibrium . . .	117
4.2.2	The mass distribution of star-forming dwarf galaxies . . .	119
4.2.3	The gas velocity dispersion	121
4.3	Sample description	122
4.3.1	Atomic gas kinematics and surface density	122
4.3.2	Star formation rate surface density	124
4.4	Results	126
4.4.1	The scale height	126
4.4.2	The volumetric star formation law	127
4.5	Discussion	131
4.5.1	Systematic effects due to the molecular gas content	132
4.5.2	Systematic effects on the star formation rate surface density	133
4.5.3	Validity of the hydrostatic equilibrium	134
4.5.4	Comparison with other works	135
4.5.5	On the physical implications of the VSF law	138
4.6	Summary and conclusions	140
Appendix 4.A	Radial profiles of Σ_{HI} , σ_{HI} , and Σ_{SFR}	142
5	Evidence for supernova feedback sustaining gas turbulence in nearby star-forming galaxies	145
5.1	Introduction	147
5.2	Observations and galaxy sample	149
5.2.1	Atomic gas distribution and kinematics	150
5.2.2	Molecular gas distribution and kinematics	151
5.2.3	Star formation rate surface density	151
5.3	Methods	152
5.3.1	Energy components	152
5.3.2	Comparison of the model with the observations	157
5.4	Results	159
5.4.1	Cold atomic gas	159
5.4.2	Warm atomic gas	162

5.4.3	Two-phase atomic gas	164
5.4.4	Molecular gas	166
5.5	Discussion	169
5.5.1	A ‘global’ SN efficiency for nearby galaxies?	169
5.5.2	Empirical evidence for the self-regulating cycle of star formation?	171
5.5.3	Comparison with previous works on SN feedback	172
5.5.4	Possible caveats on the analysis and stability of the results	173
5.5.5	Other turbulence sources	176
5.6	Summary and conclusions	180
	Appendix 5.A Detailed molecular gas kinematics	182
	Appendix 5.B Hierarchical Bayesian inference	191
	Appendix 5.C SN efficiency radial gradient	194
6	Conclusions and future prospects	199
6.1	Summary and highlights	200
6.1.1	The flaring of gas discs in galaxies	200
6.1.2	The volumetric star formation law	201
6.1.3	Supernova-driven turbulence	203
6.2	Future developments	203
6.2.1	Measuring the thickness of discs	203
6.2.2	Where star formation laws dare: taking the VSF law to extremes	204
6.2.3	Gas cycles in star-forming discs	205
	Bibliography	207
	Summary	221
	Samenvatting	229
	Sommario	237
	Acknowledgments	245

CHAPTER 1

Thesis introduction

Abstract

This first Chapter aims to introduce the important topics for this Ph.D. thesis, maintaining a particular focus on star-forming galaxies in the local Universe. In Sect. 1.1, we briefly describe the types and main properties of present-day galaxies. Sect. 1.2 reviews the components of the interstellar medium of star-forming galaxies and how these are accessible to observations. Then, in Sect. 1.3, we describe the approaches that are typically adopted to study the gas distribution and kinematics in disc galaxies. Sect. 1.4 focuses on star formation, starting from the diagnostics used to measure the star formation rate (SFR) of galaxies and then moving to the empirical relations between the gas and the SFR densities. We also summarise simple theoretical models to explain these relations and describe the evolution of supernova remnants and wind bubbles in the ISM. Lastly, in Sect. 1.5, we briefly outline the content of the rest of this thesis.

1.1 Galaxy bimodality in the local Universe

Present-day galaxies can be divided in two main classes: early-type galaxies (ETG; or passive, quiescent galaxies) and late-type galaxies (LTG; or star-forming, disc galaxies). The former class typically includes ellipticals and lenticulars, while the latter consists of spirals and irregulars. Star formation activity, measured by the star formation rate (SFR), is a key property to distinguish between these galaxy types: it is weak or absent in ETGs, ongoing and sometimes vigorous in LTGs.

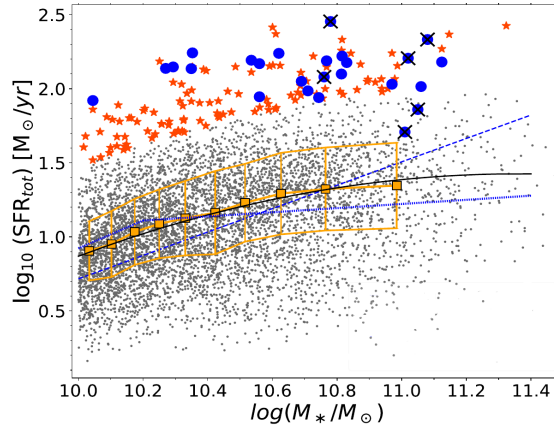
Another important difference between quiescent and star-forming galaxies is represented by their gas reservoir. Disc galaxies host a significant amount of cold gas (both atomic and molecular) which is mostly distributed in a rotating disc. The dominant gaseous component in passive galaxies is instead ionised gas at a temperature largely exceeding million degrees (e.g. Pellegrini, 2011). Cold gas disc are also observed but they typically represent a negligible fraction of the baryonic mass of ETGs (e.g. Oosterloo et al., 2007b; Serra et al., 2014; Young et al., 2011; Davis et al., 2013). In the following, we focus on star-forming galaxies, their properties and their structure.

1.1.1 Star-forming galaxies

In the local Universe, star-forming galaxies can be divided in two sub-classes, spirals and dwarf irregulars. Spiral galaxies typically have large stellar masses ($10^9 M_\odot \lesssim M_\star \lesssim 10^{11} M_\odot$; Lelli et al. 2016), mainly consisting of a rotating stellar disc and a spheroidal bulge (when present). They host large (10-100 kpc) and massive ($10^8 M_\odot \lesssim M_{\text{HI}} \lesssim 10^{10} M_\odot$; Lelli et al. 2016; Catinella et al. 2018) atomic gas discs and, in most cases, molecular gas discs in the inner regions (e.g. Leroy et al., 2008; Saintonge et al., 2017). The SFR of these galaxies ranges from $\sim 0.1 M_\odot \text{ yr}^{-1}$ to a few tens $M_\odot \text{ yr}^{-1}$ (e.g. Saintonge et al., 2017; Catinella et al., 2018). Dwarf irregulars have instead smaller stellar masses ($10^5 M_\odot \lesssim M_\star \lesssim 10^9 M_\odot$; Zhang et al. 2012; Lelli et al. 2016), no bulge, and $10^{-4} M_\odot \text{ yr}^{-1} \lesssim \text{SFR} \lesssim 1 M_\odot \text{ yr}^{-1}$ (Tolstoy et al., 2009). The baryonic mass of dwarfs is typically dominated by the atomic gas ($10^6 M_\odot \lesssim M_{\text{HI}} \lesssim 10^9 M_\odot$; Hunter et al. 2012; Iorio et al. 2017), while the fraction of molecular gas is highly uncertain (Madden & Cormier, 2019). If the star formation activity is unusually high (a factor 10 or more higher than the average at a certain M_\star , see Fig. 1.1) a galaxy is called starburst, both in the regimes of dwarf and spiral galaxies.

In this Ph.D. thesis, we are going to study star-forming galaxies in the mass range of both dwarf irregulars and spiral galaxies, while the regime of massive starbursts is not investigated. The gas content of LTGs is of primary importance in star formation and star formation itself has a strong impact on the surrounding medium. For instance, stellar feedback can significantly modify the gas distribution and reservoir of a galaxy (see Sect. 1.4.4).

Figure 1.1 – Correlation between the stellar mass and the SFR in SFGs, or star formation main sequence (SFMS) at low redshift ($0.5 < z < 0.9$). The grey points show normal SFG and the red stars and the blue dots represent starbursts, which lie above the SFMS. The orange points are obtained as the median of the grey points in bins of stellar mass. The curves indicate fits to the SFMS obtained by different authors (see Calabrò et al., 2018).



1.2 Interstellar medium of star-forming galaxies

The gas in the ISM is present in a variety of phases, which are characterised by the following temperatures (T) and densities (n) (e.g. Wolfire et al., 2003; Tielens, 2005):

- hot ionised medium (HIM) with $T \sim 10^6$ K and $n \sim 10^{-3} \text{ cm}^{-3}$;
- warm ionised medium (WIM) with $T \sim 10^4$ K and $n \sim 10^{-1} \text{ cm}^{-3}$;
- photo-ionised medium with $T \sim 10^4$ K and $n \sim 1 - 10^5 \text{ cm}^{-3}$;
- warm neutral medium (WNM) with $T \approx 8000$ K and $n \sim 10^{-1} \text{ cm}^{-3}$;
- cold neutral medium (CNM) with $T \approx 80$ K and $n \sim 10 \text{ cm}^{-3}$;
- molecular gas with $T \sim 10$ K and $n > 10^2 \text{ cm}^{-3}$.

In star-forming galaxies, the most abundant components are the neutral atomic gas and the molecular gas, which are the fuel for star formation, and the photo-ionised gas, which is produced by star formation.

1.2.1 Atomic gas

About 90% of the neutral gas in star-forming galaxies is atomic hydrogen (HI), which is observed in the local Universe via the 21-cm emission line. The 21-cm line was originally predicted theoretically by van de Hulst (1946) and then observed in the Milky Way (MW) by Ewen & Purcell (1951). This line is one of the best tools to study the mass, the distribution and the kinematics of gas in star-forming galaxies. The total HI flux of a galaxy can be directly linked to the total mass of atomic gas under the assumption of an optically thin

medium.¹ Most of the atomic gas is distributed in a disc and rotates in circular orbits. Hence, to obtain the total HI flux, the monochromatic flux needs to be integrated over the line-of-sight velocity covered by the source. Once the total flux F_{HI} and the distance D of the source are known, the HI mass can be derived as (Cimatti, Fraternali, & Nipoti, 2019)

$$M_{\text{HI}} \simeq 2.343 \times 10^5 (1+z)^{-1} \left(\frac{D}{1 \text{ Mpc}} \right)^2 \left(\frac{F_{\text{HI}}}{\text{Jy km s}^{-1}} \right) M_{\odot}. \quad (1.1)$$

HI discs are typically more extended than the stellar discs (see Fig. 1.2): in the case of spiral galaxies, the HI emission can reach distances from the galaxy center of $\sim 10 - 100$ kpc (e.g. Wang et al., 2013; Martinsson et al., 2016), while in dwarf irregulars HI discs have typical sizes of a few kiloparsec (e.g. Hunter et al., 2012; Iorio et al., 2017).

The observed Doppler shift of the 21-cm emission line allows us to study the rotation of the HI in galaxies, while the line broadening (i.e. velocity dispersion) yields valuable information on the disordered motions in the neutral gas (i.e. thermal speed, turbulence). Radio interferometry and deep HI observations have dramatically improved our knowledge about the atomic gas distribution in nearby galaxies (e.g. Walter et al., 2008). In particular, high spatial resolution observations have shown that HI discs are not smooth but pierced by holes (see right panel of Fig. 1.2), which are usually ascribed to stellar feedback phenomena such as supernova explosions and super-bubble blowouts (see Sect. 1.4.4; Kamphuis et al., 1991; Puche et al., 1992; Walter & Brinks, 1999; Boomsma et al., 2008).

Neutral hydrogen is mostly distributed in two phases, CNM and WNM (Field, 1965; Wolfire et al., 1995, 2003). In the MW, there are observational indications that the fraction of WNM is approximately 60% in the solar neighborhood at latitudes larger than 10° (Heiles & Troland, 2003; Murray et al., 2018). Pineda et al. (2013) found that the fraction of WNM is $\sim 30\%$ and $\sim 80\%$ within and beyond the solar radius, respectively. Apart from these two distinct phases, there are indications that up to $\sim 50\%$ of the HI in our Galaxy may have temperatures intermediate between the CNM and the WNM ($T \approx 500 - 5000$ K; Heiles & Troland, 2003; Kalberla & Haud, 2018; Murray et al., 2018). For external galaxies, other authors estimated values of the WNM fraction that are nearly similar to those in the MW. Dickey & Brinks (1993) measured that the WNM is $\sim 60\%$ of the total HI in M31, while this fraction is $\sim 85\%$ in M33. In the Large Magellanic Cloud, Marx-Zimmer et al. (2000) found that the WNM is about 65%, while Dickey et al. (2000) estimated a lower limit of $\sim 85\%$ for the Small Magellanic Cloud (see also Jameson et al., 2019).

In addition to the gas in the disc, a significant fraction (10 – 20%) of HI is located in a gaseous halo above the galaxy midplane, the so-called ‘extra-planar’ gas (e.g. Oosterloo et al., 2007a; Marasco et al., 2019). There are strong

¹The HI becomes optically thick at column densities above a few 10^{21} cm^{-2} .

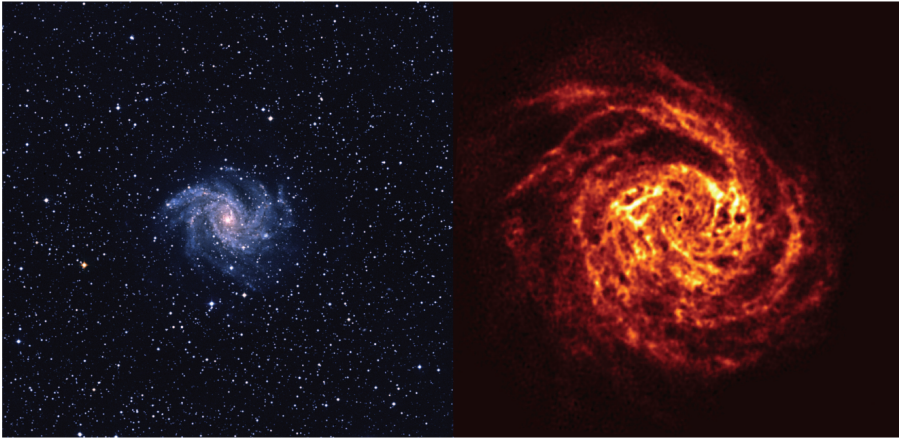


Figure 1.2 – Optical image of NGC 6946 (left) from the Digitized Sky Survey plates. Deep HI map (right), on the same scale as the optical, obtained with the Westerbork Synthesis Radio Telescope. From Boomsma et al. (2008).

observational indications that most of this gas has an internal origin related to stellar feedback (i.e. galactic fountain, see Fraternali & Binney 2006, 2008; Marasco et al. 2012). A small fraction of this extra-planar gas may also be explained by external accretion (e.g. gas stripped from satellites; see Sancisi et al. 2008 and references therein).

1.2.2 Molecular gas

The most abundant molecule in the Universe is molecular hydrogen (H_2), which is formed from low-temperature and high-density HI. However, the emission of this molecule is not accessible to observations in normal ISM conditions, therefore emissions of other molecules are usually adopted to trace the distribution of molecular gas. In nearby galaxies, carbon monoxide (CO) is the most used tracer of molecular gas. CO is the second most abundant molecule in the ISM and its low-energy rotational transitions (e.g. $J=1-0$, $J=2-1$) are easily detectable in relatively high-density regions.

When observed at relatively low spatial resolution, CO in star-forming galaxies appears to be distributed in a disc. This CO disc is typically less radially extended than the HI disc, but the central HI depletion usually observed in the inner regions of galaxies is filled by the peak of the molecular gas density (e.g. Frank et al., 2016). By observing CO in the MW or at high spatial resolution in nearby galaxies (e.g. Schinnerer et al., 2019), we see that the molecular gas is typically located in clouds, which are nearly gravitationally bound structures with very low gas temperatures ($T \sim 10$ K) and masses of $10^5 - 10^7 M_\odot$. Thanks to modern radio interferometers, observations with remarkably high

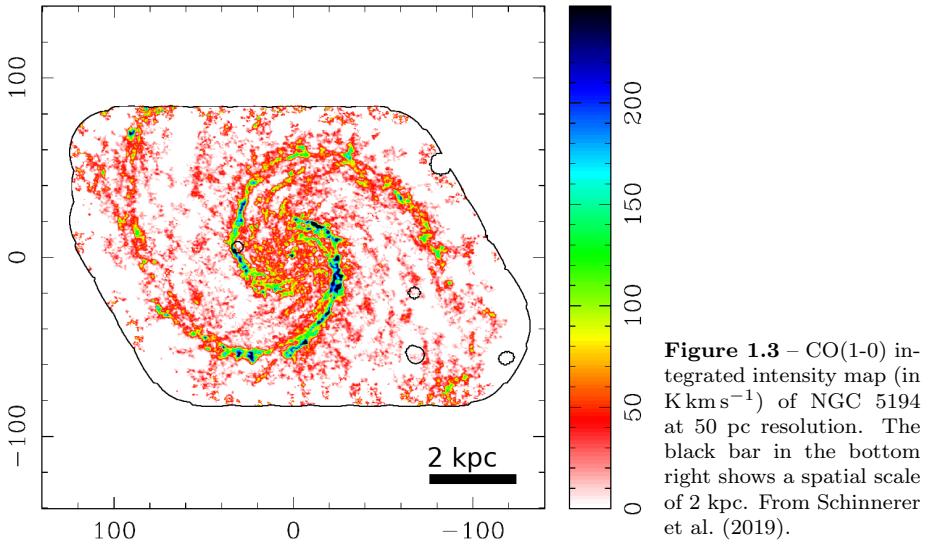


Figure 1.3 – CO(1-0) integrated intensity map (in K km s^{-1}) of NGC 5194 at 50 pc resolution. The black bar in the bottom right shows a spatial scale of 2 kpc. From Schinnerer et al. (2019).

spatial resolution are now available (Fig. 1.3), allowing to resolve the single molecular clouds and filaments in nearby galaxies and study their individual properties (e.g. Sun et al., 2018; Herrera et al., 2020).

Regardless the spatial resolution, the flux of CO emission lines is commonly used to estimate the total mass of molecular gas (e.g. Frank et al., 2016; Saintonge et al., 2017). The typical approach consists in adopting a CO-to- H_2 conversion factor, called X_{CO} , to derive the H_2 mass from the CO luminosity (Bolatto et al., 2013). The conversion factor is called α_{CO} when the correction for helium is included. The value of X_{CO} was calibrated in the Milky Way using different methods to estimate the relation between CO(1-0) line flux and H_2 mass, but there are indications that this factor varies both between different galaxies and with the galactocentric distance (Sandstrom et al., 2013). The value of X_{CO} likely depends on the gas metallicity, as CO emission is expected to be faint or absent in metal-poor environments (e.g. dwarf galaxies), resulting in higher values of the conversion factor with respect to metal-rich gas (e.g. Hunt et al., 2014; Amorín et al., 2016; Madden & Cormier, 2019). Therefore, the estimates of the molecular gas mass in galaxies are typically more uncertain with respect to those of the atomic gas mass (Eq. 1.1). When CO(1-0) line is not accessible, higher rotational transitions must be used, at the price of an additional assumption about the spectral energy distribution of CO to convert the flux of these emission lines to the CO(1-0) flux (Saintonge et al., 2017).

Despite these uncertainties on the mass determinations, CO emission lines are very useful to study the kinematics of molecular gas in the inner regions of galaxies. Indeed, molecular gas emission is particularly bright in these parts but hardly extends beyond their stellar disc. Depending on the spatial resolution

of the observations, it is also possible to study the large scale rotation of the molecular disc (e.g. Frank et al., 2016) and the chaotic motions between the individual clouds (see e.g. Caldú-Primo et al., 2013; Mogotsi et al., 2016, and Chapter 3) or inside a molecular cloud (e.g. Sun et al., 2018; Utomo et al., 2019).

1.2.3 Other ISM components

The ISM components in star-forming galaxies are not limited to atomic and molecular gas. Ionised gas is one of these components. The atomic gas located close to massive stars emitting ultra-violet (UV) photons is partially or completely ionised by radiation reaching a typical temperature $T \sim 10^4$ K (see Sect. 1.4.1). These regions filled with photo-ionised atomic hydrogen are called HII regions and can be observed via recombination lines (e.g. $H\alpha$ and $H\beta$ in the local Universe), forbidden lines (e.g. [OII]), and continuum free-free radiation. In particular, $H\alpha$ emission can be very useful to estimate the SFR in disc galaxies, as it traces stellar populations younger than 10 Myr. Atomic hydrogen can also be collisionally ionised by strong shocks in the ISM produced by stellar feedback (see Sect. 1.4.4). This gas is typically at $T \sim 10^6$ K and emits most of its radiation in the soft-X rays.

Despite its negligible mass, dust is another important component of the ISM as dust grains are the main catalyst for the formation of molecular hydrogen. In addition, dust absorbs the UV emission from massive stars and re-emits it as mid-infrared (MIR) and far-infrared (FIR) radiation, which can therefore be used to trace the dust-obscured component of the SFR in galaxies (see Kennicutt & Evans, 2012, and references therein).

Synchrotron emission detected in star-forming galaxies indicates that the ISM is magnetised. The strength of the magnetic field in nearby galaxies is typically of a few μG on the scale of the HI disc, with significant enhancements measured in the inner regions of some galaxies, within spiral arms, and inside molecular clouds (e.g. Beck et al., 1996; Chyży & Buta, 2008; Redaelli et al., 2019). The magnetic field might play an important role in star formation by contrasting the gravitational collapse of molecular clouds (Shu, 1977; McKee & Ostriker, 2007). Moreover, some authors have proposed that magnetic tension is effective in transferring part of the rotational energy of galactic discs to turbulence motions of the atomic gas (Velikhov, 1959; Chandrasekhar, 1960; Balbus & Hawley, 1991).

Lastly, cosmic rays produced by supernovae (SNe) also influence the ISM conditions, as they can dissociate the molecules in the inner and dense parts of molecular clouds. In addition, numerical simulations of the stratified ISM in disc galaxies have shown that anisotropic diffusion of cosmic rays can have an important impact on the gas vertical distribution (Simpson et al., 2016; Pfrommer et al., 2017).

1.3 Structure and kinematics of gas discs

Observations of 21-cm and CO emission lines allow to study not only the distribution of neutral gas in galaxies, but also its kinematics. Spectroscopic observations can be stored in a data cube whose three dimensions contain different pieces of information: x and y corresponds to the coordinates in the sky plane, while the third axis contains the spectral information. By slicing a data cube perpendicularly to the frequency axis, we obtain channel maps showing the intensity of the emission line at fixed Doppler shift with respect to the reference frequency. A galaxy moves as a whole at a systemic velocity (V_{sys}) with respect to an observer. This shifts the line centroid to longer (red-shift) or shorter (blue-shift) wavelengths depending on whether the galaxy motion is approaching to or receding from the observer. For a disc galaxy, the line centroid is also Doppler shifted by the large-scale rotation of the gas in the disc (Sect. 1.3.1), whereas the line profile broadening (i.e. velocity dispersion) is due to disordered motions of thermal and non-thermal nature (Sect. 1.3.3).

A possible approach to study the distribution and kinematics of gas in disc galaxies is based on moment maps. In particular, the 0th moment map obtained from a data cube gives the line intensity distribution on the sky, the 1st moment map yields the velocity field, and the 2nd moment map shows the line broadening. Position-velocity (PV) diagrams, which are also very useful to analyse gas kinematics, are obtained by slicing a data cube through the spectral axis and along a spatial direction. PV-diagrams are usually derived along the kinematic major axis of a disc to study its rotation curve, while slicing along the disc minor axis can give useful information about the gas velocity dispersion and radial motions.

1.3.1 The tilted-ring approach

A rotation curve of a galaxy is the one-dimensional representation of the circular velocity as a function of radius. The standard method to study the rotation curve of discs is the so-called ‘tilted-ring model’, which was first used by Rogstad et al. (1974) on the warped galaxy M83. After this pioneering work, the tilted-ring method has been successfully and extensively applied to several galaxies, both in the local and in the distant Universe (e.g. Begeman, 1987; Swaters, 1999; Battaglia et al., 2006; Di Teodoro & Fraternali, 2015; Iorio et al., 2017; Di Teodoro et al., 2016; Rizzo et al., 2018; Lelli et al., 2018). In this approach, the disc is assumed to be made of concentric thin annuli with increasing radius in which the emitting material is rotating in circular orbits. Each ring is described by four geometric and three kinematic parameters that vary with the galactocentric radius:

- the two coordinates of the ring centre (x_0, y_0) ;
- the inclination angle i between the galaxy plane and the line of sight;

- the positions angle θ , defined as the angle in the anti-clockwise direction between the north and the major axis of the receding side of a disc;
- the systemic velocity V_{sys} , which is the heliocentric velocity of the ring centre;
- the rotation velocity V_{rot} of the gas in circular orbits;
- the radial velocity, which takes into account non-circular motions.

This tilted-ring model can be fitted to galaxy observations in order to obtain the set of parameters which best reproduces the data to derive the disc rotation curve. To this aim, two fitting approaches are possible: one works in 2D and is based on velocity field map, while the other works 3D and uses all the information stored in the data cube. 2D methods have been successfully applied to high-resolution observations yielding reliable rotation curves and kinematic models (e.g. de Blok et al., 2008). In practice, for a certain position (x,y) in the plane of the sky, the observed velocity field (V_{los}) is fitted with the relation

$$V_{\text{los}}(x, y) = V_{\text{sys}} + V_{\text{rot}}(R) \sin i \cos \theta, \quad (1.2)$$

which yields the rotation velocity as a function of the galactocentric radius R .² However, this approach is affected by a severe issue, called beam smearing, when used on low resolution data. At low angular resolution, the finite size of the beam of a telescope causes the line emission to be smeared on the adjacent regions, where the emitting material has different projected rotation velocity. This results in an artificial broadening of the profile and, consequently, the rotation velocity and the velocity dispersion can be underestimated and overestimated, respectively (see Fig. 1.4). This effect is particularly important if there are strong velocity gradients, as in the case of the inner regions of massive galaxies where the rotation curve steeply rises.

An alternative approach to derive the disc kinematics consists in fitting the tilted-ring model to the whole data cube. This 3D method is much less affected by beam smearing and can obtain robust rotation curves and velocity dispersion also from observations at low spatial resolution (e.g. Swaters, 1999). In this Ph.D. thesis, we have used the software ^{3D}BAROLO (Di Teodoro & Fraternali, 2015) to model the kinematics of the atomic and the molecular gas in the disc of nearby galaxies using HI and CO emission line observations. This software has been extensively tested on emission line data cubes of both nearby and high-redshift galaxies to study the gas kinematics, performing significantly better than 2D methods (see Di Teodoro et al., 2016).

Rotation curve decomposition

The rotation curves obtained through HI and CO observations are very good tracers of the circular speed as a function of the galactocentric radius and of the

²For simplicity, in Eq. 1.2 we have neglected radial motions.

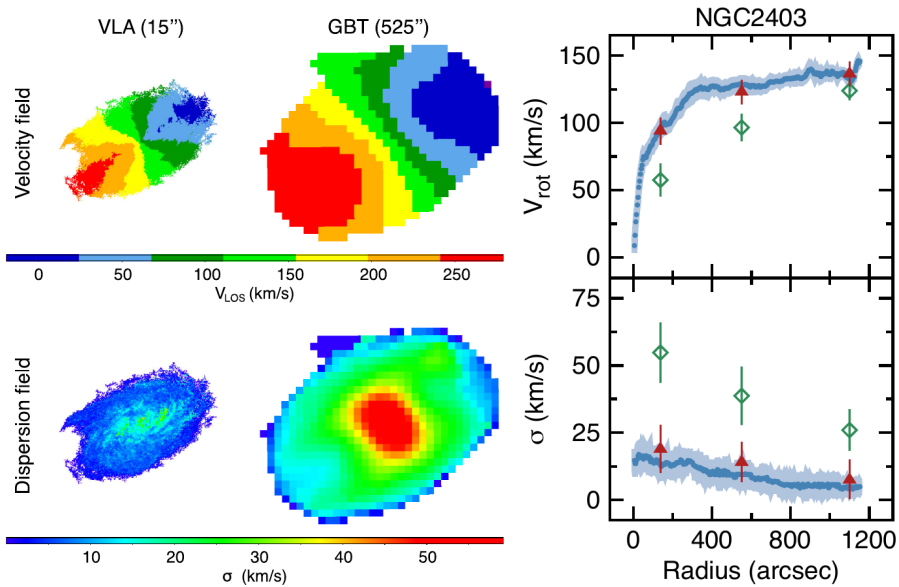


Figure 1.4 – *Left*: Beam smearing effect on the HI velocity field (1st moment map) and velocity dispersion field of the nearby spiral galaxy NGC 2403. The maps on the left are obtained from the high-resolution data cube from Fraternali et al. (2002), while those on the right are derived using low-resolution data (de Blok et al., 2014). *Right*: rotation curve (top) and velocity dispersion radial profile (bottom) of NGC 2403 obtained using the 2D approach on the low-resolution maps (green open diamonds) and ^3D BAROLO on either the high- (blue points) or the low-resolution (red triangles) data cube. From Di Teodoro & Fraternali (2015).

mass distribution of a galaxy. This is always true when the rotation velocity is much larger than the velocity dispersion (e.g. spiral galaxies). However, in the case of dwarf galaxies the velocity dispersion can be comparable to the rotation velocity, meaning that the pressure support against gravity is not negligible. Then, in order to obtain the circular speed, the rotation velocity must be corrected for this contribution (asymmetric drift correction; see e.g. Iorio et al., 2017).

The total mass distribution of a galaxy can be inferred by decomposing the observed rotation curve into the contributions of the single mass components, which are gas, stars and dark matter (DM; e.g. van Albada et al., 1985; Battaglia et al., 2006; Read et al., 2017; Li et al., 2020). From the HI and CO distributions, the contributions of the gaseous discs can be obtained in a relatively straightforward way. Concerning the stellar disc and bulge, their surface brightness can be measured using optical or near-IR (NIR) observations, but the main source of uncertainty on their mass distributions is the mass-to-light (M/L) ratio. A possible approach consists in assuming the stellar M/L given by stellar population synthesis models, which give M/L of 0.2-0.7 in

the NIR bands. The circular speed obtained by considering all the baryonic components is lower than the observed rotation curve, a discrepancy which is usually ascribed to an additional mass component, the DM halo (Rubin et al., 1978; Bosma, 1981; van Albada et al., 1985). In order to be fitted to the rotation curve, a density profile of the DM halo has to be assumed a priori. In the literature, different profiles depending on a number of free parameters can be found (see e.g. Li et al., 2020). Typically, spiral galaxies have rising rotation curves in the inner regions which flatten in the outskirts, hence a DM halo with a central density cusp reproduces well the observations (see e.g. de Blok et al., 2008; Frank et al., 2016; Li et al., 2020). Dwarf galaxies have instead slowly rising rotation curves and light stellar discs, suggesting that a cored DM profile is more appropriate in this case than a cusped one (e.g. Oh et al., 2008; Read et al., 2017).

Throughout this thesis, we make use of parametric mass models of nearby galaxies obtained through the decomposition of the rotation curve in order to derive the gravitational potential (Φ) of our galaxies. The assumptions of axisymmetry and centrifugal equilibrium for a rotating disc yield the relation between the circular speed and the potential (e.g. van Albada et al., 1985)

$$V_c^2(R) = -R \left[\frac{\partial \Phi(R, z)}{\partial R} \right]_{z=0}, \quad (1.3)$$

where $V_c(R)$ is the circular speed in the disc midplane $z = 0$. Hence, by integrating Eq. 1.3, it is possible to derive the gravitational potential of a galaxy once its circular speed (or mass distribution) is known.

1.3.2 Measuring the thickness of gaseous discs

Gaseous discs in galaxies are expected to be in vertical hydrostatic equilibrium, meaning that the vertical gravitational force generated by the galactic potential pulls the gas towards the midplane, but its action is balanced by the gradient along the vertical direction of the gas pressure due to thermal and non-thermal motions (velocity dispersion). As a function of the distance from the galaxy centre, the gravitational force weakens and the gas velocity dispersion decreases, becoming nearly flat beyond the stellar disc. The general effect on the distribution of the gas in vertical hydrostatic equilibrium is that gas scale height increases with the galactocentric radius (i.e. the disc flares).

The first direct measurements of the thickness of a galactic disc were obtained in the Milky Way using the HI observations (e.g. Burke, 1957; Kerr et al., 1957). Later, the flaring was confirmed also using CO observations (e.g. Sanders et al., 1984; Grabelsky et al., 1987). In nearby galaxies, the thickness has been studied mostly in edge-on systems using HI observations.

Sancisi & Allen (1979) used the apparent width of the edge channels in the HI data cube of NGC 891 to estimate the thickness of the gas layer at the

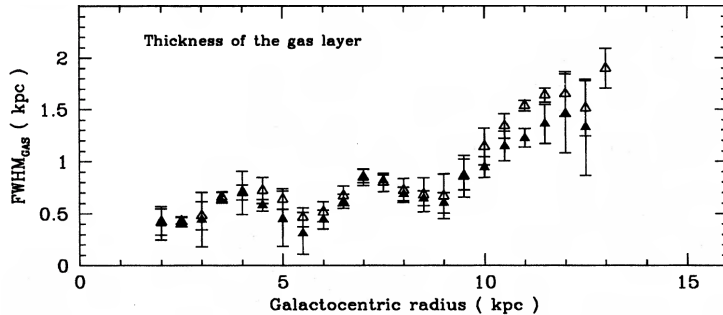


Figure 1.5 – Full-width-at-half-maximum of the HI layer for the edge-on galaxy NGC 4244. From Olling (1996).

disc edge, finding values of 1-2 kpc. A different methodology was proposed by Olling (1995) based on the assumption of hydrostatic equilibrium. Using the constraints given by the velocity dispersion and the rotation curve of the gas, he showed that it is in principle possible to determine the shape of the DM halo from the thickness of a disc seen edge-on or at relatively high inclination with respect to the line of sight. Olling (1996) measured the HI thickness in NGC 4244, an edge-on spiral galaxy, and found that this disc flares from about 400 pc in the inner regions to about 1.5 kpc at the largest radius (Fig. 1.5). Later, the thickness of edge-on or highly inclined gas discs (of either HI or CO) in nearby galaxies was investigated using similar methods by other authors (e.g. Kregel et al., 2004; O’Brien et al., 2010; Yim et al., 2011, 2014; Peters et al., 2017b; Yim et al., 2020). Every study found indications of the presence of the flaring.

However, the degeneracy between the inclination of the galaxy and the thickness of the HI disc can severely affect the observational determination of the flare (Swaters et al., 1997; Iorio, 2014, 2018). Other possible limitations are due to the presence of extra-planar gas and warps along the line of sight (Swaters et al., 1997), and the severe difficulty in measuring the velocity dispersion radial profile in edge-on galaxies (Sicking, 1997). The extra-planar gas appears to be ubiquitous in star-forming galaxies (Marasco et al., 2019) and, if not taken into account, can result in a significant overestimation of the gas disc thickness; a warp along the line of sight produces a similar effect (Zschaechner et al., 2011). Measuring the thickness of gas discs and the gas velocity dispersion is therefore a challenging task which requires a careful modelling of the kinematics of all the gas components of a galaxies, as well as suitable observations with high spatial resolution (to avoid beam smearing and resolve the disc vertical extent) and good signal-to-noise ratio.

1.3.3 Gas turbulence

As mentioned earlier in this Chapter, the velocity dispersion of neutral atomic gas measured from the emission line broadening is typically larger (10-15 km s^{-1}) than expected from the gas temperature ($\lesssim 8 \text{ km s}^{-1}$), indicating the presence of strong non-thermal motions. These latter are usually ascribed to turbulence, which consists of disordered motions between macroscopic portions of fluid.

Much theoretical effort has been put in order to develop an analytical theory to describe turbulence, but the complexity of this physical phenomenon did not allow to formulate a general model (Elmegreen & Scalo, 2004). For the scope of this thesis, we can focus on a relatively simple treatment of gas turbulence, which is called Kolmogorov theory (Kolmogorov, 1941). In this framework, the gas is assumed to be incompressible, meaning that the density of a fluid element cannot vary with time. In this regime, the turbulent entities, called ‘eddies’, have various physical sizes, which we define λ . The largest eddies form at the so-called driving scale L_D . The specific energy of the largest eddies is $\mathcal{E} \sim v_D^2$, where v_D is their turbulent speed on scales L_D . These large eddies transfer their kinetic energy to smaller scales by breaking down into smaller eddies, generating a turbulent cascade. The turbulence crossing time at the driving scale is $\tau_D \sim L_D/v_D$, hence the rate of specific energy transfer to smaller scales is $\dot{\mathcal{E}} \sim \mathcal{E}/\tau \sim v_D^3/L_D$. The energy is conserved throughout this cascade until the dissipation scale l_d is reached. Hence, the energy transfer rate at any scale λ , with $l_d < \lambda < L_D$, is $\dot{\mathcal{E}} \sim v_\lambda^3/\lambda$. This inertial scales are the range of validity of the Kolmogorov-Obukhov law (Kolmogorov, 1941; Obukhov, 1962) $v_\lambda \sim v_D(\lambda/L_D)^{1/3}$, which states that the turbulent velocity scales with the eddy size to the 1/3 power, thus most of the kinetic energy is in the largest eddies.

Below l_d , viscosity converts the kinetic energy into thermal energy. In order to have a stationary regime, the same amount of turbulent energy lost at the dissipation scale must be supplied at the driving scale. Turbulence is ubiquitously observed in the ISM, suggesting that some physical mechanism is continuously supplying kinetic energy. SN explosions are the prime suspect, as they can inject an enormous amount of energy in the ISM (for more details, see the reviews Mac Low & Klessen, 2004; Elmegreen & Scalo, 2004). Some authors (Tamburro et al., 2009; Utomo et al., 2019) however found that, in order to maintain turbulence with SNe alone, most of or all their energy should be used, in contrast with the value of a few percent expected from analytical and numerical models of SN remnant evolution (see Sect.1.4.4). Therefore, other mechanisms (e.g. gas accretion, rotational shear, magneto-rotational instability, gravitational instability) have been proposed to drive and sustain turbulence on the scale of galactic discs, but a general consensus on yet reached (e.g. Mac Low & Klessen, 2004). This conundrum is specifically addressed in Chapter 5, where we show that SNe are sufficiently energetic to sustain turbulence.

However, the assumption of incompressibility is likely a poor approximation for the ISM, where supersonic motions (e.g. SNe explosions) can produce shocks and enhance the gas density. In this case, compressible and incompressible modes of turbulence are present (e.g. Elmegreen & Scalo, 2004). The latter are solenoidal and conserve the kinetic energy, while the former do not. Indeed, shocks convert kinetic energy into internal energy, which can also be lost radiatively. In this scenario, the kinetic energy is not conserved throughout the cascade and part of it can be dissipated at any scale. Based on the Helmholtz decomposition theorem (Helmholtz, 1896), it is possible to separately study compressible and incompressible modes in realistic ISM conditions, but the applicability of this approach is unfortunately limited by the continuous transfer of kinetic energy between compressible and incompressible modes (e.g. through oblique shocks). Solenoidal modes are expected to be dominant with respect to compressible ones (e.g. Elmegreen & Scalo, 2004). In molecular clouds, this is suggested by observations in our Galaxy (Orkisz et al., 2017) and numerical simulations of SN-driven supersonic turbulence, which predict that the ratio between compressible and solenoidal motions is about $1/3 - 1/2$ (Padoan et al., 2016; Pan et al., 2016). Hence, the assumption of incompressibility might not be an excessively coarse approximation in the ISM.

Before moving to the next section, it is worth to mention that turbulence likely plays an important role in star formation. The turbulent energy contributes to counteract the gravitational collapse of molecular clouds and turbulent fragmentation shapes their internal structure and mass distribution (Alves et al., 2007; Henshaw et al., 2020). Indeed, recent theories of star formation in disc galaxies propose that supersonic turbulence in the ISM controls the process both on the scales of molecular clouds and globally on the whole disc (e.g. Mac Low & Klessen, 2004; McKee & Ostriker, 2007; Krumholz, 2014).

1.4 Star formation in the nearby Universe

1.4.1 Star formation diagnostics

As mentioned at the beginning of this Chapter, the SFR is a key property to classify galaxies and understand their evolutionary stage. This quantity can be measured using different diagnostics and tracers of recent star formation, depending on the distance and dust content of the observed system (Kennicutt & Evans, 2012).

In molecular clouds in our Galaxy, the SFR can be directly measured by counting young stellar objects within the cloud. In galaxies within a few Mpc, it is possible to resolve individual stars with photometric observations and build color-magnitude diagrams (CMDs). These diagrams can be analysed using synthetic stellar populations obtained from stellar evolution libraries in order to derive the star formation history (SFH) of a stellar system (Tolstoy et al.,

2009; McQuinn et al., 2015). Using the SFH, the SFR averaged over a given time interval can be estimated.

When resolved stellar populations are not accessible to observations, the UV emission from young and massive O-B stars can be used to directly trace the SFR (e.g. Leroy et al., 2008; Bigiel et al., 2008). In particular, FUV emission traces stars with ages up to 100 Myr, while the NUV emission includes the contribution of slightly older stars with ages up to 200 Myr. The main drawback of using UV light to estimate the SFR is due to dust attenuation, which absorbs UV photons and re-emits them in the IR wavelengths. It is possible to correct for dust attenuation by assuming an intrinsic FUV-NUV color, but this method was found to be affected by large uncertainties (Kennicutt & Evans, 2012; McQuinn et al., 2015). Hence, other approaches based on the combination of FUV and IR luminosities have been developed (e.g. Leroy et al., 2008; Hao et al., 2011).

Emission lines from photo-ionised gas are other useful SFR indicators, which can trace the most recent star formation events (e.g. Kennicutt, 1983, 1998). One of the most used emission lines is $H\alpha$, which is produced by stars younger than 10 Myr and, like UV light, needs to be corrected for the dust attenuation. However, in low-density regions of galaxies, the SFR is typically low and the initial mass function is not sampled uniformly, in particular in the high-mass end, suppressing $H\alpha$ emission (e.g. Lee et al., 2009). Similarly, the lifetime of UV-emitting stars spans a wider range than the stars responsible for $H\alpha$ emission, hence UV emission is less affected by temporal stochasticity (e.g. Weisz et al., 2012, see also Kennicutt & Evans 2012 and references therein).

As mentioned above, the IR light is very useful to derive the total SFR of a galaxy including also the dust-obscured component. To this aim, the typical approach is using relations which combine the FUV or $H\alpha$ luminosities with the IR luminosity (either total or at a specific wavelength; Leroy et al., 2008; Hao et al., 2011). It is worth to notice that, by using IR emission only, one can underestimate the actual SFR as the unattenuated components is not included.

Other SFR indicators which can be used to derive the SFR of a galaxy are the radium continuum, which is produced by free-free emission from HII regions, and the X-ray emission associated with very young stellar objects, such as very massive stars and SNe (see Kennicutt & Evans, 2012, and reference therein).

These diagnostics have been extensively used in the literature for many applications, including empirical studies of the relation between the gas content of a galaxy and its SFR as we see below.

1.4.2 Empirical star formation laws

Star formation laws are fundamental relations between the SFR surface density and the gas surface density. Schmidt (1959) was the first to propose a power-law star formation relation based on the volume densities of the atomic gas ρ_{HI} and the SFR ρ_{SFR} , which reads $\rho_{\text{SFR}} \propto \rho_{\text{HI}}^n$. Using the distribution of young stars in the MW, he estimated that the index n of this power law is between 2 and

3. Later empirical works used instead the observed surface densities as they are directly accessible by observations (e.g. Sanduleak, 1969; Kennicutt, 1989, 1998). We briefly review in this section the different star formation laws derived in the literature, distinguishing between relations based on global or local quantities. More details can be found in the introductory sections of Chapters 2, 3 and 4.

Among global relations, we find the most famous star formation law, the so-called Schmidt-Kennicutt (SK) relation (Fig. 1.6). This was derived using the total gas (HI+H₂; Σ_{gas}) and the SFR (Σ_{SFR}) surface densities averaged over the star-forming disc (Kennicutt, 1998; de los Reyes & Kennicutt, 2019, e.g.). The SK relation is $\Sigma_{\text{SFR}} \propto \Sigma_{\text{gas}}^N$ with $N \simeq 1.4$ for gas densities above $10 M_{\odot} \text{pc}^{-2}$, while a turnover appears below this density. Some authors also found global correlations between the mass (or luminosity) of tracers of dense molecular gas, such as CO and hydrogen cyanide (HCN), and the total SFR of normal star-forming galaxies and starbursts in the local Universe (e.g. Gao & Solomon, 2004; de los Reyes & Kennicutt, 2019; Jiménez-Donaire et al., 2019).

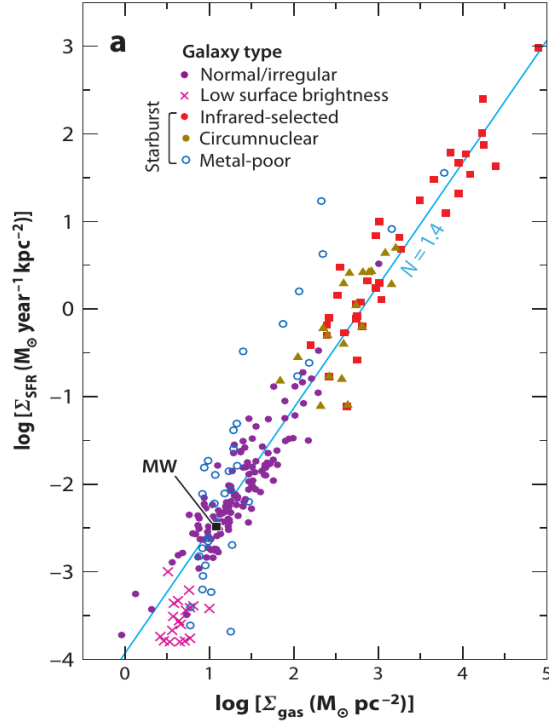
The results of studies on spatially resolved galaxies are in general similar to those obtained using global quantities. In particular, many authors have investigated the SK law between the gas and the SFR using azimuthally averaged radial profiles, pixel-by-pixel measurements and quantities averaged over sub-kiloparsec regions of the star-forming disc (e.g. Kennicutt, 1989; Wong & Blitz, 2002; Kennicutt et al., 2007; Schuster et al., 2007; Leroy et al., 2008; Bigiel et al., 2008), confirming the presence of the break in the SK relation in the low-density, HI-dominated and metal-poor environments. Also the correlation between the molecular gas and the SFR was assessed at kiloparsec and sub-kiloparsec scales in high-density, molecular gas- and metal-rich regions (Wong & Blitz, 2002; Heyer et al., 2004; Kennicutt et al., 2007; Bigiel et al., 2008; Marasco et al., 2012; Leroy et al., 2013).

1.4.3 Theories of galactic-scale star formation

Empirical star formation relations are often interpreted from a theoretical point of view, aiming to understand the physical mechanism which regulates the conversion of gas into stars. In this section, we adopt a top-down approach based on the idea that the SFR is mostly driven by galactic-scale processes (Krumholz, 2014). Clearly, this approach is not applicable to molecular clouds or filaments in the ISM, but investigating this regime of star formation is beyond the scope of this thesis.

The most straightforward explanation of the SK law with $N \simeq 1.4$ is based on the gravitational instability and postulates that the SFR surface density is given by the gas mass per unit surface which is converted into stars per unit free-fall timescale (Madore, 1977). This simple model implicitly assumes that the disc is thin or has a constant thickness, which implies that the surface densities are proportional to the volume densities. An alternative gravity-driven model is based on the local disc instability for a rotating disc experiencing

Figure 1.6 – Global SK law based on the surface densities SFR and gas (HI+H₂) averaged over the star-forming disc; each point is an individual galaxy. Purple points represent normal spiral and irregular galaxies, red squares IR-selected starburst galaxies, and golden triangles indicate circumnuclear starbursts. The black square shows the MW position and magenta crosses represent nearby low-surface-brightness galaxies. Open blue circles denote low-mass irregular and starburst galaxies with metal abundances $< 0.3 Z_{\odot}$, which indicate a systematic deviation from the SK relation with slope $N = 1.4$ shown by light blue line (not a fit to these data). From Kennicutt & Evans (2012).



a density perturbation (Toomre, 1964). This model predicts that the disc locally fragments in star-forming clouds where the so-called Toomre criterion for instability is verified. One advantage of this model is that it predicts the presence of a density threshold for star formation based on Toomre criterion, which may explain the observed density threshold of the SK law. A second advantage of this model is that Toomre criterion depends on the epicycle frequency, suggesting that the timescale of the process depends on the rotation velocity of the disc. This may explain the empirical correlation with the orbital period found by some authors (e.g. Kennicutt, 1998; de los Reyes & Kennicutt, 2019). Models based on disc gravitational instabilities are disfavoured by spatially resolved observations showing that star formation is actually ongoing in regions which are stable according to Toomre criterion (Hunter et al., 1998a; Thilker et al., 2007a; Boissier et al., 2007; Leroy et al., 2008). However, even if the Toomre criterion is not fully satisfied, it is possible that discs are marginally unstable against non-axisymmetric perturbations (e.g. Romeo & Falstad, 2013, and § 8.3.3 in Cimatti, Fraternali, & Nipoti 2019). Other classes of models have also tried to explain the empirical correlation with the orbital period in terms of cloud collisions or spiral-arm shocks (e.g. Wyse, 1986; Wang & Silk, 1994a; Shu et al., 2007).

Strong observational evidence, such as holes in HI discs and SN remnants, indicate that stellar feedback influences the surrounding ISM. Indeed, theoretical models of feedback-regulated star formation have been investigated by many authors using both an analytical approach and numerical simulations (Talbot & Arnett, 1975; Dopita, 1985; Ostriker et al., 2010; Agertz et al., 2013; Hu et al., 2016). In particular, some of these models predict that the SFR surface density should correlate with the gas and the stellar surface density (Σ_*) as $\Sigma_{\text{SFR}} \propto \Sigma_{\text{gas}}^n (\Sigma_{\text{gas}} + \Sigma_*)^m$ (e.g. Talbot & Arnett, 1975; Dopita & Ryder, 1994). This correlation, the so-called ‘extended-Schmidt law’, has been observed on global scales for nearby star-forming galaxies (Shi et al., 2011; Roychowdhury et al., 2017; Shi et al., 2018), but it does not appear to work significantly better than the SK law in spatially resolved galaxies (e.g. Boissier et al., 2003, see also Krumholz et al. 2012). For example, in the self-regulating scenario proposed by Ostriker et al. (2010), star formation in spiral galaxies is regulated by UV radiation produced by young stars which heats the gas in the disc just as much as it is required to balance the vertical gravitational force. These authors assumed that the mass exchange between the self-gravitating gas and the diffuse ISM components is regulated by thermal and vertical dynamical equilibrium, and that the SFR is proportional to the mass of the self-gravitating component. This model predicts that Σ_{SFR} is a function of the total gaseous surface density and the midplane density of stars plus DM. However, this relation had limited success in reproducing the observed radial profile of the SFR surface density in nearby spiral galaxies.

Krumholz et al. (2012) formulated a theory based on a molecular and volumetric star formation law in which star formation is regulated by gravitational instability, hence the SFR per unit volume is given by the fraction of gas mass which is converted into stars per free-fall time (τ_{ff}) and per unit volume (see also Madore, 1977). In this model, the diversity of the empirical correlations between the gas and the SFR is the result of the different three-dimensional sizes and internal clumpiness of various star-forming environments. In other words, the volume of the observed star-forming region can be very different at fixed surface density, producing different correlations in different environments. These projection effects were taken into account by calculating the free-fall time specifically for different regimes, from molecular clouds to high redshift galaxies. This method was applied to a collection of measurements of the gas and the SFR surface densities in MW molecular clouds, local galaxies, and unresolved local discs and high redshift starbursts, finding that the same correlation ($\Sigma_{\text{SFR}} \propto \Sigma_{\text{gas}}/\tau_{\text{ff}}$) holds for these different star-forming environments. However, Krumholz et al. (2012) did not explore the regime of dwarf galaxies, hence the validity of this model in the low-density and HI-dominated environments remains unclear.

These are only some examples of the variety of models which aim to explain or predict empirical star formation relations. Some discrepancies between

theory and observations are however still present, preventing to reach definitive conclusions on which physical mechanism is regulating the conversion of gas into stars.

1.4.4 Stellar feedback

Young and massive stars significantly influence the ISM of galaxies via stellar winds, ionising radiation, and SN explosions. These forms of feedback can have either a positive (e.g. shock compression, gas accretion) or a negative (e.g. gas ejection or heating) effect on star formation. As mentioned in Sect. 1.3.3, feedback from SN explosions is likely the engine of turbulence in the ISM, as we will see in Chapter 5. Indeed, SNe are the most powerful form of stellar feedback and are expected to inject a significant amount of energy in the surrounding medium.

Supernova remnant evolution

When a SN explodes, a large amount of gas is ejected in the ISM with highly supersonic speed, producing a strong shock in the surrounding gas (e.g. Chevalier, 1974; Chevalier & Gardner, 1974; Cimatti, Fraternali, & Nipoti, 2019). The shocked material forms an expanding shell, which is called SN remnant (SNR). The evolution of this SNR can be divided in two phases, the adiabatic (or Sedov) phase and the radiative phase. In the former, which lasts for $\sim 10^4$ yr, the SN energy is conserved and equally distributed in kinetic and internal energy. The shell radius and speed are of the order of ten parsec and a few hundreds km s^{-1} , respectively, with very weak dependence on the ambient density. The adiabatic phase ends when radiative losses become significant. In the second phase, radiative losses are generated by the thin expanding shell, while the hot interior remains adiabatic. The shell is larger (a few tens of parsec) but expands more slowly ($\lesssim 100 \text{ km s}^{-1}$) than in the adiabatic phase. After a few Myr, the radiative phase ends and the shell expansion stops as its speed reaches the typical values of the ISM motions (i.e. $\sim 10 \text{ km s}^{-1}$). Then, the SNR mixes with the surrounding gas and releases its kinetic energy in the ISM. Despite the initial SN energy was mostly kinetic, the energy equipartition in the adiabatic phase and the radiative losses imply that only a very small fraction ($\lesssim 10\%$) of the SN energy is transferred as kinetic energy to the ISM. This fraction is typically used to define the SN efficiency η , which is a fundamental parameter to understand the role of SN feedback in sustaining turbulent motions in the ISM (see Chapter 5).

Evolution of stellar wind bubbles

Massive OB stars eject a significant amount of gas in the ISM through powerful winds, which expand as bubbles. These latter can be divided in three regions

(Weaver et al., 1977). The innermost one is constituted by the expanding wind, which is continuously emitted by the star. The outermost region is a shell of shocked ISM that surrounds the intermediate region composed of wind material perturbed by a so-called reverse shock. This latter is generated by the impact between the wind and the outermost shell. The gas in the bubble is very hot and behaves adiabatically, while the external shell evolves radiatively. Concerning the energy budget of wind bubbles, half of the total emitted energy of the wind goes into internal energy of the bubbles. The remaining energy goes in the shell and about 20% of this is in the form of kinetic energy. Nearly all this fraction of the wind total energy is transferred to the ISM at the end of the expansion, meaning that stellar winds are in principle more efficient than SNe.

Super-bubbles

Massive OB stars are typically located in associations and evolve nearly simultaneously. Therefore, when these stars emit winds, the individual bubbles merge forming a large and common super-bubble delimited by a super-shell. Progressively, these stars stop emitting winds and start to explode as SNe (Mac Low & McCray, 1988). In this phase, the super-shell expands driven by the SN explosions, which represent a powerful and long-lasting source of kinetic energy. Inside the super-bubble, the medium is more rarefied than the ISM outside the super-shell, hence super-bubbles encounter less resistance in their expansion and are therefore more efficient in transferring kinetic energy to the ISM with respect to a single SNR. Super-bubbles can reach much larger sizes than SNRs and eventually exceed the scale height of the gas disc, resulting in a so-called ‘blow-out’ (Mac Low et al., 1989; Koo & McKee, 1992; Keller et al., 2014). In this case, part of the gas in the super-shell and in the super-bubble is expelled from the disc into the gaseous halo (e.g. Melioli et al., 2008, 2009), leaving a characteristic hole in the gas distribution (e.g. Kamphuis et al., 1991; Puche et al., 1992; Boomsma et al., 2008). The fate of this gas can either be to fall back into the disc, in the so-called galactic fountain cycle (Shapiro & Field, 1976; Bregman, 1980), or to leave the galaxy if its speed exceeds the escape speed (galactic wind; Veilleux et al., 2005; Melioli et al., 2015; McQuinn et al., 2018). The fact that super-bubbles can reach the size of the disc thickness will be crucial for the study of ISM turbulence in Chapter 5.

1.5 Thesis outline

In this Ph.D. thesis, we address two important aspects of the link between star formation and neutral gas in disc galaxies: star formation laws and the origin of ISM turbulence. The common theme throughout this work is the importance of the gas disc thickness and the crucial role of the flaring. In particular, we calculated the scale height of gas discs in dwarf and spiral galaxies in the nearby

Universe, relying on the assumption of vertical hydrostatic equilibrium. To do so, we analysed the kinematics of HI and CO using emission line data cubes and adopting the 3D tilted-ring modelling approach, which allowed us to obtain a robust measurement of the gas velocity dispersion. We used parametric models of the mass distribution obtained through the decomposition of the rotation curve to calculate the gravitational potential of these galaxies.

In Chapter 2, we use the scale height to convert the projected surface densities of the atomic gas, the molecular gas, and the SFR to the corresponding volume densities. We apply this methodology then to a sample of 12 nearby galaxies in order to derive volumetric star formation (VSF) laws. Due to dearth of information about the vertical distribution of the SFR in our galaxies, we could not derive precisely the index of these relations involving the volume densities.

Chapter 3 aims to overcome this latter issue by measuring the scale height of SFR tracers in our Galaxy. In particular, we use classical Cepheids and compare their scale height with that of the gas in hydrostatic equilibrium. We also derive the volume densities of the atomic gas, the molecular gas and the SFR in our Galaxy, finding that the same VSF laws found in Chapter 2 are valid in the MW.

In Chapter 4, we extend the study of these volumetric relations to the regime of dwarf galaxies aiming to test their validity in HI-dominated and low-metallicity environments, where star formation laws based on the surface densities break down. The outermost star-forming regions of spiral galaxies are also included in this study.

Chapter 5 aims to understand whether the ISM turbulence can be maintained by SN explosions alone. The novelty of our model consists in taking into account the flaring of the gas discs in the dissipation timescale of the turbulent energy. Using a sample of ten nearby galaxies, we compare the energy expected from this model with the observed kinetic energy of the neutral gas. This latter is calculated using the velocity dispersion and the surface density of the gas. We also investigate the contribution of the gas thermal energy to the observed energy.

Finally, Chapter 6 summarises the main results of this thesis and provides a brief outlook for future applications.

CHAPTER 2

**Volumetric star formation
laws of disc galaxies**

based on

— C. Bacchini, F. Fraternali, G. Iorio, and G. Pezzulli —

Astronomy & Astrophysics, 2019, 622, A64.

Abstract

Star formation (SF) laws are fundamental relations between the gas content of a galaxy and its star formation rate (SFR) and play key roles in galaxy evolution models. In this Chapter, we present new empirical SF laws of disc galaxies based on volume densities. Following the assumption of hydrostatic equilibrium, we calculated the radial growth of the thickness of the gaseous discs in the combined gravitational potential of dark matter, stars, and gas for 12 nearby star-forming galaxies. This allowed us to convert the observed surface densities of gas and SFR into the deprojected volume densities. We found a tight correlation with slope in the range 1.3 – 1.9 between the volume densities of gas (HI+H₂) and the SFR with a significantly smaller scatter than the surface-based (Kennicutt) law and no change in the slope over five orders of magnitude. This indicates that taking into account the radial increase of the thickness of galaxy discs is crucial to reconstruct their three-dimensional density profiles, in particular in their outskirts. Moreover, our result suggests that the break in the slope seen in the Kennicutt law is due to disc flaring rather than to a drop of the SF efficiency at low surface densities. Surprisingly, we discovered an unexpected correlation between the volume densities of HI and SFR, indicating that the atomic gas is a good tracer of the cold star-forming gas, especially in low density HI-dominated environments.

2.1 Introduction

The first formulation of an empirical star formation (SF) law was proposed by Schmidt (1959) in the shape of a power law

$$\rho_{\text{SFR}} \propto \rho_{\text{HI}}^n, \quad (2.1)$$

where ρ_{SFR} is the star formation rate (SFR) per unit volume and ρ_{HI} is the HI volume density; at that time, it was not possible to observe molecular gas emission. Using the distribution of young stars in the Milky Way (MW), he suggested that the index n of this power law is between 2 and 3. Unfortunately, if we focus on galaxies outside the MW, we can directly observe only the projected quantities, for example the surface densities, so Schmidt's approach is less suitable.

The works of Kennicutt (1989, 1998) set the current standard method to investigate SF law. Using a sample of nearby star-forming galaxies, Kennicutt (1989) derived a relation involving the radial profiles of the gas and the SFR surface densities (see also Martin & Kennicutt, 2001; Kennicutt et al., 2007). The so-called Kennicutt (or Schmidt-Kennicutt) law is

$$\Sigma_{\text{SFR}} \propto \Sigma_{\text{gas}}^N, \quad (2.2)$$

where Σ_{SFR} and Σ_{gas} are the surface densities of SFR and total gas (HI+H₂). However, this surface-based power law showed a break at densities below a threshold value. Later, Kennicutt (1998) collected a sample of spiral galaxies and starbursts to study the SF law over a range of seven orders of magnitude. Using surface densities integrated over the entire disc, he found a single power-law correlation with an index of $N = 1.4 \pm 0.15$. In the next two decades, there was much work on two main issues of the SF law: the first issue refers to the gas phase that better correlates with SF and the second concerns the possibility that the power-law index changes in particular environments, producing a break in the relation.

About the first issue, several observational studies claimed that the vital fuel of SF is molecular gas. Indeed, a gas cloud can gravitationally collapse only if its temperature is low enough, and molecules are very efficient coolants. Bigiel et al. (2008) studied the SFR-H₂ relation in 18 nearby galaxies through pixel-to-pixel analysis and radial profiles extraction. These authors found, on a sub-kiloparsec scale, a linear correlation between SFR and molecular gas surface densities (see also Wong & Blitz, 2002; Kennicutt et al., 2007; Bolatto et al., 2011; Schrubba et al., 2011; Marasco et al., 2012; Leroy et al., 2013). Similarly, Lada et al. (2010) found a linear relation linking the mass of Galactic molecular clouds and the number of hosted young stellar objects.

However, molecular clouds form from atomic gas and, after the SF has occurred, they are destroyed by stellar feedback. Hence, we would expect the atomic or total gas to correlate with SFR, as originally found by Schmidt (1959).

On the contrary, Leroy et al. (2008) found no correlation on sub-kiloparsec scale between HI and SFR in nearby star-forming galaxies (see also Kennicutt et al., 2007). The picture changes in HI-dominated environments such as the outskirts of spiral galaxies and dwarf galaxies, where the SFR seems to correlate also with atomic gas, but the efficiency of SF dramatically drops at these low surface densities (e.g. Ferguson et al., 1998; Bigiel et al., 2010; Bolatto et al., 2011; Schruba et al., 2011; Yim & van der Hulst, 2016).

The second issue about the Kennicutt law concerns the shape of the classical relation involving the total gas and the SFR. Bigiel et al. (2008) found that the Kennicutt law index changes at $\Sigma_{\text{gas}} \approx 9 \text{ M}_{\odot} \text{ pc}^{-2}$, which approximately corresponds to the transition to low-density and HI-dominated environments (see also Bolatto et al., 2011; Schruba et al., 2011; Dessauges-Zavadsky et al., 2014). As a consequence, a surface-based, double power-law relation was proposed and its break was explained as an abrupt change in the efficiency of SF at a specific threshold density (see also Schaye, 2004). Similarly, Roychowdhury et al. (2015) studied the Kennicutt law in HI-dominated regions of nearby spirals and dwarf irregulars, and found a power-law relation with slope 1.5 for both kind of galaxies. Their relation showed however an offset of one order of magnitude with respect to the SF law for more central regions, where the gas surface density is higher. Despite that the existence of the break is not firmly confirmed as several authors recovered the classical single power law, sometimes with a different index. For example, Boissier et al. (2003) and Barnes et al. (2012) estimated $N \approx 2$ and $N = 2.8 \pm 0.3$, respectively, in nearby star-forming galaxies, Heyer et al. (2004) found $N \approx 3.3$ for M33, and Sofue (2017) measured $N = 1.12 \pm 0.37$ in the MW.

From a theoretical point of view, it is possible to predict the power-law index assuming that a given physical process regulates the birth of stars. The simplest model involves the gravitational collapse and the SF timescale is set by the free-fall time (Madore, 1977). As a result, the SFR is given by the fraction of gas converted into stars per free-fall time, so $\rho_{\text{SFR}} \propto \rho_{\text{gas}}^{1.5}$. This corresponds to $\Sigma_{\text{SFR}} \propto \Sigma_{\text{gas}}^{1.5}$ if the disc thickness is constant with the galactocentric radius. This basic model has been proposed to explain the observed Kennicutt law with index $N \approx 1.4$. Another possible SF timescale is the orbital time in the disc, which is related to the rotation velocity of the galaxy (e.g. Kennicutt, 1998; Kennicutt et al., 2007; Boissier et al., 2003; Bolatto et al., 2017). Alternatively, if the balance between turbulent motions and gravity is assumed to regulate SF, the predicted slope is $N \approx 2$ (e.g. Larson, 1981; Elmegreen, 2015). Another class of models aims to predict the critical density for the broken power law. For example, Toomre (1964) formalism allows us to estimate the critical density above which a gas disc is gravitationally unstable and the shear is low enough to have SF (e.g. Kennicutt, 1989; Romeo, 1990, 1992; Pickering et al., 1999; Hunter et al., 1998b; Pickering et al., 1999; Martin & Kennicutt, 2001). These are only a few examples among the plenty of possible models that have been

proposed to explain or predict observations (see Krumholz 2014 and references within).

Overall, the picture is very complex and the shape of the relation between gas and SF remains unknown. Moreover, it is unclear which gas phase matters most for SF, whether molecular or atomic or both. Having a robust recipe for SF is very important, as the SF law is a key ingredient of numerical simulations and theoretical models of galaxies formation and evolution (e.g. chemical evolution of discs). All the SF laws mentioned so far (except that in Schmidt, 1959) are based on surface densities because they are easy to observe, but the volume densities are likely more physically meaningful quantities than surface densities. In addition, gas discs in galaxies are expected to be nearly in hydrostatic equilibrium, so their thickness grows going from the inner radii to the outskirts and the resulting projection effects are not negligible (e.g. van der Kruit & Searle, 1981a; Abramova & Zasov, 2008; Banerjee et al., 2011; Elmegreen, 2015). The purpose of this Chapter is to build a volumetric star formation (VSF) law through a method to convert surface densities to volume densities in local disc galaxies. The general model is described in Sect. 2.2, then Sect. 2.3 explains how we selected the sample of galaxies to test this model. The thickness of the gas disc for each galaxy is calculated in Sect. 2.4 and the resulting volumetric correlations are shown in Sect. 2.5. In Sect. 2.6, our results are discussed and compared to other works. Finally, we provide summary and conclusions in Sect. 2.7.

2.2 Volume densities from hydrostatic equilibrium

In order to build the VSF law, we need the volume densities of atomic gas (ρ_{HI}), molecular gas (ρ_{H_2}), and SFR (ρ_{SFR}). In the following, we show how the simple assumption of the vertical hydrostatic equilibrium allows us to estimate these quantities and the ingredients that are needed to calculate them.

2.2.1 Hydrostatic equilibrium

Let us consider a rotating disc of gas in hydrostatic equilibrium in the gravitational potential Φ of a galaxy, which is assumed to be symmetric with respect to the rotation axis (axisymmetry) and the plane $z = 0$ (midplane). The vertical distribution of the gas density $\rho(R, z)$ can be described by the stationary Euler equation in the z direction as follows:

$$\frac{\partial\Phi(R, z)}{\partial z} = -\frac{1}{\rho(R, z)} \frac{\partial P(R, z)}{\partial z}, \quad (2.3)$$

where $P(R, z)$ is the gas pressure due to the combination of thermal and turbulent motions. At a given galactocentric radius R , we take the three

components of the velocity dispersion of the gas to have the same value in all directions $\sigma_x(R) = \sigma_y(R) = \sigma_z(R) = \sigma(R)$ (isotropy). Then, we assume that the velocity dispersion σ is constant along z (vertically isothermal gas). Therefore, on galactic scales, the global profile of σ depends only on R and the gas pressure can be written as (e.g. Olling, 1995)

$$P(R, z) = \sigma^2(R)\rho(R, z) \quad (2.4)$$

and Eq. 2.3 can be solved for the density profile

$$\rho(R, z) = \rho(R, 0) \exp \left[-\frac{\Phi(R, z) - \Phi(R, 0)}{\sigma^2(R)} \right], \quad (2.5)$$

where $\rho(R, 0)$ and $\Phi(R, 0)$ are the radial profiles of the gas volume density and the total gravitational potential evaluated in the midplane of the galaxy.

2.2.2 Gravitational potential

The gravitational potential of a galaxy can be obtained through the Poisson equation for gravity once its mass distribution is known. The main mass components of star-forming galaxies are dark matter (DM), stars in the form of a disc and a bulge (if present), and gas.

Dark matter halo

The DM distribution can be modelled as a pseudo-isothermal halo (van Albada et al., 1985) or a Navarro-Frenk-White (NFW) halo (Navarro et al., 1996). For simplicity, the DM halo distribution is assumed spherical. The pseudo-isothermal density profile is

$$\rho_{\text{DM}}(r) = \rho_{\text{DM},0} \left(1 + \frac{r^2}{r_c^2} \right)^{-1}, \quad (2.6)$$

where $\rho_{\text{DM},0}$ is the central volume density and r_c the core radius. The NFW profile is

$$\rho_{\text{DM}}(r) = \rho_{\text{DM},0} \left(\frac{r}{r_s} \right)^{-1} \left(1 + \frac{r}{r_s} \right)^{-2}, \quad (2.7)$$

where r_s is defined by $c \equiv r_{200}/r_s$ with c the concentration parameter and r_{200} the radius within which the average density contrast with respect to the critical density of the Universe equals 200. The spherical radius is $r = \sqrt{R^2 + z^2}$ in cylindrical coordinates.

Stellar disc

The stellar disc mass distribution is modelled with an exponential radial profile and a sech^2 vertical profile (van der Kruit & Searle, 1981b),

$$\rho_{\star}(R, z) = \rho_{\star,0} \exp\left(-\frac{R}{R_{\star}}\right) \text{sech}^2\left(\frac{z}{z_{\star}}\right), \quad (2.8)$$

where $\rho_{\star,0}$ is the central density, R_{\star} is the stellar scale length, and z_{\star} the scale height, which is assumed to be $z_{\star} = R_{\star}/5$ (see van der Kruit & Freeman 2011 and references within).

Stellar bulge

The bulge mass distribution is modelled using a sphere with exponential profile,

$$\rho_{\text{b}}(r) = \rho_{\text{b},0} \exp\left(-\frac{r}{r_{\text{b}}}\right), \quad (2.9)$$

where $\rho_{\text{b},0}$ and r_{b} are central density and scale radius. The justification for the choice of Eq. 2.9 is discussed in Sect. 2.3.2.

Gas surface density

In order to model the variety of gas distributions in galaxies (both for the atomic and molecular phases), we need a flexible model. Hence, we combined a polynomial and an exponential function

$$\Sigma(R) = \Sigma_0 \left(1 + C_1 R + C_2 R^2 + C_3 R^3 + C_4 R^4\right) \exp\left(-\frac{R}{R_{\Sigma}}\right), \quad (2.10)$$

where Σ_0 is the central surface density, R_{Σ} is the scale radius, and C_i are the polynomial coefficients.

2.2.3 Velocity dispersion

In previous works (e.g. Abramova & Zasov, 2008; Leroy et al., 2008; Elmegreen, 2015), the gas velocity dispersion was assumed to be constant with radius. On the contrary, several measurements of the velocity dispersion in nearby galaxies and in the MW show that it decreases with increasing galactocentric radius, following an exponential or linear trend (e.g. Fraternali et al., 2002; Boomsma et al., 2008; Tamburro et al., 2009; Mogotsi et al., 2016; Marasco et al., 2017). Hence, we derived the profile of $\sigma(R)$ from the observations (Sect. 2.4.1) and modelled it, for the atomic and molecular phases, with the exponential function

$$\sigma(R) = \sigma_0 \exp\left(-\frac{R}{R_{\sigma}}\right), \quad (2.11)$$

where σ_0 is the velocity dispersion at the galaxy centre and R_σ is a scale radius. This function can also adequately model a linear decline for large R_σ compared to the galaxy size.

2.2.4 Scale height definition

By means of a second order Taylor expansion of Φ (see e.g. Olling, 1995; Koyama & Ostriker, 2009), Eq. 2.5 can be approximated near the midplane by a Gaussian profile,

$$\rho(R, z) = \rho(R, 0) \exp \left[-\frac{z^2}{2h^2(R)} \right], \quad (2.12)$$

where the radial profile of the vertical scale height $h(R)$ is

$$h(R) \equiv \sigma(R) \left[\left(\frac{\partial^2 \Phi(R, z)}{\partial z^2} \right)_{z=0} \right]^{-\frac{1}{2}}. \quad (2.13)$$

The roles of the gravitational potential and the velocity dispersion are opposite, as the first drags the gas towards the midplane, while the second gives rise to a force directed upward. As shown in Sect. 2.4, in real galaxies both terms decrease with radius, but the global result is an increase of the scale height with radius.

Eq. 2.13 is an analytical approximation for the scale height and it is valid if the vertical gradient of the gravitational potential is null within small heights above the midplane. In addition, Eq. 2.13 does not take into account the self-gravity of the gas, which could become significant at large radii. As a consequence, we do not calculate the scale height analytically with Eq. 2.13, but we use a numerical method to estimate the scale height from Eq. 2.5. In Appendix 2.A, we however show that this approximation is not as coarse as it may seem, but it gives results that are compatible with the numerical scale heights.

2.2.5 From surface densities to volume densities

Let us now look at the gas disc from the perspective of an external observer who measures the radial profile of the gas density; we are assuming a face-on disc for simplicity. The observed profile of the surface density is the projection along the line of sight of the corresponding volume density profile as follows:

$$\Sigma(R) = 2 \int_0^{+\infty} \rho(R, z) dz. \quad (2.14)$$

Substituting Eq. 2.12 in Eq. 2.14 and solving the integral, we obtain the volume density in the midplane

$$\rho(R, 0) = \frac{\Sigma(R)}{\sqrt{2\pi}h(R)}. \quad (2.15)$$

Hence, Eq. 2.15 gives us the volume density from the observed surface density and the scale height. This is valid for any component, in particular HI, H₂ and SFR. The gaseous and the SFR components require separate brief discussions.

Gas volume densities

As mentioned in Sect. 2.2.4, the scale height of a gas disc depends on the velocity dispersion of the gas. The molecular and the atomic phase are characterised by different values for the velocity dispersion (e.g. Mogotsi et al., 2016; Marasco et al., 2017). Hence, we must consider these components as distributed into two separate discs both in hydrostatic equilibrium and each one with its own scale height (h_{HI} and h_{H_2}). Therefore, Eq. 2.15 can be written both for HI and H₂ and the volume density of the total gas (HI+H₂) in the midplane becomes

$$\begin{aligned} \rho_{\text{gas}}(R, 0) &= \rho_{\text{HI}}(R, 0) + \rho_{\text{H}_2}(R, 0) = \\ &= \frac{\Sigma_{\text{HI}}(R)}{\sqrt{2\pi}h_{\text{HI}}(R)} + \frac{\Sigma_{\text{H}_2}(R)}{\sqrt{2\pi}h_{\text{H}_2}(R)}. \end{aligned} \quad (2.16)$$

In this way we defined three quantities (ρ_{HI} , ρ_{H_2} and ρ_{gas}) that we compare to the SFR volume density.

Star formation rate volume density

The SFR vertical distribution is not known a priori but, as stars form from gas, it is reasonable to assume that an equation analogous to Eq. 2.15 applies to newborn stars as well, given some suitable definition of the SFR scale height (h_{SFR}). For this latter, we decided to make two extreme assumptions. The first consists in supposing that h_{SFR} is a function of the scale heights of the two gas phases. Thus, we assumed it to be the mean of the scale heights of both gas phases weighted for the respective gas fractions,

$$h_{\text{SFR}}(R) = h_{\text{HI}}(R)f_{\text{HI}}(R) + h_{\text{H}_2}(R)f_{\text{H}_2}(R), \quad (2.17)$$

where $f_{\text{HI}}(R) \equiv \Sigma_{\text{HI}}(R)/\Sigma_{\text{gas}}(R)$ and $f_{\text{H}_2}(R) \equiv \Sigma_{\text{H}_2}(R)/\Sigma_{\text{gas}}(R)$ are the fraction of HI and H₂ with respect to the total gas. With this choice, if the atomic gas is fully dominant with respect to the molecular phase (as in the outskirts of spirals and in dwarfs), $h_{\text{SFR}}(R)$ coincides with h_{HI} and viceversa with h_{H_2} . If both gas phases are present in a comparable amount, then $h_{\text{SFR}}(R)$ is simply a weighted mean of h_{H_2} and h_{HI} . For the second choice, we assumed a constant h_{SFR} , we took $h_{\text{SFR}} = 100$ pc as a fiducial value (Barnes et al., 2012). We note that choosing a different constant would change only the normalisation factor for the SFR volume density. It is reasonable to expect that the true SFR scale height lies between these two extreme choices (see also Chapters and). We could also consider h_{HI} or h_{H_2} as alternative definitions of $h_{\text{SFR}}(R)$. We explore these cases in Sect. 2.5.2 and Sect. 2.5.3.

2.3 Sample description

In order to estimate the volumetric densities, we need a sample of star-forming galaxies with known gravitational potentials and their observed surface densities of gas and SFR as a function of galactocentric radius R . We selected the galaxies starting from the sample of The HI Nearby Galaxy Survey (THINGS; Walter et al., 2008), which includes 34 objects.

2.3.1 Surface densities

Among the THINGS sample, we selected all the 23 galaxies in the sample of Leroy et al. (2008), who provide the surface density radial profiles for HI and SFR. Leroy et al. (2008) derived the atomic gas distribution from the THINGS 21-cm emission maps. The SFR distribution was obtained combining the far-ultraviolet (unobscured SF) emission maps from the Galaxy Evolution Explorer (GALEX; Gil de Paz et al., 2007) and the 24 μm (obscured SF) emission maps from the Spitzer Infrared Nearby Galaxy Survey (SINGS; Kennicutt et al., 2003). These authors divided each galaxy in rings and calculated the surface densities at a certain radius as azimuthal averages inside that ring. This method is supposed to smooth the distributions and cancel azimuthal variations due to over- or under-dense regions as holes or spiral arms. Leroy et al. (2008) used the CO(2-1) transition maps from the HERA CO-Line Extragalactic Survey (HERACLES; Leroy et al., 2005) and the CO(1-0) transition maps from the Berkeley-Illinois-Maryland Association Survey Of Nearby Galaxies (BIMA SONG; Helfer et al., 2003) to calculate the H_2 surface densities for about half of the galaxies in their sample. These authors also used the MW α_{CO} to convert the integrated CO intensity to H_2 surface density. However, as shown by Narayanan et al. (2012), the choice of α_{CO} is crucial as it influences the shape of SF laws, in particular at high surface density regimes. Hence, we took the profiles for molecular gas from Frank et al. (2016), who used the same data as Leroy et al. (2008) but adopted the α_{CO} factor reported by Sandstrom et al. (2013). These authors took account of the dust-to-gas ratio and the metallicity gradient to obtain an accurate estimate of the α_{CO} radial variation in 26 nearby galaxies. They found that the radial profile of α_{CO} is nearly constant for all the galaxies, except in the central regions, where it tends to decrease and becomes 5-10 times smaller than the MW value in the most extreme cases. For example, the inner H_2 surface densities in NGC 4736 and NGC 5055 that were calculated by Sandstrom et al. (2013) differ from Leroy et al. (2008) results by one order of magnitude. For NGC 2403, Frank et al. (2016) used the MW α_{CO} as this galaxy was not included in Sandstrom et al. (2013) study.

2.3.2 Selection based on mass models

Among Leroy et al. (2008) sample, we selected the galaxies with parametric mass models in de Blok et al. (2008) or Frank et al. (2016). In particular, de Blok et al. (2008) decomposed high quality HI rotation curves for a sample of 19 THINGS galaxies to obtain mass models using a DM halo, a stellar disc, a bulge (if present), and an atomic gas disc. Concerning the DM component, the authors adopted either an isothermal (Eq. 2.6) or a NFW profile (Eq. 2.7): in the first case they provide the best-fit central volume density $\rho_{\text{DM},0}$ and core radius r_c , while in the second case the parameters are the concentration c and V_{200} , which is the circular velocity at r_{200} . For the stellar disc component, de Blok et al. (2008) fitted the $3.6 \mu\text{m}$ intensity profile with Eq. 2.8 leaving R_\star and the mass-to-light ratio M/L as free parameters. In a small number of galaxies, they found an additional central component in the $3.6 \mu\text{m}$ surface brightness distribution, which is related to the stellar bulge. These authors fitted the light profile using the same profiles of the stellar disc (Eq. 2.8) instead of a more generic Sersic profile $R^{1/n}$ (Sérsic, 1963). The main reason for this choice was the limited radial range over which the bulge profile dominated the total emission and this avoided the need for the determination of the index n . They checked that assuming a different functional form did not significantly impact on their final mass models. Concerning the atomic gas component, de Blok et al. (2008) assumed that it is distributed in an infinitely thin disc. Later, Frank et al. (2016) repeated the de Blok et al. (2008) analysis including the molecular gas contribution for 12 galaxies; the molecular gas disc was also assumed to be infinitely thin in the modelling. Frank et al. found a good agreement with de Blok et al. (2008) results and improved the DM halo parametric mass model for some galaxies.

Cross-matching de Blok et al. (2008) and Leroy et al. (2008) samples, we ended up with a sample of 12¹ nearby star-forming galaxies with surface densities of gas and SFR, and parametric mass models. In our sample, there are six normal spirals and six low-mass galaxies, whose circular velocity do not exceed 150 km s^{-1} (DDO 154 is a dwarf galaxy). DDO 154², IC 2574, and NGC 7793 were not included in Frank et al. (2016) sample as no CO emission was detected, for these we used the mass models reported in de Blok et al. (2008). The main properties of the galaxies and the parameters of their mass models are summarised in Tables 2.1 and 2.2, respectively.

For the sake of accuracy, we checked that the distances reported by de Blok et al. (2008) and Frank et al. (2016) are compatible with those reported in Lelli et al. (2016), who carefully selected the most reliable measurements in literature

¹We excluded NGC 3521 from our study as its HI disc shows a prominent warp along the line of sight. This feature complicates the analysis of the HI kinematics and the determination of its velocity dispersion.

²In dwarf galaxies, the asymmetric-drift correction should be, in principle, included in the derivation of the circular velocity. However, Iorio et al. (2017) showed that its contribution is negligible in the case of DDO 154, which is the least massive galaxy in our sample.

(except for NGC 0925 and NGC 4736, which are not included in the Lelli et al. 2016 sample). For some galaxies (DDO 154, IC 2574, NGC 5055, NGC 6946, and NGC 7793), the difference between the two distances is not negligible and could slightly influence the rotation curve. Hence, we decided to adopt Lelli et al. (2016) distances and correct the surface densities of Leroy et al. (2008) accordingly.

Table 2.1 – Properties of the sample galaxies: (1) morphological type; (2) distance; (3) mean value of the flat part of the rotation curve (from Lelli et al., 2016, except for NGC 0925, NGC 4736, and NGC 7793, see Appendices 2.B and 2.C for details); (4) inclination; (5) position angle.

Galaxy	Type	D (Mpc)	V_{flat} (km s^{-1})	i ($^{\circ}$)	P.A. ($^{\circ}$)
	(1)	(2)	(3)	(4)	(5)
DDO 154	Im	4.04	47.0	65.0	224.0
IC 2574	Sm	3.91	66.4	53.0	56.0
NGC 0925	SABd	9.20	117.5	58.0	287.0
NGC 2403	Scd	3.16	131.2	61.0	124.5
NGC 2841	Sb	14.10	284.8	73.7	152.6
NGC 2976	Sc	3.58	85.4	61.0	334.5
NGC 3198	Sc	13.80	150.1	71.5	216.0
NGC 4736	SABa	4.70	151.7	41.4	306.7
NGC 5055	Sbc	9.90	179.0	55.0	101.8
NGC 6946	Scd	5.52	158.9	33.0	243.0
NGC 7331	Sb	14.70	239.0	75.8	167.7
NGC 7793	Sd	3.61	121.8	47.0	290.1

Galaxies with bulge

As mentioned above, de Blok et al. (2008) modelled the mass distribution of the bulges using Eq. 2.8, i.e. as they were exponential discs. This is not convenient for our purpose as the vertical pull near the midplane in the potential of this flattened component is stronger than the same force in the potential of a more realistic spheroidal distribution with the same mass. Therefore, the scale height would be significantly smaller, at least for the innermost regions where the bulge is likely the dominant component of the total gravitational potential.

To alleviate this problem, we built the alternative bulge model described in Sect. 2.2.2 using an exponential sphere (Eq. 2.9). In this way, the observed exponential light distributions are preserved, but the mass distributions are no more flattened across the midplane.

We want our model of the exponential sphere to have the same circular velocity as the (bulge) model of exponential disc of de Blok et al. (2008) for each galaxy with significant contribution from the bulge (NGC 2841, NGC 4736, NGC 5055, NGC 6946, and NGC 7331). To this purpose, we fitted the circular velocity of the exponential sphere

$$V_{c,b}(r) = \sqrt{4\pi G \rho_{b,0} \frac{r_b}{r} [2r_b^2 - (r^2 + 2rr_b + 2r_b^2) e^{-r/r_b}]} \quad (2.18)$$

to the circular velocity of de Blok et al. (2008) flat bulge, leaving $\rho_{b,0}$ and r_b as free parameters. In the end, our models for the bulges are given by Eq. 2.9 with the best-fit $\rho_{b,0}$ and r_b reported in Table 2.2.

2.4 Gas disc thickness

In this section, we calculate the scale height of HI, H₂, and SFR distributions. As mentioned in Section 2.2, the vertical distribution of the gas (Eq. 2.5) is regulated by the total gravitational potential of the galaxy and the gas velocity dispersion, which have opposite roles. The main obstacle to the scale height calculation is accounting for the gas self-gravity. Indeed, the total gravitational potential of a galaxy Φ must include also the gas contribution, which depends on the gas distribution itself and thus on the scale height.

In order to include the self-gravity, we used the publicly available software GALPYNAMICS³ (Iorio, 2018) to compute the gas potential and scale height through an iterative algorithm (see also Abramova & Zasov, 2008; Banerjee et al., 2011), which we explain in this section in a broad outline. In order to choose a simple example, let us consider a galaxy composed of DM, stars and atomic gas (including He).

1. As a preliminary stage, the software calculates the potential of DM and stars, which is defined as the external and fixed potential Φ_{ext} .
2. In the zero-order step, GALPYNAMICS assumes a razor-thin ($h_{\text{HI}} = 0$) mass distribution for the HI disc and calculates its gravitational potential Φ_{HI} . The total gravitational potential of the galaxy is then set to $\Phi = \Phi_{\text{ext}} + \Phi_{\text{HI}}$.
3. The first iteration begins. The HI vertical profile is given by Eq. 2.5, where the velocity dispersion is given by Eq. 2.11, and it is fitted with a Gaussian

³<https://github.com/iogiul/galpynamics>

Table 2.2 – Parametric mass models for DM and stellar components of the sample galaxies. DM halo profile: (1) type, ISO=isothermal, NFW=Navarro-Frenk-White; (2) concentration (NFW) or central density (ISO); and (3) V_{200} (NFW) or core radius (ISO). Stellar disc: (4) central surface density $\Sigma_{*,0} = \rho_{*,0}/(2R_*)$; (5) scale radius; and (6) scale height. Bulge (as exponential sphere): (7) central density and (8) scale radius.

Galaxy	Dark matter halo			Stellar disc			Bulge	
	Type (1)	$c - \rho_{DM,0}$ (adim. $-10^6 M_{\odot} \text{kpc}^{-3}$) (2)	$V_{200} - r_c$ ($\text{km s}^{-1} - \text{kpc}$) (3)	$\Sigma_{*,0}$ ($10^6 M_{\odot} \text{kpc}^{-2}$) (4)	R_* (kpc) (5)	z_* (kpc) (6)	$\rho_{b,0}$ ($10^{10} M_{\odot} \text{kpc}^{-3}$) (7)	r_b (kpc) (8)
DDO 154	ISO	28.5	1.32	5.7	0.72	0.144	-	-
IC 2574	ISO	5.0	6.18	14.5	2.85	0.57	-	-
NGC 0925	ISO	6.5	8.90	68.6	4.1	0.82	-	-
NGC 2403	ISO	144.4	1.50	176.4	1.81	0.362	-	-
NGC 2841	NFW	24.8	172.6	684.4	4.2	0.84	1.24	0.394
NGC 2976	ISO	42.8	2.60	247.4	0.9	0.18	-	-
NGC 3198	ISO	45.2	2.80	302.3	3.06	0.612	-	-
NGC 4736	NFW	108.3	40.9	529.8	1.99	0.398	5.3	0.144
NGC 5055	ISO	11.1	7.15	1179.0	3.2	0.64	3.0	0.19
NGC 6946	ISO	31.4	4.80	752.2	2.97	0.594	21.0	0.08
NGC 7331	NFW	9.3	171.2	1160.9	3.3	0.66	10.8	0.175
NGC 7793	ISO	93.5	1.95	420.7	1.3	0.26	-	-

function (Eq. 2.12) to infer the new scale height h'_{HI} . The next evaluation of the HI gravitational potential Φ'_{HI} is done for a disc with thickness h'_{HI} . Then, we are able to update the total potential to $\Phi' = \Phi_{\text{ext}} + \Phi'_{\text{HI}}$.

4. Using Φ' in Eq. 2.5, we find more accurate vertical distribution and scale height h''_{HI} for the atomic gas, which allow us to better estimate Φ''_{HI} and then Φ'' .

This procedure is iterated until two successive computations of the scale height differ by less than a tolerance factor, chosen by the user. This software was extensively tested using mock data (see Iorio, 2018).

Most of the galaxies in our sample have both the atomic and molecular gas components. We first calculate the HI scale height in the gravitational potential of stars and DM, and then the scale height for H_2 but including also the HI gravitational potential. This choice implies that the HI distribution is not influenced by the H_2 distribution and that we obtain two different scale heights for each gas phase, h_{HI} and h_{H_2} . We expect that including the molecular gas distribution to the potential does not affect the HI scale height, as the total mass of molecular gas is about one order of magnitude smaller than the total amount of atomic gas (see Leroy et al., 2008). Moreover, the molecular phase is concentrated in the inner regions of galaxies, where stars are the dominant mass component, and becomes negligible in the outskirts. On the other hand, the atomic gas is distributed out to larger radii, so its contribution to the total gravitational potential there could become truly significant.

2.4.1 Flaring HI disc

In order to calculate the HI scale height, GALPYNAMICS needs, in addition to the external potential Φ_{ext} , the HI radial profiles of the surface density $\Sigma_{\text{HI}}(R)$ and velocity dispersion $\sigma_{\text{HI}}(R)$.

HI surface density

As mentioned in Sect. 2.2.2, we modelled the atomic gas distribution using a combination of an exponential and a polynomial (Eq. 2.10), which was fitted on the observed azimuthally averaged radial profiles of Leroy et al. (2008) leaving $\Sigma_{\text{HI},0}$, R_{Σ} , and C_i as free parameters (the helium correction of 1.36 is included). In Fig. 2.1, the observed $\Sigma_{\text{HI}}(R)$ for each galaxy is shown by the blue points and the corresponding best-fit model is represented by the light blue curve. It is clear that the best fits reproduce well the observed radial profiles save negligible and small differences, which do not affect the computation of the scale height.

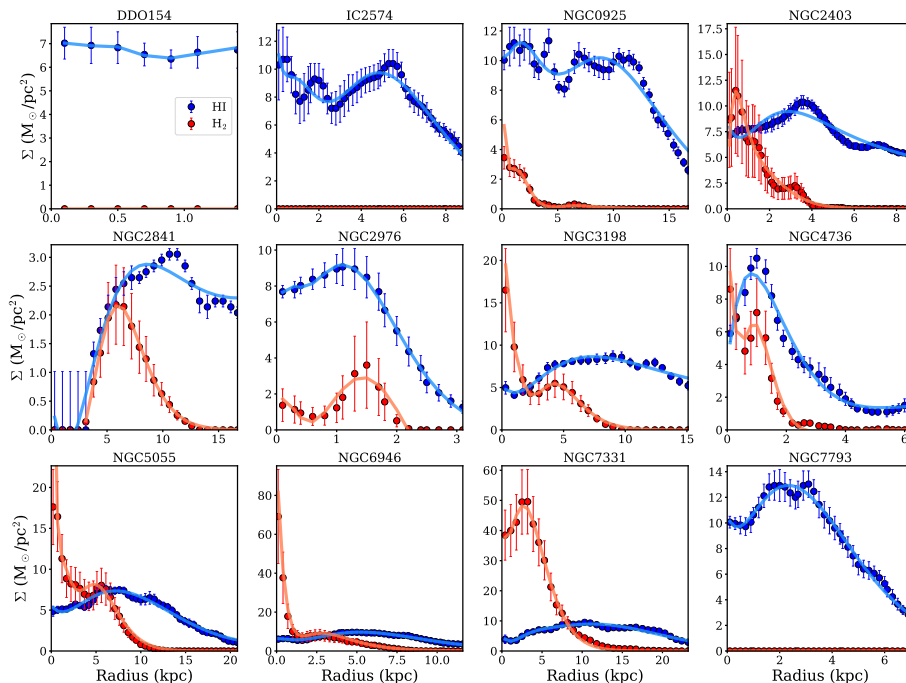


Figure 2.1 – HI (Leroy et al., 2008, blue points) and H₂ (Frank et al., 2016, red points) observed surface densities radial profiles. The light blue and coral curves show the models used to compute the scale heights and are obtained by fitting Eq. 2.10 to the observed profiles. Only the ranges where the SFR is measured are shown.

HI velocity dispersion

As shown by Eq. 2.5, we expect the scale height to linearly depend on the velocity dispersion, so an accurate modelling of $\sigma_{\text{HI}}(R)$ radial profile is fundamental. To this aim, we derived the radial profiles of the velocity dispersion in our galaxies using the publicly available software ^{3D}BAROLO⁴ (Di Teodoro & Fraternali, 2015), hereafter 3DB, on THINGS data cubes (Walter et al., 2008). The 3DB software performs a tilted-ring model fitting directly on the data cube, allowing us to correct for the beam smearing, which can significantly modify the resulting velocity dispersion and rotation curve (e.g. Swaters, 1999). Moreover, the rotation velocity and velocity dispersion are fitted simultaneously rather than as separate components, as done in the classical 2D approach based on velocity dispersion maps (e.g. Tamburro et al., 2009; Romeo & Mogotsi, 2017). We chose 400 pc as a common spatial resolution for the data cubes of our galaxies, which is a compromise between negligible gas streaming motions within our beam and sufficient signal-to-noise ratio (S/N) in low column density

⁴<http://editeodoro.github.io/Bbarolo/>

areas. Details on the properties of the data cubes and the 3DB input parameters can be found in Appendix 2.B. Fig. 2.2 shows the velocity dispersion measured by 3DB for all the galaxies in the sample. Our results are in agreement with previous works showing that the velocity dispersion decreases with the radius from 12-20 km s^{-1} in the inner parts of local spirals and dwarfs down to 5-7 km s^{-1} in the outskirts (e.g. Narayan & Jog, 2002; Boomsma et al., 2008; Tamburro et al., 2009).

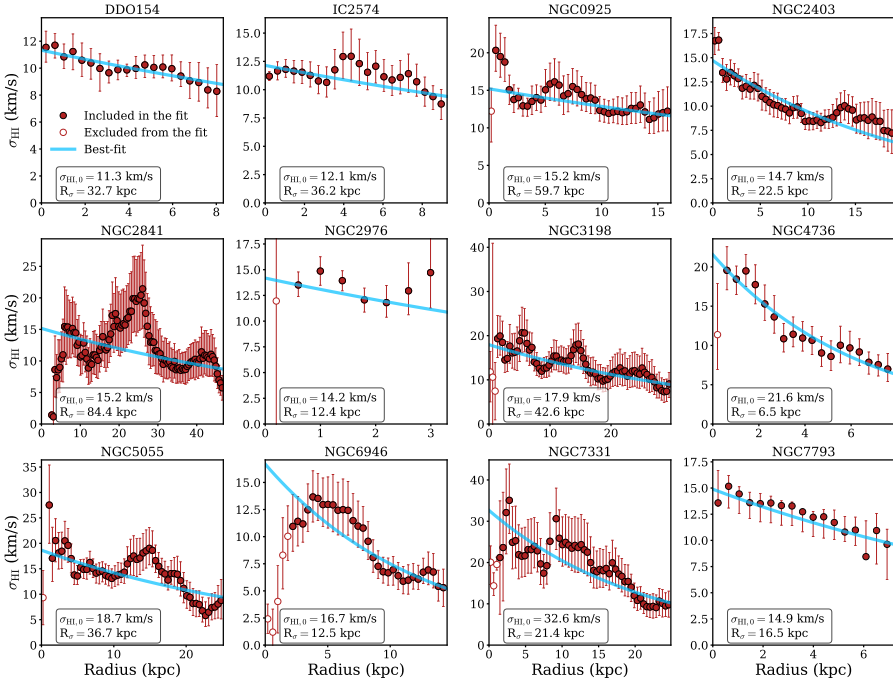


Figure 2.2 – HI velocity dispersion measured using 3^{D} BAROLO (filled and empty circles) for our galaxies with a common sampling of about 400 pc (for NGC 2841 we show one data point every two). The best-fit models (Eq. 2.11) are shown by the light blue curves, whose parameters ($\sigma_{\text{HI},0}$ and R_{σ}) are reported in a box in the lower left corner of each panel. The points indicated by empty circles are excluded from the fit.

The velocity dispersion of NGC 7331 is probably overestimated. Indeed, if we compare this profile to that of the other galaxies, we see that it is systematically higher. This increase likely originates from projection effects due to the galaxy inclination angle and the HI disc thickness or non-circular motions along the line of sight, which bias the velocity dispersion towards high values. NGC 7331 is indeed the most inclined galaxy in our sample ($i \approx 76^\circ$), so the line of sight intercepts regions with different rotation velocity, broadening the line profile. Such effects may be present in the profiles of two further highly inclined

galaxies, NGC 2841 and NGC 3198, but they seem to be less affected. NGC 2841 velocity dispersion shows a peculiar sharp increase of 10 km s^{-1} extending from 15 kpc to 30 kpc, whose origin we discuss in Appendix 2.D.

Having measured $\sigma_{\text{HI}}(R)$, the model for the velocity dispersion (Eq. 2.11) was fitted to the data points leaving $\sigma_{\text{HI},0}$ and R_σ as free parameters. The model must reproduce the radial decrease of the velocity dispersion, leaving aside the most peculiar features differing from the global trend, which could be due to low S/N regions or some residual beam smearing effect in the very innermost radii. Therefore, we excluded the innermost point of NGC 0925, NGC 2841, NGC 2976, NGC 3198, NGC 4736, NGC 5055, and NGC 7331. For NGC 6946, we rejected the inner five velocity dispersion measurements after a comparison with the velocity dispersion profile of Boomsma et al. (2008), who found that $\sigma_{\text{HI}} \approx 12 - 15 \text{ km s}^{-1}$ for the central radii. Thus, the drop that we observe is likely an artefact due to low S/N of our data, which have higher angular resolution with respect to Boomsma et al. (2008). In Fig. 2.2, the excluded points are shown as empty circles, while the measurements used for the fit are shown as the filled circles.

HI scale height

We calculated $h_{\text{HI}}(R)$ for our galaxies using their gravitational potential and the surface density and velocity dispersion of the atomic gas. Before describing the full sample, it is useful to focus on a single galaxy in order to understand which mass component drives the trend of the scale height with radius. In Fig. 2.3, we show three different HI scale heights out to $R = 20 \text{ kpc}$ for NGC 2403: each of these scale heights is obtained with a different gravitational potential but the same velocity dispersion radial profile $\sigma_{\text{HI}}(R)$. In the presence of the stellar disc only (dashed orange line), the scale height increases exponentially out to about $R = 7 \text{ kpc}$, then the growth becomes milder and h_{HI} reaches 1.8 kpc at $R = 20 \text{ kpc}$. This is because the disc mass distribution fades within a short length, so the gravitational pull towards the midplane quickly weakens. As a consequence, the HI disc becomes thicker and thicker with radius, despite the decrease of the velocity dispersion; if the velocity dispersion were constant, then the flaring would be more prominent. For the DM only potential (dashed grey line), the pull towards the midplane is still significant in the outskirts, as the radial decrease of the DM density is significantly slower with respect to an exponential profile. In the combined potential of stars and DM (solid blue), the scale height is mainly driven by the stellar disc in the inner regions and by the DM halo in the outskirts (see also Sarkar & Jog, 2018). At the end, h_{HI} increases by a factor of about 8 within 20 kpc in radius. We note that the scale height in the single component potentials is always larger with respect to the combined potential, so neglecting one or the other component causes an overestimate of the scale height.

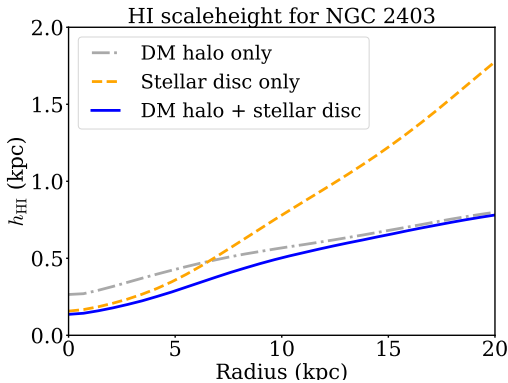


Figure 2.3 – HI scale height radial profiles in the presence of three different gravitational potentials (including the HI self-gravity) but with the same velocity dispersion. The orange and grey dashed curves, respectively, show $h_{\text{HI}}(R)$ for the stellar disc only and DM halo only potentials taken from NGC 2403 mass model. The total potential of NGC 2403 gives the blue solid curve.

The radial profiles of the HI scale height for the all galaxies in our sample are shown by the blue curves in Fig. 2.4, and the associated uncertainties are represented by the faded blue area. In Appendix 2.E, we provide details about the estimates of the uncertainties, which include the errors on σ_{HI} . We note the global trend of the flaring is similar for all the galaxies. We emphasise that the HI disc flaring is significant, regardless of the galaxy type, so assuming a thin gaseous disc or a constant thickness is never a good approximation. The presence of the bulge (NGC 2841, NGC 4736, NGC 5055, NGC 6946, and NGC 7331) reduces the scale height in the innermost regions. However, the mass model for the bulge is more uncertain (see Sect. 2.2.2) and the velocity dispersion in the centre of galaxies has large errors, so it is likely that the scale height in the innermost radii of these galaxies is underestimated or at least uncertain. The projection effects are particularly significant in the outskirts, therefore we expect that the intrinsic volume densities distribution with radius will differ from the observed surface densities distribution. We anticipate that the VSF law will have different shape than the law based on surface densities.

2.4.2 Flaring H_2 disc

The molecular gas scale height was estimated using the gravitational potential of stars, DM, and the HI disc with flaring thickness. Moreover, we needed the surface density and velocity dispersion of the molecular gas.

H_2 surface density

As in Sect. 2.4.1, the model for the H_2 distribution (Eq. 2.10) was fitted to the radial profile of the observed surface density (including the correction for Helium), leaving $\Sigma_{\text{H}_2,0}$, R_Σ , and C_i as free parameters. In Fig. 2.1, the observed Σ_{H_2} from Frank et al. (2016) are shown by the red points and the corresponding

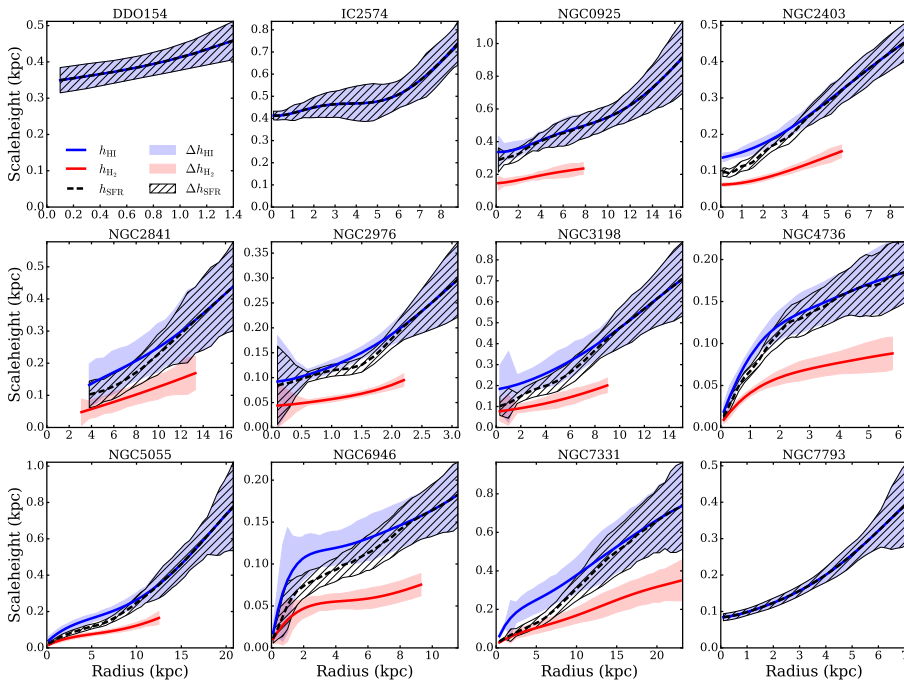


Figure 2.4 – Scale height radial profiles: $h_{\text{HI}}(R)$ (solid blue) and $h_{\text{H}_2}(R)$ (solid red) are calculated by GALPYNAMICS, while $h_{\text{SFR}}(R)$ (dashed black) is estimated using Eq. 2.17. We note that $h_{\text{H}_2}(R)$ is shown out to the radius where CO emission is detected. The faded regions indicate the uncertainties on the gas scale heights, while the black hashed regions are the uncertainties on $h_{\text{SFR}}(R)$.

best-fit models are represented by the coral curves. The error bars include the uncertainties on α_{CO} as reported in Sandstrom et al. (2013).

H₂ velocity dispersion

As for σ_{HI} (Sect. 2.4.1), we modelled σ_{H_2} using an exponential profile, which should be fitted to the observed velocity dispersion radial profiles. The spatial and spectral resolution are crucial in measuring the molecular gas velocity dispersion, as they could artificially broaden the observed emission line. The first typically affects the velocity dispersion in the central parts of the galaxies and the second acts as an additional broadening component.

There are scarce high resolution observations of the molecular gas emission in our sample galaxies. In the literature, three studies measured the CO velocity dispersion radial profile using the HERACLES data cubes of the CO(2-1) emission line with spatial resolution of $13''$. In particular, Caldú-Primo et al. (2013) used the data cubes with spectral resolution of 2.6 km s^{-1} and stacked

the CO (and also HI) line profiles over kiloparsec-sized regions to improve the S/N. They used the HI velocity fields as a guide to align the profile centroids and measured the velocity dispersions by fitting a Gaussian function to the stacked profiles. They estimated the ratio of the HI to H₂ velocity dispersion to be $\sigma_{\text{HI}}/\sigma_{\text{H}_2} \approx 1$. However, the stacking method easily introduces an artificial broadening if the profiles are not perfectly aligned, so their result could be overestimated. Later, Mogotsi et al. (2016) (see also Romeo & Mogotsi, 2017) used Hanning smoothed data cubes with spectral resolution of 5.2 km s^{-1} and fitted a Gaussian function to the line profiles in each pixel with $\text{S/N} > 4$, finding $\sigma_{\text{HI}}/\sigma_{\text{H}_2} \approx 1.4$. Unfortunately, their resolution ($\approx 5 \text{ km s}^{-1}$) is probably too low to measure the molecular gas velocity dispersion in the galaxy outskirts, where it can easily drop below 5 km s^{-1} as shown by Marasco et al. (2017). These latter authors used the Leiden-Argentine-Bonn (LAB) all-sky 21-cm survey (Kalberla et al., 2005) and the CO(2-1) survey (Dame et al., 2001) to measure the distribution and kinematics of atomic and molecular gas in the Milky Way with spectral resolution of about 2 km s^{-1} . They reproduced the observed emission building a model of the Galactic disc made of concentric and co-planar rings defined by rotation velocity, velocity dispersion, midplane volume density, and scale height. Marasco et al. (2017) showed that the radial trends of σ_{HI} and σ_{H_2} are approximately the same (see also Mogotsi et al., 2016), while their mean values are $8.9 \pm 1.5 \text{ km s}^{-1}$ and $4.4 \pm 1.5 \text{ km s}^{-1}$, respectively.

Hence, we decided to assume $\sigma_{\text{HI}}/\sigma_{\text{H}_2} \approx 2$ and estimated the radial profile of σ_{H_2} from the σ_{HI} radial profiles.⁵ In practice, the model for the molecular gas velocity dispersion is given by Eq. 2.11 with $\sigma_{\text{H}_2,0} = 0.5\sigma_{\text{HI},0}$ and the same R_σ reported in Fig. 2.2. However, we tested that assuming 1.4 for $\sigma_{\text{HI}}/\sigma_{\text{H}_2}$ does not significantly affect our results. For completeness, we also compared our σ_{H_2} radial profile for NGC 2403, NGC 4736, and NGC 5055 with those reported by Wilson et al. (2011). They measured σ_{H_2} using CO(3-2) emission data cubes with spectral resolution of 0.43 km s^{-1} and spatial resolution of $14.5''$. Our profiles are compatible within the uncertainties with Wilson et al.'s results save for the very central regions ($< 1 - 2 \text{ kpc}$), where the beam smearing likely acts as an additional broadening component on their profiles.

H₂ scale height

In Fig. 2.4, we show the H₂ scale heights with their associated uncertainty for all the galaxies in our sample. In Appendix 2.E, we explain how the errors on h_{H_2} were estimated to take account of the uncertainties on σ_{H_2} . We note that $h_{\text{H}_2} \approx 0.5h_{\text{HI}}$, save for negligible discrepancies, as the main driver of the difference in the flaring of HI and H₂ discs is the velocity dispersion.

⁵In Chapter 5 (Appendix 5.A), we provide the analysis of the molecular gas kinematics using the CO(2-1) emission line data cubes from HERACLES, which allowed us to obtain robust measurements of the CO velocity dispersion and to verify the assumption $\sigma_{\text{HI}}/\sigma_{\text{H}_2} \approx 2$.

2.4.3 Star formation rate scale height

Knowing the scale heights of the HI and H₂, we estimated the scale height of the SFR vertical distribution using Eq. 2.17. In Fig. 2.4, we show $h_{\text{SFR}}(R)$ (black dashed curve) as a function of radius and its uncertainties (see Appendix 2.E for details). Clearly, in the case of DDO 154, IC 2574, and NGC 7793, $h_{\text{SFR}}(R)$ coincides with h_{HI} as CO emission is not detected.

2.5 Volumetric star formation laws

Having all the scale heights, we converted surface densities to volume densities through Eq. 2.15. In Appendix 2.E, we describe the calculation of the uncertainties on the volume densities, which include the errors on the observed surface densities and on the scale heights.

Fig. 2.5 illustrates the effect of the conversion to volume densities on the correlation between gas and SFR for the galaxy NGC 5055. The left panel shows the classical surface-based correlation with each point coloured according to the radius. As can be seen from the central panel, the conversion of gas surface densities to volume densities using the constant h_{SFR} stretches the points along the x -axis. Indeed, low density points typically belong to the outskirts, therefore they undergo the most significant leftward shift. In this case, the SFR surface density profile is divided by a constant value, so its trend is not modified. In the right panel, the gas volume densities are the same as in the central panel, but the flaring $h_{\text{SFR}}(R)$ (Fig. 2.4) is assumed, so the points are also stretched along the y -axis.

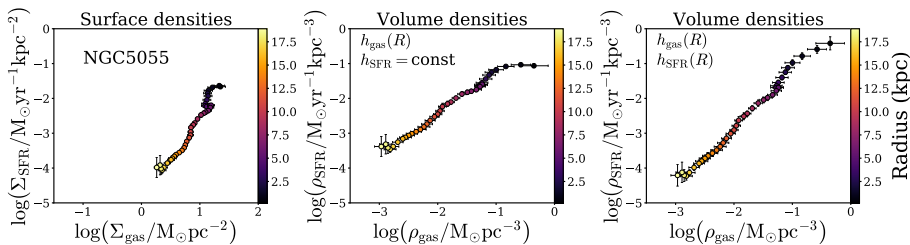


Figure 2.5 – Correlations between gas and SFR surface densities (left) and volume (centre and right) densities for NGC 5055; h_{SFR} is assumed to be constant and flaring (Eq. 2.17) in the central and right panels, respectively. Each point is obtained as an azimuthal average and coloured according to its galactocentric radius. The slope of the VSF law is shallower than for the surface-based law. This is a consequence of taking the flaring of the gas (and the SFR) into account.

2.5.1 Relation between total gas and star formation rate

We now consider the full sample of galaxies. Figure 2.6 compares the surface-based (left) and the volume-based (centre and right) correlations between gas and SFR with the points colour-coded according to the galaxy of origin. By-eye, it is clear that the surface-based correlation is more scattered than any of the volume-based correlations. The change in the SF efficiency seen by Leroy et al. (2008) and Bigiel et al. (2010) is partially reduced in the left panel thanks to the improvement in the α_{CO} measurement by Sandstrom et al. (2013) included in this study. However, some galaxies in the left panel (e.g. NGC 5055 and NGC 7793) seem to follow a steeper SF law with respect to the others (e.g. NGC 4736 and NGC 7331). Indeed, the observed surface density corresponds to the integral of the column of gas along the line of sight and the height of this gas column increases with radius. Hence, high surface densities can be present not only in the central parts of galaxies, but also in the external regions, where the volume density is instead low and a few stars form. On the other hand, using the volume densities, we found a tight correlation between SFR and gas over 4-5 orders of magnitude. Even by eye, it is clear that the scatter reduces as the galaxies tend to align on the top of each other.

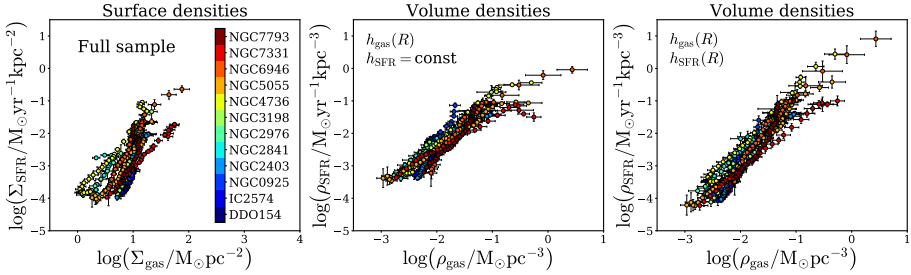


Figure 2.6 – Same as the upper row but for all the galaxies in our sample. Each galaxy has its own colour as shown by the colour bar. The VSF law has considerably less scatter than the surface based version. Each panel shows similar ranges in x and y . No obvious break in the SF efficiencies is found at low densities after correcting for disc thickness.

Fig. 2.7 is the same as Fig. 2.6 but the points are coloured according to the HI fraction, $f_{\text{HI}}(R) = \Sigma_{\text{HI}}(R)/\Sigma_{\text{gas}}(R)$; the blue and red points are HI-dominated and H_2 -dominated, respectively. Going from left to right along the x -axis of all panels, the molecular phase becomes more and more important, but the low density gas is mainly atomic. We note how the scatter in the HI-dominated regime is much reduced by the conversion from surface to volume densities.

We then looked for a correlation between gas and SFR volume densities in the form of a power law as follows:

$$\rho_{\text{SFR}} = A\rho_{\text{gas}}^\alpha. \quad (2.19)$$

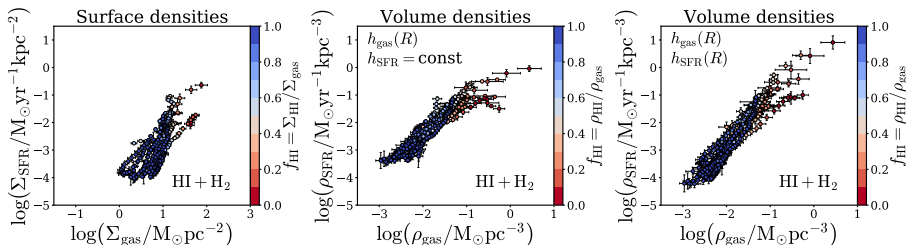


Figure 2.7 – Same as Fig. 2.6 but the points are colour-coded according to the HI fraction; blue and red points come from HI and H₂ dominated regions, respectively. The VSF law appears tight and straight even if only HI-dominated regions are considered.

The relation is univocally described by the normalisation A and the index α . We sampled the parameters space through the Monte Carlo - Markov Chain (MCMC) method implemented in the Python package `emcee` (Foreman-Mackey et al., 2013). In logarithmic scale, the model is a simple linear relation with slope α and y -intercept $\log A$

$$\log \rho_{\text{SFR}} = \log A + \alpha \log \rho_{\text{gas}}, \quad (2.20)$$

where ρ_{gas} is in $\text{M}_{\odot} \text{pc}^{-3}$ and ρ_{SFR} is in $\text{M}_{\odot} \text{yr}^{-1} \text{kpc}^{-3}$. We also included an intrinsic scatter, σ_{\perp} , which is orthogonal to the linear relation. We left slope, y -intercept, and scatter as free parameters in the Bayesian fit (see Appendix 2.F for details). The case with constant h_{SFR} and that with flaring $h_{\text{SFR}}(R)$ were studied separately. The best-fit parameters are reported in Table 2.3; we found a slope of about 1.3 with $h_{\text{SFR}} = 100$ pc and about 1.9 with the flaring $h_{\text{SFR}}(R)$. This means that the slope of the VSF law cannot be univocally determined. However, if the true SFR scale height is between the two extreme choices, it is reasonable to think that also the true slope is between 1.3 and 1.9. The best-fit intrinsic scatter is very small in both cases ($\sigma_{\perp} \approx 0.1$ dex). In Fig. 2.8, volume densities appear as contours and the panels show ρ_{SFR} in the constant (left) and the flaring $h_{\text{SFR}}(R)$ (right) case. The best-fit relation is represented by the solid black line with the dashed lines showing $\pm\sigma_{\perp}$. In order to test the robustness of our results, we tried alternative formulations for $h_{\text{SFR}}(R)$ as a function of the gas scale heights (e.g. harmonic mean) but the best-fit relations were compatible with those reported in Table 2.3 within the scatter of the VSF law.

The high volume density regime above $0.1 \text{ M}_{\odot} \text{pc}^{-3}$ is the less sampled part of the plot and the scatter seems to increase there. Indeed, these points come from the innermost and H₂-dominated regions of massive galaxies, where the α_{CO} factor probably acts as an additional source of uncertainty on the surface density measurement. In particular, Sandstrom et al. (2013) discussed the reliability of their estimate of the α_{CO} in the inner regions of galaxies, as they found that it is lower than the MW value and also well below the galaxy average. Out

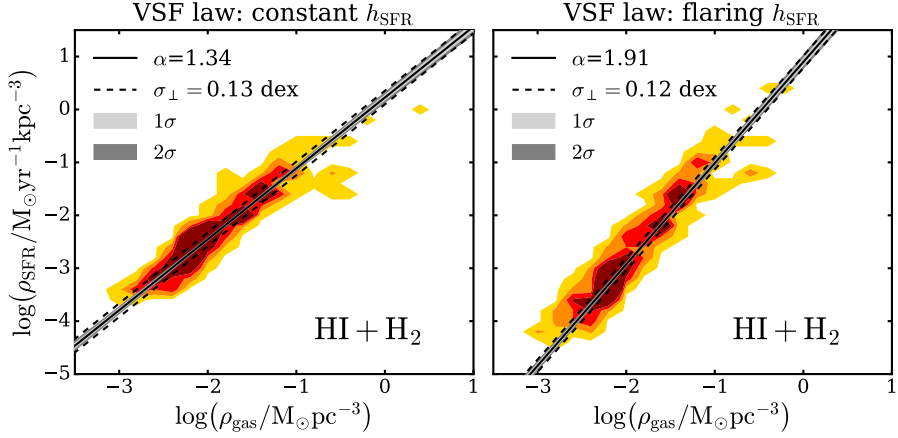


Figure 2.8 – VSF law between total gas and SFR. The solid black line is the best-fit relation with slope α and orthogonal intrinsic scatter σ_{\perp} (dashed lines). The grey bands show 1σ and 2σ uncertainties on the fit. In the left panel, ρ_{SFR} is calculated with the constant h_{SFR} , while in the right panel $h_{\text{SFR}}(R)$ flares with radius (Eq. 2.17). The volume densities radial profiles are shown as contours containing 95% (yellow), 75% (orange), 50% (red), and 25% (dark red) of the data points.

of a total of about 400 volume densities for our 12 galaxies, the H_2 fraction of only 25 points at most may be underestimated, so it is unlikely that our results would be influenced. As further test of the effect of α_{CO} on the best fit, we repeated the whole procedure, including the scale heights calculation, using the H_2 surface densities of Leroy et al. (2008), which were obtained assuming the MW α_{CO} for all the galaxies. We found $\alpha = 1.03 \pm 0.03$ and $\sigma_{\perp} = 0.21 \pm 0.01$ in the case with the constant h_{SFR} and $\alpha = 1.56 \pm 0.03$ and $\sigma_{\perp} = 0.28 \pm 0.01$ with $h_{\text{SFR}}(R)$.

2.5.2 Atomic gas versus star formation rate

We then investigated if some correlation exists between SFR and gas in the atomic phase. In Sect. 2.2.5, the flaring $h_{\text{SFR}}(R)$ is defined as the weighted mean between h_{HI} and h_{H_2} according to the gas fractions. Given that only the atomic gas is considered in this case, the SFR flaring scale height is assumed equal to the HI scale height, while the constant h_{SFR} remains 100 pc as in Sect. 2.5.1. Figure 2.9 compares the correlations between HI and SFR based on surface or volume densities, the points are colour-coded according to the HI fraction with respect to the total amount of gas (as in Fig. 2.7). As expected, we found no correlation in the surface-based panel (left), as one order of magnitude in range of HI surface density corresponds to almost four orders of magnitude in range of SFR surface densities. On the contrary, a tight correlation emerges using the

volume densities. The implications of this remarkable result are discussed in Sect. 2.6.

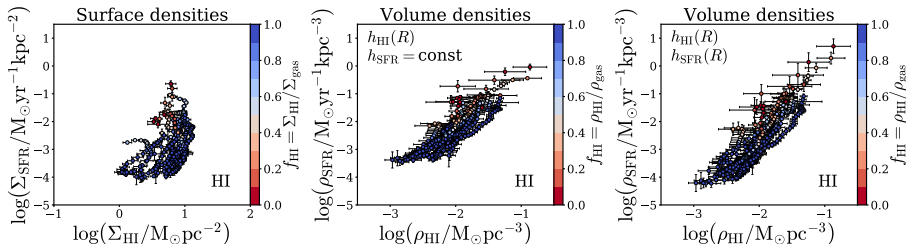


Figure 2.9 – Same as Fig. 2.7 but with the x -axis showing the HI alone surface and volume densities.

To determine the HI VSF law parameters, we followed the same procedure as in Sect. 2.5.1, but we defined the model in the MCMC fitting (see Appendix 2.F for details) as

$$\log \rho_{\text{SFR}} = \log B + \beta \log \rho_{\text{HI}}, \quad (2.21)$$

where ρ_{HI} is in $\text{M}_{\odot} \text{pc}^{-3}$ and ρ_{SFR} is in $\text{M}_{\odot} \text{yr}^{-1} \text{kpc}^{-3}$. We found the slope and the intrinsic scatter, respectively, between 2.1 and 2.8 and 0.15 dex and 0.13 dex, depending on the choice of h_{SFR} . This result indicates a strong link between SF and the atomic gas, in particular in low density environments, where the HI disc is considerably thick. Figure 2.10 shows the volume density data points as contours and the best-fit relation $\pm \sigma_{\perp}$ is represented by the solid black line. For completeness, we compared this correlation with that obtained with the $h_{\text{SFR}}(R)$ for the case with total gas (instead of $h_{\text{SFR}}(R) = h_{\text{HI}}(R)$), finding no significant difference between the results in the two cases.

2.5.3 Molecular gas versus star formation rate

Let us now focus on the correlation between the SFR and the molecular gas phase. In this case the flaring SFR scale height is equal to h_{H_2} . Figure 2.11 compares the correlations between H_2 and SFR surface and volume densities with the points coloured according to the HI fraction with respect to the total amount of gas. As expected, there is a clear sign of some H_2 -SFR correlation in all the three panels, but the volumetric relations appear to be more scattered than both the total gas-SFR and the HI-SFR VSF laws. In addition, it seems that the molecular correlation is no more valid in the low density regime or that it is not a single power law. Indeed, there are hints of a bend both in the surface and volume density plots located at about $1 \text{ M}_{\odot} \text{pc}^{-2}$ and $0.01 \text{ M}_{\odot} \text{pc}^{-3}$, respectively, where the environment is no more H_2 -dominated (see Sect. 2.6 for discussion).

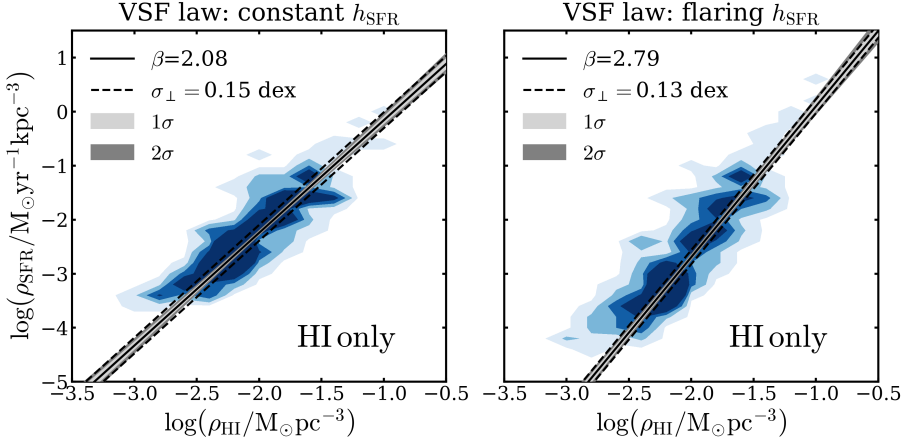


Figure 2.10 – VSF law between SFR and HI volume densities. See Fig. 2.8 for description.

Again, we performed an MCMC fitting to determine the parameters of the H_2 -SFR VSF law, which was modelled as

$$\log \rho_{\text{SFR}} = \log \Gamma + \gamma \log \rho_{\text{H}_2}, \quad (2.22)$$

where ρ_{H_2} is in $\text{M}_\odot \text{pc}^{-3}$ and ρ_{SFR} is in $\text{M}_\odot \text{yr}^{-1} \text{kpc}^{-3}$. We found that the slope is between 0.5 and 0.7 but, in this case, the intrinsic scatter is 0.3-0.4 dex, so two times larger than the previous cases with the total and atomic gas. Figure 2.12 shows the volume density data points as contours and the best-fit relation as the solid black line. As in Sect. 2.5.2, we tested the case with the $h_{\text{SFR}}(R)$ for total gas (instead of $h_{\text{SFR}}(R) = h_{\text{H}_2}(R)$) and found no significant difference between the results.

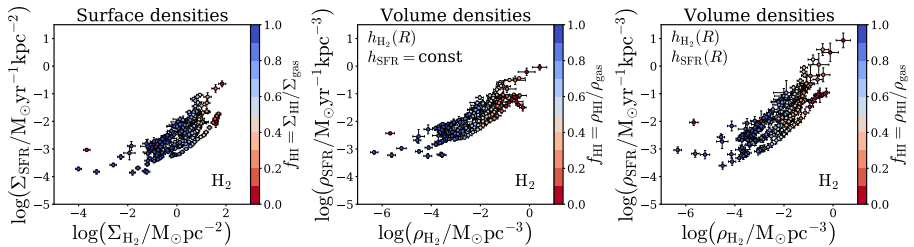


Figure 2.11 – Same as Fig. 2.7 but with the x -axis showing the H_2 alone surface and volume densities.

We could argue that the molecular gas VSF law may be sensitive to the possible underestimate of the α_{CO} factor (see Sandstrom et al., 2013), as there are fewer ρ_{H_2} points than those of ρ_{gas} . However, given the scatter of the relation

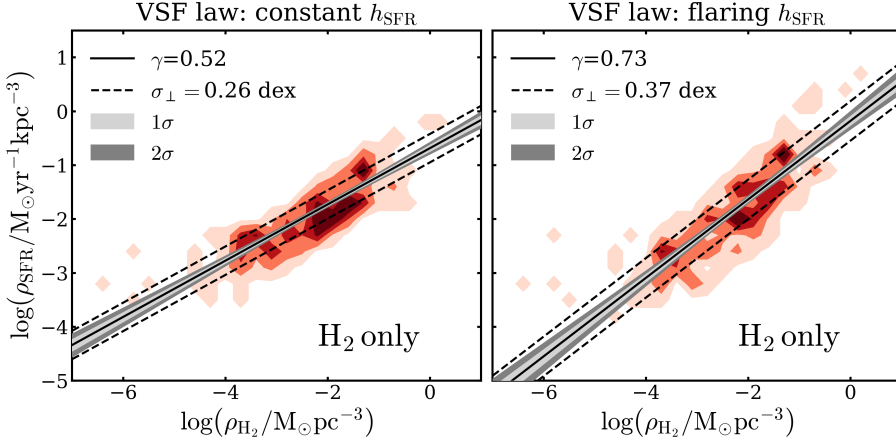


Figure 2.12 – VSF law between SFR and H_2 volume densities. See Fig. 2.8 for description.

in Fig. 2.12, it is unlikely that shifting rightward 25 points out of a total of 249 could affect the best-fit parameters significantly. As further test of the influence of α_{CO} on the VSF laws parameters, we repeated the entire procedure and the MCMC fit using the molecular gas surface densities of Leroy et al. (2008). We found $\gamma = 0.60 \pm 0.03$ and $\gamma = 0.95 \pm 0.03$ with the constant h_{SFR} and $h_{SFR}(R)$, respectively, and $\sigma_{\perp} = 0.60 \pm 0.03$ in both cases.

To quantitatively compare the molecular VSF law with its surface-based version (e.g. Bigiel et al., 2008), we used an MCMC fitting on the H_2 surface densities leaving the slope, the y -intercept and σ_{\perp} free. The resulting best-fit relation is flatter than a linear correlation; indeed the slope is 0.62. However σ_{\perp} is 0.3, so the molecular surface-based relation is more scattered than both the total gas and the HI VSF laws. Probably, the reason why we find a different slope with respect to the unitary value estimated by some authors (e.g. Bigiel et al., 2008) is the α_{CO} factor, as the linear relation is usually obtained using the MW α_{CO} factor for all the galaxies. If we fix the slope to 1 and repeat the fit, the resulting scatter is even larger, about 0.4 dex. The latter is compatible with the intrinsic scatter of the molecular VSF law (0.25-0.37 dex), thus the volume-based approach does not improve the scatter significantly with respect to the surface-based relation. Indeed, the molecular gas distribution typically extends to smaller radii with respect to the atomic gas distribution (Fig. 2.4). This means that the scale height at the outermost radius where the H_2 is measured is only slightly higher than that at the innermost radii. Hence, the conversion to volume densities through the scale height has typically a much milder effect on the molecular gas distribution with respect to the atomic gas. Moreover, the α_{CO} factor is a further source of scatter in the H_2 -SFR relation which cannot be reduced by our method.

Table 2.3 – MCMC best-fit parameters of VSF laws. The first and second columns report the gas phases and the SFR scale height involved. The other columns provide best-fit slope, orthogonal intrinsic scatter σ_{\perp} , and y -intercept with their uncertainties for the VSF laws. These values are given for ρ_{gas} (Eq. 2.20), ρ_{HI} (Eq. 2.21), and ρ_{H_2} (Eq. 2.22) in $M_{\odot}\text{pc}^{-3}$, and ρ_{SFR} in $M_{\odot}\text{yr}^{-1}\text{kpc}^{-3}$.

Gas	h_{SFR}	Slope	σ_{\perp} (dex)	y -intercept $\left(\log \frac{\rho_{\text{SFR}}}{M_{\odot}\text{yr}^{-1}\text{kpc}^{-3}}\right)$
HI+H ₂	constant	$1.34^{+0.02}_{-0.02}$	$0.13^{+0.01}_{-0.01}$	$0.23^{+0.01}_{-0.01}$
HI+H ₂	flaring	$1.91^{+0.03}_{-0.03}$	$0.12^{+0.01}_{-0.01}$	$0.90^{+0.02}_{-0.02}$
HI	constant	$2.09^{+0.06}_{-0.06}$	$0.15^{+0.01}_{-0.01}$	$1.93^{+0.02}_{-0.02}$
HI	flaring	$2.79^{+0.08}_{-0.08}$	$0.13^{+0.01}_{-0.01}$	$2.89^{+0.03}_{-0.02}$
H ₂	constant	$0.52^{+0.02}_{-0.02}$	$0.26^{+0.02}_{-0.01}$	$-0.68^{+0.02}_{-0.02}$
H ₂	flaring	$0.73^{+0.03}_{-0.03}$	$0.37^{+0.02}_{-0.02}$	$-0.18^{+0.03}_{-0.03}$

2.6 Discussion

2.6.1 Comparison with other works on gas and star scale heights

The thickness of gaseous and stellar discs in galaxies has been studied for years using both theoretical and observational approaches. For example, our method is very similar to that implemented by Banerjee et al. (2011). They calculated the atomic gas scale heights for DDO 154 and IC 2574 through an iterative algorithm based on the hydrostatic equilibrium. The parametric mass models of DDO 154 and IC 2574 were taken from de Blok et al. (2008) and Oh et al. (2008), thus the first is equal to the model in Table 2.2 and the second does not differ significantly. These works adopted the velocity dispersion measured by Tamburro et al. (2009) using the 2D method on THINGS data cubes. In order to directly compare the scale heights, we must verify that Banerjee et al. (2011) velocity dispersion is the same as we measured. For DDO 154, they assumed $\sigma_{\text{HI}} = 8 \text{ km s}^{-1}$ and constant with radius, so that their outermost scale height ($R \approx 6 \text{ kpc}$) is about 1 kpc. Within uncertainties, their result is compatible with our scale height at 6 kpc, which is 1.4 kpc as our velocity dispersion is about 10 km s^{-1} (25% higher). For IC 2574, the declining radial profile of the velocity dispersion assumed by Banerjee et al. (2011) is 20% lower everywhere than that shown in Fig. 2.2. The resulting scale height profiles are perfectly compatible within the errors.

Recently, Patra (2018) estimated the scale heights of the HI and H₂ discs in hydrostatic equilibrium for NGC 7331. The gravitational potential model

was taken from de Blok et al. (2008), therefore it is similar to that reported in Table 2.2. There are two differences from our method. The first is that the stellar disc was assumed to be in “hydrostatic equilibrium”, so the stellar scale height was derived iteratively as for the gas components. The second difference is that the author assumed the velocity dispersion to be constant with radius. As a consequence, the comparison is not straightforward but, for $\sigma_{\text{HI}} = 10 \text{ km s}^{-1}$, Patra found $h_{\text{HI}} \approx 230 \text{ pc}$ at $R = 10 \text{ kpc}$, which is compatible with our result of about 400 pc at same radius but with $\sigma_{\text{HI}} = 20 \text{ km s}^{-1}$.

None of the galaxies in our sample are edge-on, so an accurate direct measurement of the gas disc thickness is not possible. However, there are several observational clues that gas discs flares with radius; we give just two recent examples. Yim et al. (2011, 2014) adopted the method proposed by Olling (1996) to measure simultaneously the inclination of the galaxy and the thickness of stellar and gaseous discs. For four star-forming nearby galaxies, they found that both the thicknesses of the atomic gas disc (see also Peters et al., 2017b) and stellar disc flare with radius. They also derived the thickness of the CO disc finding clear signs of the flaring for NGC 891, while the CO flare was not clearly visible for the other galaxies, given the larger uncertainties.

In the MW, Marasco et al. (2017) measured the scale height of HI and H₂ vertical distributions and found that the HI scale height increases of a factor 2 from about 100 pc at $R \approx 2.5 \text{ kpc}$ to about 200 pc in the solar neighbourhood. The molecular gas scale height was instead found to be nearly constant with radius, given the large associated uncertainties (see Chapter 4).

Concerning the SFR scale height, if our assumption is correct and the scale height of SFR flares with radius, we should observe that the thickness of the disc of young stellar populations in galaxies increases with radius, at least in the outskirts. Mackereth et al. (2017) used SDSS-APOGEE survey data to decompose the MW stellar disc according to age, metallicity, and $[\alpha/\text{Fe}]$, and analysed the radial and vertical distributions the different populations. They found that the scale height of young populations, which have mainly high metallicity and low $[\alpha/\text{Fe}]$, flares with radius (see also Xiang et al., 2018). On the other hand, the scale height of old stars, which tend to have high $[\alpha/\text{Fe}]$ and low metallicity, is higher but radially flatter than that of the young populations. We fully explore this in Chapter 4.

2.6.2 Comparison with other works on volume-based SF laws

Other authors investigated the existence of a volumetric relation. The first VSF law was proposed by Schmidt (1959), who linked the HI and SFR through a single power law with slope between 2 and 3. Hence, we should compare his result with our VSF law with HI alone. Interestingly, the best-fit slope found in Sect. 2.5.2 is perfectly compatible with Schmidt’s estimate, suggesting the existence of a universal correlation involving the atomic phase of gas.

Abramova & Zasov (2008) is probably the work most similar to ours. For a sample of seven galaxies (including the MW), they calculated the HI and the H₂ scale heights assuming hydrostatic equilibrium (see also Narayan & Jog, 2002) and then converted the azimuthally averaged surface density radial profiles to volume densities. For the SFR scale height, they tried two approaches: one assumed a constant scale height and the other used the stellar disc thickness. However, they neglected the radial decrease of the velocity dispersion for the gas components, which is the most significant difference with our approach. They found that the gas and SFR volume densities are better correlated with respect to the surface densities, but the slope of the volumetric relation for their galaxies has large variations between 0.8 and 2.4, which are on average close to 1.5. They drew the same result for the molecular gas alone with average slope close to 1. Given the significant difference between the slope of SF laws for single galaxies, they concluded there was an absence of a universal relation. This is probably due to the assumption of radially constant velocity dispersion profiles; our result is however in agreement within the uncertainties with their average slope of 1.5.

More recently, Barnes et al. (2012) studied the link between gas and SFR in the outer disc of seven nearby star-forming galaxies. They found a very steep surface-based SF law in the form of a single power law with index 2.8 ± 0.3 . Then, they estimated the HI disc thickness through the full width at half maximum (FWHM) of the gas vertical profile (Eq. 20 in van der Kruit & Freeman, 2011), finding that this thickness flares with radius. They used this proxy to convert the total gas surface densities radial profiles to volume densities and assumed 100 pc as fiducial value for the SFR scale height. They found a volume-based correlation with index 1.5 ± 0.1 between gas and SFR, which is in agreement with our result (see Tenjes & Haud 1991 for a similar study on M31).

Concerning Galactic studies, Sofue (2017) used 3D maps of HI from the LAB survey (Kalberla et al., 2005) and H₂ from the CO survey (Dame et al., 2001) to estimate the gas volume densities out to 20 kpc. Sofue measured the SFR volume density from the HII region catalogue and investigated the existence of volumetric correlations with total gas, HI only, and H₂ only. The author used two approaches: the first consists in dividing the data in radial bins, while the second considers the whole radial range (0-20 kpc). In the first case, they found that any VSF law showed radial variations both in the index and the normalisation. On the other hand, the second method revealed a correlation with index of 2.01 ± 0.02 for the VSF law with total gas, while the relations involving the molecular and the atomic gas only were found to have a slope of 0.70 ± 0.07 and of 2.29 ± 0.03 , respectively. These results are in excellent agreement with our findings.

Krumholz et al. (2012) formulated a theory involving a molecular and volumetric SF law and compared it to the observed correlations. They gathered a collection of the correlations between gas and SFR using both resolved observations of MW molecular clouds and Local galaxies, and unresolved

observations of local discs and high redshift starbursts. These authors explained the diversity of the observed gas-SFR correlations as the result of the variety of three-dimensional sizes and internal clumpiness, as the volume of the observed region can be very different at fixed surface density. Hence, they removed these projection effects by calculating the free-fall time specifically for each different regime, from molecular clouds to high redshift galaxies, and found that all the data fall on a single power-law relation. In other words, they did not convert the surface densities to volume densities, but they instead built the free-fall timescale using a different prescription for molecular clouds, disc galaxies, and starbursts, obtaining a correlation between Σ_{SFR} and $\Sigma_{\text{gas}}/t_{\text{ff}}$. However, the approach of Krumholz et al. (2012) differs from ours in many aspects. For example, they assumed that the star-forming gas is exclusively molecular, so the free-fall time is always calculated for the molecular phase. In addition, they did not take into account the vertical hydrostatic equilibrium for the gas and neglected the scale height flaring with radius.

2.6.3 Physical interpretation

We conclude by discussing some potential physical interpretations of our findings, starting from the most straightforward. In order to form stars, the gas must be cold and dynamically unstable, therefore the SF timescale is given by the longest between the dynamical and cooling timescales (see e.g. Ciotti & Ostriker, 2007). A key result of our investigation is the superlinear correlation between the SFR and total gas volume densities in the form of a single power law. If we believe that the true SFR scale height is bracketed between the constant and the flaring profiles, the index of the VSF law with total gas should reasonably be between the best-fits slopes of 1.3 and 1.9. If the index is 1.5, then the physical explanation of the correlation may come from the gravitational instability of the gas, indicating that the cooling timescale is shorter than the dynamical timescale. Hence, $\rho_{\text{SFR}} \propto \rho_{\text{gas}}/\tau_{\text{ff}} \propto \rho_{\text{gas}}^{3/2}$ (e.g. Madore, 1977; Li et al., 2006). On the other hand, it is well known that the interstellar medium is not a continuous fluid, but it is mostly in gas clouds and filaments, therefore this interpretation of the global correlation may be not suitable to describe SF on the scales of single clouds. However, our results appear to indicate that the average SFR density at different locations in a galaxy disc is rather precisely regulated by the total volume density of the locally available gas.

Moreover, the fact that the observed break in the Kennicutt law disappears after the conversion to volume densities indicates that it is probably caused by the flaring of the gas disc. This was also suggested by Elmegreen (2015), who aimed to explain the change in the index of the surface-based SF laws. He showed that the classical Kennicutt law between total gas and SFR surface densities is valid in the main regions of spiral galaxies, where he assumed that the scale height is almost constant. In the outskirts instead, he found a steeper index of 2 for the surface-based law, as the gas disc thickness increases with

radius. However, the DM contribution was not included in the model of the galactic gravitational potential, thus the gas is completely self-gravitating in the outer regions and the resulting gas scale height is overestimated.

The tight correlation between the atomic gas and the SFR is the most surprising result of our work. In this case, the interpretation is more difficult and uncertain. If the molecular gas is the prerequisite for SF, why should we observe a correlation between HI and SFR? It is well known that the molecular gas forms from atomic gas, so the possible explanation for the HI VSF law is that the atomic gas is a good tracer of the cold (and molecular) star-forming gas both in low density and, to some extent, high density regions. Indeed, the outskirts of spiral galaxies and dwarf galaxies are often metal poor and low density environments, hence the amount of CO is probably too low to be detected. This scenario could explain the observed extended UV discs (XUV) (Thilker et al., 2007a,b; Donovan et al., 2009), showing that SF can occur also in the outermost and HI-dominated regions of disc galaxies (see also Ferguson et al., 1998), where the metallicity is expected to be very low.

Taken to extremes, the HI VSF law could also mean that molecular gas is not always a prerequisite for SF and the atomic gas plays a key role in the process. Krumholz (2012) showed that SF can occur in cold atomic gas (at extremely low metallicity) rather than in molecular gas, thanks to the efficient cooling by C^+ . In such peculiar conditions, the timescale to convert HI to H_2 is longer than the timescales to reach the thermal equilibrium (cooling time) and gravitational collapse (free-fall time). Hence, atomic gas can efficiently cool and form stars, but it does not have enough time to turn into a significant amount of H_2 . Similarly, Glover & Clark (2012) investigated whether or not the molecular gas is essential for SF. They performed a set of numerical simulations of dense clouds using different chemical prescriptions: one in which the gas remains atomic for the whole cloud evolution, a second including H_2 formation, and a third following both H_2 and CO formation. They found that the SF process is very similar in all the simulations and concluded that the molecular gas is not a prerequisite for SF, as the gas can efficiently cool thanks to C^+ line emission at low density and by energy transfer from gas to dust at high density. On the contrary, they found that including or not the dust shielding is fundamental, as it allows the gas to cool below 100 K and form stars. In other words, the ability of clouds to shield themselves from the interstellar radiation field is the key to SF. Moreover, the authors concluded that the observed correlation between the molecular gas and SFR surface densities originates from the fact that both the terms correlate with a third factor, which is the clouds ability to self-shield (see also Krumholz & Thompson, 2007).

Concerning the H_2 VSF law, the interpretation is even more difficult, as the estimate of the molecular gas volume density is problematic. This correlation seems to hold for the central parts of galaxies, despite the large uncertainties associated with the α_{CO} factor, velocity dispersion, and bulge

potential. Probably, the interplay of these factors causes the large scatter of the molecular VSF law. However the surface density law has a similar scatter. The molecular gas is mostly in giant molecular clouds, but we are not including any clouds filling factor in our study. Thus, the volume density that we calculate is simply a mean value in a region of $\Delta z \approx h_{\text{H}_2}$ perpendicular to the midplane, so our estimate of the volume density is very different from the volume density inside a cloud. This could explain why the molecular gas volume densities reach values lower than $10^{-3} \text{ M}_\odot \text{ pc}^{-3}$, which corresponds to about 10^{-2} H_2 particles per cm^3 .

It is interesting to compare our results with the recent work by Catinella et al. (2018). They presented the extended GALEX Arecibo SDSS Survey (xGASS), a census of 1179 galaxies selected by stellar mass ($10^9 \text{ M}_\odot < \text{M}_\star < 10^{11.5} \text{ M}_\odot$) and redshift ($0.01 < z < 0.05$). They measured stellar masses, SFRs, and HI masses for all the galaxies and H_2 masses for 532 galaxies. They found that the gas reservoir in galaxies is on average HI-dominated, while the ratio of the HI to H_2 masses slightly increases with increasing stellar mass. Moreover, for the whole mass range, the HI mass tightly correlates with the dust-unobscured SFR traced by near-ultraviolet- r colour. In light of these results, our correlation between HI and SFR volume densities is not surprising.

The tight VSF law between total gas and SFR corroborates the idea that the whole gas, including the atomic phase, traces SF in galaxies. Then, the HI and H_2 VSF laws could help in understanding the mechanism of the conversion of atomic gas to molecular gas and how important this is in the whole SF process.

2.7 Summary and conclusions

We have investigated the existence of a fundamental SF law based on volume densities of gas and SFR. We built VSF laws using the volume densities radial profiles calculated from the surface density profiles of 12 nearby galaxies. To make the conversion to volume densities possible, we assumed the hydrostatic equilibrium and calculated the HI, H_2 , and SFR scale heights, which required two preliminary steps: the first to calculate the total gravitational potential and the second to measure the gas velocity dispersion. Using volume densities, we found a correlation between the total gas (HI+ H_2) and the SFR, which is less scattered than the classical surface-based law. Moreover, an unexpected and tight relation between HI and SFR volume densities was discovered, suggesting a profound link between the atomic phase of gas in galaxies and SF. The H_2 -only version of the VSF law was found to have a larger scatter with respect to the HI-only and total gas relations, it seems to break down in low density and HI-dominated environments.

Hence, our conclusions are the following.

1. The thickness of gas discs in hydrostatic equilibrium shows a significant flaring with radius, regardless of the galaxy type. This means that assuming a constant scale height for gaseous discs is not a good approximation.
2. The total gas and the SFR volume densities are linked by a tight and single power law with index between 1.3 and 1.9, depending on whether a flare in the SFR scale height itself is taken into account or not.
3. The break observed in the Kennicutt law may not be indicative of a low SF efficiency of atomic gas at low surface density, but rather be a consequence of the radial flaring of the gas discs.
4. The SFR volume density also correlates with the HI alone volume density through a single power law with small scatter and index between 2.1 and 2.8.

The VSF law is likely more fundamental and general than surface-based laws, as it takes into account the three-dimensional distribution of gas and SFR. The unexpected and tight correlation between HI and SFR volume densities may be important to unveil the mechanisms that regulate the conversion of gas into stars, in particular in low density and HI-dominated environments as dwarf galaxies and the outskirts of spiral galaxies (see Chapter 4).

Acknowledgements

C. B. is grateful to A. Marasco, L. Posti, M. Nori, V. Ghirardini, and E. di Teodoro for inspiring conversations and advice, and to Bradley Frank for sharing the surfaced density profiles of molecular gas.

Appendix 2.A VSF law using the analytical approximation for the scale height

In Sect. 2.2.4, we reported an analytic approximation (Eq. 2.13) for the scale height of the vertical distribution of a gas disc in hydrostatic equilibrium (see Romeo 1990, 1992 for a rigorous analytic study of the vertical structure of galactic discs). We now show that the results obtained through this definition are compatible with what we have found using the numerical (and more accurate) method. Through the Poisson equation of gravity in the z direction, we know that

$$\frac{\partial^2 \Phi(R, z)}{\partial z^2} = 4\pi G \rho_{\text{tot}}(R, z) - \frac{1}{R} \frac{\partial}{\partial R} \left(R \frac{\partial \Phi(R, z)}{\partial R} \right), \quad (2.A.1)$$

where $\rho_{\text{tot}}(R, z)$ is the total mass distribution of the galaxy components. In the midplane, $\frac{\partial \Phi(R, 0)}{\partial R} = \frac{V_c(R)^2}{R}$, where V_c is the galaxy circular velocity. Hence, the r.h.s. of Eq. 2.A.1 is

$$\frac{\partial^2 \Phi(R, z)}{\partial z^2} \approx 4\pi G [\rho_{\text{tot}}(R, 0) + \rho_{\text{rot}}(R)], \quad (2.A.2)$$

where the rotational density ρ_{rot} is (see Bahcall, 1984; Bahcall & Casertano, 1984; Olling, 1995)

$$\rho_{\text{rot}}(R) \equiv -\frac{1}{2\pi G} \frac{V_c(R)}{R} \frac{\partial V_c(R)}{\partial R}. \quad (2.A.3)$$

Substituting Eq. 2.A.2 in Eq. 2.13, we find the following simple and generic analytical formulation for the scale height that can be used once the mass distribution of the galaxy components are known:

$$h(R) \simeq \frac{\sigma(R)}{\sqrt{4\pi G [\rho_{\text{tot}}(R, 0) + \rho_{\text{rot}}(R)]}}. \quad (2.A.4)$$

We note that, with this approximation, the gas self-gravity is not included and we are assuming a cylindrical mass distribution which, at fixed R , does not vary with z with respect to its value in the midplane.

For the galaxies in our sample, we assumed that the main mass components are the spherical DM halo and the stellar disc, which are modelled by Eq. 2.6 or Eq. 2.7 and Eq. 2.8, respectively. The rotational density for the NFW halo is (with $x = r/r_s$)

$$\rho_{\text{rot}}(x) = -\rho_{\text{DM},0} \left[\frac{x(2x+1) - (1+x^2)\log(x+1)}{(1+x^2)x^3} \right]. \quad (2.A.5)$$

For the isothermal halo, we have (with $y = \sqrt{1+r^2/r_c^2}$)

$$\rho_{\text{rot}}(y) = -\rho_{\text{DM},0} \left[\frac{\arctan(y)(1+y^2) - y}{(1+y^2)y^3} \right]. \quad (2.A.6)$$

The exponential disc circular velocity is given by Eq. 2.165 in Binney & Tremaine (2008), so the rotational density is

$$\rho_{\text{rot}}(k) = -\frac{\Sigma_{\star,0}}{16R_{\star}} [kA(k/2) + 8B(k/2)], \quad (2.A.7)$$

where $k = R/R_{\star}$, $A(k/2) = 3K_0I_1 + K_2I_1 - 3K_1I_0 - I_2K_1$ and $B = I_0K_0 - I_1K_1$ being K_0 , K_1 , I_0 , and I_1 the modified Bessel functions. The stellar bulge is modelled as an exponential sphere (Eq. 2.9) with circular velocity given by Eq. 2.18, so

$$\rho_{\text{rot}}(R) = \frac{V_c^2}{4\pi GR^2} - \rho_b(R). \quad (2.A.8)$$

Table 2.2 provides all the parameters to calculate the mass distributions and rotational densities. Figure 2.A.1 compares h_{HI} and h_{H_2} calculated through Eq. 2.A.4 and with GALPYNAMICS, the velocity dispersion is modelled as explained in Sect. 2.4.1 and Sect. 2.4.2. For the majority of the galaxies in our sample, the analytical estimate is compatible with the numerical scale height within the uncertainties. Hence, the SFR scale height calculated through Eq. 2.17 but using the approximated h_{HI} and h_{H_2} is approximately equivalent to that shown in Fig. 2.4.

Then, we use the analytical scale heights to convert the observed surface densities (see Sect. 2.3.1) to volume densities through Eq. 2.15. We have therefore all the elements to build the VSF laws and perform an MCMC fitting to derive slope, y -intercept and scatter of the VSF laws with total gas, HI only, and H₂ only. The results are reported in Table 2.A.1 and are compatible within the uncertainties with those in Table 2.3.

Table 2.A.1 – MCMC best-fit parameters for the VSF laws in the analytical approximation for the scale heights. The first and second columns report the gas phases and the SFR scale height involved. The other columns provide best-fit slope, orthogonal intrinsic scatter σ_{\perp} , and y -intercept with their uncertainties. These values are given for ρ_{gas} (Eq. 2.20), ρ_{HI} (Eq. 2.21), and ρ_{H_2} (Eq. 2.22) in $\text{M}_{\odot}\text{pc}^{-3}$, and ρ_{SFR} in $\text{M}_{\odot}\text{yr}^{-1}\text{kpc}^{-3}$.

Gas	h_{SFR}	Slope	σ_{\perp} (dex)	y -intercept $\left(\log \frac{\rho_{\text{SFR}}}{\text{M}_{\odot}\text{yr}^{-1}\text{kpc}^{-3}}\right)$
HI+H ₂	constant	$1.31^{+0.03}_{-0.02}$	$0.13^{+0.01}_{-0.01}$	$0.25^{+0.02}_{-0.02}$
HI+H ₂	flaring	$1.91^{+0.03}_{-0.03}$	$0.11^{+0.01}_{-0.01}$	$0.94^{+0.02}_{-0.02}$
HI	constant	$1.97^{+0.06}_{-0.06}$	$0.15^{+0.01}_{-0.01}$	$1.79^{+0.02}_{-0.02}$
HI	flaring	$2.70^{+0.07}_{-0.07}$	$0.13^{+0.01}_{-0.01}$	$2.76^{+0.02}_{-0.02}$
H ₂	constant	$0.52^{+0.02}_{-0.02}$	$0.27^{+0.02}_{-0.01}$	$-0.66^{+0.02}_{-0.02}$
H ₂	flaring	$0.73^{+0.03}_{-0.03}$	$0.37^{+0.02}_{-0.02}$	$-0.18^{+0.03}_{-0.03}$

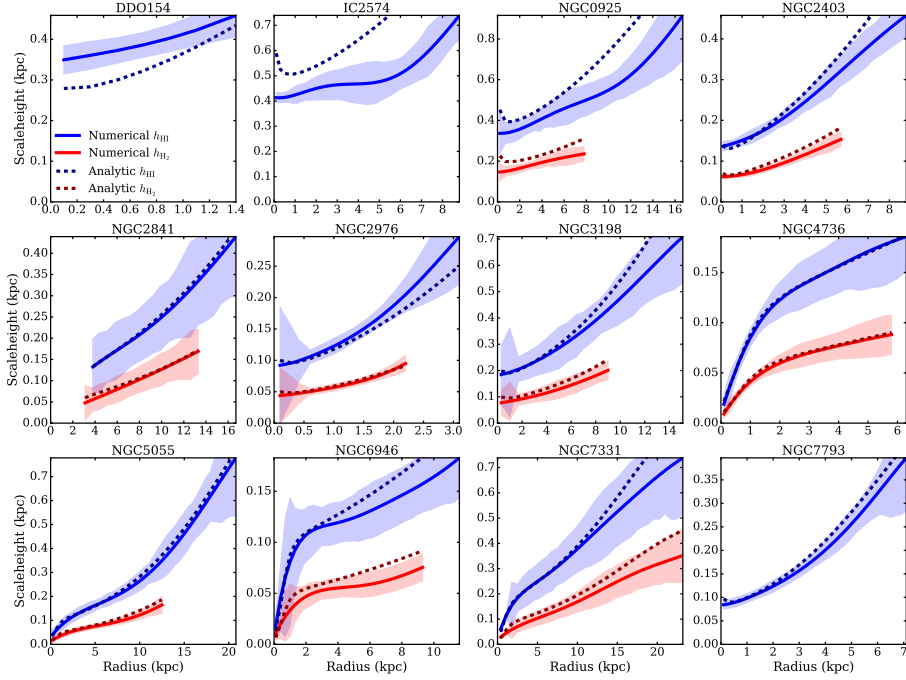


Figure 2.A.1 – Comparison of the scale heights calculated by Eq. 2.A.4 (dashed line) and by GALPYNAMICS (solid line). The HI and H₂ scale heights are in blue and red, respectively.

Appendix 2.B ^{3D}Barolo set-up

As mentioned in Sect. 2.4.1, we derived the HI velocity dispersion using 3DB on publicly available 21-cm data cubes from the survey THINGS. In a broad outline, the tilted-ring modelling consists in decomposing the rotating disc of a galaxy into a series of circular rings with radius R and characterised by kinematic and geometrical parameters. For each sampling radius, 3DB first builds a ring model described by inclination, position angle, and rotation velocity, then the model is compared to real data and the parameters of the ring are updated until the residuals between the model and observations are minimised. Before the comparison, the model is convolved with the point spread function (PSF) by degrading it to the same spatial resolution of the observations. This step is fundamental to account for the beam smearing, which can affect the determination of the velocity dispersion. Each ring is fully described by the following parameters: the spatial coordinates of the centre (x_0, y_0) , systemic velocity V_{sys} , inclination i , position angle ϕ , rotation velocity V_{rot} , velocity dispersion σ_{HI} , face-on HI column density Σ_{HI} , and scale height of the gas layer z_0 .

We used the robust weighted data cubes to ensure a reliable measurement of the line broadening due to the gas turbulence. Indeed, Ianjamasimanana et al. (2017) showed that the shape of the beam of natural weighted data cubes significantly differs from a Gaussian, causing an overestimate of the velocity dispersion, while the robust weighted data cubes are less affected by this bias. Leroy et al. (2008) measured the surface densities of gas and SFR at resolutions of 400 pc and 800 pc for dwarf galaxies and normal spirals, respectively. For all the galaxies, we aimed to have a common spatial resolution that is not only compatible with their surface density measurements, but also as high as possible to preserve a good sampling of the velocity dispersion radial trend. The most distant galaxy, NGC 2841, was observed at about 400 pc of spatial resolution, and consequently this is our upper limit for homogeneous resolution. Hence, we smoothed all data cubes to the same spatial resolution of about 400 pc to improve the S/N in the data cubes (see Table 2.B.2 for corresponding beam size). Secondly, this resolution is compatible with the drift scale, which is the displacement between a young star and its parent cloud (see Koda, 2008).

In order to set 3DB initial parameters, we made the following assumptions.

- *HI column density:* Σ_{HI} was removed from the list of free parameters choosing one of the two 3DB normalisation methods. It is possible to normalise the model flux to the observed intensity map by a pixel-by-pixel (local) or azimuthal comparison. The local normalisation better represents the non-axisymmetric features and prevents under-dense or over-dense regions from influencing the residuals minimisation. However, the weakness of this choice is that, in some cases, the algorithm is not able to reliably estimate the radial variation of the inclination and thus the output profile for the inclination varies unrealistically. Therefore, it is advisable to set the inclination to a fixed value when using the local normalisation. For this reason, when the S/N in the 400 pc resolution data cube is low (as for the most distant galaxies, NGC 2841, NGC 3198, and NGC 7331), we choose the azimuthal normalisation. The normalisation for each galaxy is reported in Table 2.B.2 (L=local, A=azimuthal). In the vast majority of cases, the assumption on the normalisation does not affected the fit nor the dispersion velocity measurements.
- *Scale height:* 3DB is insensitive to the scale height as the tilted ring fitting procedure is done ring-by-ring, while for thick discs one line of sight can intersect emission from different annuli because of the projection effects of inclination. Iorio et al. (2017) found that assuming a constant scale height does not significantly affect the estimate of the kinematical parameters in their sample of dwarf galaxies or, at least, these differences are compatible with the errors. The galaxies in our sample are more massive than Iorio et al. (2017) dwarfs, so the thickness bias is expected to be even milder for our galaxies. Following Iorio et al. (2017), we adopted $z_0 = 100$ pc, which is smaller than the spatial resolution and constant for each ring.

- *Systemic velocity:* Before fixing V_{sys} , we compared the values reported in de Blok et al. (2008) with the systemic velocity obtained from the global line profile by $V_{\text{sys}} = 0.5 (V_{\text{app}}^{20\%} + V_{\text{rec}}^{20\%})$, where $V_{\text{app}}^{20\%}$ and $V_{\text{rec}}^{20\%}$ are the velocities corresponding to the 20% of flux peak for the approaching and receding sides of the galaxy. The results are compatible for all the galaxies except IC 2574. In this case, we found $V_{\text{sys}} = 44.9 \text{ km s}^{-1}$, which is lower than the 53.1 km s^{-1} estimate by de Blok et al. (2008) but compatible with the measurement with 3DB, so we chose the former.
- *Galaxy centre:* (x_0, y_0) is fixed to the optical centre coordinates from the NASA/IPAC Extragalactic Database (NED).

Figures 2.B.2–2.B.14 provide a comprehensive view of the kinematical properties of our sample of galaxies and show the comparison between the observations and the best-fit models obtained with 3DB. The description of each panel follows below.

- Panel A: stellar emission in R band (Kennicutt et al., 2003; Baillard et al., 2011; Cook et al., 2014) overlaid with the iso-density contours of the total HI emission. The thick contour indicates the $3\text{-}\sigma$ noise in the total map (see Lelli et al., 2014b; Iorio et al., 2017). The cross corresponds to the galaxy center and the ellipse shows the outermost fitted ring.
- Panel B: velocity field or 1st moment map of the data cube. The thick contour shows the systemic velocity and the black circle in the bottom right corner represents the beam of the telescope or the adopted beam after smoothing (see Table 2.B.2).
- Panel C: velocity dispersion map obtained as the 2nd moment map of the data cube. The black bar in the bottom right corner shows the physical scale of the observations.
- Panel D: HI gas surface density as a function of the galactocentric radius R .
- Panel E: rotation velocity as a function of R .
- Panel F: velocity dispersion radial profile obtained through the 3D modelling (not from the 2nd moment map).
- Panels G and H: inclination and position angle of the rings. The dashed grey line shows the mean value and the red curve (when present) indicates the regularised profile used to obtain the final model (see Di Teodoro & Fraternali 2015 for details).
- Panels I and J: position–velocity diagrams along the major and the minor axis of the HI disc. The black and the red contours are the iso-density

Table 2.B.2 – 3DB input parameters and characteristics of data cubes. (1) Beam size of the data cube (NGC 2841, NGC 3198, and NGC 7331 are at the original resolution); (2) channel width; (3) noise in the channels; (4) noise in the total map; (5) outermost fitted radius; (6) sampling radius; (7,8) centre coordinate; (9) systemic velocity; and (10) normalisation method (L=local, A=azimuthal).

Galaxy	Beam (")	Δv (km s^{-1})	σ_{ch} (mJy/beam)	σ_{tot}	R_{max} (kpc)	ΔR (pc)	centre RA (hh mm ss.s)	centre DEC (dd mm ss)	V_{sys} (km s^{-1})	norm
	(1)	(2)	(3)	(4)	(5)	(6)	(7)	(8)	(9)	(10)
DDO 154	21 x 21	2.6	1.366	6.3	8.3	412	12 54 6.35	27 09 0.5	375.2	L
IC 2574	22 x 22	2.6	1.793	10	9.6	418	10 28 23.5	68 24 44	44.9	L
NGC 0925	9 x 9	2.6	0.820	5.002	16.1	401	02 27 16.9	33 34 45	546.3	L
NGC 2403	27 x 27	5.2	0.0326	0.154	19	413	07 36 51.4	65 36 09	133.2	L
NGC 2841	6.06 x 5.79	5.2	0.3917	2.745	46.8	410	09 22 02.6	50 58 35	633.7	A
NGC 2976	23 x 23	5.2	0.934	3.769	3.2	400	09 47 15.4	67 54 59	1.1	L
NGC 3198	7.64 x 5.62	5.2	0.382	0.198	31.4	474	10 19 54.9	45 32 59	657	A
NGC 4736	18 x 18	5.2	0.895	4.502	7.8	410	12 50 53.0	41 07 14	306.7	L
NGC 5055	9 x 9	5.2	0.499	2.839	33.3	432	13 15 49.3	42 01 45	496.7	L
NGC 6946	15 x 15	2.6	1.556	10.179	14.5	402	20 34 52.3	60 09 14	48.7	L
NGC 7331	4.94 x 4.6	5.2	0.505	3.318	24.8	357	22 37 04.0	34 24 56	818.3	A
NGC 7793	24 x 24	2.6	2.343	16.634	7.14	420	23 57 49.8	-32 35 28	226.2	A

contours of the galaxy and the best-fit model, respectively. The grey contours correspond to the regions with negative flux. The horizontal black dashed line shows the systemic velocity.

We note that, for some galaxies, the radial profiles of the HI surface density are a factor $\approx 1.5 - 2$ higher than the those from Leroy et al. (2008) used in this work. This is partially due to the masking applied to the HI data cubes for the modelling of the kinematics, as we created “loose” masks in order to include the whole galaxy emission in the masked cubes. The main cause of the discrepancies in the HI surface density is however the fact that the noise in the data cubes of some galaxies is not uniform (e.g. IC 2574, NGC 7331). Hence, the smoothing in spatial resolution that was applied to the observations likely increased the total flux in the data cube because of the noise contribution. We recall that these HI surface densities were not used in this work.

Concerning individual galaxies, there are a few notes on the kinematical model which are worth to mention. In the pv-diagram of NGC 0925 (Fig. 2.B.4, panel I), a small contribution from residual beam smearing is present for the first ring of the model. The data cubes of IC 2574, NGC 2403, NGC 2976, and NGC 6946 contain the 21-cm emission of the Milky Way. In order to obtain a satisfactory fit, we removed the channel with the Galactic emission from NGC 2403 data cube, while we performed a channel-by-channel selection for NGC 2976. Figure 2.B.13 and Figure 2.B.14 show respectively the models with the declining and the flat rotation curve (see Sect. 2.C for details), which both reproduce the observations.

Appendix 2.C Revisited mass model for NGC 7793

The observed HI rotation curve of NGC 7793 has a declining profile in de Blok et al. (2008) (green points in Fig. 2.C.15). The authors interpreted this shape as a signature of a maximum stellar disc, but they found relatively low best-fit M/L values of 0.22 or 0.31 depending on the assumed initial mass function. In order to find a reliable mass model, we decided to interpret the declining rotation curve as the result of a small warp in inclination beyond 4 kpc. In practice, we first performed the tilted-ring fitting using 3DB to determine a first guess of the rotation curve. Then, we repeated the fit using this rotation curve for the rings at $R < 4$ kpc but fixing V_{rot} at its peak (121.8 km s^{-1}) for the rings beyond 4 kpc. The resulting best-fit inclination starts to decrease at 4 kpc from about 44° to about 40° .

In Fig. 2.C.15, the difference between our rotation curve and that of de Blok et al. (2008) is due to the radial variation of the inclination. Our best-fit inclination is systematically lower than that of de Blok et al. (2008), so our rotation curve tends to be higher. We note that both rotation curves

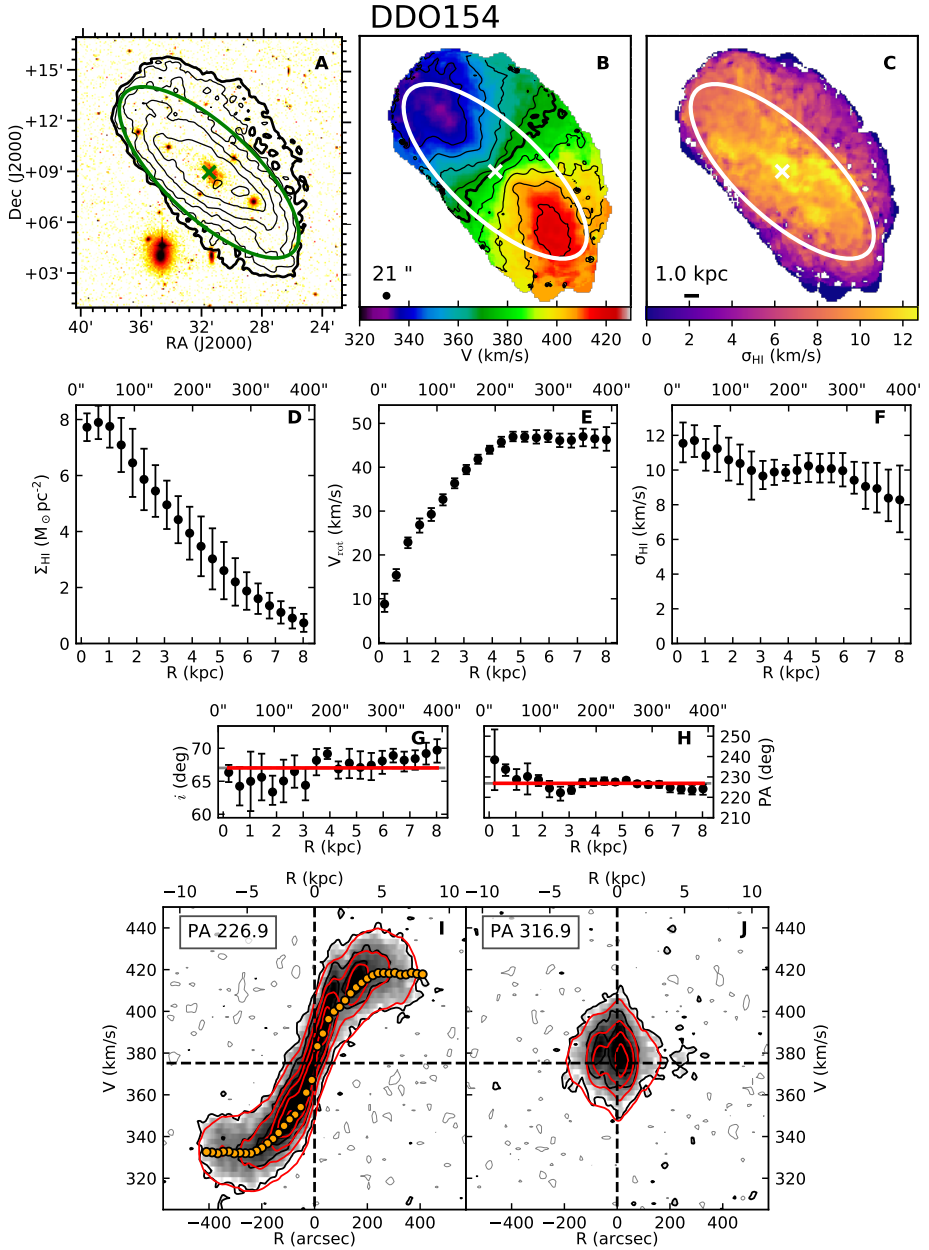


Figure 2.B.2

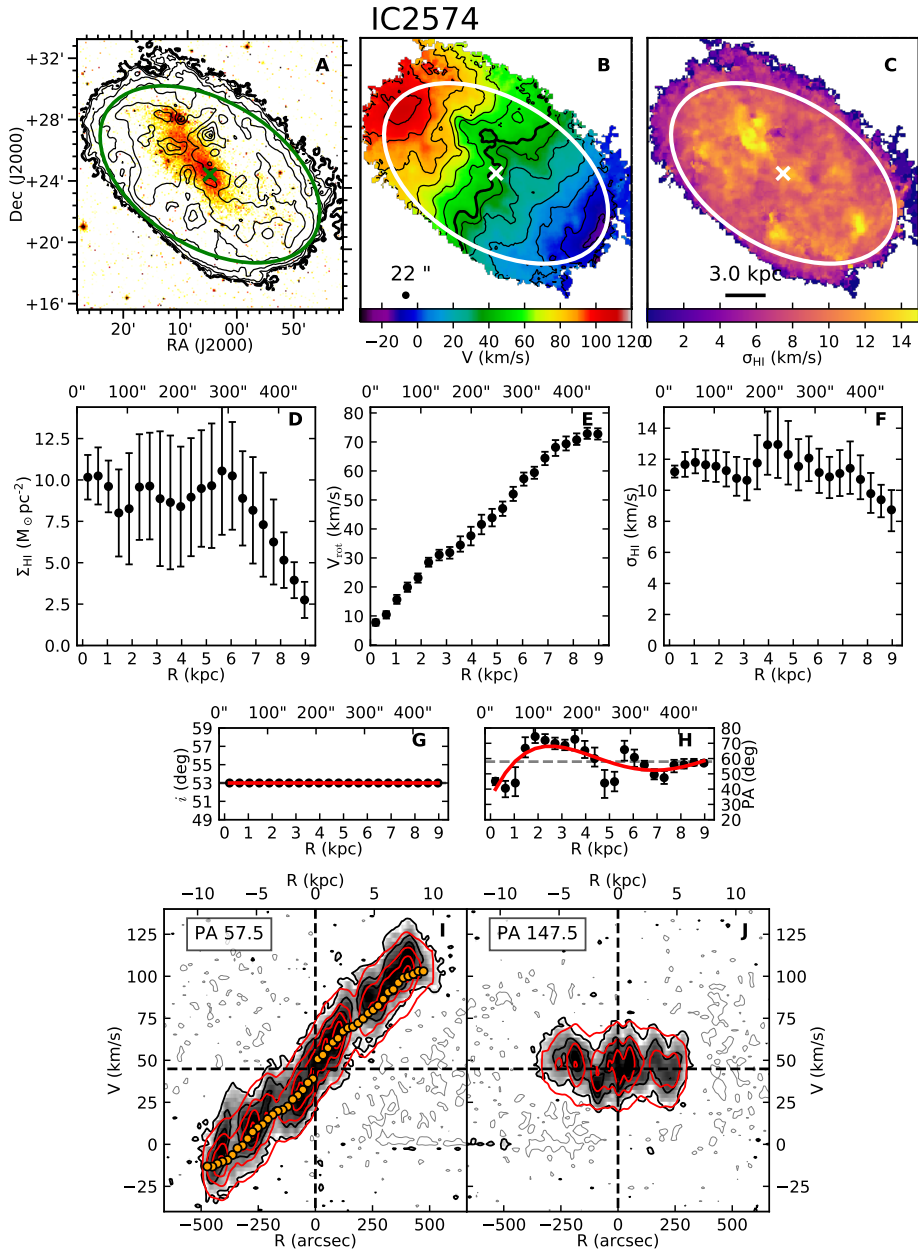


Figure 2.B.3

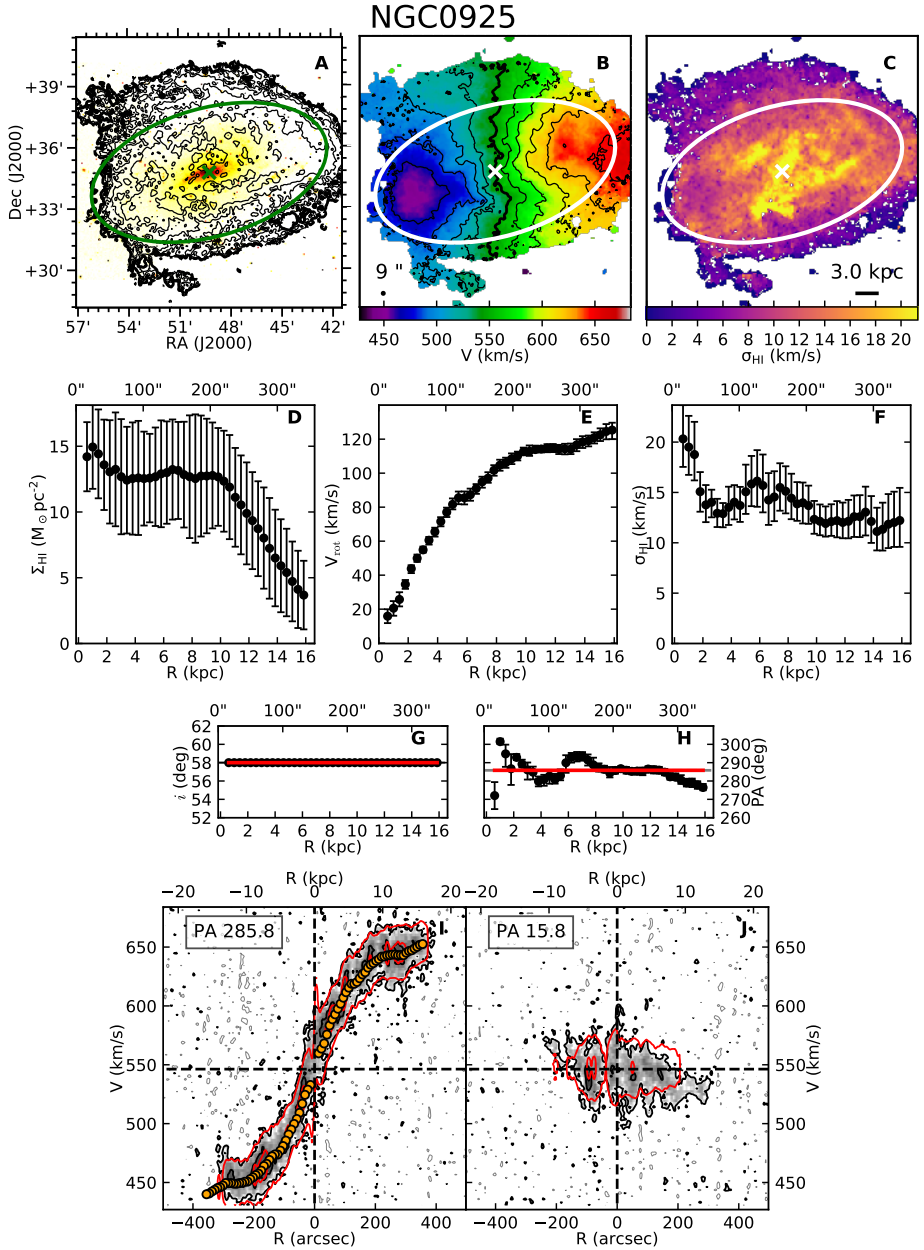


Figure 2.B.4

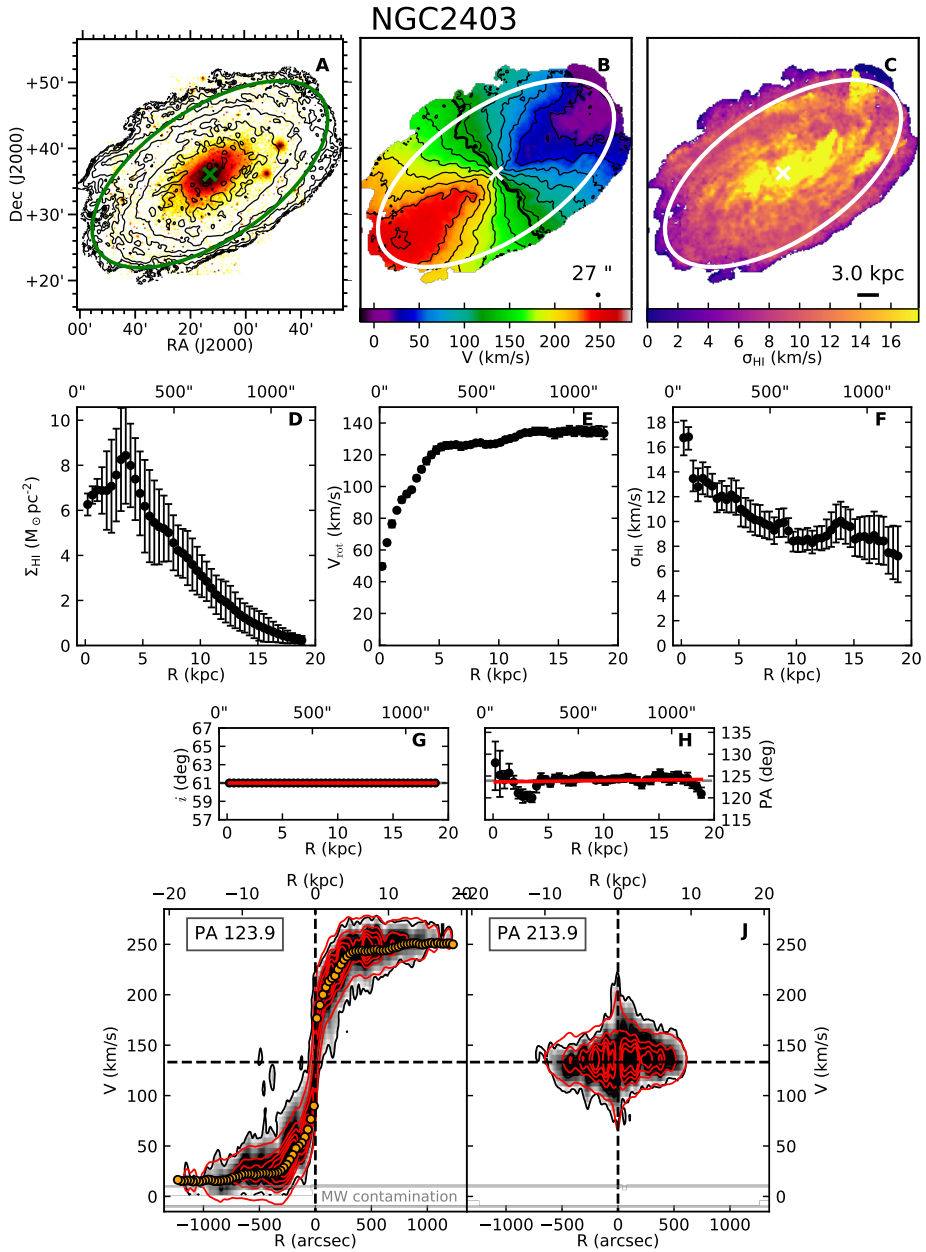


Figure 2.B.5

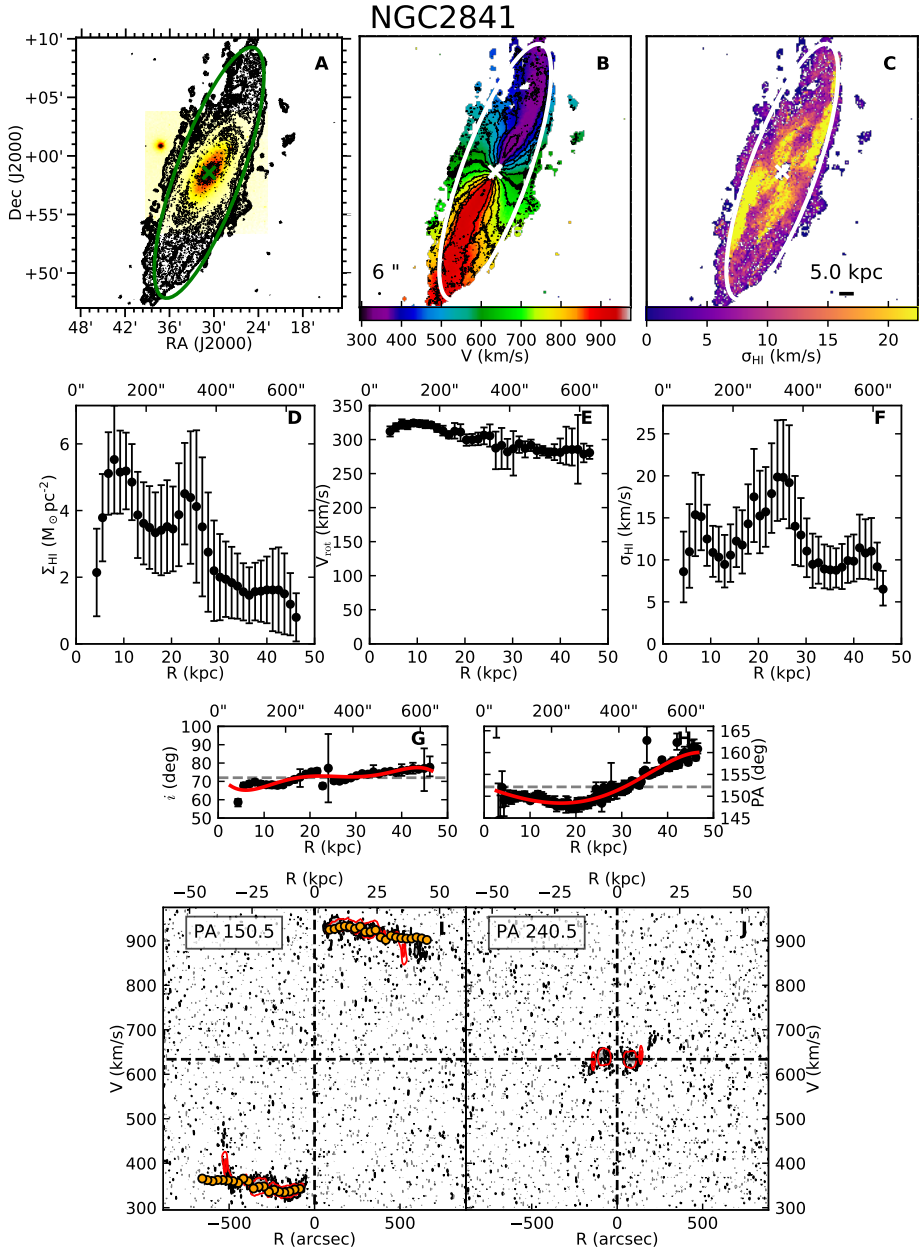


Figure 2.B.6 – To improve the clarity of panels D, E, and F, we plotted one point each 3 rings.

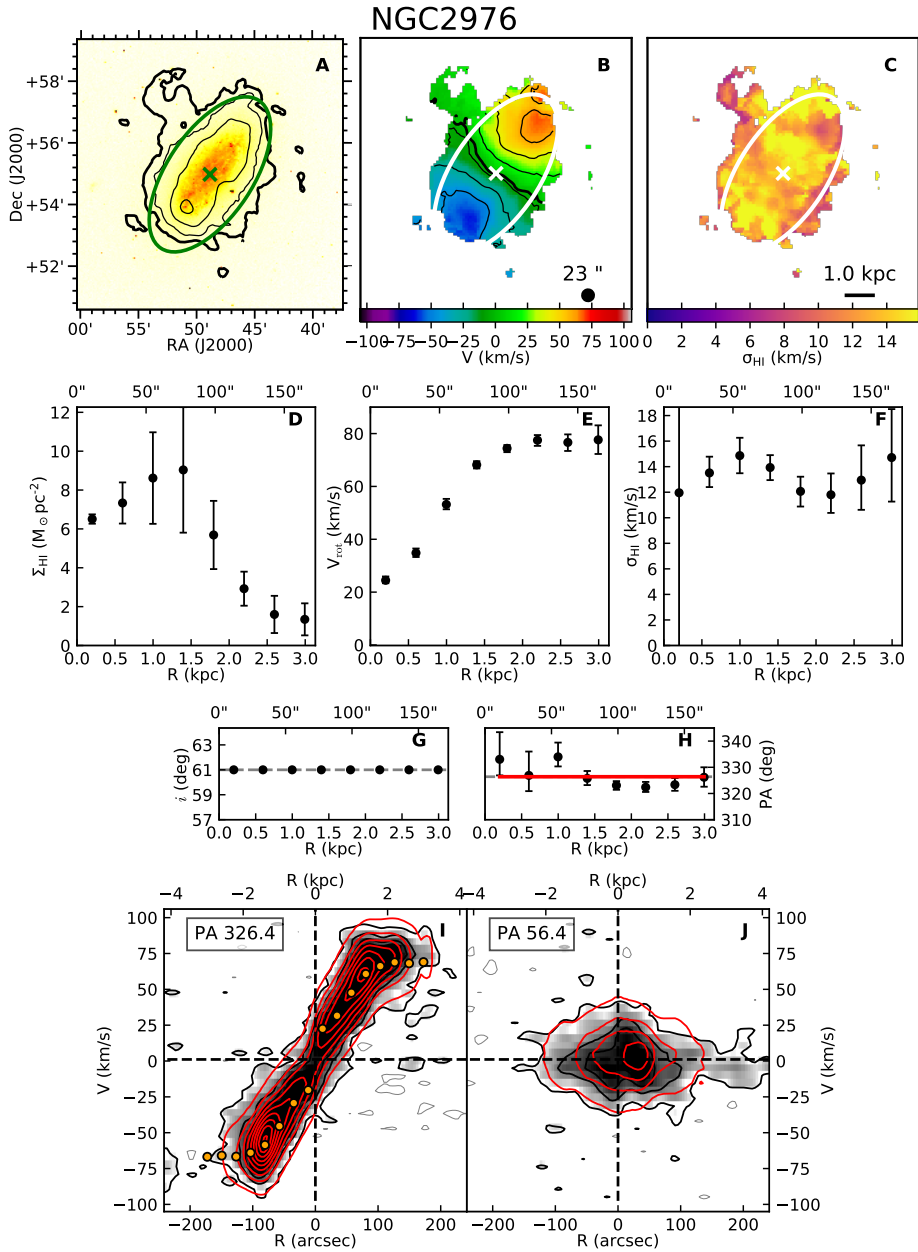


Figure 2.B.7

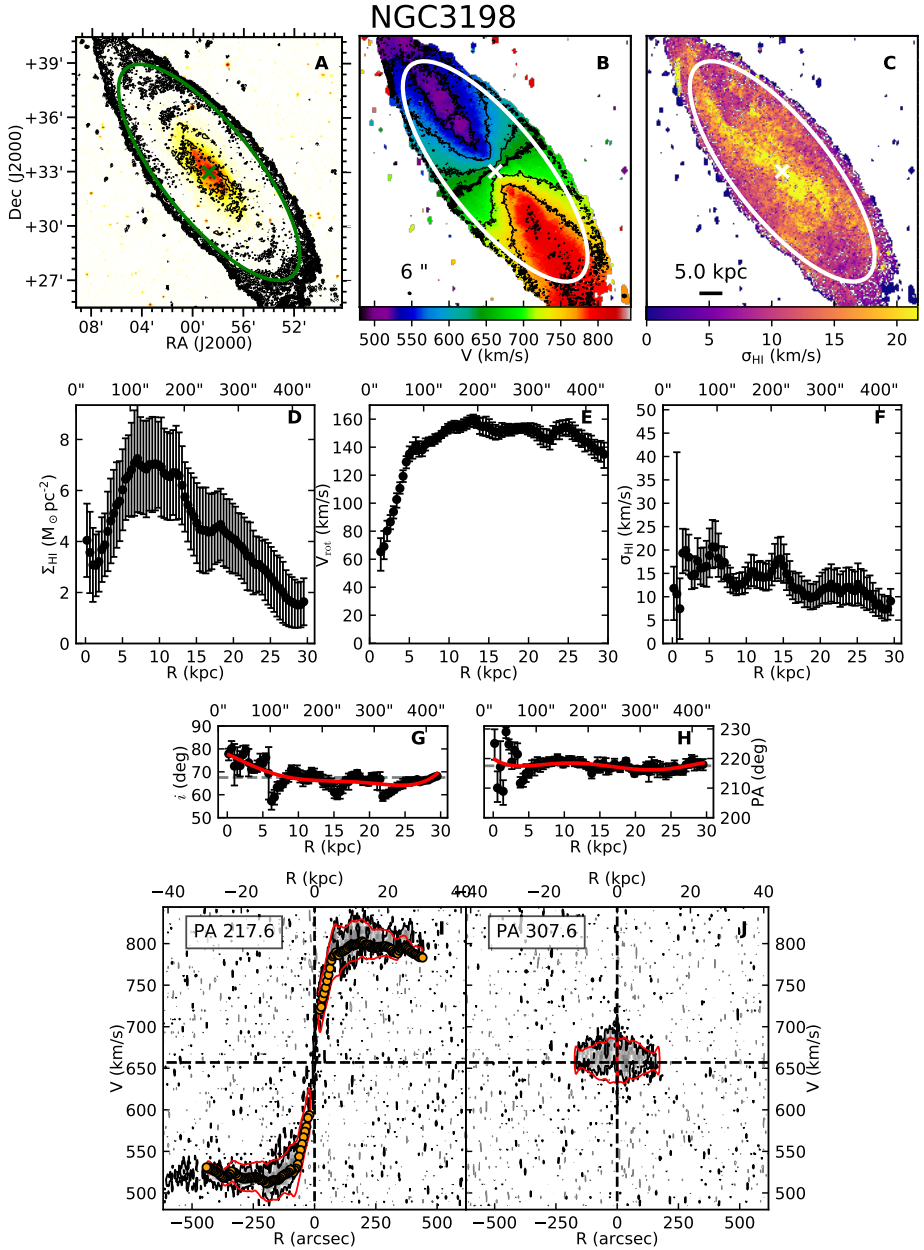


Figure 2.B.8

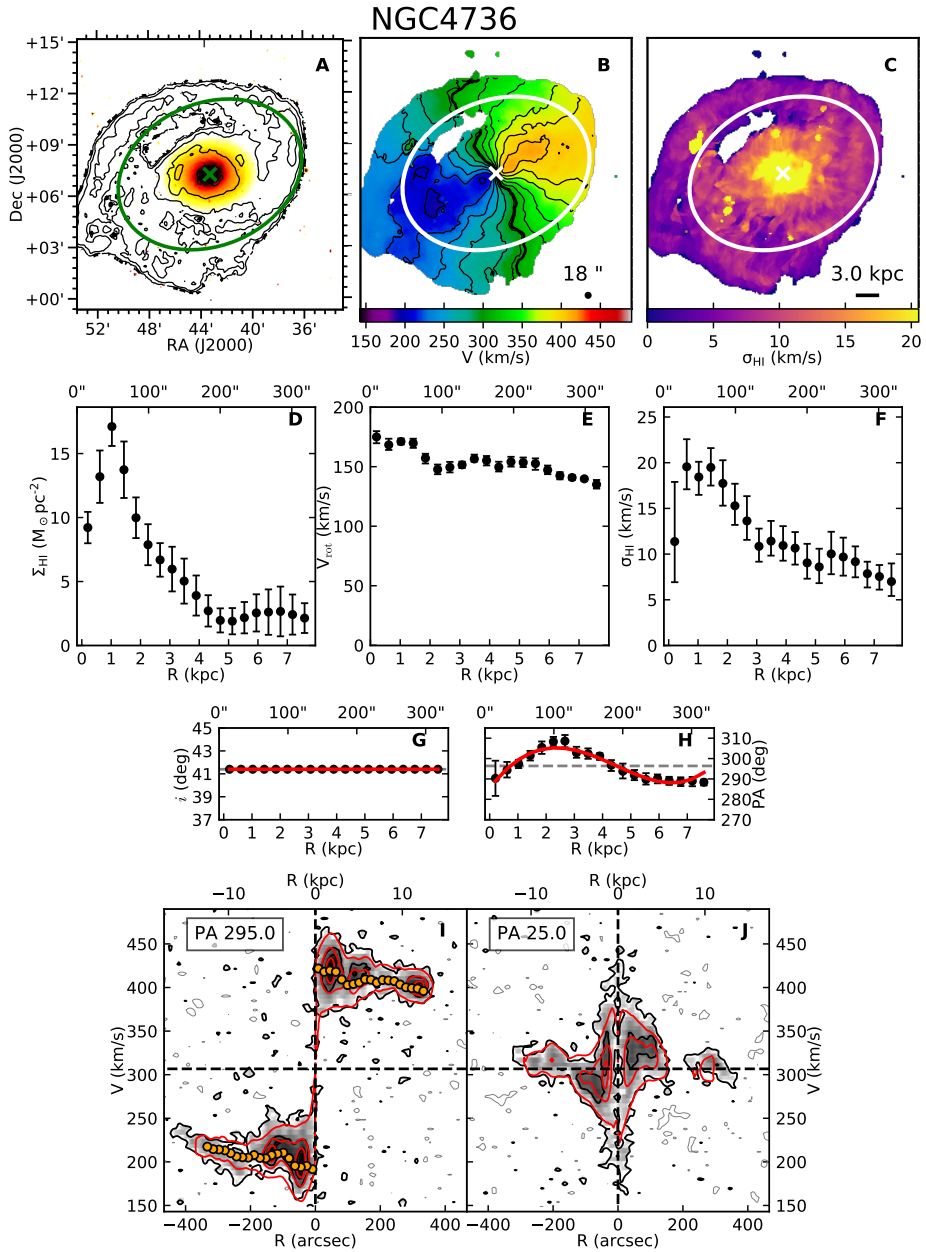


Figure 2.B.9

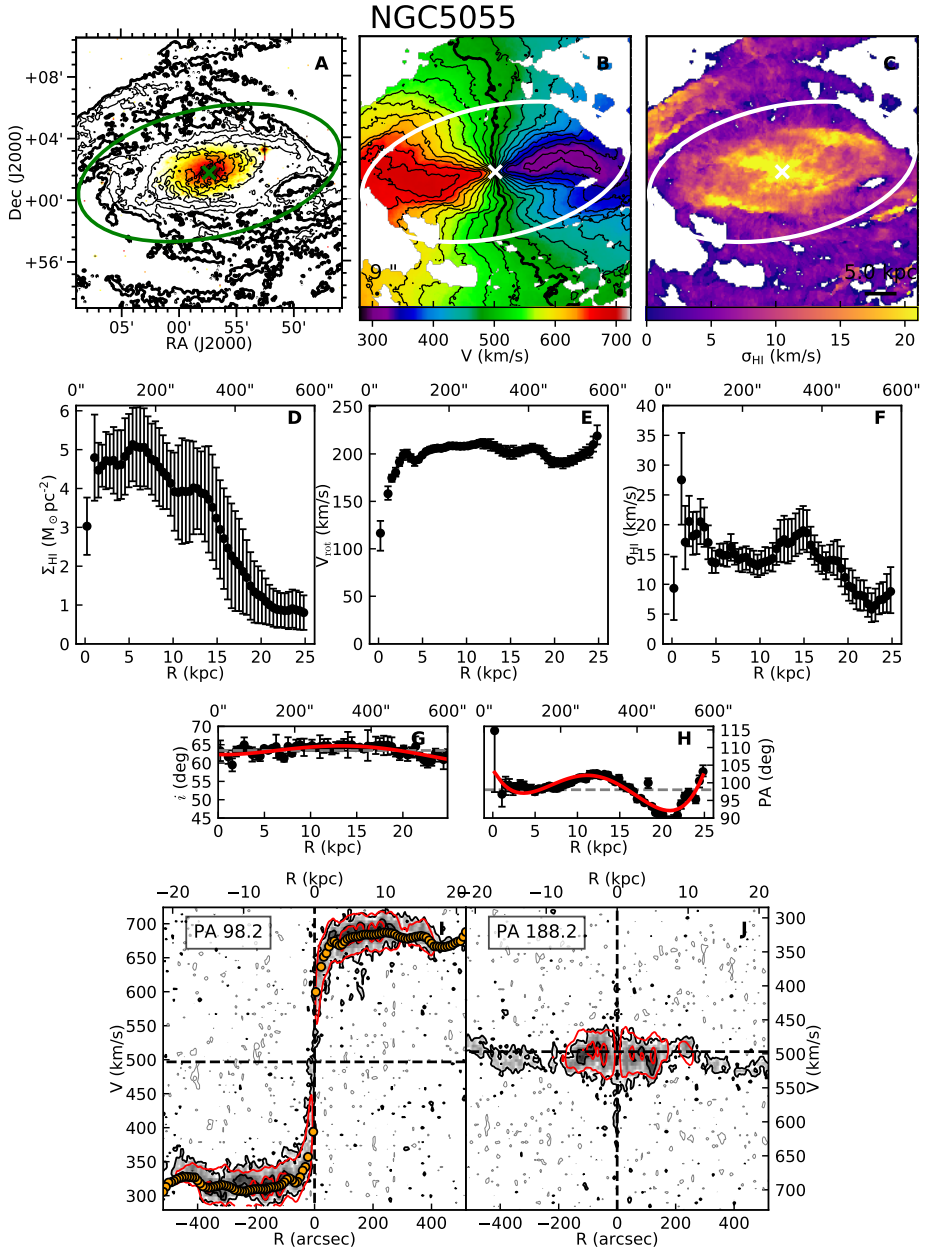


Figure 2.B.10 – The fit with 3DB was performed only for the inner parts of the HI disc where the S/N in the rings is relatively high for all azimuthal angles.

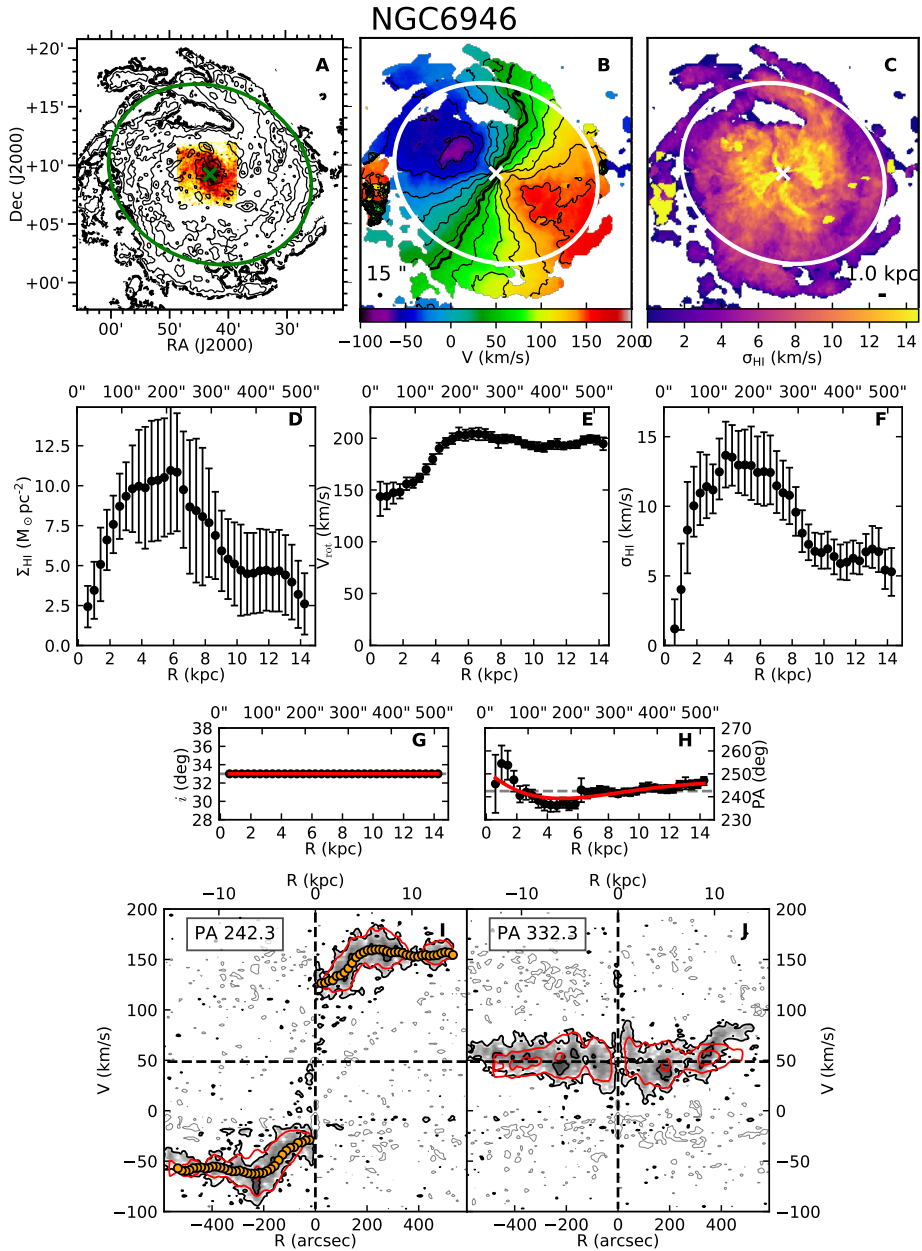


Figure 2.B.11

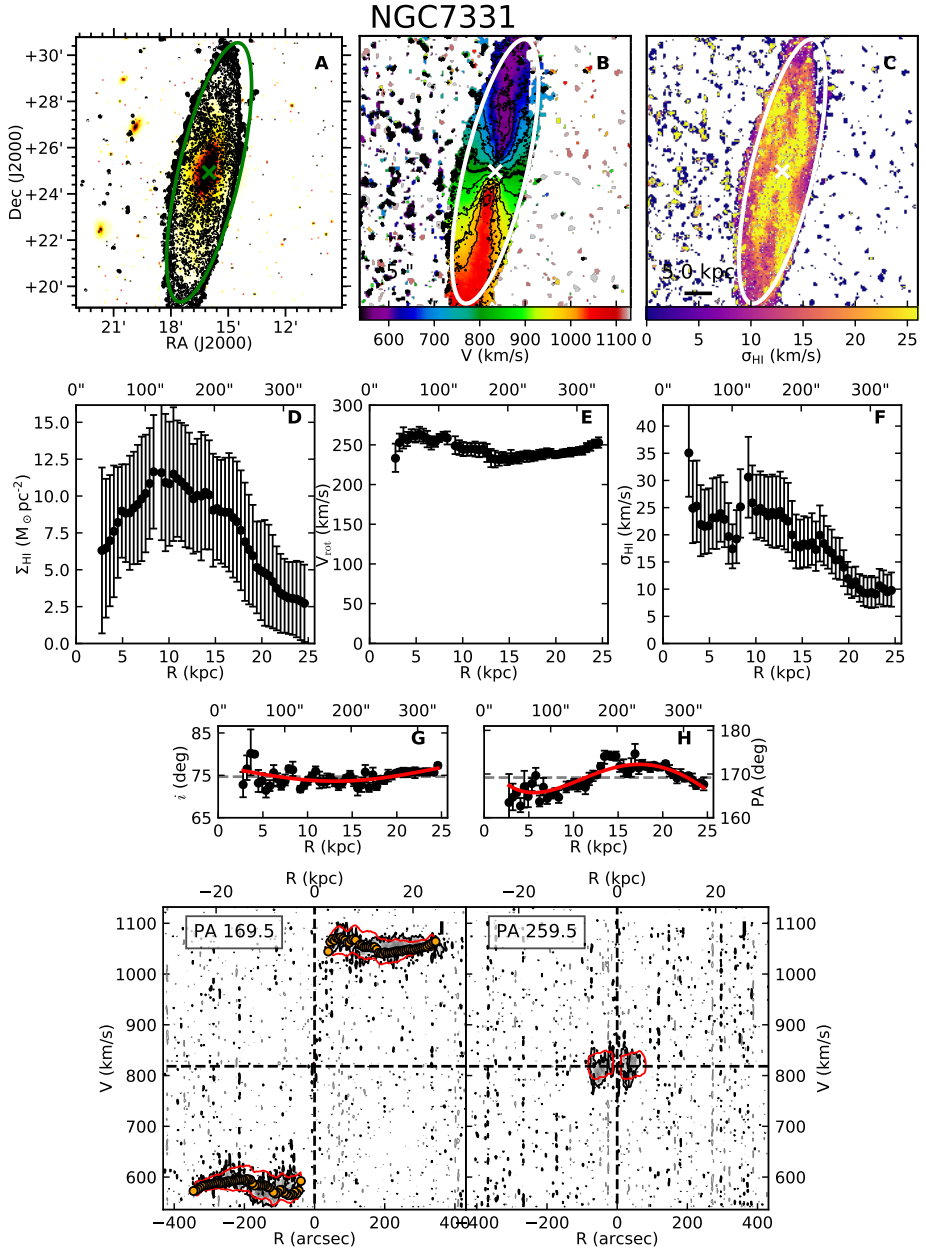


Figure 2.B.12

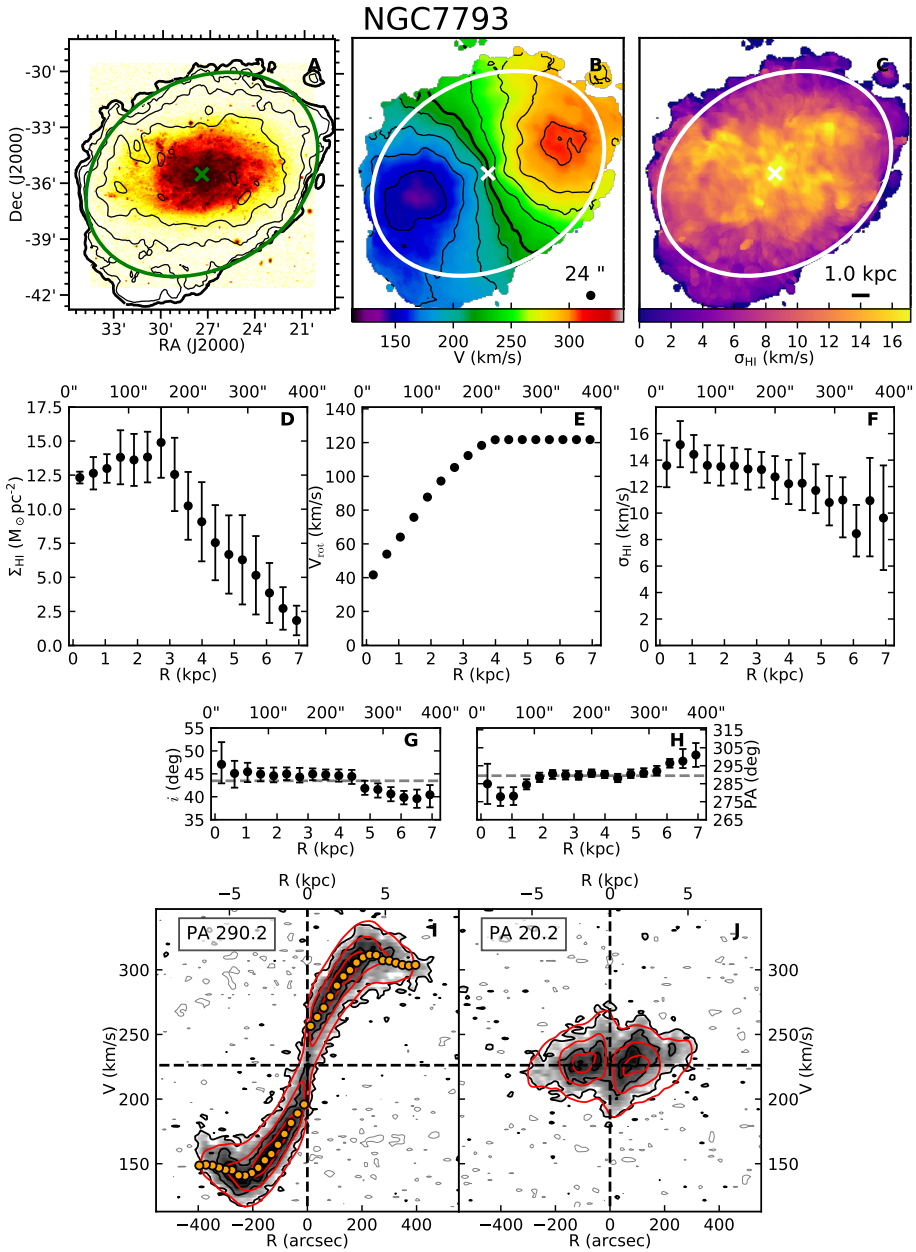


Figure 2.B.13

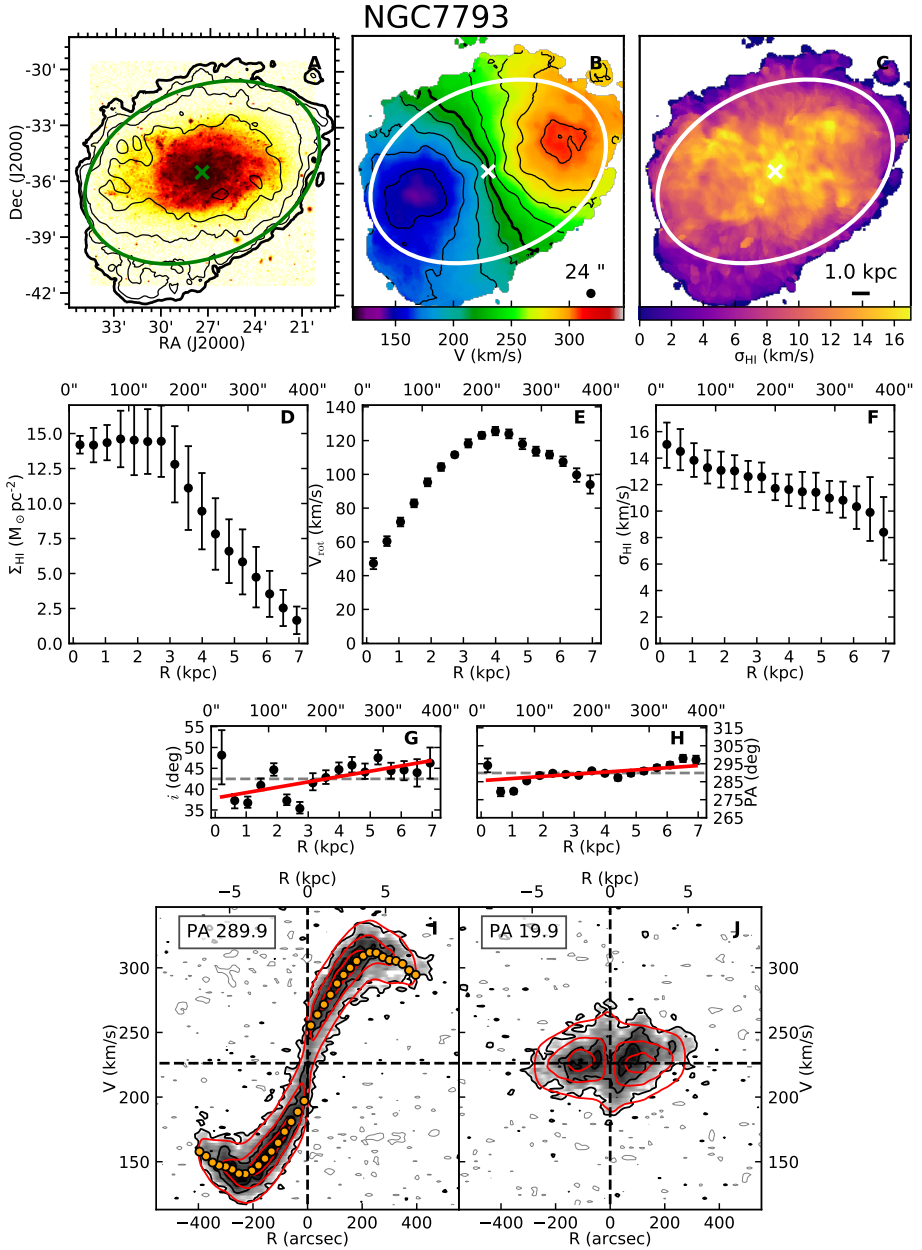
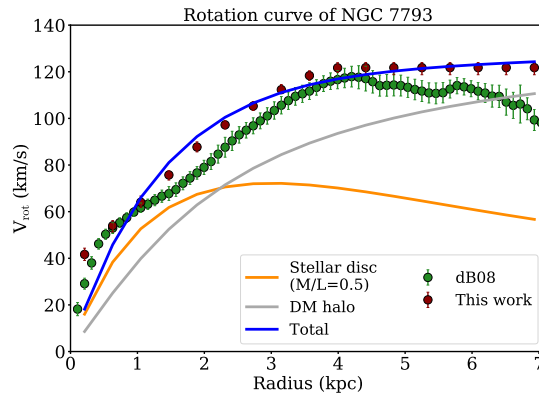


Figure 2.B.14

Figure 2.C.15 – HI rotation curve of NGC 7793 assuming a flat rotation curve (red points), the errors are of the order of 5 km s^{-1} . The solid lines show our mass model: the stellar disc with $M/L=0.5$ and the DM contributions are shown in orange and grey, while the resulting total rotation curve is in blue. The green points show the rotation curve measured by de Blok et al. (2008).



are realistic, but removing the decreasing part allows us to find a parametric mass model for the DM halo that reproduces the observed rotation much better. However, line-of-sight warps are notoriously difficult to trace with fitting algorithms (Gentile et al., 2003). To set the mass model parameters, we fixed the M/L ratio of the stellar disc to 0.5 (Lelli et al., 2016) and repeated the isothermal halo fit on the flat rotation curve, leaving $\rho_{\text{DM},0}$ and r_c as free parameters. In Fig. 2.C.15, we show that our model can reproduce the whole rotation curve. For completeness, we checked if the measurement of the velocity dispersion profile is influenced by the assumption of the flat rotation curve beyond 4 kpc. We found a slight offset between the σ_{HI} radial profiles with the flat and declining $V_{\text{rot}}(R)$, but the two are fully compatible within the uncertainties (see Fig. 2.B.13 and Fig. 2.B.14).

Appendix 2.D NGC 2841, an example of the scale height imprint on the velocity dispersion field

In Fig. 2.2, the velocity dispersion profile of NGC 2841 shows a sudden increase by 10 km s^{-1} between 15 kpc to 30 kpc in radius. An inspection of the velocity dispersion map can help us understand the origin of this feature. In Fig. 2.D.16, the galaxy is coloured according to the velocity dispersion value in each pixel. The red cross shows the centre of the galaxy (Table 2.B.2) and it is surrounded by an HI hole delimited by the red ellipse, which corresponds to an annulus of radius of 3 kpc. The centre of the galaxy is deficient in both HI and H_2 , as also pointed out by Frank et al. (2016). However, we want to focus on the most prominent feature of the map, which is the yellow X-shaped region with $\sigma_{\text{HI}} > 15 \text{ km s}^{-1}$ approximately delimited by the white ellipses. This X-shaped feature is typical of thick discs and warped galaxies (Sicking, 1997; Iorio, 2018),

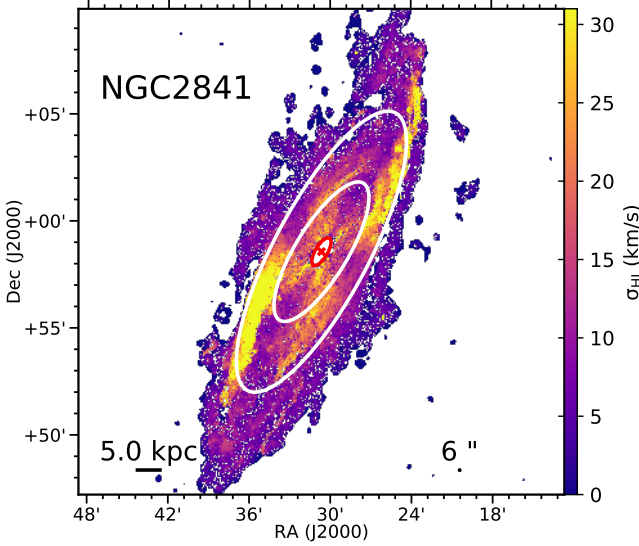


Figure 2.D.16 – HI velocity dispersion map of NGC 2841. We note the X-shaped region where $\sigma_{\text{HI}} > 15 \text{ km s}^{-1}$; the white ellipses correspond to the $R = 15 \text{ kpc}$ and $R = 30 \text{ kpc}$ annuli. The red cross indicates the centre and the red ellipse delimits the gas depleted region. The black dot (lower right) shows the beam size.

as it is due to different line-of-sight velocities being mixed in projections along selected directions. Therefore, the azimuthal average in these regions can be biased towards high values, which is exactly what happens between the annuli with $R = 15 \text{ kpc}$ and $R = 30 \text{ kpc}$. We conclude that the high velocity dispersion measured in this region is spurious and can be safely ignored in our modelling.

The more the galaxy is inclined with respect to the line of sight, the more important is the effect of increasing the velocity dispersion. NGC 2841, NGC 3198, and NGC 7331 are the galaxies in the sample with $i > 70^\circ$. The effect of inclination on σ_{HI} profile of NGC 3198 is less prominent with respect to NGC 2841, as the former galaxy is less inclined. On the other hand, the whole velocity dispersion profile of NGC 7331 is likely overestimated, but the associated uncertainties are probably large enough to account for this effect.

Appendix 2.E Uncertainties on scale heights and volume densities

In this section, we explain how the uncertainties on scale heights (Δh) and volume densities ($\Delta \rho$) are estimated. Let us first focus on the gas component and then on the SFR.

For a gas disc in hydrostatic equilibrium, the scale height can be calculated using the approximated Eq. 2.13. Applying the rules of the propagation of

uncertainty, we find

$$\Delta h = \left\{ \left(h \frac{\Delta \sigma}{\sigma} \right)^2 + \left[\frac{h}{2} \Delta \left(\frac{\partial^2 \Phi(R, z)}{\partial z^2} \right)_{z=0} \left(\frac{\partial^2 \Phi(R, z)}{\partial z^2} \right)_{z=0}^{-1} \right]^2 \right\}^{\frac{1}{2}},$$

where $\Delta \sigma$ and $\Delta \left(\frac{\partial^2 \Phi(R, z)}{\partial z^2} \right)$ are the uncertainties on the velocity dispersion and the second derivative of the gravitational potential. In our case, $\Delta \sigma$ coincides with the error on the velocity dispersion measured by 3DB, but finding $\Delta \left(\frac{\partial^2 \Phi(R, z)}{\partial z^2} \right)$ would be much more problematic. The uncertainty on $\frac{\partial^2 \Phi(R, z)}{\partial z^2}$ is linked to the uncertainty on the total volume density of DM and stars through the Poisson equation, so we should use the uncertainties on the mass decomposition. However, we expect that the parametric mass models of stars and DM do not significantly change within the errors on the fit and the observed rotation curve in de Blok et al. (2008). For simplicity, we assume that $\Delta \sigma / \sigma \gg \Delta \left(\frac{\partial^2 \Phi(R, z)}{\partial z^2} \right) / \frac{\partial^2 \Phi(R, z)}{\partial z^2}$, therefore

$$\Delta h_{\text{HI}} = h_{\text{HI}} \frac{\Delta \sigma_{\text{HI}}}{\sigma_{\text{HI}}}; \quad \Delta h_{\text{H}_2} = h_{\text{H}_2} \frac{\Delta \sigma_{\text{H}_2}}{\sigma_{\text{H}_2}}. \quad (2.E.9)$$

Then, the general equation for the uncertainties on the volume densities is derived from Eq. 2.15:

$$\Delta \rho = \rho \left[\left(\frac{\Delta \Sigma}{\Sigma} \right)^2 + \left(\frac{\Delta h}{h} \right)^2 \right]^{\frac{1}{2}}, \quad (2.E.10)$$

where $\Delta \Sigma$ is the uncertainty on the observed surface densities. Therefore, the errors on HI, H₂, and total gas volume densities are

$$\Delta \rho_{\text{HI}} = \rho_{\text{HI}} \left[\left(\frac{\Delta \Sigma_{\text{HI}}}{\Sigma_{\text{HI}}} \right)^2 + \left(\frac{\Delta h_{\text{HI}}}{h_{\text{HI}}} \right)^2 \right]^{\frac{1}{2}}, \quad (2.E.11)$$

$$\Delta \rho_{\text{H}_2} = \rho_{\text{H}_2} \left[\left(\frac{\Delta \Sigma_{\text{H}_2}}{\Sigma_{\text{H}_2}} \right)^2 + \left(\frac{\Delta h_{\text{H}_2}}{h_{\text{H}_2}} \right)^2 \right]^{\frac{1}{2}}, \quad (2.E.12)$$

$$\Delta \rho_{\text{gas}} = (\Delta \rho_{\text{HI}}^2 + \Delta \rho_{\text{H}_2}^2)^{\frac{1}{2}}. \quad (2.E.13)$$

We neglect the covariance between the error on Σ_{HI} and on h_{HI} as the scale height depends on the dominant mass components (the stellar disc and DM

halo), so these two quantities can be considered independent; the same is valid for the molecular gas.

Concerning the constant SFR scale height, the uncertainty is null by construction ($\Delta h_{\text{SFR}} = 0$), so the error on the SFR volume density derived from Eq. 2.E.10 is

$$\Delta \rho_{\text{SFR}} = \frac{\Delta \Sigma_{\text{SFR}}}{\sqrt{2\pi} h_{\text{SFR}}}. \quad (2.E.14)$$

In the case of the flaring SFR scale height, the error is derived from Eq. 2.17

$$\Delta h_{\text{SFR}} = \left[\left(\frac{\Sigma_{\text{HI}} \Delta h_{\text{HI}}}{\Sigma_{\text{gas}}} \right)^2 + \left(\frac{\Sigma_{\text{H}_2} \Delta h_{\text{H}_2}}{\Sigma_{\text{gas}}} \right)^2 + \frac{(\Sigma_{\text{H}_2}^2 \Delta \Sigma_{\text{HI}}^2 + \Sigma_{\text{HI}}^2 \Delta \Sigma_{\text{H}_2}^2) (h_{\text{HI}} - h_{\text{H}_2})^2}{\Sigma_{\text{gas}}^4} \right]^{\frac{1}{2}}. \quad (2.E.15)$$

Therefore, the uncertainty on the volume density is

$$\Delta \rho_{\text{SFR}} = \rho_{\text{SFR}} \left[\left(\frac{\Delta \Sigma_{\text{SFR}}}{\Sigma_{\text{SFR}}} \right)^2 + \left(\frac{\Delta h_{\text{SFR}}}{h_{\text{SFR}}} \right)^2 \right]^{\frac{1}{2}}. \quad (2.E.16)$$

When we build the HI-SFR and H₂-SFR relations, we are implicitly assuming that $h_{\text{SFR}} = h_{\text{HI}}$ and $h_{\text{SFR}} = h_{\text{H}_2}$, so $\Delta h_{\text{SFR}} = \Delta h_{\text{HI}}$ and $\Delta h_{\text{SFR}} = \Delta h_{\text{H}_2}$. As a consequence, Eq. 2.E.16 becomes

$$\Delta \rho_{\text{SFR}} = \rho_{\text{SFR}} \left[\left(\frac{\Delta \Sigma_{\text{SFR}}}{\Sigma_{\text{SFR}}} \right)^2 + \left(\frac{\Delta h_{\text{HI}}}{h_{\text{HI}}} \right)^2 \right]^{\frac{1}{2}}, \quad (2.E.17)$$

$$\Delta \rho_{\text{SFR}} = \rho_{\text{SFR}} \left[\left(\frac{\Delta \Sigma_{\text{SFR}}}{\Sigma_{\text{SFR}}} \right)^2 + \left(\frac{\Delta h_{\text{H}_2}}{h_{\text{H}_2}} \right)^2 \right]^{\frac{1}{2}}. \quad (2.E.18)$$

Appendix 2.F Likelihood and posterior distributions of Bayesian fittings

In order to include both the orthogonal intrinsic scatter and the x and y errors on the volume densities, the logarithmic likelihood is written as (Ponomareva et al., 2017; Posti et al., 2018)

$$\ln \mathcal{L} = -\frac{1}{2} \sum_{i=1}^N \left[\frac{d_i^2}{\sigma_{\text{tot}}^2} + \ln(2\pi\sigma_{\text{tot}}^2) \right]. \quad (2.F.19)$$

In this equation, N is the number of data points, d_i is the distance between a given data point (x_i, y_i) and the model (e.g. Eq. 2.20), being $x_i = \log \rho_{\text{gas}}$ and $y_i = \log \rho_{\text{SFR}}$. Then, $\sigma_{\text{tot}}^2 = \sigma_{\perp}^2 + \sigma_{x_i, \perp}^2 + \sigma_{y_i, \perp}^2$, where σ_{\perp} is the orthogonal intrinsic scatter and $\sigma_{x_i, \perp} = \sigma_{x_i} \cos \theta$ and $\sigma_{y_i, \perp} = \sigma_{y_i} \sin \theta$ are the projections of the x and y uncertainties on data points σ_{x_i} and σ_{y_i} using the angle θ , which is the arctangent of the slope of the relation. The prior distribution of the free parameters is uniform and spans from $-\infty$ to $+\infty$ for the slope and y -intercept, and from 0 to $+\infty$ for the intrinsic scatter. Before the fitting, the origin of the data points coordinate system is shifted to the median of ρ_{gas} and ρ_{SFR} (x_{m} and y_{m} in logarithmic scale) to reduce the covariance between α and $\log A$. In practice, the axes of the new coordinate system $x' - y'$ are defined as $y' = y - y_{\text{m}}$ and $x' = x - x_{\text{m}}$, therefore the best-fit $\log A$ in the $x - y$ system becomes $\log A = y_{\text{m}} - \alpha x_{\text{m}} + \log A'$, where $\log A'$ is the best-fit intercept in the $x' - y'$ system. Clearly, when we consider only the atomic (molecular) gas phase in Sect. 2.5.3 (Sect. 2.5.2), we use the same method but with $x_i = \log \rho_{\text{HI}}$ ($x_i = \log \rho_{\text{H}_2}$) and the slope and normalisation are defined as β and $\log B$ (γ and $\log \Gamma$). In the case with total gas, $x_{\text{m}} = -1.94$ and $y_{\text{m}} = -2.30$ ($y_{\text{m}} = -2.74$) with the constant (flaring) h_{SFR} . In the case with atomic gas, $x_{\text{m}} = -2.02$ and $y_{\text{m}} = -2.30$ ($y_{\text{m}} = -2.76$) with the constant (flaring) h_{SFR} . In the case with molecular gas, $x_{\text{m}} = -2.05$ and $y_{\text{m}} = -1.86$.

Figure 2.F.17, Figure 2.F.18 and Figure 2.F.19 show the marginalised posterior distributions of free parameters for the MCMC fittings of the VSF laws. Figure 2.F.17 refers to the VSF law between the SFR and total gas (Eq. 2.20). Despite the axes shifting, there is still a small covariance between α and $\log A'$ but all the parameters are well constrained and clearly indicate the existence of a correlation between the volume densities of gas and SFR. Unfortunately, we are not able to find an unambiguous best-fit slope, as it depends on the choice of h_{SFR} , but the intrinsic scatter is small (0.12-0.13 dex) in both cases. Figure 2.F.18 and Figure 2.F.19 are the same as the first but for the VSF laws with HI (Eq. 2.21) and H₂ (Eq. 2.22), respectively. The relation with HI is steeper and has a small scatter compared to the relation with H₂.

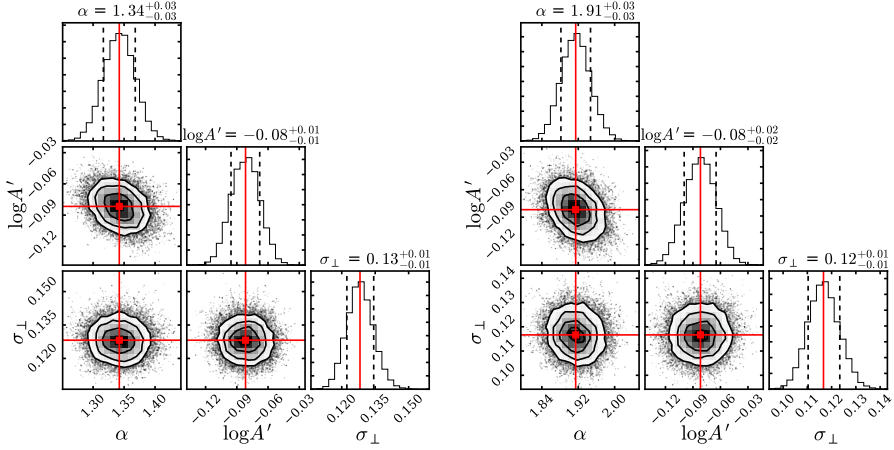


Figure 2.F.17 – Marginalised posterior distributions of free parameters in the Bayesian fittings of VSF laws with total gas. In the left panel h_{SFRR} is constant at 100 pc, while in the right panel it flares with radius (Eq. 2.17). The contours of the 2D posteriors (corners) encompass the 68.3%, 86.6%, and 95.4% probability and the red squares and lines indicate the best-fit parameters. In the 1D posteriors (diagonals), the best-fit parameters are indicated by the red line and the 16th and 84th percentiles are indicated by the black dashed lines.

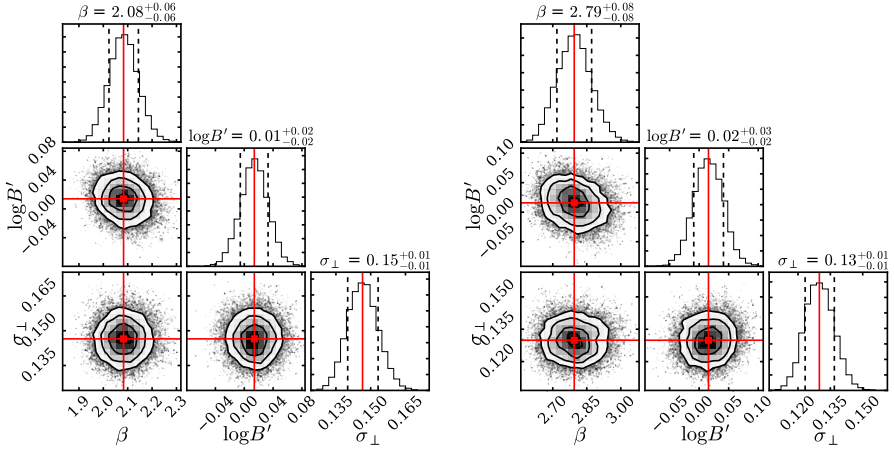


Figure 2.F.18 – Same as Fig. 2.F.17 but for the VSF laws with HI only.

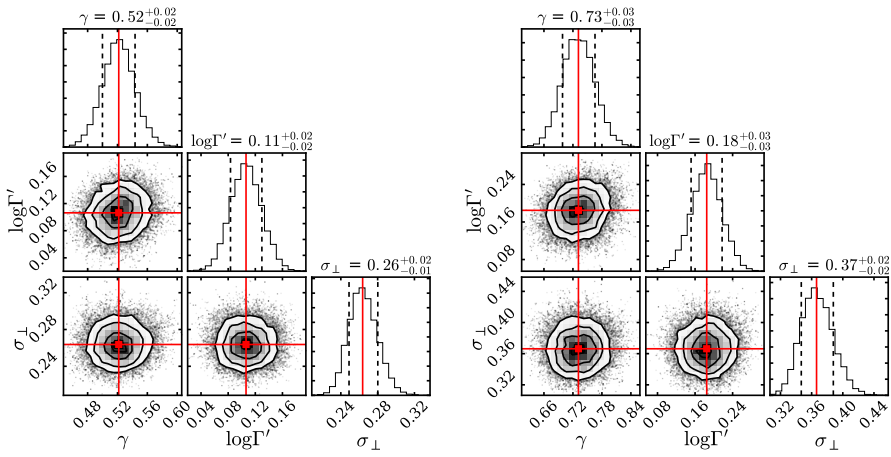


Figure 2.F.19 – Same as Fig. 2.F.17 but for the VSF laws with H_2 only.

CHAPTER 3

**The volumetric star
formation law in the
Milky Way**

based on

— C. Bacchini, F. Fraternali, G. Pezzulli, A. Marasco, G. Iorio,
and C. Nipoti —

Astronomy & Astrophysics, 2019, 632, A127.

Abstract

Several open questions on galaxy formation and evolution have their roots in the lack of a universal star formation law that could univocally link the gas properties, such as its density, to the star formation rate (SFR) density. In Chapter 2, we used a sample of nearby disc galaxies to infer the volumetric star formation (VSF) law, a tight correlation between the gas and the SFR volume densities derived under the assumption of hydrostatic equilibrium for the gas disc. However, due to the dearth of information about the vertical distribution of the SFR in these galaxies, we could not find a unique slope for the VSF law, but two possible values. In this Chapter, we use the scale height of the SFR density distribution in our Galaxy adopting classical Cepheids (age $\lesssim 200$ Myr) as tracers of recent star formation. We show that the SFR scale height is fully compatible with the flaring scale height expected from gas in hydrostatic equilibrium. These scale heights allowed us to convert the observed surface densities of gas and SFR into the corresponding volume densities. Our results indicate that the VSF law, namely $\rho_{\text{SFR}} \propto \rho_{\text{gas}}^\alpha$ with $\alpha \approx 2$, is valid in the Milky Way as well as in nearby disc galaxies.

3.1 Introduction

Sixty years ago, Schmidt (1959) theorised the first star formation law for the Milky Way (MW): a power law linking the star formation rate (SFR) and the atomic gas volume densities, that is $\rho_{\text{SFR}} \propto \rho_{\text{HI}}^n$. He estimated $2 < n < 3$ from the HI and young stars distributions in our Galaxy. To date, much effort has gone into finding a universal relation between gas and SFR densities among all types of star-forming galaxies. We could divide the star formation laws proposed in the literature into three main groups, according to the physical quantities and scales considered.

The so-called “global” Schmidt-Kennicutt (SK) law involves the surface densities of gas (HI+H₂; Σ_{gas}) and SFR (Σ_{SFR}) averaged over the whole star-forming disc. This correlation was proposed by Kennicutt (1998) using a sample of regularly star-forming disc galaxies and starbursts, and it reads $\Sigma_{\text{SFR}} \propto \Sigma_{\text{gas}}^N$ with $N \approx 1.4$. Recently, Kennicutt & Evans (2012) showed that the MW is compatible with the integrated SK law, while low surface brightness galaxies depart from the relation (see also Pickering et al., 1997; Wyder et al., 2009; de los Reyes & Kennicutt, 2019).

For spatially resolved galaxies, it is possible to derive the “local” SK law (e.g. Kennicutt, 1989; Martin & Kennicutt, 2001), which involves the gas and the SFR surface densities measured either in kiloparsec or sub-kiloparsec regions, or their radial profiles (i.e. azimuthal averages). However, like its integrated version, this correlation seems to break in low-density environments, as found by several authors in dwarf galaxies and the outskirts of spirals (e.g. Kennicutt et al., 2007; Bolatto et al., 2011; Dessauges-Zavadsky et al., 2014). This is often ascribed to a drop in the star formation efficiency at a threshold density of about $10 M_{\odot} \text{ pc}^{-2}$ (e.g. Schaye, 2004; Leroy et al., 2008; Bigiel et al., 2008, 2010); however, the physical explanation for this behaviour is still a matter of debate (e.g. Krumholz 2014 and references therein). In our Galaxy, it is unclear whether the index of the resolved SK law is 1.4 (e.g. Fraternali & Tomassetti, 2012) or higher (Wong & Blitz, 2002; Boissier et al., 2003; Misiriotis et al., 2006), which may be an indication of the presence of the break (Sofue, 2017).

Given that stars are thought to form from cold and dense gas, the SFR surface density is expected to correlate with the molecular gas surface density, following some molecular star formation law. This correlation is observed in high gas density regions of spiral galaxies, although its index has not been firmly established yet. Some authors find a linear correlation (e.g. Bigiel et al., 2008; Schruba et al., 2011; Marasco et al., 2012), while others derive an index around 1.4 (e.g. Wong & Blitz, 2002; Heyer et al., 2004; Kennicutt et al., 2007; Liu et al., 2011). In our Galaxy, Luna et al. (2006) have investigated the molecular SK law using the SFR density traced by the far-infrared emission (i.e. dust heated by massive young stars), finding a power-law with index of 1.2 ± 0.2 . However, Kennicutt & Evans (2012) show that the H₂ surface density drops faster with radius than the SFR distribution derived using HII regions (Misiriotis et al.,

2006; Sofue, 2017). Moving to much smaller spatial scales, Lada et al. (2010) find a linear correlation between the number of young stellar objects in Galactic molecular clouds and the mass of dense gas above an extinction threshold of 0.8 magnitudes in K band, corresponding to about $116 M_{\odot} \text{ pc}^{-2}$. The origin of this correlation is unclear, but it could be a consequence of the scaling relation between mass and size of molecular clouds (Lada et al., 2013).

In Chapter 2, we proposed a new volumetric star formation (VSF) law, a tight correlation between the SFR and the gas (HI+H₂) volume densities derived for a sample of 12 nearby star-forming galaxies. The conversion of the observed surface densities into volume densities requires the knowledge of the gas and SFR scale heights. In particular, the scale heights of the HI and H₂ components were computed assuming the vertical hydrostatic equilibrium in the galactic potential. A key feature of this approach is that it takes into account radial variations of the gas scale height (also called flaring) and the consequent non-linear conversion between the observed surface density and the intrinsic volume density (see also Elmegreen, 2015, 2018). In the absence of observational measurements of the radial variation of the SFR vertical distribution, we decided to make two extreme assumptions for the SFR scale height. The first consisted in assuming a constant value for the entire disc (and the same for all galaxies), while the second was based on the idea that the SFR scale height is proportional to that of the most abundant gas phase, whether atomic or molecular. Clearly, these definitions for the SFR scale height led to two different radial profiles for the SFR volume density. In both cases we found a tight power-law relation, but with different indexes, 1.34 ± 0.03 and 1.91 ± 0.03 .

In this Chapter, we show that the issue regarding the SFR scale height can be overcome in the MW, where the 3D structure of the tracers of recent star formation can be directly retrieved from observations, and we assess the validity of the VSF law in our Galaxy. Section 3.2 describes the model of the gas distribution and defines the volume densities. Section 3.3 presents the observations of the distributions of gas and SFR available in the literature and used in this study. Our results are presented in Sect. 3.4 and discussed in Sect. 3.5. Finally, in Sect. 3.6 we summarise the work and draw our main conclusions.

3.2 Volume densities

In order to derive the volume densities, we use the same approach described in Chapter 2 for external galaxies, with the exception of the SFR scale height.

3.2.1 Distribution of gas in hydrostatic equilibrium

We assume that the HI and H₂ discs are in vertical hydrostatic equilibrium in the total gravitational potential of the MW, which consists of a dark matter

halo, a stellar bulge, a thin and a thick stellar disc, plus the contribution of the gas self-gravity. In general, for a given gravitational potential and gas density profile, it is possible to calculate the scale height of the gaseous component once its velocity dispersion (σ) is known, assuming that the pressure is $P = \rho\sigma^2$. The density distribution can be written as

$$\rho_i(R, z) = \rho_i(R, 0) \exp \left[-\frac{\Phi(R, z) - \Phi(R, 0)}{\sigma_i^2} \right], \quad (3.1)$$

where i stands for HI or H₂, $\rho_i(R, 0)$ is the volume density in the midplane as a function of the Galactocentric radius R , and Φ is the total gravitational potential.

We calculate the scale height via numerical integration using the software GALPYNAMICS¹ (Iorio, 2018), which uses an iterative algorithm to account for the gas self-gravity. In practice, the code first calculates the external potential plus the contribution of a razor-thin gas distribution from a given parametric mass model. A first guess of the scale height is estimated by fitting Gaussian profiles (e.g. Olling, 1995; Koyama & Ostriker, 2009) to the vertical gas distribution resulting from Eq. 3.1. The scale height (h) is defined as the standard deviation of this profile. Then Φ is updated with the potential of the new gas distribution, which includes the scale height found in the previous step, and a second estimate of the scale height is obtained by the Gaussian fitting. This procedure is iterated until two successive calculations differ by less than a given tolerance.

Therefore, the necessary ingredients to calculate the scale heights of HI and H₂ are their surface densities and velocity dispersions (see Sect. 3.3.1), and a parametric mass model of the Galaxy components. In particular, we adopted the models for the stellar and dark matter distributions by McMillan (2011, 2017), which take into account observational requirements on the kinematics of gas, stars, and masers, and on the total mass of the Galaxy out to 50 kpc.

3.2.2 Definitions of volume densities

We define the gas volume density in the Galaxy midplane as

$$\begin{aligned} \rho_{\text{gas}}(R, 0) &= \rho_{\text{HI}}(R, 0) + \rho_{\text{H}_2}(R, 0) \\ &= \frac{\Sigma_{\text{HI}}(R)}{\sqrt{2\pi}h_{\text{HI}}(R)} + \frac{\Sigma_{\text{H}_2}(R)}{\sqrt{2\pi}h_{\text{H}_2}(R)}, \end{aligned} \quad (3.2)$$

where $\rho_{\text{HI}}(R, 0)$ and $\rho_{\text{H}_2}(R, 0)$ are the volume densities of HI and H₂ in the midplane, and $\Sigma_{\text{HI}}(R)$ and $\Sigma_{\text{H}_2}(R)$ are the corresponding radial profiles of the surface densities. The last equality in Eq. 3.2 holds under the assumption of a Gaussian vertical profile for HI and H₂, and h_{HI} and h_{H_2} are the standard

¹<https://github.com/iogiul/galpynamics>

deviations of these profiles. These latter were calculated using the procedure described in Sect. 3.2.1 based on the assumption of hydrostatic equilibrium.

We assume that the SFR is distributed in a disc with surface density $\Sigma_{\text{SFR}}(R)$ and scale height $h_{\text{SFR}}(R)$. Hence, the volume density of SFR in the midplane is

$$\rho_{\text{SFR}}(R, 0) = \frac{\Sigma_{\text{SFR}}(R)}{\sqrt{2\pi}h_{\text{SFR}}(R)}. \quad (3.3)$$

The main difference with respect to approach adopted in Chapter 2 is that, for our Galaxy, we measured $h_{\text{SFR}}(R)$ from observations.

3.3 Observations in the Milky Way

In this section, we describe the set of measurements of the gas distribution and kinematics used for our analysis. We also explain how the SFR surface density and scale height were derived from the literature and the observations, respectively.

3.3.1 Gas distribution and kinematics

Several works in the literature studied the gas distribution (i.e. its surface density, volume density, and scale height) in our Galaxy adopting the kinematic distance method (Westerhout, 1957). This latter relies on an assumed model of the Galactic rotation curve to transform the line-of-sight velocity into a distance from the solar position. The derived distances can then be used to obtain a full 3D reconstruction of the gas component. This method has been successfully and widely employed to map the gas densities in the entire Galaxy, but it is affected by the so-called near-far problem within the solar circle (e.g. Burton, 1974; Marasco et al., 2017): the same line-of-sight velocity can be associated with two opposite distances, one between the observer and the tangent point, defined as the location where the line of sight is perpendicular to the Galactocentric distance (R), and one beyond it.

For this work we decided to derive the volume densities from the surface densities in the literature using the scale height calculated with the hydrostatic equilibrium. This approach allows us to compare, in a consistent way, the VSF law in the MW with that obtained in Chapter 2. In Appendix 3.A we discuss the difference between the volume density and the scale heights estimated in the literature and those derived using the hydrostatic equilibrium.

Inside the solar circle

Marasco et al. (2017) studied the distribution and kinematics of the gas inside the solar circle through a novel approach that models the observed emission

of HI and CO, overcoming the near–far problem. They assumed that the gas is in circular motion and divided the Galaxy in concentric and co-planar rings described by rotation velocity, velocity dispersion, scale height, and midplane volume density. Then they used a Bayesian method to fit these four parameters to the HI and the CO line emission from the Leiden-Argentine-Bonn survey (Kalberla et al., 2005) and the CO(J=1→0) survey of Dame et al. (2001). This model also takes into account the extra-planar gas contribution, which was included as an additional HI component with both radial and vertical infall motions, and a lagging rotational velocity with respect to the HI in the midplane (see Marasco & Fraternali, 2011).² The best-fit model of Marasco et al. (2017) can reproduce in detail the gas distribution and kinematics of the receding and approaching quadrants of the Galaxy. However, the assumption of pure circular orbits does not hold in the innermost 3 kpc, where the gravitational potential of the bar (Bland-Hawthorn & Gerhard, 2016; Helmi, 2020, and references therein) makes the gas distribution non-axisymmetric and induces non-circular motions (see Binney et al. 1991; Sormani & Magorrian 2015; Sormani et al. 2015; Armillotta et al. 2019). We excluded the region $R < 3$ kpc in this work as our model also assumes axisymmetry.

The profiles of the surface density, the volume density, and the scale height provided by Marasco et al. (2017) show three peaks that could be related to the intersection of the line of sight with spiral arms, where the density is above the mean value. Therefore, we smoothed all the profiles, including those of the velocity dispersion, from a resolution of 0.2 kpc to 1.0 kpc, adopting the same procedure for each radius and for both the HI and H₂ profiles. We divided the radial range 3 kpc $< R \leq 8$ kpc in 6 bins of 1 kpc width and derived a single value for the quantity of interest (i.e. surface density and velocity dispersion) by fitting a Gaussian distribution to the data points in each bin (taking into account the error bars). At each radius, the resulting best-fit Gaussian is centred on the final value and its standard deviation is a first estimate of the error. In particular, the upper errors on Σ_{HI} were estimated from the standard deviation of the Gaussian, while the lower errors were found using Σ_{HI} derived in optically thin regime (see Marasco et al. 2017 for details). This sort of correction was done for consistency with Chapter 2, in which we used Σ_{HI} of external galaxies derived under the assumption of 100% optically thin HI. Concerning the molecular gas, we followed the same approach as Marasco et al. (2017) and associated an error of 30% to Σ_{H_2} , based on the uncertainty on the CO-H₂ conversion factor estimated by Bolatto et al. (2013). The fiducial profiles of the surface densities

²The extra-planar gas is a faint layer of HI, observed both in the MW and in nearby galaxies (Fraternali et al., 2001; Oosterloo et al., 2007a; Gentile et al., 2013; Marasco et al., 2019), which is likely generated by the galactic fountain flow (Fraternali, 2017). This component rotates with slower velocity with respect to the gas in the midplane, and reaches heights of a few kpc above the disc. If not taken into account, the extra-planar gas can lead to a slight overestimation of the scale height ($\sim 20\%$ for our Galaxy; see Marasco et al. 2017).

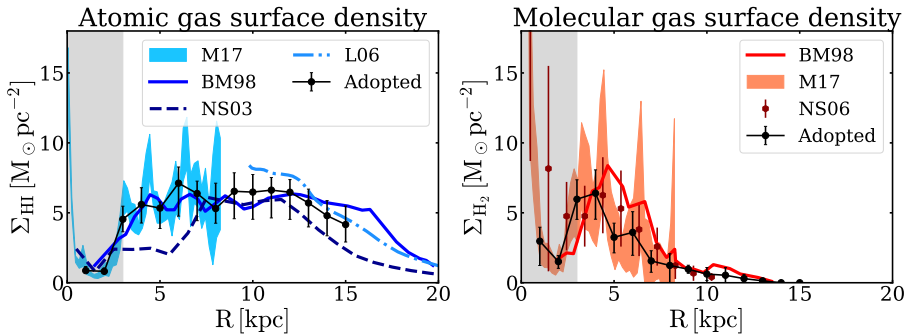


Figure 3.1 – Surface density radial profiles of the atomic gas (left) and the molecular gas (right) adopted in this work (black points). The other profiles show the measurements from the literature used to derive these fiducial profiles (see text). A factor 1.36 for the helium correction is included. In the legends: BM98=Binney & Merrifield (1998), NS03=Nakanishi & Sofue (2003), NS06=Nakanishi & Sofue (2006), Le06=Levine et al. (2006), and M17=Marasco et al. (2017). The grey area represents the region influenced by the bar, which was excluded from this study.

are shown in Fig. 3.1 by the black points and are compared to other estimates in the literature in Appendix 3.A.

Beyond the solar circle

In order to derive a fiducial profile of $\Sigma_{\text{HI}}(R > R_{\odot})$ and robust uncertainties, we used a similar procedure to the one described for the regions within the solar circle but, in each radial bin, we adopted data points from different profiles in the literature. We included the measurements by Binney & Merrifield (1998), Nakanishi & Sofue (2003), and Levine et al. (2006), who all used the kinematic distance method, but assumed slightly different Galactic rotation curves.³ For example, Levine et al. (2006) aimed to study the warp of the HI disc, which is present beyond $R \sim 12$ kpc, and thus assumed that the Galaxy circular speed is constant at 220 km s^{-1} for $R > R_{\odot}$. On the other hand, Nakanishi & Sofue (2003) adopted the rotation curve from Dehnen & Binney (1998), which slightly decreases beyond R_{\odot} . These authors assumed an opaque regime for the HI, but did not explore the optically thin case, thus we used the Gaussian standard deviation for the error. Similarly, we used the profiles from Binney & Merrifield (1998) and Nakanishi & Sofue (2006) to calculate Σ_{H_2} . These fiducial profiles of the surface densities are shown in Fig. 3.1.

Concerning the HI and H₂ velocity dispersion, there are no available measurements of their profiles beyond R_{\odot} , at least to our knowledge. However,

³We did not include the Kalberla & Dedes (2008) measurements in the estimate of our fiducial Σ_{HI} as their density profile is more than a factor of ≈ 2 higher than the other estimates in the literature (see Appendix 3.A.1).

several authors (e.g. Fraternali et al., 2002; Boomsma et al., 2008; Tamburro et al., 2009, see also Sect. 2.4.1) have shown that in nearby spiral galaxies σ_{HI} decreases with radius until it reaches values of about 8 km s^{-1} and then remains roughly constant. This value is in agreement with the outermost measurements (i.e. at R_{\odot}) by Marasco et al. (2017). These latter also estimated $\sigma_{\text{HI}}/\sigma_{\text{H}_2} \approx 0.5$ within R_{\odot} , thus we decided to assign $\sigma_{\text{HI}} = 8 \pm 2 \text{ km s}^{-1}$ and $\sigma_{\text{H}_2} = 4 \pm 1 \text{ km s}^{-1}$ to all radii beyond R_{\odot} , which are typical values for the atomic and the molecular phases (see Kramer & Randall 2016 and references therein, and Appendix 5.A in Chapter 5).

3.3.2 SFR distribution

In the literature, the SFR of our Galaxy has been estimated using various tracers of recent star formation and different methods, resulting in a range of values from $1 \text{ M}_{\odot}\text{yr}^{-1}$ to $3 \text{ M}_{\odot}\text{yr}^{-1}$ (or even higher; see e.g. McKee & Williams 1997; Misiriotis et al. 2006; Robitaille & Whitney 2010). Chomiuk & Povich (2011) found that different measurements of the global SFR average to $\simeq 1.9 \pm 0.4 \text{ M}_{\odot}\text{yr}^{-1}$ (see also Licquia & Newman, 2015), if re-scaled to the Kroupa initial mass function (Kroupa & Weidner, 2003) and the same stellar population synthesis models.

SFR surface density

We took as reference the work by Green (2015), who carefully collected a sample of 69 bright supernova remnants (SNRs) in order to avoid strong selection effects.⁴ He derived the radial distribution of SNRs and found that it is more concentrated towards the Galactic centre with respect to the previous estimate by Case & Bhattacharya (1998). We derived $\Sigma_{\text{SFR}}(R)$ by normalising the radial profile of SNR surface density to the total SFR of the MW. In Appendix 3.B.1, we show that the resulting $\Sigma_{\text{SFR}}(R)$ is compatible with other estimates obtained with different tracers and methods, in the light of the large scatter.

SFR scale height

To reliably measure $h_{\text{SFR}}(R)$, we must select a tracer of recent star formation with accurate distance determination and a sample that is statistically significant. Therefore, we chose classical Cepheids (CCs), which are variable stars typically younger than $\approx 200 \text{ Myr}$ (e.g. Bono et al., 2005; Dékány et al., 2019) whose distance can be accurately determined thanks to the period-luminosity relation (e.g. Leavitt & Pickering, 1912; Caputo et al., 2000; Ripepi et al., 2019). We note that SNRs and CCs are not perfectly coeval (age gap 50-100 Myr), but

⁴In the MW, SNRs can be considered good tracers of recent ($\lesssim 50 \text{ Myr}$) star formation events as, in Sbc galaxies, the rate of SNe Ia is $\sim 4 - 5$ times lower than the rate of SNe II and Ibc (Li et al., 2011).

the dynamical processes that could modify the distribution of a population of stars with respect to the parent gas (e.g. radial migration) are effective on timescales much longer than this age gap (Sellwood, 2014). Moreover, the stellar discs of star-forming galaxies grow in radius (inside-out growth) of $\approx 3\%$ in 1 Gyr (Muñoz-Mateos et al., 2011; Pezzulli et al., 2015). Hence, we expect that both SNRs and CCs represent the parent gas distribution (see also Fig. 3.B.4 for a comparison between tracers of different ages).

In a recent paper, Chen et al. (2019) collected data for 1339 CCs with distance accuracy of 3-5% from the Wide-field Infrared Survey Explorer catalogue of periodic variables (Chen et al., 2018) and from the Gaia Data Release 2 (Gaia Collaboration et al., 2018) in order to study the warp of the Galactic disc. They found that the warp seen in the distribution of CCs is compatible with that determined using pulsars (Yusifov & Küçük, 2004a) and atomic gas (Levine et al., 2006). After subtracting the warp contribution, these authors found evidence of a flare in the z -distribution of CCs compatible with that traced by red giant stars (Wang et al., 2018) and HI (Wouterloot et al., 1990) in the MW (see Appendix 3.A.2).

We studied the radial profile of the scale height using the residual z -coordinates provided by Chen et al. (2019) (see their Fig. 4), for which the signature of the Galactic warp was already modelled and filtered out. We built radial bins of $\Delta R = 1$ kpc from $R = 5$ kpc to $R = 19$ kpc containing enough stars (from 8 to 200) to obtain a reasonable sampling of their vertical distribution in each bin using the Freedman–Diaconis estimator (Freedman & Diaconis, 1981) implemented in the `scipy` Python package (Jones et al., 2001). By analogy with a Gaussian distribution, we calculated the scale height at each radius (i.e. the width of the vertical distribution in each bin) as

$$h_{\text{Cep}} = \frac{p_{84} - p_{16}}{2}, \quad (3.4)$$

with p_{16} and p_{84} being the 16th and the 84th percentiles of the distribution in the bin. The uncertainty on this estimate is the sum in quadrature of two contributions,

$$\Delta h_{\text{Cep}} = \left[\left(p_{50} - \frac{p_{84} + p_{16}}{2} \right)^2 + \left(\frac{h_{\text{Cep}}}{\sqrt{N}} \right)^2 \right]^{\frac{1}{2}}, \quad (3.5)$$

where p_{50} and N are respectively the median of the distribution (i.e. the midplane) and the number of CCs in each bin. The first term comes from the asymmetry with respect to the midplane (with the warp contribution already subtracted), while the second term accounts for the statistical error.

Figure 3.2 shows the scale height of CCs: we clearly see that there is a flaring. In particular, the scale height is about 100 pc at the solar position and increases with radius, reaching about 500 pc at $R \approx 18$ kpc. This is a strong

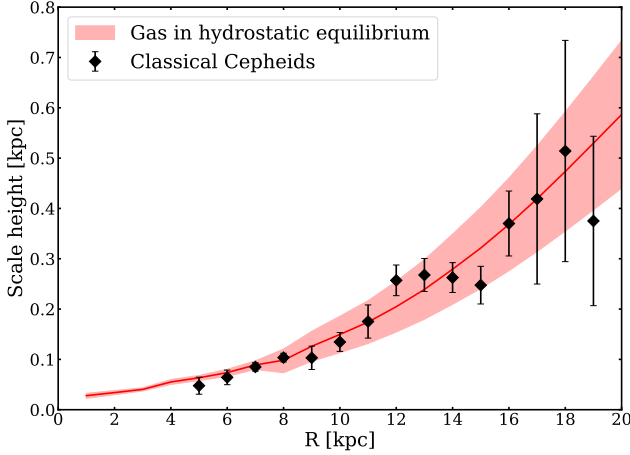


Figure 3.2 – Scale height of CCs (data from Chen et al. 2019) as a function of the Galactocentric radius (black diamonds). The red curve is given by Eq. 3.6, which corresponds to the weighted average of the HI and the H₂ scale heights from hydrostatic equilibrium.

indication that the flaring SFR distribution is more realistic than that with a constant thickness, allowing us to disentangle between the two approaches adopted in Chapter 2 and choose the flaring $h_{\text{SFR}}(R)$ instead of the constant value. In Appendix 3.B.2, the scale height of CCs is compared to the scale height of other SFR tracers provided in the literature, which are in agreement within the uncertainties.

We note that the scale height of CCs shown in Fig. 3.2 is compatible with that reported by Chen et al. (2019), despite the different definitions adopted. As a further test, we took the catalogue of CCs by Skowron et al. (2019), which includes also the age of each star. We selected the youngest population ($20 \text{ Myr} < \text{age} \leq 90 \text{ Myr}$) and calculated its scale height, finding that it is compatible with that obtained using the sample of Chen et al. (2019). Moreover, our scale height of young CCs is the same as that estimated by Skowron et al. (2019) for the sample including all ages, which indicates that the scale height of CCs does not significantly depend on age.

3.4 Results

3.4.1 Scale heights of classical Cepheids and gas in hydrostatic equilibrium

Our first aim is to test the assumption made in Chapter 2, where we conjectured that the SFR scale height could be approximated by the weighted average of h_{HI} and h_{H_2} calculated assuming the hydrostatic equilibrium

$$h_{\text{SFR}}(R) = h_{\text{HI}}(R)f_{\text{HI}}(R) + h_{\text{H}_2}(R)f_{\text{H}_2}(R), \quad (3.6)$$

where f_{HI} and f_{H_2} are the HI and the H₂ fractions with respect to the total gas. To obtain h_{HI} and h_{H_2} , we derived the vertical distribution of HI and H₂ (Eq. 3.1) as explained in Sect. 3.2.1. For consistency, we adopted the mass distribution for the gaseous components described in Sect. 3.3.1 rather than those in McMillan (2017) model. This choice has a negligible effect on the gravitational potential, as the gas is dynamically sub-dominant with respect to the stars and the dark matter (see also Appendix 3.C). In Sect. 3.A.2, we compare the scale heights of HI and H₂ obtained with the hydrostatic equilibrium with other determinations from previous studies.

In Fig. 3.2, the red curve shows the scale height of the gas defined by Eq. 3.6 and the red band is the associated uncertainty calculated with Eq. 2.E.15. The scale height profiles of CCs and of the gas in hydrostatic equilibrium (i.e. weighted average of h_{HI} and h_{H_2}) are in excellent agreement with each other, suggesting that the definition of $h_{\text{SFR}}(R)$ adopted in Chapter 2 is optimal in describing the flaring of the SFR vertical distribution.

3.4.2 VSF laws in the Milky Way

Given the promising result discussed above, we investigated the location of the MW points on the volumetric correlations found in Chapter 2.

Total gas

In Fig. 3.3 we show the correlations between Σ_{gas} and Σ_{SFR} (left panel) and ρ_{gas} and ρ_{SFR} (right panel), with the points colour-coded according to the distance from the Galactic centre. We also include the sample of disc galaxies from Chapter 2 (grey points) in order to show that the MW follows the same trend as external galaxies. We note that the scatter is large in the surface-based panel, in particular for $\Sigma_{\text{gas}} < 10 M_{\odot} \text{ pc}^{-2}$. As shown in the left panel of Fig. 2.6, a correlation close to $\Sigma_{\text{SFR}} \propto \Sigma_{\text{gas}}^{1.4}$ is visible at high densities, but some galaxies, including the MW, seem to follow a steeper relation with respect to the others.

On the contrary, a different picture emerges from the right panel, where we can see that the MW volume densities follow remarkably well the VSF law with slope $\alpha = 1.91$ (black solid line) and intrinsic scatter $\sigma = 0.12$ dex (red band) found in Sect. 2.5.1 for nearby galaxies. We recall that ρ_{gas} for the MW (Eq. 3.2) was calculated using the scale heights derived with the hydrostatic equilibrium, consistently with the analysis done in Chapter 2 for nearby galaxies. Instead, ρ_{SFR} for the MW was estimated through Eq. 3.3 adopting the scale height of CCs, and not with Eq. 3.6 as was done for external galaxies. We discuss the relevance of this result in Sect. 3.5. For completeness, in Sect. 3.5.1 we compare the VSF law in Fig. 3.3 with the volume density of gas and SFR estimated using other measurements in the literature.

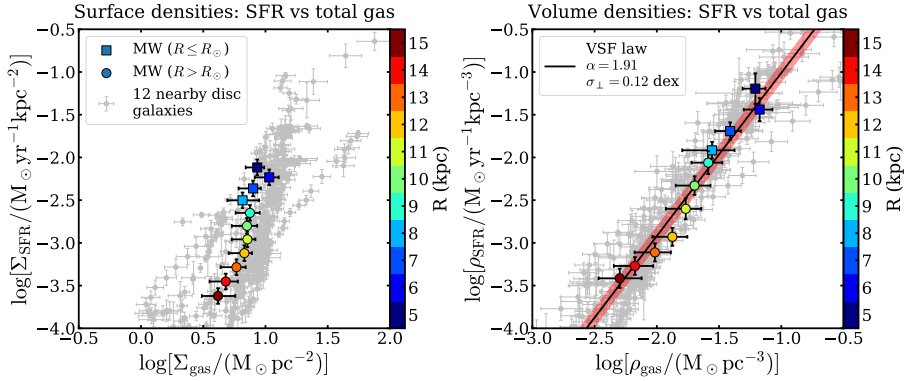


Figure 3.3 – Correlations between the surface density (left) and the volume density (right) of the gas and the SFR in the MW, colour-coded according to the Galactocentric radius. The squares indicate the values for $R \leq R_{\odot}$, while the circles are for $R > R_{\odot}$ (see Sect. 3.3.1 for details). The grey points are the surface and the volume densities for the sample of 12 nearby disc galaxies studied in Chapter 2 (see Fig. 2.6 for the whole range of densities). The solid line in the right panel is the VSF law obtained in Chapter 2 with its intrinsic scatter (red band).

Atomic gas

In Sect. 2.5.2, we found that there is a surprisingly tight correlation between the atomic gas and the SFR volume densities. This is different with respect to the results obtained by other authors using the corresponding surface densities, that seems to be completely uncorrelated (e.g. Bigiel et al., 2010; Schruba et al., 2011). The left panel of Fig. 3.4 shows the atomic gas surface densities in the MW (points colour-coded with the Galactocentric distance) and in the sample of nearby disc galaxies of Chapter 2 (grey points). The MW is consistent with the other galaxies also in the plane $\Sigma_{\text{HI}}-\Sigma_{\text{SFR}}$, as in the case of total gas, and it is clear that there is very little or no correlation between these two quantities.

On the contrary, the right panel shows that the MW volume densities of atomic gas and SFR correlate, following remarkably well the VSF law with slope $\beta = 2.79 \pm 0.08$ found for external galaxies. The validity of this relation in the MW confirms the existence of a link between atomic gas and star formation. We discuss this apparently controversial result in Sect. 3.5.3.

Molecular gas

The left panel of Fig. 3.5 shows the surface densities of molecular gas and SFR in the MW (coloured points) superimposed on those of the sample of disc galaxies in Chapter 2 (grey points). These latter were derived by Frank et al. (2016) using the CO conversion factor (α_{CO}) measured by Sandstrom et al. (2013), which varies not only from galaxy to galaxy, but also with the galactocentric

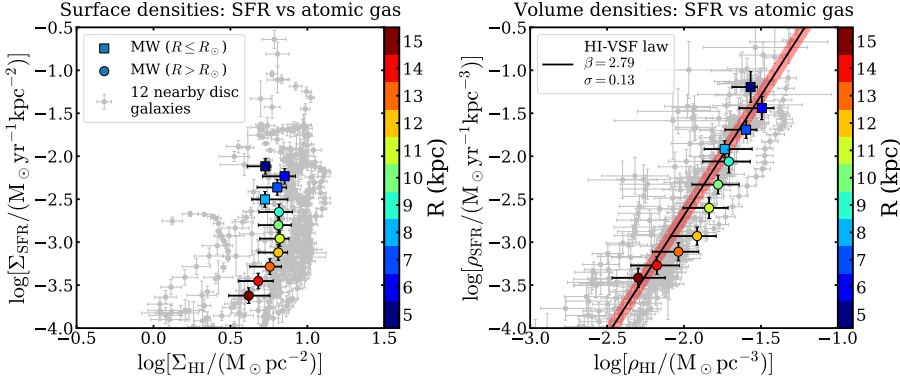


Figure 3.4 – Same as Fig. 3.3, but the gas densities are for the atomic gas only.

radius. The points of the MW are compatible with the relation obtained in Sect. 2.5.3 by fixing the slope to $\gamma = 1$, as suggested by several authors (e.g. Wong & Blitz, 2002; Kennicutt et al., 2007; Schrubba et al., 2011; Marasco et al., 2012). We note that the molecular gas is not detected beyond $R = 13$ kpc, while Σ_{SFR} is still measured.

Concerning the volume densities, the right panel of Fig. 3.5 shows that the MW points are compatible with external galaxies. The large error bars are mainly due to the uncertainty on α_{CO} (see Bolatto et al., 2013). However, as we found in Sect. 2.5.3, the scatter of the relation is not significantly improved by the conversion from surface densities to volume densities. We also note that by comparing Fig. 3.5 with Fig. 3.3 and Fig. 3.4, the scatter is larger in the case of molecular gas densities than in the case of atomic and total gas.

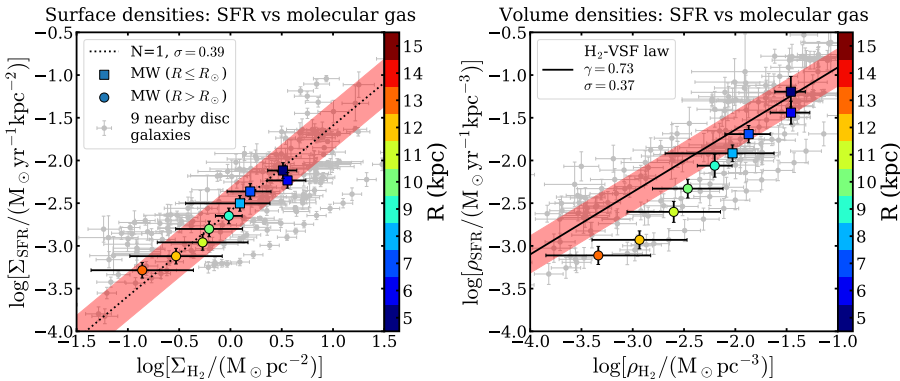


Figure 3.5 – Same as Fig. 3.3, but the gas densities are for the molecular gas only.

3.5 Discussion

In this section, we first assess the validity of the VSF law in our Galaxy using a different tracer of recent star formation (i.e. HII regions) and explore the effect of removing the assumption of the hydrostatic equilibrium. Then, we compare our work with similar studies in the literature and suggest possible interpretations of our results.

3.5.1 VSF law with alternative determinations from the literature

In the following, we build the VSF law for the MW using other estimates of the gas and the SFR volume densities. The aim of this exercise is to demonstrate that the MW is compatible with the VSF law no matter which measurement we choose or whether the hydrostatic equilibrium is assumed or not. In both panels of Fig. 3.6, the circles show the profile adopted in this work (see Sect. 3.3.1 and Sect. 3.3.2), and are the same as in Fig. 3.3. We also show the volume densities of the sample of galaxies studied in Chapter 2 (grey contours) and the VSF law with slope $\alpha = 1.91 \pm 0.03$.

In the left panel the squares indicate ρ_{SFR} calculated using the surface density and the scale height radial profiles of HII regions provided by Paladini et al. (2004). The two determinations are closely compatible except for the points at $R \approx 7$ kpc, where there is a gap between the scale height of CCs and that of HII regions, and also the surface densities are marginally different (see Fig. 3.B.4). The agreement between the two determinations is remarkable and significantly consolidates our results.

In the right panel, we show different estimates of ρ_{gas} taken from the exhaustive collection in Kramer & Randall (2016), who provide the volume densities of the atomic and the molecular gas by Burton & Gordon (1978) and Nakanishi & Sofue (2003, 2006) (the uncertainties are unfortunately not available), and from Marasco et al. (2017). All the points in Fig. 3.6 are colour-coded according to the Galactocentric radius, and the spread in the points with the same colour (i.e. at the same R) can be interpreted as the uncertainty on the volume density measurements at that radius. The MW points are generally compatible with those of nearby galaxies and the VSF law, although the large scatter makes the comparison itself uncertain. The MW points beyond R_{\odot} and derived without using the assumption of hydrostatic equilibrium seem to suggest a shallower slope (≈ 1.5) for the VSF law.⁵ However, Wouterloot et al. (1990) and Kalberla & Dedes (2008) measured higher values for the atomic gas volume density in these regions with respect to the estimate by Burton & Gordon (1978) and Nakanishi & Sofue (2003) shown in Fig. 3.6 (see Fig. 3.A.3). The points at

⁵We stress that the VSF law shown in Fig. 3.6 is not a best-fit to the MW volume densities, but it was obtained in Chapter 2 for a sample of 12 nearby galaxies.

$R > R_\odot$ would be shifted on the VSF law by using these other measurements, which were not included in Fig. 3.6 as Wouterloot et al. (1990) and Kalberla & Dedes (2008) did not derive the molecular gas volume density. Hence, we conclude that the deviation of the points beyond R_\odot might be explained by the uncertainties in deriving the gas distribution in our Galaxy (e.g. modelling of the extra-planar gas, assumed rotation velocity), rather than a different slope for the VSF law.

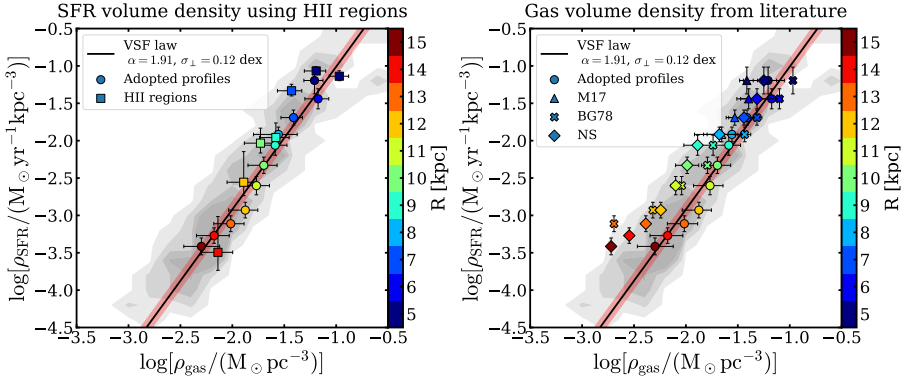


Figure 3.6 – *Left panel*: comparison between ρ_{SFR} derived with the surface density of SNRs and the scale height of CCs (circles, as in Fig. 3.3) and ρ_{SFR} calculated with the surface density and the scale height of HII regions (squares). In both cases, ρ_{gas} is calculated with hydrostatic equilibrium (see Sect. 3.3.1). *Right panel*: comparison between ρ_{gas} derived with the hydrostatic equilibrium (circles, as in Fig. 3.3) and ρ_{gas} from different works in the literature (M17=Marasco et al. 2017, BG78=Burton & Gordon 1978, NS=Nakanishi & Sofue 2003, 2006), all with the ρ_{SFR} used in this work (see Sect. 3.3.2). In both panels, the symbols are colour-coded according to the Galactocentric radius, and the solid line and the red band show the VSF law and its intrinsic scatter derived for nearby disc galaxies, whose volume densities are represented by the grey contours containing, from lightest to darkest, 95%, 75%, 50%, and 25% of the points.

3.5.2 Previous works on star formation laws in the Milky Way and nearby disc galaxies

Several studies in the literature aimed to find a model of star formation that could reproduce the radial profile of the SFR in our Galaxy, given a gas distribution. For example, Boissier et al. (2003) adopted the Toomre criterion for the stability of galactic discs (Toomre, 1964) proposed by Wang & Silk (1994b), in order to account for the contribution of the stellar disc. They found that this criterion applies in the MW, but it has limited success in reproducing the profiles of the SFR surface densities in their sample of 16 disc galaxies. Moreover, the authors investigated the validity of the classical SK law, that is $\Sigma_{\text{SFR}} \propto \Sigma_{\text{gas}}^n$ (Kennicutt, 1998), and of two modified versions, which make either

use of the galactic orbital time, namely $\Sigma_{\text{SFR}} \propto \Sigma_{\text{gas}}^n V_c/R$ (Ohnishi, 1975), or the stellar surface density, viz. $\Sigma_{\text{SFR}} \propto \Sigma_{\text{gas}}^n (\Sigma_{\text{gas}} + \Sigma_{\star})^m$ (Dopita & Ryder, 1994).⁶ They found that the two modified versions of the SK law work slightly better than the classical relation in both the MW and the external galaxies, but the scatter remains large. It is interesting to note that both modified SK relations are in some way included in our VSF law. Indeed, the orbital time and, in particular, the rotation curve of a galaxy depend on its gravitational potential, hence including this term in the correlation could partially account for the role of the gravitational pull in shaping the gas vertical distribution (see Eq. 3.1). Moreover, the stellar mass component dominates the gravitational potential in the inner regions of disc galaxies, hence the scale height significantly depends on the stellar distribution.

Our approach is based on the assumption that the vertical distribution of gas in galaxies is shaped by the hydrostatic equilibrium. This idea shares similarities with that proposed by Blitz & Rosolowsky (2006). These authors collected a sample of 14 nearby star-forming galaxies, including both dwarfs and spirals, and HI-rich and H₂-rich galaxies. They found that the ratio of the molecular to the atomic gas content correlates with the midplane pressure calculated using the hydrostatic equilibrium. Therefore, they proposed that this “hydrostatic pressure” regulates the SFR surface density, which has two formulations, one when low-pressure (HI-dominated) environments are considered and the other for high-pressure (H₂-dominated) environments. These results are somewhat different from ours as we do not find two regimes of star formation, but instead a monotonic relation that encompasses the HI- and H₂-dominated regions. We think that these differences may be explained, at least partially, by drawbacks in the Blitz & Rosolowsky (2006) methodology. The most critical is that they neglected the dark matter component in the mass distribution calculation. As a consequence, their gravitational force and hydrostatic pressure are significantly underestimated, in particular in the outer regions of galaxies. Moreover, they ignored the radial gradient of the circular speed (e.g. Bahcall, 1984; Bahcall & Casertano, 1984; Olling, 1995). This term is non-negligible in the inner regions of galaxies, where most star formation takes place, and has an impact on the correct determination of the hydrostatic pressure. Finally, Blitz & Rosolowsky (2006) assumed that the gas velocity dispersion is constant with the galactocentric radius at 8 km s⁻¹, which is a factor of 1.5-2 lower than the typical values in the inner regions of galaxies (e.g. Fraternali et al., 2002; Boomsma et al., 2008, and Fig. 2.2).

Recently, Sofue (2017) used the volume densities and the surface densities to study power-law correlations between the SFR and the atomic gas, the molecular gas, and the total gas in our Galaxy. He found that the index and the

⁶This formulation is almost equivalent to the so-called extended-Schmidt law ($\Sigma_{\text{SFR}} \propto \Sigma_{\text{gas}} \Sigma_{\star}^{1/2}$), which was originally proposed by Talbot & Arnett (1975) and then observationally studied by Shi et al. (2011, 2018) and Roychowdhury et al. (2017).

normalisation of all the power-laws both vary with the Galactocentric radius, and that all the relations tend to steepen in the outer regions of the Galaxy ($8 \text{ kpc} < R \leq 20 \text{ kpc}$) with respect to the inner regions ($0 \text{ kpc} \leq R \leq 8 \text{ kpc}$), suggesting the existence of a density threshold.⁷ In agreement with our findings, he obtained that the HI-SFR volume density correlations are steeper than those involving the total gas relations, which are in turn steeper than the H₂-SFR relations. Despite evident similarities, there are significant differences between our approach and that of Sofue (2017), as we discuss in Sect. 3.3.1 and Appendix 3.A concerning the gas distribution. In addition, the SFR distribution adopted by Sofue (2017) was derived in a previous paper (Sofue & Nakanishi, 2017) using HII regions and adopting the kinematic distance method to infer their positions in the Galaxy. They decided to convert the surface density of SFR to the volume density using a constant value for h_{SFR} as they found that the scale height of HII regions is $\sim 50 \text{ pc}$ within $R \leq 10 \text{ kpc}$, showing clear flaring only beyond 15 kpc. This result is in contrast with that of Paladini et al. (2004), who also studied the distribution of HII regions, and with the measurements of the scale height of other SFR tracers (see Appendix 3.B.2). Possibly, the h_{SFR} by Sofue & Nakanishi (2017) is contaminated by the uncertainties on the distance determination related to the kinematic method, which we avoided by using standard candels as CCs. Interestingly, Sofue (2017) also measured the index of the power laws considering the whole radial range, from the centre out to 20 kpc, and found 2.01 ± 0.02 for the correlation with the total gas volume density (see also Abramova & Zasov, 2008), 0.7 ± 0.07 for that with the molecular gas only, and 2.29 ± 0.3 for the atomic gas only (see also Nakai & Sofue, 1982), which are roughly consistent with our findings.

3.5.3 Physical interpretation of the VSF law

In our VSF law, the SFR volume density is regulated by the square of the total gas volume density. In the following, we discuss possible interpretations of this correlation. The first issue to bear in mind is that the correlations that we found are valid on kiloparsec scales, but are likely not applicable to a single molecular cloud or filament. Moreover, the exact value of α remains slightly uncertain (see Sect. 3.5.1).

Our VSF law can be written as

$$\rho_{\text{SFR}} = \epsilon_{\text{sf}} \frac{\rho_{\text{gas}}}{\tau_{\text{sf}}}, \quad (3.7)$$

where ϵ_{sf} is a dimensionless efficiency parameter, usually assumed constant, and τ_{sf} is some physically meaningful timescale, which is different for different models and can have an explicit dependence on the gas density. A natural timescale for star formation may be the free-fall time $\tau_{\text{ff}} \propto (G\rho_{\text{gas}})^{-1/2}$ (e.g. Madore,

⁷The variation of the index and the normalisation was also measured on shorter scales by dividing the Galaxy in annuli of 2 kpc width.

1977; Krumholz et al., 2012), which implies an index of 1.5. This is usually invoked to explain the SK relation with slope 1.4, with the implicit assumption of a constant scale height, both for the gas and the SFR distributions. In this Chapter and in Sect. 2.4, we show that these scale heights instead increase with radius, for the MW and for nearby disc galaxies (see also Abramova & Zasov 2008 and Elmegreen 2015, 2018). Moreover, our results indicate that the slope is closer to 2 rather than 1.5, suggesting that another timescale is driving star formation on kiloparsec scales or is involved in the process. Potentially interesting and physically relevant timescales are the cooling time of warm gas ($T \approx 10^4$ K) and the timescale to reach the equilibrium between the formation and destruction of H_2 , as suggested by Sofue (2017) for example. We note that both these timescales are inversely proportional to ρ_{gas} (see e.g. Hollenbach & McKee, 1979; Ciotti & Ostriker, 2007; Krumholz, 2014), which, when inserted in Eq. 3.7, would predict a VSF law with index 2, in agreement with our findings.

Leaving aside these considerations about the slope of the VSF law, it is interesting to qualitatively interpret our results in the picture of a self-regulating star formation model. Our ρ_{gas} is the highest gas density (i.e. that in the midplane) at which the pressure–gravity balance holds (see Eq. 3.1 and Eq. 3.2). Therefore, it is probably a good estimate of the gas volume density (averaged on kiloparsec scale) in star-forming clouds, as suggested by the small scatter of the VSF law. Turbulent motions are likely sustained by stellar feedback, whose strength is expected to be proportional to the SFR density itself (see Chapter 5). The higher the SFR density per unit volume, the more the turbulent pressure helps the thermal pressure to contrast gravity. As a consequence, the gas z -distribution broadens and the scale height increases, thus the volume density in the midplane decrease and so does the SFR density. Then the pressure support against gravity weakens because of the reduction of turbulence injection, and the gas z -distribution narrows, increasing the gas volume densities in the midplane and consequently the SFR density. The influence of stellar feedback on the ISM turbulence is still a matter of debate (e.g. Tamburro et al., 2009; Utomo et al., 2019) and we specifically address the topic in Chapter 5. This interpretation is similar to the self-regulating scenario proposed by Ostriker & Shetty (2011), who assumed that star formation in spiral galaxies is regulated by the pressure support of gas turbulence against gravity (the radiation pressure may become dominant in the most extreme starburst regions). Investigating the compatibility of this model with our results goes however beyond the scope of this thesis.

The unexpected correlation between the SFR and the atomic gas volume densities suggests that the HI can be a good tracer of the star-forming gas over a broad range of densities, from spiral to dwarf galaxies (see Chapters 2 and 4). On the contrary, the scatter in the H_2 -SFR relations is large, with no significant improvement from the conversion of surface densities to volume densities. In addition, the molecular gas, which is typically traced using CO emission, is

often detected only in the inner regions of star-forming galaxies (including the MW). This may seem counter-intuitive, as star formation is observed to occur in molecular clouds. A possible explanation of the HI-SFR correlation is that molecular clouds form from the atomic gas and are rapidly swept away by stellar feedback, leaving only the parent atomic gas. Therefore, we could expect to see the HI-SFR correlation if the timescale for the formation of a new molecular clouds were longer than the lifetime of star formation tracers. The timescale of molecular cloud formation depends on the physical mechanism that regulates the process. It is probably between a few 10^7 yr and 10^8 yr, subject to the ISM local conditions (see e.g. McKee & Ostriker, 2007). Star formation tracers are characterised by timescales that typically range from a few 10^6 yr to about 10^8 yr (Kennicutt & Evans, 2012). Therefore, the comparison between the two timescales is very uncertain. In low-density and/or metal-poor regions, the CO emission likely becomes a bad tracer of the total molecular gas (H_2) (e.g. Schrubba et al., 2012; Hunt et al., 2015; Seifried et al., 2017). The existence of a HI-VSF law that extends to these environments seems to indicate that HI can efficiently trace also the CO-dark H_2 . Nevertheless, this correlation may also suggest that the atomic gas has an important, albeit non-trivial, role in star formation, and that the molecular gas is not always a prerequisite for creating new stars (Glover & Clark, 2012; Krumholz, 2012).

3.6 Summary and conclusions

Star formation laws are undoubtedly of fundamental importance to understand galaxy formation and evolution. It is generally acknowledged that the formation of stars in galaxies is regulated by their gas reservoir, but studying the intrinsic distributions of the gas and the SFR is hampered by the difficulty of measuring the volume densities in galaxies. The surface densities, observable in external galaxies, are affected by projection effects due to the flaring of the thickness of gas discs. Therefore, the relation between the surface density and the volumetric density is non-trivial and similar values of surface density can be measured where the volume density is low and the gas disc is thick, or vice versa.

In Chapter 2, we used a sample of 12 nearby disc galaxies to derive the volume densities of the gas (HI and H_2) from the observed surface densities using the scale height calculated under the assumption of hydrostatic equilibrium in the galactic gravitational potential. We find that the gas and the SFR volume densities correlate following a tight power-law relation, the VSF law, whose index is either ≈ 1.3 or ≈ 1.9 depending on whether the scale height of the SFR is assumed to be constant or flaring with the galactocentric radius.

In this Chapter, we investigated the VSF law in our Galaxy using the same method as for external galaxies, but with a crucial improvement. We used classical Cepheids as tracers of the recent star formation and thereby we directly derived the thickness of their vertical distribution as a function of the

Galactocentric radius. This allowed us to convert the SFR surface density to volume density, and to find a unique slope of the VSF law. Our main conclusions are the following:

1. The vertical distribution of the SFR density flares with the Galactocentric radius and its scale height is fully compatible with the scale height of cold gas (HI+H₂) calculated assuming the hydrostatic equilibrium.
2. We explored the correlations between the volume density of the SFR and the volume densities of the total gas, the atomic gas only, and the molecular gas only, finding that the MW follows the same relations found in nearby disc galaxies.
3. The VSF law involving the total gas, that is $\rho_{\text{SFR}} \propto \rho_{\text{gas}}^\alpha$ with $\alpha \approx 2$, is the tightest correlation.

We stress that the flaring of the gas thickness is significant and must be taken into account in studies of the gas distribution in galaxies, not only in dwarfs but also in spirals (see Wilson et al. 2019 for an application to ultra-luminous infrared galaxies). The VSF law is described by a single index across the whole density range, which means that there is no volume density threshold and that the breaks previously observed in the resolved and integrated SK laws are due to the disc flaring, rather than to a drop in the star formation efficiency (see also Elmegreen 2015, 2018).

A physical interpretation of the VSF law is currently lacking and we hope that it will stimulate future investigations. The assumption of the hydrostatic equilibrium for the gas in galaxies should also be tested, but measuring the vertical distribution of gas in galaxies is not an easy task.

Our VSF laws are simple recipes for star formation that could be included in analytical or semi-analytical models of the formation and evolution of galaxies. Moreover, the VSF laws could be easily compared with the correlations between the SFR and the gas volume densities predicted by numerical simulations of star formation on small scales, with the advantage of avoiding the 2D projection to obtain the surface densities involved in the SK law.

Acknowledgements

We would like to thank X. Chen, T. Mackereth, and Y. Sofue for sharing their data and results. FF and AM thank Lotte Elzinga for her preliminary investigation of hydrostatic equilibrium in the Milky Way during her Bachelor project.

Appendix 3.A The Milky Way gas distribution compared with the literature

In the following, we compare the radial profiles of the surface density, the volume density, and the scale height adopted in this work with those available in the literature, for the HI, the H₂, and the total gas.

3.A.1 Gas surface densities

In Sect. 3.3.1, we derived the fiducial profiles of the atomic gas and the molecular gas surface densities using relatively recent measurements from the literature. These profiles are represented by the black points in Fig. 3.A.1, where we show the atomic gas in the upper left panel, the molecular gas in the upper right panel, and the total gas in the lower panel. The other estimates available in the literature are also provided for a comparison. All the profiles are re-scaled to the same value for R_{\odot} and include a factor 1.36 for the helium correction. The most uncertain profile is probably Σ_{HI} , while the different estimates of Σ_{H_2} and Σ_{gas} seem approximately compatible. The discrepancies between the HI profiles could be due to the differences in the assumed rotation curve, which has an important effect on the kinematic distance method (see Burton, 1974; Marasco et al., 2017).

3.A.2 Gas scale height

There have been several attempts to infer the gas scale height in our Galaxy directly from the data, and it is interesting to compare these determinations with those we calculated with the hydrostatic equilibrium (see also Narayan & Jog, 2002). These latter are represented by the black points in Fig. 3.A.2, where the left and the right panel respectively show the HI and the H₂ scale heights. Despite the very different methods, all the profiles show a flaring. The scale height of HI in hydrostatic equilibrium is compatible with the results of Lockman (1984), Wouterloot et al. (1990), Levine et al. (2006), and Kalberla & Dedes (2008). The last work in particular assumed the hydrostatic equilibrium a priori and modelled the ISM as a two-phase fluid, in which the warm neutral medium and the cold neutral medium have different scale heights. They found that the final model is close to a single-component medium with constant velocity dispersion of 8.3 km s^{-1} , which is similar to the values we adopted for the HI. This can explain the agreement between the scale heights, despite the significant differences between the mass models (see Kalberla et al., 2007).

However, our scale height differs from those derived by Nakanishi & Sofue (2003)⁸ and Marasco et al. (2017) by $\approx 50\%$ (see left panel in Fig. 3.A.2).

⁸Nakanishi & Sofue (2003) assumed a sech^2 profile for the HI vertical distribution, so we re-scaled their HWHM by a factor 0.8 to obtain the equivalent quantity for a Gaussian profile.

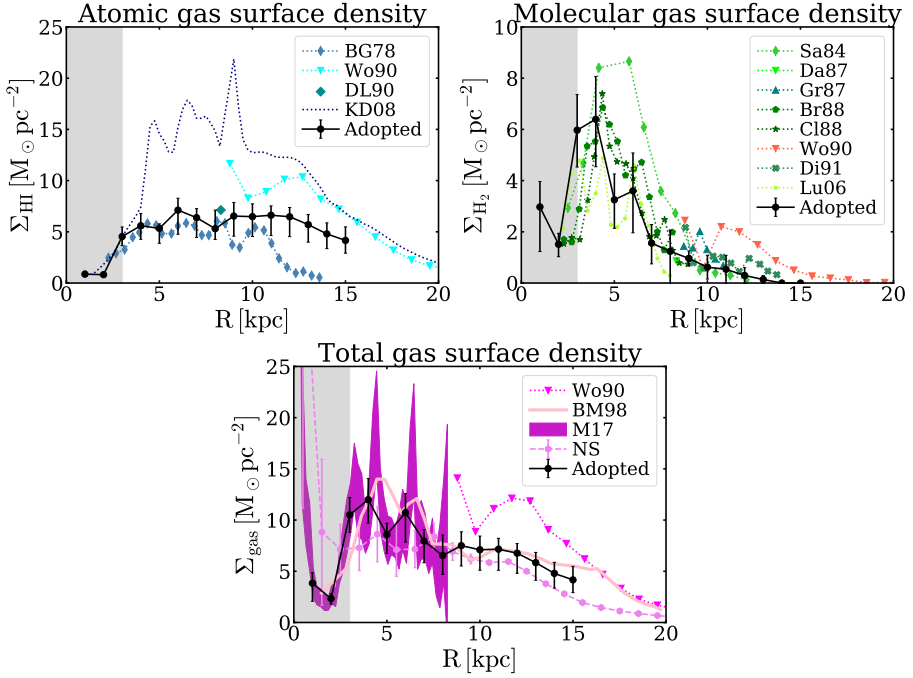


Figure 3.A.1 – Surface density radial profiles of the atomic gas (upper left), the molecular gas (upper right), and the total gas (lower panel) from the literature compared to the profile adopted in this work (black points). In the upper left panel: BG78=Burton & Gordon (1978), Wo90=Wouterloot et al. (1990), DL90=Dickey & Lockman (1990), and KD08=Kalberla & Dedes (2008). In the upper right panel: Sa84=Sanders et al. (1984), Da87=Dame et al. (1987), Gr87=Grabelsky et al. (1987), Br88=Bronfman et al. (1988), Cl88=Clemens et al. (1988), Di91=Digel (1991), and Lu06=Luna et al. (2006). In the lower panel: BM98=Binney & Merrifield (1998), NS=Nakanishi & Sofue (2003, 2006), M17=Marasco et al. (2017).

Nakanishi & Sofue (2003) adopted the kinematic distance method to measure the HI distribution and removed the emission of high-altitude and diffuse HI, so a direct comparison is not straightforward. The discrepancy with Marasco et al. (2017) scale height deserves further discussions, as we adopted their velocity dispersion profile to calculate h_{HI} , hence we expected the scale heights to be compatible within the uncertainties. There are some possible explanations for this difference. Marasco et al. (2017) found that HI in the midplane could be best described by a two-component model, where 80%-85% of the atomic gas has low velocity dispersion ($\sim 8 \text{ km s}^{-1}$), while the remaining has a much higher velocity dispersion ($15\text{-}20 \text{ km s}^{-1}$). Likely, this second component has a larger scale height than the first one, in which case it could dominate the HI emission above the midplane. The vertical distribution of the gas was instead modelled using a single component, thus it is possible that the resulting h_{HI} is closer to

the scale height of the high- σ_{HI} component than to that of the low- σ_{HI} one. In order to calculate the scale height from hydrostatic equilibrium, we adopted the average velocity dispersion between the two components (i.e. the high- σ_{HI} gas and the low- σ_{HI} gas), but this approach implicitly relies on the assumption that the velocity dispersion is isotropic and constant along z . However, this latter property may not be true if the high- σ_{HI} component is more abundant than the low- σ_{HI} one at high latitudes above the midplane. Alternatively, we could speculate that some (anisotropic) force contributes to balancing the gravitational pull towards the midplane, for instance magnetic tension or cosmic rays. In particular, recent magneto-hydrodynamical simulations of stratified gas in galaxies (e.g. Simpson et al., 2016; Pfrommer et al., 2017) show that the anisotropic diffusion of cosmic rays can contribute to the vertical gradient of the gas pressure, but investigating such scenarios is beyond the aim of this thesis.

Figure 3.A.2 shows that the molecular gas scale height based on the hydrostatic equilibrium resembles the h_{H_2} profiles found by Nakanishi & Sofue (2006) and Marasco et al. (2017) within the uncertainties. The h_{H_2} profiles from Sanders et al. (1984), Grabelsky et al. (1987), and Wouterloot et al. (1990) are also in approximate agreement with our scale height, while the Bronfman et al. (1988) scale height shows some discrepancies for $3 \text{ kpc} \lesssim R \lesssim 8 \text{ kpc}$.

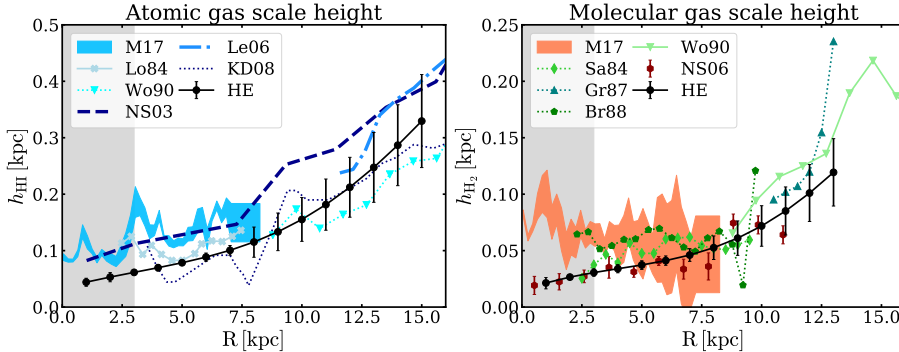


Figure 3.A.2 – Scale height radial profiles of the atomic and molecular gas from the literature (Lo84=Lockman 1984; see caption of Fig. 3.A.1 for the other labels in the legend) compared to those calculated assuming the hydrostatic equilibrium (black points).

3.A.3 Gas volume densities

In Fig. 3.A.3, the black points represent the MW volume density profiles of atomic gas (upper left), molecular gas (upper right), and total gas (lower panel) calculated with the scale height of hydrostatic equilibrium. The other points show instead the measurements available in the literature. Within the solar radius, our ρ_{HI} is systematically higher than the other estimates (except

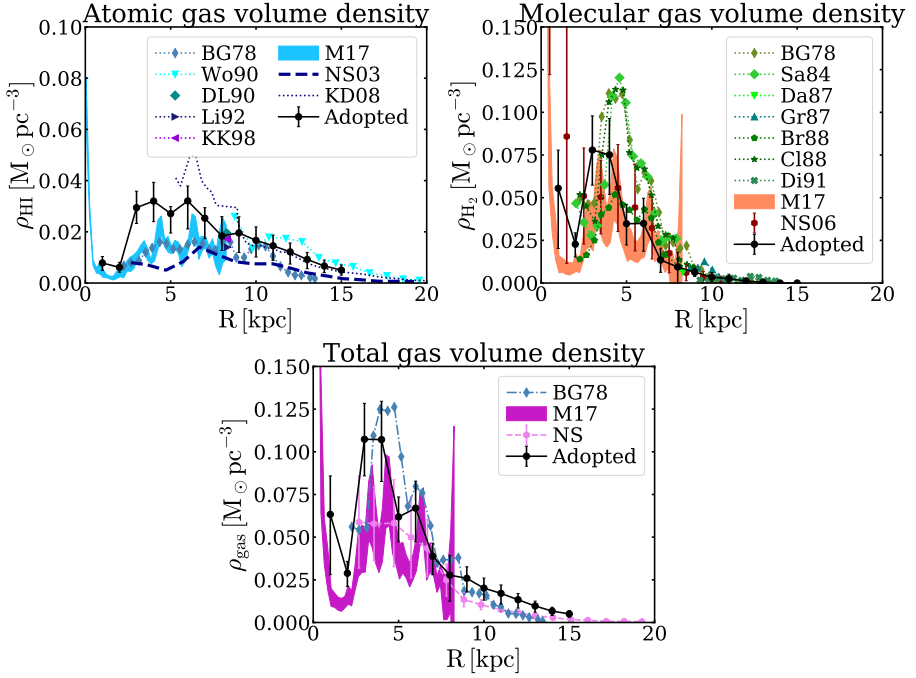


Figure 3.A.3 – Volume density radial profiles of the atomic gas (upper left), the molecular gas (upper right), and the total gas (lower panel) from the literature (Li92=Liszt 1992, KK98=Kalberla & Kerp 1998, NS=HI from Nakanishi & Sofue 2003, and H₂ from Nakanishi & Sofue 2006; see caption of Fig. 3.A.1 for the other labels in the legend) compared to the profile adopted in this work (black points). A factor 1.36 for the helium correction is included.

Kalberla & Dedes, 2008), as we expected from the discrepancy found between the scale heights. However, this difference seems to be partially accounted for by the error bars, which were calculated from the uncertainties on h_{HI} and Σ_{HI} . These latter in particular include the difference between the profiles in the literature (beyond R_{\odot}) and the uncertainty on the optical regime of atomic gas (within R_{\odot}), as explained in Sect. 3.A.1. Concerning the molecular gas, our profile for $\rho_{\text{H}_2}(R)$ is in agreement with the observations, and given that the molecular gas is mainly within the solar circle, our profile for the total gas is also approximately compatible with all the other determinations.

Appendix 3.B The Milky Way SFR distribution using different tracers

In the following, we compare the surface density and the scale height of the SFR adopted in this work with other profiles available in the literature.

3.B.1 SFR surface density

We adopted the SFR surface density profile derived by Green (2015) using SNRs to trace the distribution of recent star formation. In the left panel of Fig. 3.B.4, this profile is compared to others in the literature, all normalised to have a total SFR of $1.9 \text{ M}_{\odot} \text{ yr}^{-1}$ (Chomiuk & Povich, 2011). The discrepancy with Case & Bhattacharya (1998), who also studied the SNR distribution, was expected (see Green 2015). The adopted $\Sigma_{\text{SFR}}(R)$ is compatible with the profile derived using pulsars (Lyne et al., 1985; Yusifov & Küçük, 2004b) and the far-infrared (FIR) emission (Misiriotis et al., 2006), except for the inner 3 kpc that are not included in our study. The profile obtained by Green (2015) is also compatible with the HII regions radial distribution (Paladini et al., 2004), except for $R \approx 5 - 6$ kpc (see Sect. 3.5.1 for further discussion).

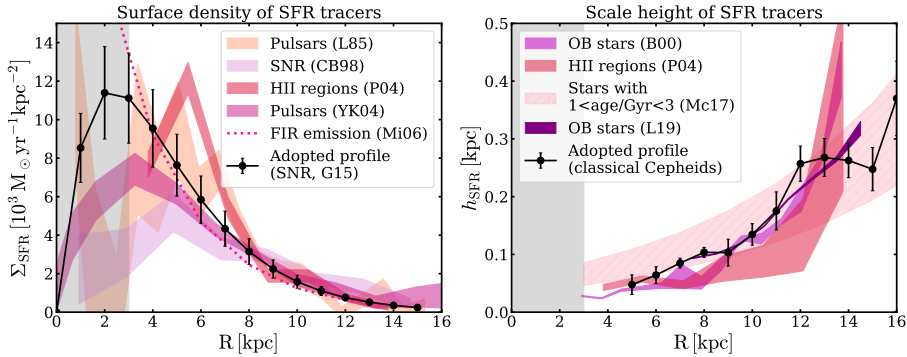


Figure 3.B.4 – Surface density (left panel) and scale height (right panel) of the SFR distribution using different tracers. The black points show the profile adopted in this work, while the others are different estimates from the literature (see text). The reference papers are indicated by the following abbreviations: L85=Lyne et al. (1985), CB98=Case & Bhattacharya (1998), P04=Paladini et al. (2004), YK04=Yusifov & Küçük (2004b), Mi06=Misiriotis et al. (2006), G15=Green (2015), B00=Bronfman et al. (2000), Mc17=Mackereth et al. (2017), and L19=Li et al. (2019).

3.B.2 SFR scale height

In order to convert Σ_{SFR} to ρ_{SFR} , we used the scale height of CCs derived in Sect. 3.3.2. The right panel of Fig. 3.B.4 shows the comparison between the

scale height of CCs (black points) with the scale height of other tracers of star formation: OB stars (Bronfman et al., 2000; Li et al., 2019), stellar populations with age between 1 Gyr and 3 Gyr (Mackereth et al., 2017), and HII regions (Paladini et al., 2004, Table 4). Mackereth et al. (2017) and Li et al. (2019) assumed an exponential function to model the vertical profile of young stars, thus we re-scaled their profiles by a factor of $1/\sqrt{2}$ in order to be comparable with our definition of the scale height, which is equivalent to the normalised second moment of the distribution. The presence of the flare is clear in all the cases and, despite the different methods adopted, the profiles are generally compatible.

Appendix 3.C Galactic rotation curve

In Fig. 3.C.5, the observed rotation curve of the MW is compared to the circular velocity of the parametric mass model adopted in this work. The measurements of the rotation are based on CCs (Mróz et al., 2019), and on the HI and CO emission (Marasco et al., 2017). Within the solar circle, the stellar components are the main contributors to the rotation curve, while the dark matter halo dominates the gravitational potential beyond the solar circle. We note that the gas components are anywhere minor contributors, so our choice of using a different surface density profile for HI and H₂ with respect to McMillan (2017) does not significantly affect the resulting total gravitational potential nor its rotation curve. We also note that our circular velocity is compatible with both the observed rotation curve measured using different tracers as, for instance, high mass disk stars, red clump giants, blue horizontal branch stars, and the mass model reported in Bland-Hawthorn & Gerhard (2016).

We assumed that the dark matter halo has a spherical shape for consistency with McMillan (2011, 2017), who opted for this simple choice due to the uncertainty on the halo flattening (see Bland-Hawthorn & Gerhard, 2016; Helmi, 2020, and references therein). As pointed out by McMillan (2017), the flattening can impact the dynamical models of the Galaxy disc. We can expect that an oblate halo gives a less prominent flaring than a spherical one, as its density in the midplane is higher; vice versa for a prolate halo. In particular, Piffi et al. (2014) report that the axis ratio (q) of the halo can influence the derived local dark matter density as $\rho_{\text{DM}}(R_{\odot}, 0) \propto q^{-0.89} \rho_{\text{DM, sph}}(R_{\odot}, 0)$, where $\rho_{\text{DM, sph}}$ is the local density for a spherical halo. It is interesting to estimate the possible effect of q on the gas scale height to grossly quantify its impact on our results. We used the analytical formulation of h given in Sect. 2.A (Eq. 2.A.4), neglecting the rotational density as $\rho_{\text{rot}} \approx 0$ where the rotation curve is approximately flat. Thus, we obtain that $h(R_{\odot}) \propto [G\rho_{\text{DM}}(R_{\odot}, 0)]^{-1/2}$, where we have assumed that the dark matter density ρ_{DM} is the dominant component in order to investigate the case of maximum influence of the flattening. We then obtain that the scale height increases with the axis ratio approximately as $q^{0.45}$, meaning that an

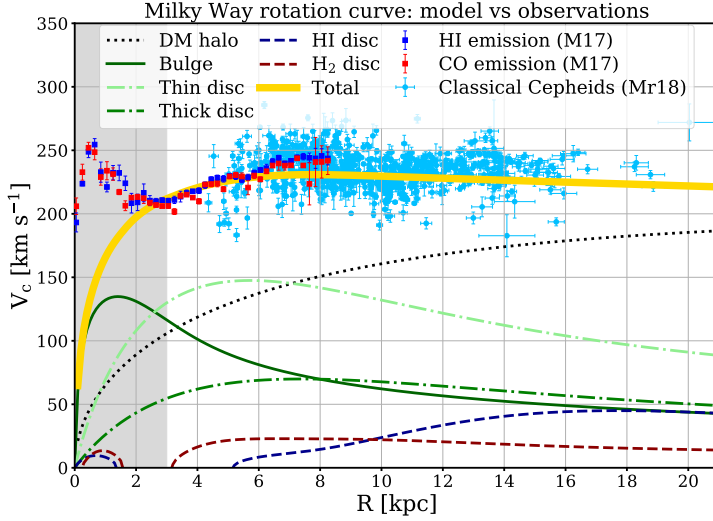


Figure 3.C.5 – MW observed rotation curve compared to the circular velocity of the parametric mass model adopted in this work (McMillan, 2017). The blue and the red squares indicate the rotation curve measured by Marasco et al. (2017) using the HI and the CO emission, while the light blue points indicate the CCs rotation velocity (Mróz et al., 2019). The dot-dashed curves indicate the stellar thin and thick discs (light-green and green, respectively). The solid dark-green curve shows the bulge. The dotted black curve is the dark matter halo, and the dark-blue and dark-red dashed curves are the atomic and the molecular discs, respectively. The yellow thick curve is the total mass model. The regions dynamically influenced by the bar (not included in our model) is denoted by the grey area.

oblate halo produces a slightly thinner gas disc, whereas a prolate halo gives a slightly thicker disc, as expected. Let us take, for example, two flattened haloes from the literature, one oblate with $q \approx 0.8$ (e.g. Piffi et al., 2014) and the other prolate with $q \approx 1.3$ (e.g. Posti & Helmi, 2019). The difference in the scale height is $\sim 10\%$ in both cases, which is typically within the uncertainties on h for the gas in hydrostatic equilibrium, indicating that a mild flattening would not significantly change our results.

CHAPTER 4

**The volumetric star
formation law for nearby
dwarf galaxies**

based on

— C. Bacchini, F. Fraternali, G. Pezzulli, and A. Marasco —

submitted to *Astronomy & Astrophysics*.

Abstract

In the last decades, much effort has been put into finding the star formation law which could unequivocally link the gas and the star formation rate (SFR) densities measured on sub-kiloparsec scale in star-forming galaxies. The conventional approach of using the observed surface densities to infer star formation laws has however revealed a major and well-known issue, as such relations are valid for the high-density regions of galaxies but break down in low-density and HI-dominated environments. Recently, an empirical correlation between the total gas (HI+H₂) and the SFR volume densities was obtained for a sample of nearby disc galaxies (see Chapter 2) and for the Milky Way (see Chapter 3). This volumetric star formation (VSF) law is a single power-law with no break and a smaller intrinsic scatter with respect to the star formation laws based on the surface density. In this Chapter, we explore the VSF law in the regime of star-forming dwarf galaxies in order to test its validity in HI-dominated, low-density, and low-metallicity environments. In addition, we assess this relation in the outskirts of spiral galaxies, which are low-density and HI-dominated regions similar to dwarf galaxies. Remarkably, we find the VSF law, namely $\rho_{\text{SFR}} \propto \rho_{\text{gas}}^\alpha$ with $\alpha \approx 2$, is valid for both these regimes. This result indicates that the VSF law, which holds unbroken for a wide range of gas (≈ 3 dex) and SFR (≈ 6 dex) densities, is the empirical relation with the smallest intrinsic scatter and is likely more fundamental than surface-based star formation laws.

4.1 Introduction

The quest for a fundamental law of star formation on kiloparsec scale has been ongoing since sixty years ago, when Schmidt (1959) proposed for the first time a power-law relation linking the star formation rate (SFR) and the atomic gas volume densities. The massive amount of literature on this topic reflects the importance of the star formation law in the context of galaxy formation and evolution. Indeed, some form of this relation can give useful constraints on the processes that regulate the conversion of gas into stars and is often implemented at sub-galactic scales, both in idealised models and cosmological simulations of galaxies. Thirty years after Schmidt’s theoretical work, a turning point in the study of star formation laws was reached with the observational determination of the so-called Schmidt-Kennicutt (SK) law linking the gas (HI+H₂) and the SFR surface densities as $\Sigma_{\text{SFR}} \propto \Sigma_{\text{gas}}^N$ with $N \approx 1.4$ (Kennicutt, 1989, 1998). Until today, versions of the star formation law involving surface densities have been widely investigated and different formulations have been proposed. However, the validity of these relations seem to be contingent upon interstellar medium (ISM) conditions and galaxy type. In particular, many authors have reported that the star formation law derived for spiral galaxies does not hold in dwarf galaxies, suggesting the existence of different regimes of star formation for different galaxy types. We can characterise different surface-based star formation laws according to the quantities involved and the regime of validity.

The first group of empirical relations involves the gas and the SFR surface densities averaged over the star-forming disc of a galaxy, which are connected by the so-called ‘global’ SK law with $N \approx 1.4$. This relation was originally proposed by Kennicutt (1998) based on a sample of normal spiral galaxies and infrared luminous starbursts. While the Milky Way (MW) seems to follow this global SK law (e.g. Kennicutt & Evans, 2012), dwarf and low-surface brightness galaxies are generally discordant, as their SFR surface densities tend to be lower than the values expected from the SK relation (Wyder et al., 2009; Gatto et al., 2013; Roychowdhury et al., 2015, 2017; de los Reyes & Kennicutt, 2019, but see Teich et al. 2016 for a different conclusion).

The second category of star formation laws is based on the local surface densities (i.e. azimuthally averaged radial profiles, surface densities measured in kiloparsec or sub-kiloparsec regions) and was derived for spatially resolved galaxies (e.g. Kennicutt, 1989; Martin & Kennicutt, 2001). Several authors found that even this ‘local’ SK relation breaks down in low-density ($\Sigma_{\text{gas}} \lesssim 10 \text{ M}_{\odot} \text{ pc}^{-2}$) and HI-dominated environments, such as the outskirts of nearby spiral galaxies and of the MW (e.g. Wong & Blitz 2002; Boissier et al. 2003; Misiriotis et al. 2006; Kennicutt et al. 2007; Bigiel et al. 2008; see also the left panels of Fig. 2.7 and Fig. 3.3), low surface brightness galaxies (e.g. Wyder et al., 2009), and dwarf galaxies (e.g. Bolatto et al., 2011; Roychowdhury et al., 2015). In these regions, the SFR surface density is very modest if compared to the values predicted by the local SK law and its correlation with the HI surface

density is extremely weak or absent (e.g. Ferguson et al. 1998; Bigiel et al. 2010; Bolatto et al. 2011; Schruba et al. 2011; Yim & van der Hulst 2016; see also the left panels of Fig. 2.9 and Fig. 3.4).

The third group of star formation laws is based on the molecular gas surface density, namely $\Sigma_{\text{SFR}} \propto \Sigma_{\text{H}_2}^N$ with $N \approx 0.6 - 1.4$ (e.g. Wong & Blitz 2002; Heyer et al. 2004; Kennicutt et al. 2007; Bigiel et al. 2008; Marasco et al. 2012; Leroy et al. 2013; Jiménez-Donaire et al. 2019; de los Reyes & Kennicutt 2019; Kumari et al. 2020; see also the left panels of Fig. 2.11 and Fig. 3.5). In particular, the emission lines of carbon-monoxide (CO) are typically used to trace the molecular gas distribution and, in order to derive the mass of the total molecular gas from the CO luminosity, it is necessary to estimate the CO-to-H₂ conversion factor (α_{CO}). Unfortunately, dwarf galaxies are unsuitable environments for this approach as, due to their low metallicity, the CO emission lines are usually not detectable or, if detected, they are faint and with low signal-to-noise ratio (see e.g. Tacconi & Young, 1987; Leroy et al., 2009; Bolatto et al., 2011; Schruba et al., 2012; Elmegreen et al., 2013; Cormier et al., 2017; Hunt et al., 2014, 2015; Hunter et al., 2019). In addition, different methods to estimate α_{CO} in dwarf galaxies yield discordant values (e.g. Bolatto et al., 2013; Hunt et al., 2015; Amorín et al., 2016; Madden & Cormier, 2019), hence it is not clear whether the low luminosity of CO lines represents an intrinsic deficiency of molecular gas or a lack of CO due to the low metallicity. Similarly to dwarf galaxies, the outskirts of spiral galaxies are low-metallicity regions where the emission of molecular gas tracers is not detected, but the formation of new stars is actually ongoing (e.g. Thilker et al., 2007a,b; Bigiel et al., 2010). Interestingly, some theoretical models show that, in conditions of extremely low metallicity, star formation can directly occur from atomic gas, without pre-existing molecular gas (e.g. Krumholz, 2012; Glover & Clark, 2012). Dwarf galaxies are therefore of primary interest in the study of star formation law in order to assess the existence of a unique relation valid for both the low-density and the high-density regions of galaxies.

While surface-based star formation laws are easily accessible to observations, it is important to ask if they are the manifestation in projection of a more fundamental star formation law based on volume densities such as the one originally proposed by Schmidt (1959). If the latter case is true, it is then possible that some of the variations observed among surface-based star formation laws can be explained as a consequence of varying disc thickness, which depends on the depth of the local gravitational potential (see also Elmegreen, 2015, 2018). In Chapters 2 and 3, we have shown the significance of the disc flaring and the importance of its effect on the observed gas distribution for a sample of ten spiral galaxies, two dwarf galaxies (with moderately-high mass), and the MW. In particular, we assumed that the gas disc is in hydrostatic equilibrium to derive the radial profile of its scale height. This latter was then adopted to convert the observed radial profiles of the gas and the SFR surface

densities to the corresponding volume densities, in order to obtain the volumetric star formation (VSF) law (see Abramova & Zasov 2008; Barnes et al. 2012; Yim et al. 2020 for either similar or different methodologies to derive volumetric relations). We found that the VSF law involving the total gas (HI+H₂) and the SFR volume densities is a power-law relation with index $\alpha \approx 2$, no break, and a smaller intrinsic scatter than the SK law. We also discovered a new correlation between the atomic gas and the SFR volume densities, which is steeper (index $\beta \approx 2.8$) than the VSF law but almost equally tight.

Gas discs in dwarf galaxies, given the shallow gravitational potential, are expected to be thick and significantly flaring in their outskirts (see also Roychowdhury et al., 2010; Banerjee et al., 2011; Iorio, 2018; Patra, 2020). Therefore, in order to measure the intrinsic gas distribution of a galaxy, it is mandatory to take into account the radial increase of its scale height. There is the compelling possibility that the inefficiency of these galaxies at forming stars may be physically explained as a natural consequence of an ‘underlying’ and fundamental VSF law subject to the projection effects due to the flaring. Moreover, extending the VSF law to the low-mass regime could allow us to answer key open questions: is the VSF law still valid in the low-density, low-metallicity, and HI-dominated environments? Is there a volume density threshold for star formation? What is the role of atomic gas in star formation?

This Chapter is organised as follows. Section 4.2 explains the main assumptions of our approach to derive the volume densities based on the hydrostatic equilibrium, describing also the adjustments required for dwarf galaxies. Section 4.3 focuses on the sample of dwarf galaxies analysed in this Chapter and the observations available in the literature. Section 4.4 presents the main results, which include the atomic gas scale heights and the VSF law for our sample. We discuss our findings in Sect. 4.5 and draw the conclusions in Sect. 4.6.

4.2 Method

In order to derive the volume densities, we adopted the same approach as in Chapter 2, which is based on the assumption of hydrostatic equilibrium for the gas disc. In this section, we recall the basic assumptions and equations involved; we also discuss the differences in the specific case of dwarf galaxies.

4.2.1 3D distribution of the gas in hydrostatic equilibrium

We modelled a given galaxy as a system which is symmetric with respect to both its rotation axis (i.e. axisymmetry) and to its midplane (i.e. $z = 0$). Hence, its gravitational potential is $\Phi = \Phi(R, z)$, where R is the galactocentric radius. We assumed that the gas (either atomic or molecular) is in vertical hydrostatic equilibrium in the galactic potential, meaning that the gas distribution is set

by the balance between the gas pressure, which tends to ‘inflate’ the gaseous disc, and the gravitational force which pulls the gas towards the midplane. The gas pressure is $P = \rho\sigma^2$, where ρ is the gas volume density and σ is the gas velocity dispersion. For simplicity, we assumed that the velocity dispersion is isotropic and the gas is vertically isothermal, thus $\sigma = \sigma(R)$. The vertical gas distribution is then (see e.g. § 4.6.2 in Cimatti, Fraternali, & Nipoti 2019)

$$\rho(R, z) = \rho(R, 0) \exp \left[-\frac{\Phi(R, z) - \Phi(R, 0)}{\sigma(R)^2} \right], \quad (4.1)$$

where $\rho(R, 0)$ and $\Phi(R, 0)$ are respectively the gas volume density and the total gravitational potential evaluated in the midplane. The gas scale height h is defined as the standard deviation of the distribution given by Eq. 4.1 and its radial profile can be calculated once σ and Φ are known.

By approximating Eq. 4.1 near the midplane and integrating along the vertical direction (e.g. Olling, 1995; Koyama & Ostriker, 2009), the radial profile of the volume density in the midplane can be obtained from the surface density $\Sigma(R)$ and the scale height given the relation $\Sigma(R) = \sqrt{2\pi}\rho(R, 0)h(R)$, which is valid for a Gaussian profile with standard deviation given by $h(R)$. This allows us to define the two quantities required to derive the VSF law. The first is the volume density of the total gas

$$\begin{aligned} \rho_{\text{gas}}(R, 0) &= \rho_{\text{HI}}(R, 0) + \rho_{\text{H}_2}(R, 0) \\ &= \frac{\Sigma_{\text{HI}}(R)}{\sqrt{2\pi}h_{\text{HI}}(R)} + \frac{\Sigma_{\text{H}_2}(R)}{\sqrt{2\pi}h_{\text{H}_2}(R)}, \end{aligned} \quad (4.2)$$

where Σ_{HI} and h_{HI} are the surface density and scale height of the atomic gas, and Σ_{H_2} and h_{H_2} are the same but for the molecular gas.¹ In the case of dwarf galaxies, where the atomic gas is likely the dominant gas component, Eq. 4.2 reduces to $\rho_{\text{gas}} \approx \rho_{\text{HI}}$. The second ingredient for the VSF law is the volume density of the SFR

$$\rho_{\text{SFR}}(R, 0) = \frac{\Sigma_{\text{SFR}}(R)}{\sqrt{2\pi}h_{\text{SFR}}(R)}, \quad (4.3)$$

where Σ_{SFR} and h_{SFR} are the SFR surface density and scale height, respectively. In Chapter 2, two possible definitions of h_{SFR} were explored, one constant (100 pc) with the galactocentric radius and the other obtained as the mean of the atomic and molecular gas scale heights weighted by their mass fractions

$$h_{\text{SFR}}(R) \equiv f_{\text{HI}}(R)h_{\text{HI}}(R) + f_{\text{H}_2}(R)h_{\text{H}_2}(R), \quad (4.4)$$

¹We use the notation ‘HI’ and ‘H₂’ to indicate the total atomic gas and the total molecular gas, meaning that the surface densities include, when needed, a multiplicative factor of 1.36 to account for the Helium fraction.

where $f_{\text{HI}} = \Sigma_{\text{HI}}/\Sigma_{\text{gas}}$ and $f_{\text{H}_2} = \Sigma_{\text{H}_2}/\Sigma_{\text{gas}}$. Eq. 4.4 is based on the idea that the SFR follows the same vertical distribution as the parent gas and gives a radially increasing profile (when the HI and the H₂ distributions flare with the galactocentric radius). In Chapter 3, we verified that assuming Eq. 4.4 is a better choice for the MW with respect to a constant scale height (e.g. Abramova & Zasov, 2008; Barnes et al., 2012; Sofue, 2017): $h_{\text{SFR}}(R)$ resulting from Eq. 4.4 is in excellent agreement with the scale height of the distributions of classical Cepheids and other tracers of recent star formation in our Galaxy. Indications of the flaring of the SFR vertical profile were also found by other authors using mid-infrared observations (i.e. dust-obscured star formation) of nearby galaxies seen at very high inclination angles (e.g. Yim et al., 2020; Elmegreen & Elmegreen, 2020). We note that, under the assumption that dwarf galaxies are HI-dominated, Eq. 4.4 leads to $h_{\text{SFR}}(R) = h_{\text{HI}}(R)$.

4.2.2 The mass distribution of star-forming dwarf galaxies

The total mass distribution of a star-forming galaxy typically includes the dark matter (DM) halo, the stellar disc, and the gaseous components (i.e. atomic gas and molecular gas). Dwarf galaxies differ from spiral ones in three important aspects. First, the DM halo is the dominant mass component at all radii and the shape of the rotation curve indicates that the DM density profile has a core in the centre (e.g. de Blok & Bosma 2002; Oh et al. 2011; but see also e.g. van den Bosch & Swaters 2001; Swaters et al. 2003 for a different perspective). We therefore chose the DM halo model proposed by Read et al. (2016a,b), which is a Navarro-Frenk-White (NFW; Navarro et al., 1996) profile with a central core (hereafter core-NFW, see Sect. 4.2.2 for details). The second difference between dwarf and spiral galaxies is related to the fact that CO emission is very faint or absent in low-metallicity gas, hence the amount of molecular gas in dwarf galaxies is very uncertain (e.g. Schrubba et al., 2012; Bolatto et al., 2013; Madden & Cormier, 2019). There are indications that the mass fraction of molecular gas is indeed very low compared to the HI mass in dwarf galaxies ($\lesssim 20 - 40\%$ Hunt et al., 2015; Hunter et al., 2019) and that, even in the extreme case of starbursting dwarfs, the H₂ contribution to the potential (traced by the rotation curve) should not exceed that of the stellar disc (e.g. Lelli et al., 2012, 2014a). Hence, we did not include the molecular gas distribution in the gravitational potential of the dwarf galaxies in this study. In Sect. 4.5.1, we discuss the possible impact on the volume density estimate due to the presence of a fixed fraction of molecular gas. The third difference with respect to spiral galaxies is that the contribution of the gas (HI) self-gravity to the gravitational potential of dwarf galaxies is comparable to or higher than that of the stellar disc. Therefore, if the gas self-gravity is neglected, the resulting gas scale height is overestimated (see Fig. 2.A.1). Crucially, as done in Chapters 2 and 3, the gas scale height was calculated numerically using an iterative algorithm which accounts for the

gas self-gravity, thus deriving the gas distribution in a self-consistent way (see Sect. 4.4.1).

The mass components of our dwarf galaxies are based on Read et al. (2017), who included the core-NFW DM halo, the stellar disc, and the atomic gas disc. In the following, we describe in detail the density profiles of these components, which depend on a set of free parameters. In particular, Read et al. (2017) derived these parameters through the decomposition of the HI rotation curves from Iorio et al. (2017). We note that the mass models used in Chapter 2 were obtained with the same technique.

The dark matter halo

As mentioned above, the DM density distribution is modelled using the NFW profile modified to account for a central core (i.e. core-NFW) from Read et al. (2016a,b). This core-NFW profile was obtained using high-resolution numerical simulations of dwarf galaxies with different halo masses evolving in isolation for 14 Gyr. Initially, these galaxies have a DM halo with a cusped NFW profile and the cosmological baryon fraction. Then, stellar feedback ‘heats’ the DM by injecting energy and momentum through supernovae, stellar winds, and radiation pressure, and the cusped profile is gradually transformed into a cored one (see also Read & Gilmore, 2005; Pontzen & Governato, 2014).² The galaxies resulting from these simulations share similar properties with observed galaxies (i.e. stellar light profile, star formation history, metallicity distribution, gas kinematics) and the density profile of their DM halo is well described by

$$\rho_{\text{cNFW}}(r) = f^n \rho_{\text{NFW}} + \frac{nf^{n-1}(1-f^2)}{4\pi r^2 r_c} M_{\text{NFW}}, \quad (4.5)$$

where r is the spherical radius ($r = \sqrt{R^2 + z^2}$ in cylindrical coordinates), ρ_{NFW} and M_{NFW} are respectively the standard NFW halo density and mass profile (Navarro et al., 1996), r_c is the core radius, and f is a function that regulates the shape and the extent of the core, defined as

$$f = \tanh\left(\frac{r}{r_c}\right), \quad (4.6)$$

while $0 < n \leq 1$ ($n = 0$ corresponds to no core). The parameter n is given by

$$n = \tanh\left(\kappa \frac{t_{\text{SF}}}{t_{\text{dyn}}}\right), \quad (4.7)$$

²For the aim of this Chapter, the exact mechanism which formed the core of the DM halo can be considered irrelevant, as the key point is adopting a functional form for the DM density distribution which can reproduce the observed rotation curve of the dwarf galaxies. Cored DM profiles are obtained also with other mechanisms, such as dynamical friction heating from gas clumps (e.g. Nipoti & Binney, 2015).

where

$$t_{\text{dyn}} = 2\pi \sqrt{\frac{r_s^3}{GM_{\text{NFW}}(r_s)}} \quad (4.8)$$

is the orbital time at the scale radius r_s of the NFW profile, $t_{\text{SF}} = 14$ Gyr is the total star formation time, and $\kappa = 0.04$. Read et al. (2017) obtained $r_c = 2.94R_\star$ with R_\star being the stellar disc scale length.

Disc components

The stellar disc mass distribution is modelled with an exponential radial profile and a sech^2 vertical profile (van der Kruit & Searle, 1981b),

$$\rho_\star(R, z) = \rho_{\star,0} \exp\left(-\frac{R}{R_\star}\right) \text{sech}^2\left(\frac{z}{z_\star}\right), \quad (4.9)$$

where $\rho_{\star,0} = \Sigma_{\star,0}/(2z_\star)$ is the central density, R_\star is the stellar scale length, and z_\star the scale height, which is assumed to be equal to $R_\star/5$ (see van der Kruit & Freeman 2011 and references therein).

We modelled the atomic gas disc using a combination of a fourth-order polynomial and an exponential function

$$\Sigma_{\text{HI}}(R) = \Sigma_{\text{HI},0} \left(1 + C_1 R + C_2 R^2 + C_3 R^3 + C_4 R^4\right) \exp\left(-\frac{R}{R_\Sigma}\right), \quad (4.10)$$

where $\Sigma_{\text{HI},0}$ is the central surface density, R_Σ is the scale radius, and C_i are the polynomial coefficients. We choose Eq. 4.10 as it is flexible and can easily model the variety of observed profiles of $\Sigma_{\text{HI}}(R)$ (see Sect. 4.3.1). The HI distribution modelled using this functional form also serves to improve the efficiency of the numerical computation of HI gravitational potential and scale height (see Sect. 4.4.1).

4.2.3 The gas velocity dispersion

The radial profile of the velocity dispersion $\sigma_{\text{HI}}(R)$ is modelled by an exponential function

$$\sigma_{\text{HI}}(R) = \sigma_{\text{HI},0} \exp\left(-\frac{R}{R_\sigma}\right), \quad (4.11)$$

where $\sigma_{\text{HI},0}$ is the velocity dispersion at the galaxy centre and R_σ is a scale radius. This functional form can satisfactorily model the shape of the radial profile of the HI velocity dispersion typically observed in nearby galaxies, including a linear decline or a constant value (Boomsma et al. 2008; Tamburro et al. 2009; Marasco et al. 2017; Iorio et al. 2017; Chapter 2). As in the case of Σ_{HI} , the use of an analytic $\sigma_{\text{HI}}(R)$ is purely for the sake of improving the computational speed of the numerical integration to derive Φ and h_{HI} .

4.3 Sample description

We selected a sample of dwarf galaxies with the following information available in the literature: *i*) robust HI kinematics (i.e. velocity dispersion and rotation curve); *ii*) parametric mass models of the mass distribution (see Sect. 4.2.2); *iii*) azimuthally averaged radial profiles of HI and SFR surface densities. A sub-sample of ten galaxies from the ‘Local Irregulars That Trace Luminosity Extremes, The HI Nearby Galaxy Survey’ (LITTLE THINGS; Hunter et al., 2012) fulfills these requirements, as we explain in the following.

4.3.1 Atomic gas kinematics and surface density

Iorio et al. (2017) analysed the HI kinematics for 17 LITTLE THINGS galaxies using the software ^{3D}BAROLO³ (Di Teodoro & Fraternali, 2015). This software performs a tilted-ring model fitting using the emission-line data cube of a galaxy and derives the geometric parameters (e.g. inclination, position angle, kinematic centre) and the kinematics (e.g. rotation curve, velocity dispersion, systemic velocity) of the gas disc. In addition, Iorio et al. (2017) included a robust estimate for the asymmetric drift correction to the gas circular speed. This correction is fundamental in the case of dwarf galaxies, where pressure support can be significant. We excluded the galaxies with disturbed HI kinematics (i.e. NGC 1569) and those with either asymmetric drift-dominated or very uncertain rotation curves (i.e. CVnIdwA, DDO 53, DDO 210, DDO 216, UGC 8508). In addition, DDO 154 was removed from the sample as it was studied already in Chapter 2. We thus obtained a sample of ten star-forming dwarf galaxies, whose main properties are reported in Table 4.1.

As already mentioned, the rotation curves of the dwarf galaxies in Iorio et al. (2017) were used by Read et al. (2017) to obtain the mass models, which include the core-NFW DM halo described in Sect. 4.2.2, a stellar disc, and an atomic gas disc. Both disc components were assumed razor-thin and with an exponentially declining radial profile, hence we substituted these models with those described in Sect. 4.2.2. We used the same stellar mass and scale length as Read et al. (2017), which are reported in Table 4.1 together with the parameters for the DM halo model. For the atomic gas disc, we derived $\Sigma_{\text{HI},0}$, C_i , and R_{HI} by fitting Eq. 4.10 to the observed surface density of HI from Iorio et al. (2017). The left panel in Fig. 4.1 shows the azimuthally averaged radial profile of the atomic gas surface density for WLM from Iorio et al. (2017), and the polynomial best-fit model (dot-dashed black curve). In Appendix 4.A, we show $\Sigma_{\text{HI}}(R)$ and the polynomial fits for the rest of the sample. We note that the profiles typically differ from an exponential and have diverse shapes. We verified that the updated atomic gas radial profile and stellar scale height do not imply significant variations in the resulting circular velocity generated by

³<http://editeodoro.github.io/Bbarolo/>

Table 4.1 – Properties of the sample galaxies (see Iorio et al. 2017 for details): (1) distance; (2) integrated SFR from FUV (see Sect. 4.3.2); (3) mean circular velocity (i.e. asymmetric-drift corrected) of the outer HI disc; (4) HI disc inclination; (5) HI disc position angle. Parameters of the best-fit model for the core-NFW halo and the stellar disc from Read et al. (2017): (6) DM mass within R_{200} ; (7) DM halo concentration; (8) index of the DM halo core function; (9) stellar mass; (10) stellar disc scale length.

Galaxy	D (Mpc)	log(SFR) ($M_{\odot}\text{yr}^{-1}$)	$\langle V_c \rangle$ (km s^{-1})	$\langle i \rangle$ ($^{\circ}$)	$\langle \text{P.A.} \rangle$ ($^{\circ}$)	M_{200} ($10^{10} M_{\odot}$)	c	n	M_{\star} ($10^7 M_{\odot}$)	R_{\star} (kpc)
	(1)	(2)	(3)	(4)	(5)	(6)	(7)	(8)	(9)	(10)
WLM	1.0	-2.13 ± 0.08	38.7 ± 3.4	74.0 ± 2.3	174.0 ± 3.1	$0.8^{+0.2}_{-0.2}$	17	0.887	1.62	0.75
DDO 52	10.3	-1.82 ± 0.08	51.1 ± 6.3	55.1 ± 2.9	6.5 ± 2.0	$1.20^{+0.29}_{-0.27}$	17.3	0.894	5.27	0.94
DDO 87	7.4	-1.95 ± 0.07	50.3 ± 9.1	42.7 ± 7.3	238.6 ± 4.7	$1.13^{+0.27}_{-0.25}$	17.6	0.900	3.3	1.13
NGC 2366	3.4	-0.97 ± 0.07	57.7 ± 5.4	65.1 ± 4.2	39.8 ± 2.8	$2.40^{+0.59}_{-0.54}$	17.3	0.894	6.95	1.54
DDO 126	4.9	-1.80 ± 0.06	38.6 ± 3.1	62.2 ± 2.9	140.7 ± 3.5	$0.6^{+0.2}_{-0.1}$	20.6	0.947	1.61	0.82
DDO 168	4.3	-1.67 ± 0.06	56.2 ± 6.9	62.0 ± 2.6	272.7 ± 4.2	$2.10^{+0.52}_{-0.48}$	16.8	0.883	5.9	0.82
DDO 133	3.5	-1.91 ± 0.05	47.2 ± 5.1	38.9 ± 3.7	-3.8 ± 8.9	$1.60^{+1.10}_{-0.44}$	25.8	0.984	3.04	0.804
DDO 50	3.4	-0.95 ± 0.04	38.7 ± 10.1	33.1 ± 4.6	174.9 ± 5.9	$0.32^{+0.16}_{-0.08}$	26.2	0.985	10.72	0.89
DDO 47	5.2	-1.61 ± 0.04	62.6 ± 5.2	37.4 ± 1.7	317.4 ± 7.3	$4.4^{+3.2}_{-1.9}$	20.5	0.946	9.4	0.7
DDO 101	6.4	-2.45 ± 0.09	52.9 ± 3.6	52.4 ± 1.7	287.4 ± 3.6	$5.2^{+0.6}_{-0.4}$	28.9	0.993	6.54	0.58

the total mass distribution of our galaxies, as a consequence of these systems being largely dark-matter dominated.

We used the radial profiles of the HI velocity dispersion derived by Iorio et al. (2017) to fit Eq. 4.11 and obtain the model for $\sigma_{\text{HI}}(R)$. We recall that this step aims to improve the computational speed in the iterative calculation of the scale height, but it does not influence the resulting $h_{\text{HI}}(R)$. The central panel in Fig. 4.1 shows, for WLM, the observed velocity dispersion of HI (red diamonds) and the best-fit exponential profile (black solid curve). The dashed black curves are the fits to $\sigma_{\text{HI}} \pm \Delta\sigma_{\text{HI}}$, where $\Delta\sigma_{\text{HI}}$ is the uncertainty, and were used to obtain the uncertainties on the atomic gas scale height (see Sect. 4.4.1). Figure 4.A.1 shows the profiles for the other galaxies in the sample. We note that the velocity dispersion is approximately constant for some galaxies (e.g. WLM, DDO 47), but in general $\sigma_{\text{HI}}(R)$ declines with increasing galactocentric radius.

4.3.2 Star formation rate surface density

In order to derive the SFR surface density for our galaxies, we used the azimuthally averaged surface photometry from Zhang et al. (2012), based on far-ultraviolet (FUV) and near-ultraviolet (NUV) images obtained with the Galaxy Evolution Explorer (GALEX, Martin et al., 2005). We calculated the FUV magnitude per square arcsecond as $\mu_{\text{FUV}} = \mu_{\text{NUV}} + (\text{FUV} - \text{NUV})$, where μ_{NUV} is the NUV AB absolute magnitude per square arcsecond and $(\text{FUV} - \text{NUV})$ is the FUV-NUV color corrected assuming Cardelli et al. (1989) dust extinction law (see Zhang et al. 2012 for details).⁴ The corresponding FUV surface brightness is

$$F_{\nu}(\text{FUV}) = 10^{-0.4\left[\left(\frac{\mu_{\text{FUV}}}{\text{mag arcsec}^{-2}}\right) + 48.6\right]} \text{erg s}^{-1} \text{cm}^{-2} \text{Hz}^{-1} \text{arcsec}^{-2}. \quad (4.12)$$

In order to estimate the SFR surface density from the FUV surface brightness, we adopted the calibration of the SFR-FUV relation by McQuinn et al. (2015). This calibration is ideally suitable for our study, as it was obtained for a sample of nearby dwarf galaxies taking into account their low metallicity and a stochastically populated initial mass function (IMF). These authors derived the SFR from resolved stellar populations by fitting the color-magnitude diagrams (CMDs) with synthetic stellar populations generated from stellar evolution libraries and used this SFR to calibrate the SFR-FUV relation. We adapted McQuinn et al. (2015)'s relation from a Salpeter IMF to a Kroupa IMF by including a multiplicative factor of 0.67 (Kennicutt & Evans, 2012; Madau & Dickinson, 2014). This correction was applied for consistency with Chapter 2, where the SFR surface densities were based on a Kroupa IMF (see Leroy et al.,

⁴We note that the dust extinction correction is typically minimal for our dwarf galaxies (see Hunter et al., 2010; Zhang et al., 2012).

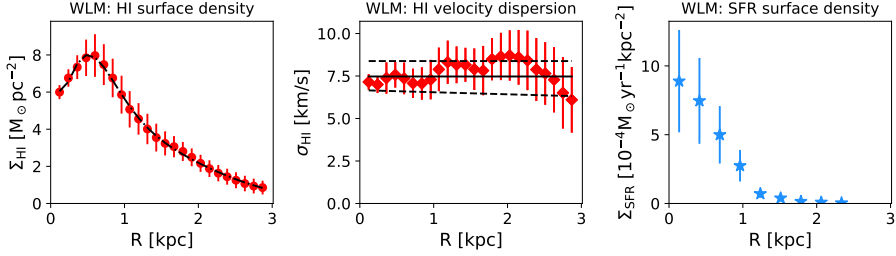


Figure 4.1 – Azimuthally averaged radial profiles of the atomic gas surface density (left panel) and the HI velocity dispersion (central panel) from Iorio et al. (2017), and of the SFR surface density (right panel) from FUV photometry (Zhang et al., 2012) for WLM. The dot-dashed black curve in the left panel is the best-fit polynomial function (Eq. 4.10) used to model the gas radial distribution. The solid and the dashed black lines in the central panel are the best-fit functions (Eq. 4.11) used to model, respectively, the velocity dispersion and its upper and lower limits, which were adopted to derive the scale height and its uncertainty.

2008). This gives the following relation between the FUV luminosity $L_\nu(\text{FUV})$ and the SFR

$$\text{SFR} = (1.37 \pm 0.54) \times 10^{-28} \left[\frac{L_\nu(\text{FUV})}{\text{erg s}^{-1} \text{Hz}^{-1}} \right] \text{M}_\odot \text{yr}^{-1}. \quad (4.13)$$

As pointed out by McQuinn et al. (2015), Eq. 4.13 yields, for the same FUV luminosity, values of SFR that are about 50–70% higher than other calibrations in the literature derived for galaxies with higher mass and metallicity than dwarf galaxies (e.g. Hao et al., 2011; Salim et al., 2007). The SFR surface density can be obtained by combining Eq. 4.12 and Eq. 4.13

$$\Sigma_{\text{SFR}} = \cos i \times 10^{-0.4 \left(\frac{\mu_{\text{FUV}}}{\text{mag arcsec}^{-2}} \right) + 7.415} \text{M}_\odot \text{yr}^{-1} \text{kpc}^{-2}, \quad (4.14)$$

where the $\cos i$ term corrects for the galaxy inclination (see Table 4.1).⁵ The uncertainty on Σ_{SFR} was calculated through error propagation in order to take into account the uncertainties on μ_{NUV} , the FUV-NUV color, i and the calibration constant in Eq. 4.13. The right panel of Fig. 4.1 shows the radial profile of the SFR surface density for WLM resulting from Eq. 4.13, while the profiles for the rest of the galaxies in our sample are shown in Fig. 4.A.1. In Table 4.1, we report the SFR integrated over the whole star-forming disc of our galaxies.

We note that the SFR surface densities adopted in Chapter 2 were taken from Leroy et al. (2008), who used a combination of FUV and $24 \mu\text{m}$ luminosities in

⁵Despite the different calibration assumed in this Chapter, the SFR surface density given by Eq. 4.14 approximately corresponds to the one reported in Elmegreen & Hunter (2015) and obtained with the SFR-FUV relation adopted in Hunter et al. (2010), which assumes a Salpeter IMF.

order to take into account the emission from massive and young stars absorbed by dust and re-radiated at the mid-infrared wavelengths. To convert these luminosities to Σ_{SFR} , these authors assumed a relation obtained for normal star-forming galaxies, which may not be applicable to dwarf galaxies (Hao et al., 2011). However, in Sect. 4.5.2, we explore the effect of using Leroy et al. (2008) prescription to derive the SFR surface density for our sample of galaxies. We anticipate that our results are not significantly affected if we use this correction.

4.4 Results

In this section, we present our findings by focusing first on the scale height of the atomic gas discs of our sample of galaxies and then on the VSF law.

4.4.1 The scale height

We derived the HI scale height using the Python module GALPYNAMICS⁶ (see Iorio, 2018). This code calculates the gravitational potential generated by one or more mass components described by a parametric model through numerical integration, allowing to derive useful quantities, such as the rotation curve and the scale height of a gaseous mass component. GALPYNAMICS is based on the assumption of vertical hydrostatic equilibrium and includes an iterative algorithm which accounts for the gas self-gravity. A detailed explanation of how this code operates is provided in Sect. 2.4. In the case of our dwarf galaxies, the mass components and their parameters are described in Sect. 4.2.2 and Table 4.1, respectively. We recall that the HI velocity dispersion and surface density are modelled using the observations described in Sect. 4.3.1.

Figure 4.2 shows the scale height of the atomic gas distribution as a function of the galactocentric radius for the galaxies in our sample. Despite the relatively small size of the discs (3-4 kpc on average), the scale heights significantly increase with the distance from the galactic centre, reaching a few hundreds of parsec at the outermost radii. The gas distribution flares of a factor ranging from a minimum of $\approx 1.1 - 1.6$ (but with large uncertainty) for DDO 101 and DDO 87 to a maximum of $\approx 4 - 4.5$ (e.g. DDO 52, DDO 47). The red band represents the uncertainty on the scale height and the lower and the upper limits on h_{HI} were calculated taking into account the uncertainties on the HI velocity dispersion (see Sect. 4.3.1), as done in Chapter 2. We have verified that the uncertainties on the DM halo masses and concentrations reported by Read et al. (2017) correspond to at most $\approx 5\%$ uncertainty on our scale height estimates, confirming the gas velocity dispersion as the main source of uncertainty in our modelling.

⁶<https://github.com/iogiul/galpynamics>

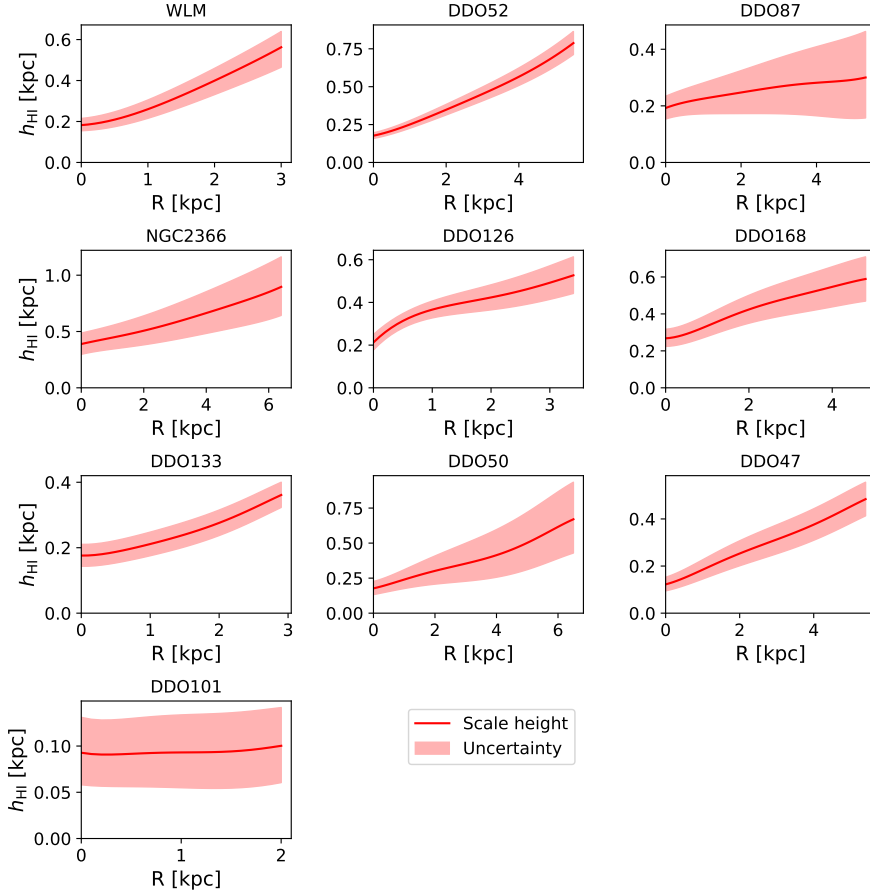


Figure 4.2 – Radial profiles of the atomic gas scale height derived under the assumption of the vertical hydrostatic equilibrium (red curve). The red area shows the uncertainty on $h_{\text{HI}}(R)$ (see text).

4.4.2 The volumetric star formation law

In order to assess the validity of the volumetric relations obtained in Chapter 2, we derived the volume densities for our sample of dwarf galaxies through Eq. 4.2 and Eq. 4.3, using the HI scale heights calculated in Sect. 4.4.1 and the surface density profiles described in Sect. 4.3.1 and Sect. 4.3.2. We recall that the sample of spiral galaxies studied in Chapter 2 has a significant fraction of molecular gas, which is typically dominant in the innermost regions (i.e. $f_{\text{H}_2} \approx 1$) but essentially negligible at larger radii. In the outskirts, the total gas volume density is dominated by the atomic gas volume density and $f_{\text{HI}} \gg f_{\text{H}_2}$. Accordingly, Eq. 4.4 results in $h_{\text{SFR}}(R)$ which is very similar or close to h_{H_2}

near the galactic centre and gradually turns into h_{HI} with increasing radius (see Fig. 2.4). In Chapter 3, the scale height of the distribution of classical Cepheids was used to calculate the SFR volume density in the MW. In addition, it was verified that the scale height of recent star formation tracers (e.g. classical Cepheids, OB stars) is very similar to that of the gas in hydrostatic equilibrium at all radii out to $R \approx 20$ kpc, indicating that our prescription for h_{SFR} (i.e. Eq. 4.4) works remarkably well in our Galaxy. In the case of dwarf galaxies, the atomic gas is likely the dominant gaseous component, therefore we chose to assume $f_{\text{H}_2} \approx 0$ as a fiducial case of study, which implies that Eq. 4.2 and Eq. 4.4 respectively reduce to $\rho_{\text{gas}} = \rho_{\text{HI}}$ and $h_{\text{SFR}} = h_{\text{HI}}$. We explore the effect of including a fraction of molecular gas in Sect. 4.5.1.

Dwarf galaxies share similarities with the outskirts of spiral galaxies, as both these environments are metal poor and HI-dominated. Hence, we extended the analysis on the galaxy sample of Chapter 2 by including also the regions beyond the stellar disc (i.e. $R > R_{25}$) where the SFR surface density is observed. We adopted the Σ_{SFR} from Bigiel et al. (2010), who used the same GALEX FUV maps and SFR-FUV relation as Leroy et al. (2008) but measured of the SFR surface density up to larger radii. The atomic gas surface density and scale height of the outermost star-forming regions are the same as those used in Chapter 5. In particular, Σ_{HI} was obtained from 21-cm data cubes using ^{3D}BAROLO and h_{HI} was derived with the same method based on the hydrostatic equilibrium as done in Chapter 2 (see also Sect. 4.4.1). This allowed us to study the VSF law up to larger radii with respect to Chapter 2: we could extend the profiles by ~ 1 kpc for 5 galaxies (DDO 154, IC 2574, NGC 0925, NGC 4736, and NGC 7793), while for NGC 2403 and NGC 3198 we increased the radial coverage by ≈ 5 kpc and ≈ 10 kpc, respectively.

In the following, we verify whether the correlations obtained in Chapter 2, namely the VSF law between the total gas and the SFR volume densities and the relation including the atomic gas only, are valid for the new sample of dwarf galaxies and the outermost star-forming regions of the galaxies in Chapter 2.

The VSF law with total gas

The gas and the SFR surface densities of our sample of dwarf galaxies are shown in the left panel of Fig. 4.3 (colored diamonds). The light blue circles represent the 12 galaxies examined in Chapter 2 and the yellow stars correspond to the MW (Chapter 3). The colored diamonds indicate the new sample of dwarf galaxies and the green ‘x’ correspond to the outermost star-forming regions of seven galaxies from the sample studied Chapter 2, as explained in the previous section. We can see that both dwarf and spiral galaxies detach from the SK law for $\Sigma_{\text{gas}} \lesssim 10 M_{\odot}\text{pc}^{-2}$. This behaviour in the low-density regime is widely reported in the literature and increases the scatter in the correlation (e.g. Kennicutt et al., 2007; Bigiel et al., 2008; Bolatto et al., 2011; Dessauges-Zavadsky et al., 2014; de los Reyes & Kennicutt, 2019). We note that the

relation shown in Fig. 4.3 is the ‘global’ SK law (de los Reyes & Kennicutt, 2019), hence a small shift (mostly in normalisation) with respect to the spatially resolved surface densities is expected (e.g. Kennicutt et al., 2007). However, this shift does not seem sufficient to describe both the regimes of dwarf and spiral galaxies, which appear to loosely follow a broken power-law with $N \approx 1.4$ in the high-density regions and $N \approx 3$ at low densities (see also Gatto et al., 2013).

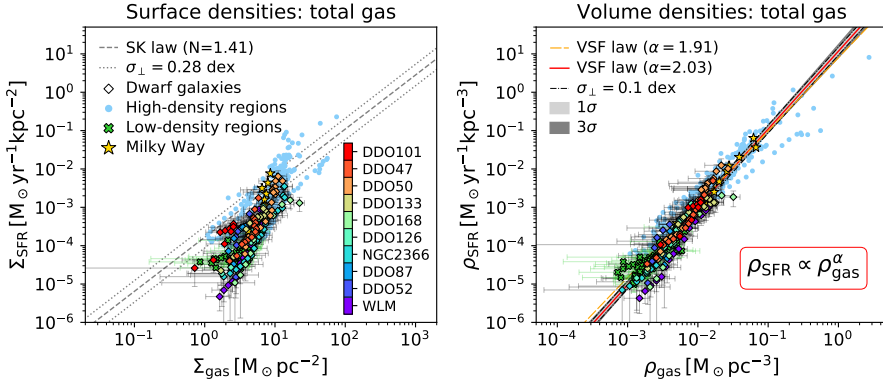


Figure 4.3 – Star formation laws based on the surface densities (left) and the volume densities (right) of the total gas and the SFR for the sample of ten dwarf galaxies studied in this Chapter (diamonds). Each color indicates the azimuthally averaged radial profile of a different galaxy according to the color-bar. The light blue points and the green crosses respectively indicate the star-forming regions within and beyond the optical radius for the sample of 12 galaxies of Chapter 2, while the yellow stars are for the MW (Chapter 3). In the left panel, the grey dashed line is the SK law from de los Reyes & Kennicutt (2019) with its intrinsic scatter (grey dotted lines). In the right panel, the long-dashed orange line shows the VSF law from Chapter 2 and the red solid line is the best-fit obtained in this work. The black dot-dashed line displays the orthogonal intrinsic scatter of the new best-fit, while the grey areas indicates the 1σ and 3σ uncertainties on the fit. The VSF law has a smaller scatter than the SK law and it is a power-law with index $\alpha \approx 2$, showing no indication for a break over a wide range of densities.

The right panel of Fig. 4.3 shows the volume densities for the various samples using the same symbols as in the left panel. The dwarf galaxies follow remarkably well the VSF law found in Chapter 2 (orange long-dashed line), extending the validity of the relation to the low-density regime down to $\rho_{\text{gas}} \sim 10^{-3} M_{\odot} \text{pc}^{-3}$. Also the range of SFR volume densities is extended downward by one order of magnitude. In Chapter 2, we obtained that the VSF law between the SFR and the total gas volume densities is described by

$$\log \left(\frac{\rho_{\text{SFR}}}{M_{\odot} \text{yr}^{-1} \text{kpc}^{-3}} \right) = \alpha \log \left(\frac{\rho_{\text{gas}}}{M_{\odot} \text{pc}^{-3}} \right) + \log A, \quad (4.15)$$

with best-fit slope $\alpha = 1.91 \pm 0.03$, normalisation $\log A = 0.90 \pm 0.02$, and perpendicular scatter $\sigma_{\perp} = 0.12 \pm 0.01$ dex. We repeated the fit including

also the sample of dwarf galaxies and the outermost star-forming regions of the sample of Chapter 2, finding $\alpha = 2.03 \pm 0.03$, $\log A = 1.10 \pm 0.01$, and $\sigma_{\perp} = 0.10 \pm 0.01$ dex. This confirms that the relation between the total gas and the SFR volume densities is $\rho_{\text{SFR}} \propto \rho_{\text{gas}}^{\alpha}$ with $\alpha \approx 2$. We note that the best-fit VSF law obtained in this Chapter and that derived in Chapter 2 are compatible within $\lesssim 2\sigma$ (see the left panel in Fig. 4.3 and the right panel in Fig. 2.8).

From a thorough inspection of Fig. 4.3, we can see that a few points belonging to three galaxies, DDO 87, DDO 168 and WLM, seem slightly detached from the VSF law. We note that DDO 168 and DDO 87 are actually compatible within the errors with the best-fit relation. The data points of WLM, instead, appear to be slightly more than 3σ from the relation (see grey band in Fig. 4.3), also in light of their relatively small error-bar. It is unlikely that this difference is entirely due to inaccuracies in the determination of ρ_{gas} as the scale height, the surface density, and their uncertainties are quite robust. The profile of the SFR surface density also seems reliable, as it is similar to other estimates in the literature obtained from FUV emission (e.g. Mondal et al., 2018). Our Σ_{SFR} does not take into account the possible contribution of dust-obscured star formation, which is instead included in Leroy et al. (2008) profiles. The effect of including the dust-obscured star formation is discussed in detail in Sect. 4.5.2, but we anticipate that the global SFR of WLM is increased of about 15% by using the same method as Leroy et al. (2008), reducing of a factor of ≈ 2 the gap with the VSF law.

Relation with the atomic gas only

Since the HI is the dominant gas component of dwarf galaxies and a large part of the disc of spiral galaxies, investigating the link between the atomic gas and the SFR is of primary interest. The left panel of Fig. 4.4 shows that the new sample exhibits the same behaviour as both the low-density and the high-density regions of the more massive galaxies: there is no correlation between the atomic gas and the SFR surface densities or, if present, it is very weak and with a large scatter (see also e.g. Ferguson et al., 1998; Bigiel et al., 2010; Bolatto et al., 2011; Schruba et al., 2011).

The right panel of Fig. 4.4 shows instead the correlation between the atomic gas and the SFR volume densities. The dwarf galaxies follow the same relation between the HI and the SFR volume densities found in Chapter 2

$$\log \left(\frac{\rho_{\text{SFR}}}{\text{M}_{\odot} \text{yr}^{-1} \text{kpc}^{-3}} \right) = \beta \log \left(\frac{\rho_{\text{HI}}}{\text{M}_{\odot} \text{pc}^{-3}} \right) + \log B, \quad (4.16)$$

with $\beta = 2.79 \pm 0.08$, normalisation $\log B = 2.89_{-0.02}^{+0.03}$, and intrinsic scatter $\sigma_{\perp} = 0.12 \pm 0.01$ dex. We indeed repeated the fit of Eq. 4.16 including also the points of the dwarf galaxies and the low-density regions, finding that the parameters of the new best-fit are compatible within the errors with those reported in

Chapter 2 (see Table 4.2). This extends the validity range of the HI-VSF law by about one order of magnitude.

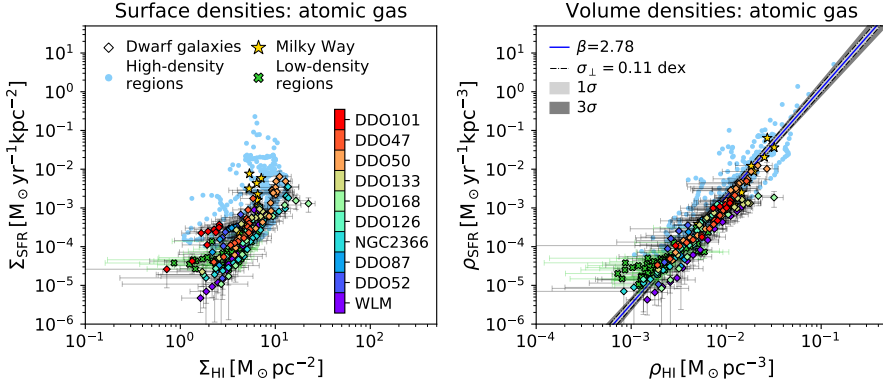


Figure 4.4 – Same as Fig. 4.3, but here the abscissae of the light blue points are the surface density (left) and volume density (right) of the atomic gas only, and the SFR scale height is the same as the atomic gas distribution (see text). The blue line shows the best-fit scatter of Eq. 4.16 obtained in this Chapter.

Table 4.2 – Best-fit parameters of the VSF law with the total gas (Eq. 4.15) and the relation with the atomic gas only (Eq. 4.16). The first and second columns report the gas phases involved and the reference Chapter, respectively. The other columns provide the slope, the orthogonal intrinsic scatter σ_{\perp} , and the y -intercept with their uncertainties.

Gas	Ref.	Slope	σ_{\perp} (dex)	y -intercept (dex)
HI+H ₂	Chapter 2	$1.91^{+0.03}_{-0.03}$	$0.12^{+0.01}_{-0.01}$	$0.90^{+0.02}_{-0.02}$
HI+H ₂	This Chapter	$2.03^{+0.03}_{-0.03}$	$0.10^{+0.01}_{-0.01}$	$1.10^{+0.01}_{-0.01}$
HI	Chapter 2	$2.79^{+0.08}_{-0.08}$	$0.13^{+0.01}_{-0.01}$	$2.89^{+0.03}_{-0.02}$
HI	This Chapter	$2.78^{+0.06}_{-0.05}$	$0.11^{+0.01}_{-0.01}$	$2.87^{+0.02}_{-0.02}$

4.5 Discussion

Remarkably, our new sample of dwarf galaxies follow the same relation as galaxies with higher masses and gas densities, suggesting the VSF law might be the general star formation law for nearby star-forming disc galaxies. In this section, we first quantify the impact of possible systematic effects on this

result due to *i*) the molecular gas content, *ii*) the fraction of dust-obscured star formation, and *iii*) the assumption of hydrostatic equilibrium. We also compare our results with other studies in the literature and, finally, we attempt some physical interpretation of our findings in order to obtain constraints on the mechanisms that may be relevant for star formation.

4.5.1 Systematic effects due to the molecular gas content

As mentioned earlier, CO emission lines in dwarf galaxies are faint or absent (e.g. Tacconi & Young, 1987; Leroy et al., 2009; Bolatto et al., 2011; Schruba et al., 2012; Cormier et al., 2014; Hunt et al., 2015; Cormier et al., 2017), but it is still unclear if this is due to the actual lack of molecular gas or simply to the low metallicity of this type of galaxies. Moreover, it is expected that some part of the molecular gas reservoir is not associated with CO in dwarf galaxies (the so-called ‘CO-dark’ gas; e.g. Wolfire et al., 2010). This is usually ascribed to a combination of efficient photo-dissociation of molecular clouds by the deeply penetrating UV radiation field from stellar clusters and the porosity of the ISM structure. As a consequence, CO is present only in small cores of molecular clouds, while it is photo-dissociated on larger spatial scales (see e.g. Cormier et al., 2015; Madden & Cormier, 2019, and references therein). Instead, H₂ can efficiently self-shield from radiation, meaning that a significant amount of the molecular gas reservoir can exist outside CO-emitting regions. It is therefore interesting to investigate whether this molecular gas could significantly affect the VSF law shown in Fig. 4.3.

In our methodology, the fraction of molecular gas impacts both the gas and the SFR volume densities of dwarf galaxies. Given our definition of the molecular gas fraction, $f_{\text{H}_2} = \Sigma_{\text{H}_2}/\Sigma_{\text{gas}}$, in Eq. 4.2 we have $\Sigma_{\text{H}_2} = f_{\text{H}_2}/(1 - f_{\text{H}_2})\Sigma_{\text{HI}}$ and, using the approximation $h_{\text{H}_2} \approx h_{\text{HI}}/2$ (see Chapter 2 and Appendix 5.A), we obtain that the gas volume density increases as $\rho_{\text{gas}} = (1 + f_{\text{H}_2})/(1 - f_{\text{H}_2})\rho_{\text{HI}}$. From Eq. 4.4, we infer that the SFR scale height is $h_{\text{SFR}} = h_{\text{HI}}(2 - f_{\text{H}_2})/2$. Hence, the SFR volume density (Eq. 4.3) increases of a factor of $2/(2 - f_{\text{H}_2})$ with respect to the case in which $f_{\text{H}_2} = 0$. In order to quantify the influence of $f_{\text{H}_2} > 0$ on our results, we explore the case with 30% of molecular gas, which approximately corresponds to the estimates in the literature (e.g. Hunt et al., 2015; Hunter et al., 2019).⁷ If $f_{\text{H}_2} = 0.3$, then $\rho_{\text{gas}} \approx 1.9\rho_{\text{HI}}$ and ρ_{SFR} increases of ≈ 1.2 , producing a rightward shift of ≈ 0.28 dex and an upward shift of ≈ 0.08 dex on the points for dwarf galaxies in Fig. 4.3. The yellow pentagons in Fig. 4.5 show the volume densities of our

⁷The measurements of the molecular gas fraction in dwarf galaxies are uncertain, as α_{CO} is poorly constrained. For example, the estimate obtained by Hunter et al. (2019) for LITTLE THINGS galaxies is based on the MW α_{CO} . Instead, Hunt et al. (2015), who used a different sample of dwarf galaxies, assumed either the MW value or, for the most metal-poor galaxies, a scaling relation with metallicity, which is a power-law with index ≈ -2 . This index is also uncertain: for instance, Amorín et al. (2016) estimated ≈ -1.5 and Madden & Cormier (2019) obtained ≈ -3.3 , which result in lower and higher molecular gas fractions, respectively.

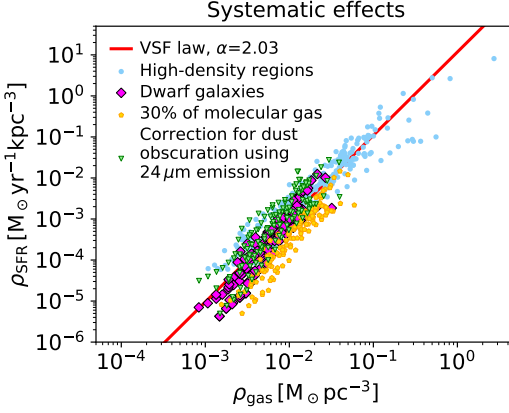


Figure 4.5 – Effect on the volume densities of including either a fraction of molecular gas of 30% (yellow pentagons) or the correction for the dust obscuration using $24\ \mu\text{m}$ emission (green triangles). For comparison, the volume densities of our sample of dwarf galaxies from our fiducial analysis are shown by the magenta diamonds and are the same as in Fig. 4.3. The light blue points are from Chapter 2 and the red line is the best-fit VSF law obtained in this Chapter.

dwarf galaxies including $f_{\text{H}_2} = 0.3$. They lie systematically below the VSF law and the magenta diamonds obtained with $f_{\text{H}_2} = 0$, but this shift is comparable to the typical error-bar of our points, indicating that the effect of f_{H_2} is small and does not strongly impact the validity of the VSF law.

4.5.2 Systematic effects on the star formation rate surface density

The SFR surface densities adopted in Chapter 2 included the correction for dust obscuration estimated from the $24\ \mu\text{m}$ luminosity (Leroy et al., 2008). Hence, in order to be fully consistent with this previous Chapter, we should take into account the $24\ \mu\text{m}$ luminosity (in addition to the FUV luminosity) also for the new sample of dwarf galaxies. We recall however that the amount of dust in dwarf galaxies is expected to be very low (e.g. Walter et al., 2007; Madden & Cormier, 2019) and the $24\ \mu\text{m}$ luminosity is unlikely to have a strong impact on the SFR surface density. In order to quantify the effect of this component, we estimated the dust-obscured SFR through the relation reported by Leroy et al. (2008) using the $24\ \mu\text{m}$ flux measured from *Spitzer* observations by Dale et al. (2009) (except for DDO 47, which is not included in their sample) and the unobscured SFR using the FUV luminosity, which was re-scaled to include the reddening (Zhang et al., 2012). NGC 2366 and DDO 101 have the highest $24\ \mu\text{m}$ fluxes, while only upper limits are available for DDO 52 and DDO 87. The green triangles in Fig. 4.5 show the effect of including the $24\ \mu\text{m}$ correction in the derivation of the SFR volume density. The agreement with the VSF law is conserved and the dwarf galaxies still follow the same trend as the galaxies studied in Chapter 2. On average, the SFR of our dwarf galaxies is increased of a factor ≈ 1.6 , corresponding to an upward shift of ≈ 0.2 dex. We point out that the inclusion of the molecular gas fraction and the correction for dust

obscuration tend to compensate, which indicates that our results would not change if both factors are taken into account.

We note that the SFR of DDO 50 (a.k.a. Holmberg II) and NGC 2366 in Table 4.1 are a factor ≈ 2 lower than the values obtained by McQuinn et al. (2015) using the CMD of resolved stellar populations. These authors reconstructed the galaxy star formation history by fitting the CMD with stellar evolutionary models and calculated the average SFR over the last 100 Myr, which corresponds to the mean age of FUV-emitting stars (Kennicutt & Evans, 2012). Aiming to assess the possible impact of this difference on our results, we re-scaled the SFR surface density radial profile adopted in this Chapter in order to have the same SFR as McQuinn et al. (2015). We found that using these modified profiles does not affect our main conclusion, as both DDO 50 and NGC 2366 remain in agreement with the VSF.

4.5.3 Validity of the hydrostatic equilibrium

As discussed in Sect. 4.4.1 and in Chapter 2, there is a general agreement between the scale heights based on the hydrostatic equilibrium derived by different authors, despite the different methods used to measure the velocity dispersion. We note however that the validity of the assumption of hydrostatic equilibrium for nearby galaxies has not been extensively tested in the literature. In Chapter 3, the radial profile of the scale height for our Galaxy derived assuming the hydrostatic equilibrium was compared with that measured by Marasco et al. (2017) using emission-line observations, both for the atomic gas and the molecular gas distributions. We found that, while the theoretical and the observed profiles are similar in the case of the molecular gas, the former tends to be ≈ 1.5 times lower than the latter for the atomic gas. This discrepancy does not necessarily mean that the hydrostatic equilibrium is not valid, as it may also indicate the presence of a second HI component with high velocity dispersion (Marasco et al. 2017). Alternatively, one could guess that some anisotropic force (e.g. magnetic tension, cosmic rays) contributes to counteracting the gravitational pull. However, in Chapter 3, we found agreement between the (measured) scale heights of star formation tracers and the (modelled) scale height of the gas in hydrostatic equilibrium, suggesting that the gas which is converted into stars is indeed in hydrostatic equilibrium.

Direct measurements of the gas scale height are of primary interest to test the validity of hydrostatic equilibrium and understand the structure of gaseous discs in galaxies. In the literature, there are some estimates of the gas scale height in edge-on galaxies (e.g. Yim et al., 2011, 2014; Peters et al., 2017b; Yim et al., 2020), but a comparison with the hydrostatic equilibrium is not provided. Moreover, highly inclined galaxies suffer strongly from projection effects: line-of-sight warps, non-circular motions and extra-planar gas can all artificially inflate measurements for both the velocity dispersion and the scale height of the gas (e.g. Swaters et al., 1997; Sicking, 1997; Oosterloo et al., 2007a; Marasco et al.,

2019). Therefore, an ‘ad hoc’ method applicable to galaxies with relatively high inclination is required in order to measure the scale height from the observations and avoid dramatic projection effects. This task is however beyond the scope of this thesis and we leave it to future investigations.

It is worth to mention that the disc thickness itself can bias the galaxy properties obtained from line emission observations with respect to the intrinsic properties (Sicking, 1997; Iorio et al., 2017; Iorio, 2018). In particular, when the thickness is non-negligible, one tends to underestimate the intrinsic inclination of a galaxy, as its gas disc appears more face-on than it actually is. Consequently, the surface density profile and the rotation curve are underestimated and overestimated, respectively. Iorio (2018) developed an innovative method to study the gas kinematics in thick discs based on combining the 3D tilted-ring modelling (i.e. ^{3D}BAROLO) with the hydrostatic equilibrium (i.e. GALPYNAMICS) using HI data cubes. This approach was tested on three dwarf galaxies, including WLM and NGC 2366, in order to derive their rotation curve, velocity dispersion, surface density, and scale height in a self-consistent way. Iorio (2018) found that the thickness bias is of second order with respect to other possible sources of uncertainty (e.g. asymmetric-drift correction, inclination). The HI scale heights of WLM and NGC 2366 obtained by Iorio (2018) are compatible with those shown in Fig. 4.2, indicating the bias due to the disc flaring is mild for our galaxies and does not significantly influence our results.

4.5.4 Comparison with other works

It is interesting to compare the scale heights obtained in Sect. 4.4.1 with those available in the literature and based on the assumption of vertical hydrostatic equilibrium. Banerjee et al. (2011) calculated the HI scale height for four dwarf galaxies, including DDO 50 (a.k.a. Holmberg II) and NGC 2366. They assumed that both the HI disc and the stellar disc are affected by their self-gravity. The only mass component of the external potential is the DM halo, which was assumed to have a pseudo-isothermal profile. We also note that, since these authors defined the scale height as the half width at half maximum (HWHM), their profiles should be divided by a factor of 1.177 when compared to ours. For DDO 50, these authors found HWHM ≈ 450 pc over the whole disc, which is approximately compatible with our scale height for $R \gtrsim 3$ kpc. However, our profile shows a clear flaring, despite the large uncertainties, while the scale height found by Banerjee et al. (2011) is practically constant. This discrepancy, which is mainly in the inner regions, can be explained by the difference in the velocity dispersion profile, which is slightly higher than ours for $R \lesssim 3$ kpc, and in the mass model of the galaxy. For NGC 2366, Banerjee et al. (2011) found that the HWHM increases from ≈ 100 pc in the inner regions to ≈ 800 pc at $R \approx 5$ kpc assuming σ_{HI} constant at 9 km s^{-1} . This velocity dispersion

is significantly different from the profile obtained by Iorio et al. (2017), which explains the disagreement with our scale height for $R \lesssim 5$ kpc (see Fig. 4.A.1).

In a recent study, Patra (2020) derived the HI scale height for a sample of 23 dwarf galaxies from LITTLE THINGS, including also those in our sample. This author used the same method as Banerjee et al. (2011) to derive the scale height, which was defined as the HWHM of the distribution of the gas in hydrostatic equilibrium. In general, the HI scale height in this study shows a flaring for all the galaxies, which is in agreement with our results. For some galaxies in common with our sample, the HWHM calculated by Patra (2020) is also compatible within the uncertainties with those in Fig. 4.2 (e.g. DDO 50, DDO 87, NGC 2366), but others are significantly different (e.g. WLM, DDO 47, DDO 101, DDO 126). For example, the flaring of the scale height is much steeper than ours in some disc outskirts (e.g. WLM) and the radial trend is clearly not monotonic with the galactocentric radius (e.g. DDO 47). These discrepancies might be partially due to the different mass models. Indeed, the HI rotation curves adopted by Patra (2020) are significantly different from those used in this Chapter (see Iorio et al. 2017 for a discussion). However, the most important source of discrepancy in the flaring determination is likely the HI velocity dispersion (see Fig. 4 in Patra 2020 vs the central panels of Fig. 4.1 and Fig. 4.A.1). Patra (2020) derived the velocity dispersion by dividing the HI disc in rings and stacking, in each ring, the line profiles along the line of sight after shifting their centroid velocity to a common value in order to remove the contribution of rotation. This method can introduce an artificial broadening in the resulting profile if the stacked ones are not perfectly aligned, or if single profiles are described by multiple kinematic components (e.g. DDO 133, NGC 1569, see Iorio et al. 2017). Instead, Iorio et al. (2017) used ^{3D}BAROLO, which simultaneously fits (for each ring) the rotation velocity and the azimuthally averaged velocity dispersion in order to minimise the residuals between the data and the model. This markedly improves the reliability of velocity dispersion estimates with respect to other 2D methods (e.g. 2th moment map of the data cube, stacking or pixel-by-pixel fitting of the line profiles) also for data with low signal-to-noise ratio (Di Teodoro & Fraternali 2015, see also Appendix 5.A).

Several authors have investigated the star formation law in different environments and interpreted their findings in the context of physical processes regulating star formation. For example, the SK law with $N \approx 1.4$ is usually explained by asserting that the timescale of the conversion of gas into stars is the free-fall time and assuming fixed scale heights for the gas and the SFR (i.e. $\Sigma_{\text{gas}} \propto \rho_{\text{gas}}$ and $\Sigma_{\text{SFR}} \propto \rho_{\text{SFR}}$). The break in the SK law at $\Sigma_{\text{gas}} \sim 10 M_{\odot} \text{pc}^{-2}$ is considered by some authors as an indication of a density threshold which needs to be exceeded to efficiently convert the gas into stars (e.g. Skillman et al., 1987; Martin & Kennicutt, 2001; Schaye, 2004; Bigiel et al., 2010), while other authors considered alternative star formation laws. In this respect, two

possibilities are the so-called ‘extended Schmidt law’ $\Sigma_{\text{SFR}} \propto \Sigma_{\text{gas}}^n \Sigma_{\star}^m$ (Talbot & Arnett, 1975; Dopita, 1985; Shi et al., 2011), which is based on the idea that the existing stellar component with surface density Σ_{\star} participate in regulating star formation, and the ‘Silk-Elmegreen relation’ $\Sigma_{\text{SFR}} \propto \Sigma_{\text{gas}}/\tau_{\text{orb}}$ (e.g. Silk, 1997; Elmegreen, 1997), which sets the timescale of star formation to the galactic orbital time τ_{orb} . Despite these alternative relations appear to have no break, their intrinsic scatter is about 0.3-0.4 dex (e.g. Shi et al., 2011; Roychowdhury et al., 2017; de los Reyes & Kennicutt, 2019), which is similar to intrinsic scatter of the ‘classical’ SK law and three-four times larger than that of the VSF law, perhaps indicating that this latter is more fundamental.

Leroy et al. (2008) compared the predictions of various models of star formation with the observed star formation efficiency (i.e. $\text{SFE} = \Sigma_{\text{SFR}}/\Sigma_{\text{gas}}$) as a function of the galactocentric radius measured in dwarf and spiral galaxies. These authors investigated ‘local’ star formation laws based on the idea that the timescale of the conversion of gas into stars is set by a given physical mechanism (i.e. gravitational instability, galactic rotation, cloud-cloud collisions, efficiency of molecular clouds in forming stars, and midplane gas pressure), but they did not find a single process that could describe both dwarf and spiral regimes. Leroy et al. (2008) also found that the observed SFE is not in agreement with the predictions of models based on a density threshold (i.e. large-scale gravitational instability of the disc, molecular clouds destruction by shear, molecular gas formation), which distinguish whether the gas is dense enough to be star-forming. Hence, they concluded that the SFE is regulated by the interplay of multiple physical mechanisms acting on scales smaller than the spatial resolution of their data. The results found in this and the previous Chapters indicate instead the existence of a unique local star formation law valid at all density regimes, which may suggest a simple and perhaps unique physical mechanism, involving exclusively the gas volume densities, at the core of star formation processes.

The importance of the gas disc flaring in shaping the star formation law was also investigated by Elmegreen (2015), who developed a model which predicts that the index of the local SK law changes from $N = 1.5$ to $N = 2$ as a consequence of the gas being self-gravitating in the outskirts of spiral galaxies and in dwarf galaxies. Star formation is assumed to be regulated by gravity and the star formation law is written in terms of surface densities as $\Sigma_{\text{SFR}} = \epsilon_{\text{ff}} \Sigma_{\text{gas}}/\tau_{\text{ff}}$, where ϵ_{ff} is the efficiency per unit free-fall timescale τ_{ff} and it is assumed constant for all galaxies. In the main disc of spiral galaxies, the scale height was taken to be approximately constant with the galactocentric radius, hence $\rho_{\text{gas}} \propto \Sigma_{\text{gas}}$ and $\tau_{\text{ff}} \propto \rho_{\text{gas}}^{-1/2} \propto \Sigma_{\text{gas}}^{-1/2}$. Therefore, the surface-based star formation law is $\Sigma_{\text{SFR}} \propto \Sigma_{\text{gas}}^{3/2}$, in agreement with the empirical SK law. In the outskirts of spiral galaxies and in dwarf galaxies, the gas disc was instead assumed self-gravitating, which implies that the gas scale height is $h_{\text{gas}} = \sigma_{\text{gas}}^2/(\pi G \Sigma_{\text{gas}})$. This results in a different index for the surface-based star

formation law, which is $\Sigma_{\text{SFR}} \propto \Sigma_{\text{gas}}^2$ (assuming constant velocity dispersion). The observed break in the SK law is then explained in terms of projection effects due to the gas disc flaring rather than a consequence of a threshold density for star formation (Elmegreen, 2018), in agreement with our conclusions. We note however that there are a number of differences between this approach and ours, the most important being the model of the galactic potential. Indeed, we did not assume that the gas is distributed in a self-gravitating disc (neither in the main disc nor in the outskirts of galaxies), as we included the gravitational potential of the DM halo. This latter is the dominant mass component in dwarf galaxies and in the outskirts of spiral galaxies, hence it is very important to take into account the DM halo in these regimes in order to derive the gas scale height (see Fig. 2.3).

4.5.5 On the physical implications of the VSF law

We have found that the VSF is tighter than surface-based star formation laws and furthermore that it is valid for both dwarf and spiral galaxies, covering a range of volume densities from $\approx 7 \times 10^{-4} \text{ M}_{\odot}\text{pc}^{-3}$ to $\approx 2 \text{ M}_{\odot}\text{pc}^{-3}$ for the gas and from $\approx 4 \times 10^{-5} \text{ M}_{\odot}\text{yr}^{-1}\text{kpc}^{-3}$ to $\approx 10 \text{ M}_{\odot}\text{yr}^{-1}\text{kpc}^{-3}$ for the SFR. Within this range, the VSF law with the total gas is $\rho_{\text{SFR}} \propto \rho_{\text{gas}}^{\alpha}$, where $\alpha \approx 2$. The lack of a break (i.e. change in the slope) has a crucial implication: there is no density threshold for star formation when the volume densities are considered (we cannot completely exclude though that some threshold may exist below $\rho_{\text{gas}} \sim 10^{-3} \text{ M}_{\odot}\text{pc}^{-3}$). The absence of a threshold implies that some star formation recipes implemented in large-scale numerical simulations and analytical models of galaxy evolution might need revision. The observed break in the SK law can thus be interpreted as due to the projection effects in the presence of disc flaring rather than to the drop of the SFE for densities below a certain threshold (see also Madore et al. 1974; Ferguson et al. 1998; but see Kumari et al. 2020 for a different perspective). This was also suggested by Elmegreen (2018) for the star formation law based on the surface densities using a model in which star formation is controlled by gravity (see Sect. 4.5.4).

In order to gain insight on the mechanisms regulating the conversion of gas into stars, let us write the ‘theoretical’ VSF law as

$$\rho_{\text{SFR}} = \epsilon \frac{\rho_{\text{gas}}}{\tau_{\text{sf}}}, \quad (4.17)$$

where ϵ is the efficiency per unit star formation timescale τ_{sf} . Given that the volume densities obtained through Eq. 4.2 and Eq. 4.3 are those at $z = 0$, we can speculate that they are a good approximation of the (azimuthally averaged) volume density close to the midplane of a galaxy, where most of the star-forming gas is concentrated. We must note though that it is not clear to what extent empirical star formation laws can capture the complexity of the conversion of gas into stars, hence it is important to bear in mind that the VSF law is meaningful

on kiloparsec scale but likely not applicable to clouds or filaments. If we assume that τ_{sf} is equal to the free-fall timescale of the gravitational instability $\tau_{\text{ff}} \propto (G\rho_{\text{gas}})^{-1/2}$ (e.g. Madore, 1977), it follows from Eq. 4.17 that the index of the ‘empirical’ VSF law (i.e. $\alpha \approx 2$) can be obtained only with $\epsilon \propto \rho_{\text{gas}}^{1/2}$. The origin of this proportionality is not clear and may arise from the combination of different factors, such as a radial variation of the molecular gas fraction (e.g. Elmegreen & Hunter, 2015), the metallicity gradient, or the degree of ionisation of the gas (e.g. McKee & Ostriker, 2007). These possibilities might be tested by looking for correlations between the scatter of the VSF law and the properties of our galaxies. The intrinsic scatter of our relation is however remarkably small, suggesting that secondary correlations are absent or too weak to be revealed.

Alternatively, we can think of some physical mechanism which may play a role in star formation and whose timescale is $\tau \propto \rho_{\text{gas}}^{-1}$ (assuming constant efficiency). In order to fragment in gravitationally bound (potentially star-forming) clouds, the diffuse ISM must first lose significant part of its thermal energy through radiative cooling. This suggests that, while the free-fall time likely governs star formation at the scales of molecular clouds, on larger (kiloparsec) scales the cooling time may be equally and perhaps more important than the free-fall time. Similar ideas were also proposed by other authors, who suggested that τ_{sf} might be the timescale of the slowest and ‘bottle-neck’ process among collapse, cooling, and molecule formation (e.g. Ciotti & Ostriker, 2007; Krumholz, 2013). Both the cooling time and the timescale to reach the equilibrium between formation and destruction of H_2 are inversely proportional to the gas density (e.g. Hollenbach & McKee, 1979; Krumholz, 2014), resulting in $\alpha = 2$ in Eq. 4.17 and thus in agreement with the empirical VSF law.

Finally, let us briefly discuss the possible origin of the volumetric relation with the atomic gas only, which is quite surprising. This correlation appears to have a larger scatter in the high-density regions of galaxies, where the molecular gas is detected using CO emission, than in the other parts of the discs (see Fig. 2.9 in Chapter 2). This may indicate that, in the inner and high-density regions, the total gas is a better tracer of the star-forming gas than the HI only, but this latter becomes a good tracer where the gas density is lower (see also Elmegreen & Hunter, 2015; Hu et al., 2016). Possibly, this can be explained by the presence of a significant amount of CO-dark gas in the outskirts of galaxies. Alternatively, the relation involving the atomic gas only might be considered an indication that star formation can directly occur in the atomic gas in particular conditions (see e.g. Glover & Clark 2012; Krumholz 2012). We note that this correlation might open up to semi-empirical studies of galaxy evolution in low-density and metal-poor regions, where the molecular gas emission is not detected or very uncertain and some theoretical models of star formation yields discordant conclusions (see e.g. Ostriker et al. 2010; Krumholz 2013; § 4 and § 6 in Knapen et al. 2017 and references therein).

4.6 Summary and conclusions

The star formation law is a key relation to link the gas content of a galaxy and its SFR, fundamental to understand galaxy formation and evolution. However, when we observe the gas and the SFR distributions in a galaxy, we can directly measure only their projected surface densities, while the intrinsic volume densities, which arguably are more physically meaningful, remain inaccessible. The flaring of gas discs in galaxies complicates the task of reconstructing intrinsic volume densities from observed surface densities, preventing to derive the intrinsic distributions in a straightforward way.

In Chapters 2 and 3, we have developed and consolidated a method to convert the observed surface density radial profiles of the gas and the SFR to the corresponding volume density profiles using the scale height of their vertical distribution. This approach is based on the assumption of hydrostatic equilibrium and requires the knowledge of the gravitational potential of a galaxy and the velocity dispersion of the gas. Using this method, the volume densities of the gas and the SFR were derived for a sample of 12 nearby galaxies and for the MW. These two quantities were found to tightly follow one single power-law relation, the volumetric star formation (or VSF) law, which has a smaller scatter than the surface-based star formation laws. An unexpected correlation between the volume densities of the atomic gas and the SFR also emerged from these studies.

The main aim of this Chapter was to extend the VSF law to the regime of dwarf galaxies, which is of primary importance to investigate the presence of a density threshold for star formation in low-density and HI-dominated environments. As a consequence of the shallow gravitational potential, the gas discs in this type of galaxies are thick and significantly flaring, hence taking into account the projection effects is fundamental. We applied the method used in Chapter 2 to a sample of ten dwarf galaxies with robust HI kinematics and mass models available in the literature (Iorio et al., 2017; Read et al., 2017). The outermost star-forming regions (i.e. beyond the stellar disc) of the galaxies studied in Chapter 2 were also added in this Chapter, as they are low-density and HI-dominated parts of the disc where the flaring is prominent. We verified that both the new sample of dwarf galaxies and the star-forming outskirts follow remarkably well the VSF law, extending its validity range down to $\rho_{\text{HI}} \sim 10^{-3} \text{ M}_{\odot} \text{pc}^{-3}$ and $\rho_{\text{SFR}} \sim 10^{-5} \text{ M}_{\odot} \text{yr}^{-1} \text{kpc}^{-3}$. We confirm both the VSF law with the total gas (i.e. HI+H₂) and the correlation involving the atomic gas only. Hence, the conclusions of this Chapter are the following.

1. The VSF law, namely $\rho_{\text{SFR}} \propto \rho_{\text{gas}}^{\alpha}$ with $\alpha \approx 2$, is valid for both low-density and high-density star-forming environments in nearby disc galaxies. The intrinsic scatter of the VSF law is $\sigma_{\perp} \approx 0.1$ dex, which is significantly lower than that of the star formation laws based on the surface densities.

2. The atomic gas volume density correlates with the SFR volume densities, following the relation $\rho_{\text{SFR}} \propto \rho_{\text{HI}}^\beta$ with $\beta \approx 2.8$ and intrinsic scatter $\sigma_\perp \approx 0.1$ dex. This indicates that, contrary to previous claims based on projected surface densities, the atomic gas is a reliable tracer of the star-forming gas, which can be particularly useful in the low-metallicity regions of galaxies where the emission of molecular gas tracers is not detected.
3. We find no evidence for a break in the VSF law occurring at the transition to the low-density and HI-dominated parts of the discs, which disfavors the existence of a density threshold for star formation.

It is remarkable that the VSF law is valid for both dwarf and spiral galaxies, and for such a wide range of densities. This may indicate that our relation is the fundamental star formation law, also considering that volume densities are intrinsic quantities that are likely more physically meaningful than surface densities, which depend on projection effects. Our findings might potentially be a confirmation, after more than sixty years, of the pioneering work by Schmidt (1959), which opened up the field of star formation laws study. The VSF law is consistent with the idea that, on kiloparsec scale, gas cooling might be the primary process which sets the conversion of gas into stars, beforehand the gravitational instability is at play on cloud scales. Future investigations could aim to test the VSF law in environments that are even more extreme than dwarf galaxies, such as early-type galaxies with ongoing star formation, extended star-forming discs (e.g. Thilker et al., 2007a,b), and starbursts.

Acknowledgements

We thank Bruce Elmegreen for the stimulating discussions and for providing thorough comments on this manuscript, and Deidre Hunter for sharing the surface photometry data and the help in their usage. CB would like to thank Giuliano Iorio for the help with GALPYNAMICS.

Appendix 4.A Radial profiles of Σ_{HI} , σ_{HI} , and Σ_{SFR}

Figure 4.A.1 shows the radial profiles of the atomic gas surface density and velocity dispersion, and the SFR surface density used in this Chapter for nine out of ten galaxies in our sample (see Fig. 4.1 for the profiles of WLM). The atomic gas profiles are from Iorio et al. (2017), while the SFR surface density is obtained from the FUV photometry (Zhang et al., 2012) using Eq. 4.14 (see Sect. 4.3.2 for details).

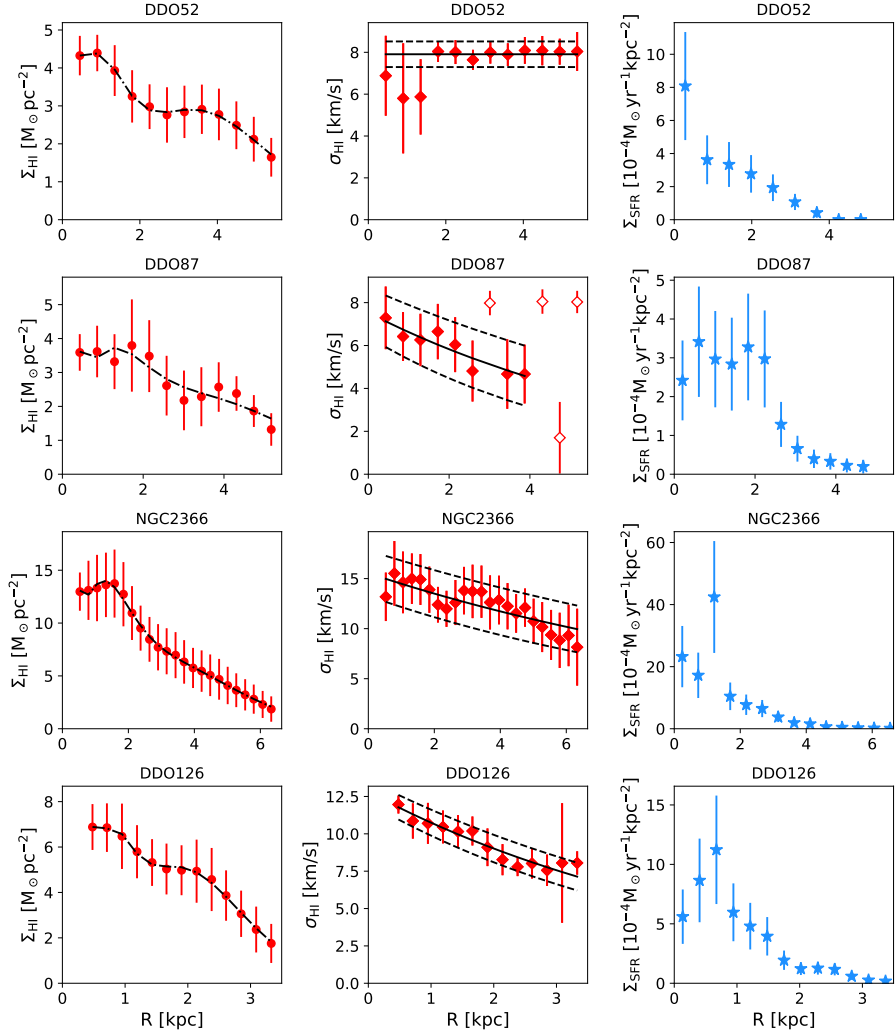


Figure 4.A.1 – Azimuthally averaged radial profiles of the atomic gas surface density (left column), the HI velocity dispersion (central column), and the SFR surface density (right column) for the dwarf galaxies studied in this Chapter. The black curves are the same fits as in Fig. 4.1.

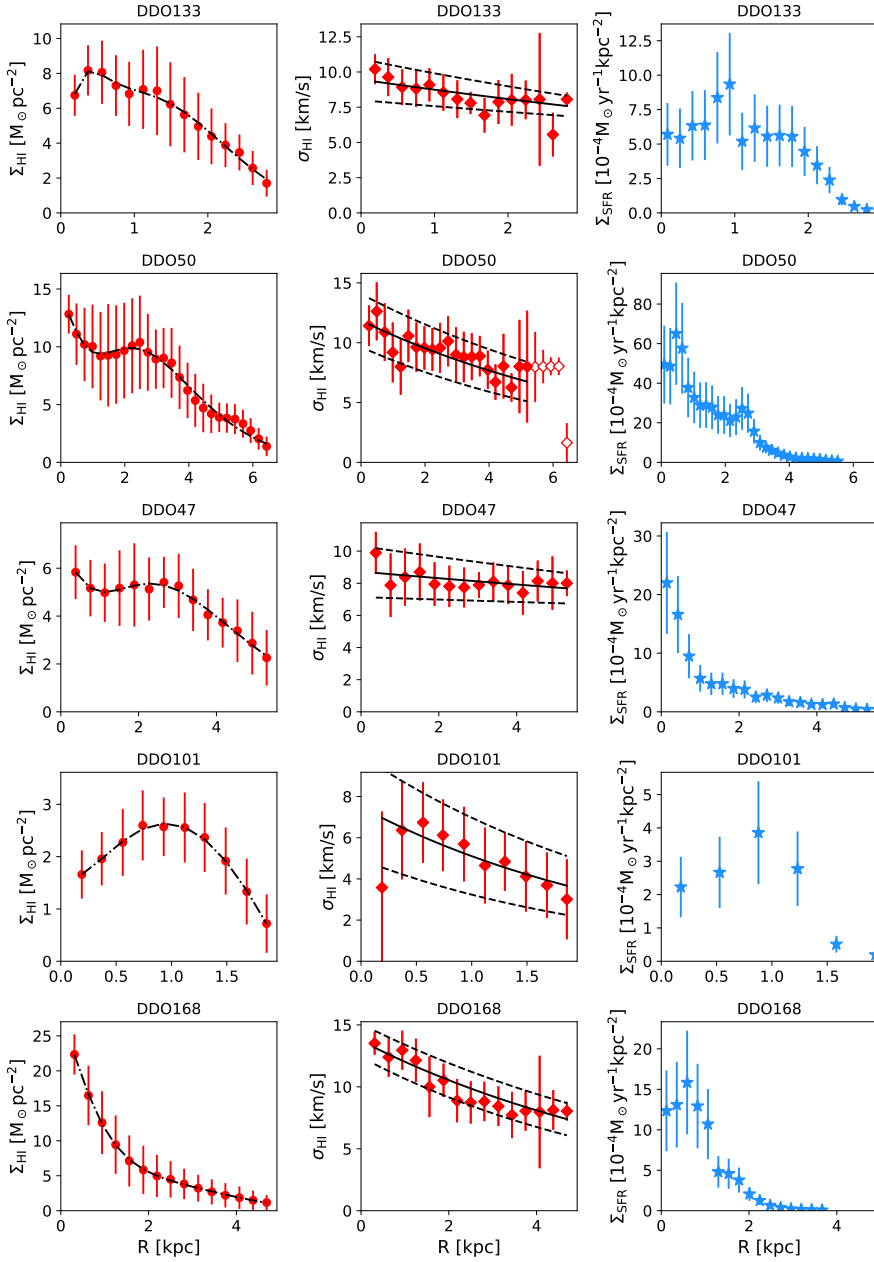


Figure 4.A.1 – Continued.

CHAPTER 5

**Evidence for supernova
feedback sustaining gas
turbulence in nearby
star-forming galaxies**

based on

— C. Bacchini, F. Fraternali, G. Iorio, G. Pezzulli, A. Marasco,
and C. Nipoti —

Astronomy & Astrophysics, in press.

Abstract

It is widely known that the gas in galaxy discs is highly turbulent, but there is much debate on which mechanism can energetically maintain this turbulence. Among the possible candidates, supernova (SN) explosions are likely the primary drivers but doubts remain on whether they can be sufficient in regions of moderate star formation activity, in particular in the outer parts of discs. Thus, a number of alternative mechanisms have been proposed. In this Chapter, we measure the SN efficiency η , namely the fraction of the total SN energy needed to sustain turbulence in galaxies, and verify that SNe can indeed be the sole driving mechanism. The key novelty of our approach is that we take into account the increased turbulence dissipation timescale associated with the flaring in outer regions of gaseous discs. We analyse the distribution and kinematics of HI and CO in ten nearby star-forming galaxies to obtain the radial profiles of the kinetic energy per unit area for both the atomic gas and the molecular gas. We use a theoretical model to reproduce the observed energy with the sum of turbulent energy from SNe, as inferred from the observed star formation rate (SFR) surface density, and the gas thermal energy. For the atomic gas, we explore the two extreme cases in which the atomic gas is made of either cold neutral medium or warm neutral medium, and the more realistic scenario with a mixture of the two phases. We find that the observed kinetic energy is remarkably well reproduced by our model across the whole extent of the galactic discs, assuming η constant with the galactocentric radius. Taking into account the uncertainties on the SFR surface density and on the atomic gas phase, we obtain that the median SN efficiencies for our sample of galaxies are $\langle\eta_{\text{atom}}\rangle = 0.015_{-0.008}^{+0.018}$ for the atomic gas and $\langle\eta_{\text{mol}}\rangle = 0.003_{-0.002}^{+0.006}$ for the molecular gas. We conclude that SNe alone can sustain gas turbulence in nearby galaxies with only few percent of their energy and that there is essentially no need for any further source of energy.

5.1 Introduction

Gas kinematics provides valuable information about the physical properties of the interstellar medium (ISM). In particular, the velocity dispersion measured from the broadening of emission lines is fundamental for the study of turbulence. Several authors have analysed the kinematics of atomic and molecular gas in nearby star-forming galaxies, finding that the velocity dispersion shows a decreasing trend with the galactocentric radius (e.g. Fraternali et al., 2002; Boomsma et al., 2008; Wilson et al., 2011; Mogotsi et al., 2016; Iorio et al., 2017, Fig. 2.2). In the inner regions of galaxies, the gas velocity dispersion is typically about $15\text{--}20\text{ km s}^{-1}$, well exceeding the expected broadening due to thermal motions alone (i.e. $\lesssim 8\text{ km s}^{-1}$). This non-thermal broadening is usually ascribed to turbulence. At large galactocentric radii instead (where the molecular gas emission is typically not detected), the velocity dispersion of HI approaches values that are compatible with the thermal broadening of the warm neutral gas (at temperature $T \approx 8000\text{ K}$).

Both thermal and turbulent motions are forms of disordered energy, but while the first is related to the temperature of the gas particles, the second can be seen as the relative velocity between macroscopic portions of the fluid. The behaviour of turbulence in incompressible fluids is well described by Kolmogorov’s theory (Kolmogorov, 1941), which we briefly outline in the following (see Elmegreen & Scalo 2004 for details). Turbulence entities are envisioned as ‘eddies’ that develop at a variety of different spatial scales. Turbulent energy is injected on a certain scale L_D , called driving scale, at which the largest eddies are formed. The largest eddies break down into smaller and smaller eddies and transfer kinetic energy to smaller scales in the so-called ‘turbulent cascade’, until the dissipation scale l_d is reached. The energy is conserved throughout this cascade for any scale between the driving scale and the dissipation scale (i.e. inertial range). At the dissipation scale instead, viscosity transforms the turbulent kinetic energy into internal energy. Kolmogorov’s framework is usually assumed to describe the ISM turbulence, despite the expectation that the gas is compressible in the presence of supersonic turbulent motions (e.g. Elmegreen & Scalo, 2004). There are indeed observational indications that Kolmogorov’s theory might be adequate for modelling ISM turbulence (e.g. Elmegreen et al., 2001; Dutta et al., 2009).

Both Kolmogorov’s theory and numerical simulations of compressible supersonic turbulence in the ISM show that the turbulent energy should be rapidly dissipated on timescales of the order of 10 Myr (e.g. Stone et al., 1998; Mac Low et al., 1998; Padoan & Nordlund, 1999; Mac Low, 1999). Hence, a continuous source of energy is needed in order to maintain the turbulence of the gas ubiquitously observed in galaxies. This issue has stimulated previous research to understand the mechanism that is feeding turbulence in galaxies (e.g. Tamburro et al., 2009; Klessen & Hennebelle, 2010; Stilp et al., 2013; Utomo et al., 2019). Among the possible candidates, there are different forms

of stellar feedback, which include proto-stellar jets, winds from massive stars, ionising radiation, and supernovae (SNe). These latter likely dominate the energy input with respect to the other mechanisms (Mac Low & Klessen, 2004; Elmegreen & Scalo, 2004). SN explosions are extremely powerful phenomena that can inject a huge amount of energy into the ISM, even though most of this energy is expected to be radiated away (e.g. McKee & Ostriker, 1977). Numerical simulations of SN remnant evolution in the ISM have consistently shown that the efficiency of SNe, which is typically defined as the fraction of the total SN energy that is injected into the ISM as kinetic energy, is ~ 0.1 (e.g. Thornton et al., 1998; Dib & Burkert, 2005; Kim & Ostriker, 2015a; Martizzi et al., 2016; Fierlinger et al., 2016; Ohlin et al., 2019, but see also Fielding et al. 2018). This appears at odds with a number of recent works showing that the observed kinetic energy of the atomic gas in nearby galaxies requires a SN feedback with a efficiency of $\approx 0.8 - 1$ (e.g. Tamburro et al., 2009; Stilp et al., 2013; Utomo et al., 2019). Therefore, other physical mechanisms have been considered as additional drivers of turbulence, like magneto-rotational instability (MRI, e.g. Sellwood & Balbus, 1999), gravitational instability (e.g. Krumholz & Burkert, 2016), rotational shear (e.g. Wada et al., 2002), and accretion flows (e.g. Klessen & Hennebelle, 2010; Krumholz & Burkert, 2010; Elmegreen & Burkert, 2010). However, quantifying the amount of kinetic energy provided by these mechanisms is not straightforward and the values predicted by the models are affected by large uncertainties on the observable quantities (e.g. mass accretion rate, magnetic field intensity). Hence, it is still not clear which (if any) of these additional sources of energy are at play.

A further difficulty in studying the turbulent energy is represented by the challenge of disentangling thermal and turbulent motions in observations. This issue is particularly significant for the neutral atomic gas (HI), which is expected to be present in two phases with different temperatures: the cold neutral medium (CNM) with $T \approx 80$ K and the warm neutral medium (WNM) with $T \approx 8000$ K (Wolfire et al., 1995, 2003). This latter can significantly contribute to the HI velocity dispersion ($\lesssim 8$ km s $^{-1}$) and the kinetic energy, but the lack of information about the relative fraction of CNM and WNM is usually an irksome obstacle to interpreting the observed velocity dispersion. In the Milky Way, Heiles & Troland (2003) estimated that approximately 60% of the atomic hydrogen in the solar neighborhood is WNM (at latitudes larger than 10° ; see also Murray et al. 2018). Pineda et al. (2013) found that the fraction of WNM is $\sim 30\%$ and $\sim 80\%$ within and beyond the solar radius respectively. However, there are indications of significant variations between galaxies, which stands in the way of adopting the Galactic values for extra-galactic studies. Indeed, Dickey & Brinks (1993) measured that the WNM represents $\sim 60\%$ and $\sim 85\%$ of the total HI in M31 and M33, respectively. In the Large Magellanic Cloud, Marx-Zimmer et al. (2000) found that the WNM is about 65%, while Dickey et al. (2000) estimated a lower limit of $\sim 85\%$ for the Small Magellanic Cloud

(see also Jameson et al., 2019). High fractions of WNM were also claimed by Warren et al. (2012), who studied HI line profiles for a sample of 27 nearby galaxies and found that, despite the CNM phase is present in almost all their galaxies, it is only a few percent of the total HI.

The purpose of this Chapter is to understand whether SNe can provide sufficient energy to maintain the turbulence of neutral gas in nearby star-forming galaxies and, in particular, to infer the SN efficiency. The main improvement with respect to previous works is that we take into account the radial flaring of gas discs in galaxies, which implies longer timescales of turbulence dissipation. Moreover, we use a Bayesian method to effectively explore the parameter space of our model of SN-driven turbulence. In this Chapter, Section 5.2 describes the sample of galaxies and the observations used to measure the kinetic energy. In Sect. 5.3, we explain how we derive the turbulent energy and the thermal energy components expected from ISM models, and the method used to obtain the SN efficiency from a set of observations. In Sect. 5.4, we show the resulting profiles of the energy components and provide the SN efficiencies for the galaxies in our sample. In Sect. 5.5, we derive a ‘global’ value for efficiency of the atomic and the molecular gas by considering the whole sample of galaxies; we then discuss our findings in the broader context of self-regulating star formation and compare our results with previous works in the literature on SN feedback and other driving mechanisms. Section 5.6 summarises this Chapter and draws our main conclusions.

5.2 Observations and galaxy sample

Given suitable emission-line spectroscopic observations, the kinetic energy per unit area of the (atomic or molecular) gas in a galaxy as a function of the galactocentric radius, R , can be estimated as

$$\begin{aligned}
 E_{\text{obs}}(R) &= \frac{3}{2} \Sigma(R) \sigma^2(R) \\
 &\simeq (3 \times 10^{46} \text{ erg pc}^{-2}) \left(\frac{\Sigma}{10 \text{ M}_{\odot} \text{ pc}^{-2}} \right) \left(\frac{\sigma}{10 \text{ km s}^{-1}} \right)^2,
 \end{aligned} \tag{5.1}$$

where $\Sigma(R)$ is the surface density, $\sigma(R)$ is the velocity dispersion, and the factor of 3 in the first equality comes from the assumption of isotropic velocity dispersion. We calculated Eq. 5.1 for the neutral gas in a sample of nearby star-forming galaxies by studying the distribution and kinematics of HI and CO, which is adopted as H₂ tracer. All the radial profiles used in this work are azimuthal averages calculated by dividing the galaxy into concentric tilted rings of about 400 pc width (see Chapter 2).

5.2.1 Atomic gas distribution and kinematics

In this Chapter, we used the velocity dispersion derived in Chapter 2, in which we studied the HI kinematics in 12 nearby star-forming galaxies using 21-cm emission line data cubes from The HI Nearby Galaxy Survey (THINGS; Walter et al., 2008). The data cubes were analysed using the software ^{3D}BAROLO (Di Teodoro & Fraternali, 2015), which carries out a tilted-ring model fitting on emission-line data cubes. ^{3D}BAROLO can take into account the beam smearing effect and robustly measure the velocity dispersion and the rotation curve of a galaxy, performing significantly better than 2D methods based on moment maps (e.g. Di Teodoro et al., 2016; Iorio et al., 2017). Figure 2.2 in Chapter 2 shows the radial profiles of the HI velocity dispersion (σ_{HI}) for the sample: typically, σ_{HI} is 15–20 km s⁻¹ in the inner regions of galaxies and 6–8 km s⁻¹ in the outskirts. For NGC 6946, we performed a new kinematic analysis using the 21-cm data cube in Boomsma et al. (2008) with a spatial resolution of 13'' (i.e. \approx 330 pc), as it has a higher signal-to-noise (S/N) ratio with respect to the THINGS data cube used in Chapter 2.

For highly inclined or warped galaxies, the line of sight intercepts regions with different rotation velocity, which can artificially broaden the line profile. This issue biases the velocity dispersion towards high values and ^{3D}BAROLO cannot correct for this effect. Hence, we decided to exclude two galaxies from this study, NGC 2841 ($i \approx 74^\circ$) and NGC 7331 ($i \approx 76^\circ$), as their average HI velocity dispersion is systematically $\gtrsim 5$ km s⁻¹ above that of the other galaxies. NGC 3198 instead, despite the relatively high inclination ($i \approx 72^\circ$), appears much less affected by this issue and is then included in our sample (see Appendix 2.D for a more detailed discussion). In addition, NGC 5055 shows a warp along the line of sight, which starts beyond $R \approx 10$ kpc (Battaglia et al., 2006). In these regions, the velocity dispersion is systematically higher than the typical values in the outer parts of star-forming galaxies (see Fig. 2.2), as the line profile is broadened by the merging of emission from different annuli intercepted by the line of sight. Hence, we excluded these regions from this study. We obtained a final sample of eight spiral galaxies and two dwarf galaxies (i.e. DDO 154 and IC 2574).

We derived the HI surface density (Σ_{HI}) as a function of the galactocentric radius with the task ELLPROF of ^{3D}BAROLO, which provides the radial profiles corrected for the galaxy inclination. For NGC 0925, NGC 2403, NGC 3198, and NGC 5055, we used the publicly available data cubes from the Hydrogen Accretion in LOcal GALaxieS (HALOGAS) Survey (Heald et al., 2011, see also Marasco et al. 2019), which have a better S/N with respect to the robust-weighted THINGS data cubes adopted in Chapter 2. DDO 154, IC 2574, NGC 2976, NGC 4736 and NGC 7793 are not included in the HALOGAS sample, hence we obtained Σ_{HI} from the natural-weighted THINGS data cubes, as they have a better S/N with respect to the robust-weighted data cubes. In the case of NGC 6946, we employed the same data cube as in Boomsma et al.

(2008). We obtained the surface density of the total atomic gas by accounting for the Helium fraction (i.e. $\Sigma_{\text{atom}} = 1.36\Sigma_{\text{HI}}$). We also verified that our profiles are compatible with previous estimates in the literature (Fraternali et al., 2002; Battaglia et al., 2006; Leroy et al., 2008; Boomsma et al., 2008; Bigiel et al., 2010; Gentile et al., 2013; Iorio et al., 2017).

5.2.2 Molecular gas distribution and kinematics

We measured the velocity dispersion of CO, the typical tracer of the molecular gas, using ^{3D}BAROLO on CO(2-1) emission line data cubes from the HERA CO-Line Extragalactic Survey (HERACLES; Leroy et al., 2005). The emission is detected in seven out of ten galaxies of our sample, except DDO 154, IC 2547, and NGC 7793. We provide the results of the kinematic analysis (e.g. moments maps, position-velocity diagrams, rotation curves) in Appendix 5.A. In Chapter 2, we did not analyse the molecular gas kinematics for each galaxy in the sample, as we relied on previous works in the literature that showed that the velocity dispersion of CO is about half of σ_{HI} (Mogotsi et al., 2016; Marasco et al., 2017; Koch et al., 2019). For the purpose of this Chapter, a robust measurement of the velocity dispersion is desirable to accurately calculate Eq. 5.1, allowing also to test the assumption used in Chapter 2 (see Appendix 5.A). We indicate the molecular gas velocity dispersion with σ_{H_2} . We must note however that it is not clear whether the nature of the non-thermal component of the molecular gas velocity dispersion is dynamic (i.e. disordered motions between self-gravitating clouds) or hydro-dynamic (i.e. disordered motions between portions of fluid, similarly to the atomic gas turbulence). Our approach based on Kolmogorov’s theory adheres to the second scenario.

We took the radial profiles of the molecular gas surface density (Σ_{mol}) from Frank et al. (2016). These authors measured the CO luminosity using HERACLES data cubes and derived Σ_{mol} using the CO-to-H₂ conversion factor from Sandstrom et al. (2013). These latter authors obtained the radial profile of the conversion factor in a sample of 26 galaxies taking into account the dust-to-gas ratio and the metallicity gradient. NGC 2403 was not included in the study of Sandstrom et al. (2013), hence Frank et al. (2016) adopted the MW value for the conversion factor. The profiles of Frank et al. (2016), which already include the Helium correction, are shown in Fig. 2.1, where the errorbars take into account the uncertainty on the CO-to-H₂ conversion factor.

5.2.3 Star formation rate surface density

To estimate the turbulent energy produced by SNe, we used the observed SFR surface density (Σ_{SFR}). We took as references two different estimates of the SFR surface density, one from Leroy et al. (2008) and Bigiel et al. (2010), and the other from Muñoz-Mateos et al. (2009). This allows us to test the possible

dependence of our results on different methods to derive the SFR surface density from the observations.

The profiles from Leroy et al. (2008) are obtained by combining the far-ultraviolet (FUV, i.e. unobscured SF) emission maps from the Galaxy Evolution Explorer (GALEX; Gil de Paz et al., 2007) and the 24- μm (obscured SF) emission maps from the Spitzer Infrared Nearby Galaxy Survey (SINGS; Kennicutt et al., 2003). We also included the profiles from Bigiel et al. (2010), which are derived from FUV GALEX maps out to larger radii with respect to Leroy et al. (2008).

For DDO 154, NGC 2403, NGC 3198 and NGC 6946, $\Sigma_{\text{SFR}}(R)$ is less radially extended than $\Sigma_{\text{HI}}(R)$, as the FUV emission from the outermost radii goes below the sensitivity limit of the observations. In particular, nine out of ten galaxies are in the sample of Bigiel et al. (2010), hence the upper limit on $\Sigma_{\text{SFR}}(R)$ is $2 \times 10^{-5} \text{ M}_{\odot}\text{yr}^{-1}\text{kpc}^{-2}$. For NGC 6946, which is not included in that study, the upper limit is $10^{-4} \text{ M}_{\odot}\text{yr}^{-1}\text{kpc}^{-2}$ (Leroy et al., 2008). In our modelling procedure (see Sect. 5.3), we use these upper limits to constrain the energy injected by SNe at large radii, rather than simply discarding the outskirts of galaxies from our analysis.

To derive a radial profile of SFR surface density from the data of Muñoz-Mateos et al. (2009), we followed the procedure described in Pezzulli et al. (2015). We adopted the UV extinction radial profiles based on the dust attenuation prescription from Cortese et al. (2008). Among our galaxies, only the dwarf galaxy DDO 154 is not included in this sample. In general, the values of the SFR surface densities derived from Muñoz-Mateos et al. (2009) are above those from Leroy et al. (2008), in particular at large radii, while $\Sigma_{\text{SFR}}(R)$ in the innermost regions of NGC 0925, NGC 3198, and NGC 6946 is reduced. We anticipate that our main conclusions do not change whether we use one or the other determination of the SFR surface density.

5.3 Methods

In this section, we first describe the energy components that we took into account to estimate theoretically the energy of the atomic gas and the molecular gas. We then explain the method used to compare this energy with the energy profiles calculated from the observations using Eq. 5.1 in order to obtain the SN efficiency.

5.3.1 Energy components

We assume that the total energy of the (atomic or molecular) gas per unit area (E_{mod}) is the sum of the turbulent energy (E_{turb}) and the thermal energy (E_{th})

$$E_{\text{mod}}(R) = E_{\text{turb}}(R) + E_{\text{th}}(R). \quad (5.2)$$

Hence, the velocity dispersion of the gas is

$$\sigma_{\text{mod}}(R) = \sqrt{v_{\text{turb}}^2(R) + v_{\text{th}}^2(R)}, \quad (5.3)$$

where v_{turb} is the turbulent velocity and v_{th} is the thermal velocity. The equation for the turbulent energy is described below in Sect. 5.3.1 and is the same for the atomic gas and the molecular gas. For the thermal component instead, we discriminate between the atomic and the molecular gas (see Sect. 5.3.1).

Turbulent energy from supernova feedback

The timescale of turbulence dissipation is defined as the ratio between the turbulent energy and its dissipation rate (e.g. Elmegreen & Scalo, 2004; Mac Low & Klessen, 2004). In the stationary Kolmogorov's regime, the dissipation rate at the viscosity scale must be equal to the injection rate at the driving scale \dot{E}_{turb} . Therefore, the dissipation timescale can be written as (e.g. Mac Low, 1999)

$$\tau_{\text{d}} \equiv \frac{E_{\text{turb}}}{\dot{E}_{\text{turb}}} = \frac{L_{\text{D}}}{v_{\text{turb}}} \simeq (10 \text{ Myr}) \left(\frac{L_{\text{D}}}{100 \text{ pc}} \right) \left(\frac{v_{\text{turb}}}{10 \text{ km s}^{-1}} \right)^{-1}, \quad (5.4)$$

which corresponds to the crossing time of turbulent gas across the driving scale L_{D} (e.g. Elmegreen, 2000). This latter is difficult to measure precisely from observations and likely depends on the size of the physical system and the mechanisms under consideration. We note that, as Eq. 5.2 and Eq. 5.3, Eq. 5.4 is valid in general for any source of turbulent energy.

This work is focused on SNe, as they are expected to dominate the energy input by stellar feedback on the scale of galactic discs (see Sect. 5.5.5 for a discussion on other possible sources). We therefore adopted a specific equation to calculate E_{turb} in Eq. 5.2 in the case of SNe (i.e. $E_{\text{turb,SNe}}$). In particular, we assumed that

$$L_{\text{D}} = 2h, \quad (5.5)$$

where h is the scale height of the gas disc, and it is h_{HI} for the atomic gas and h_{H_2} for the molecular gas. This choice is motivated by theoretical models of SN remnant evolution and by observational evidence showing that the explosion of multiple SNe generates expanding shells (super-bubbles), whose diameter can easily reach the thickness of the atomic gas disc (e.g. Mac Low et al., 1989; Boomsma et al., 2008). In addition, L_{D} corresponds to the size of the largest eddies, which are expected to be approximately as large as the physical scale of the system. We discuss in depth the assumption of Eq. 5.5 in Sect. 5.5.4.

The gas scale height for each galaxy in our sample was calculated with the same method as in Chapter 2: the gas is assumed in vertical hydrostatic

equilibrium in the galactic potential and h is derived iteratively with the Python module GALPYNAMICS¹ (Iorio, 2018) in order to also take into account the gas self-gravity. The scale height of the gas distribution increases for increasing velocity dispersion σ and for decreasing intensity of the vertical gravitational force g_z ; both g_z and σ decrease with radius, but the effect of g_z is dominant. Hence, the gas distribution flares with the radius and the scale height increases, reaching hundreds of parsecs in the outer regions of discs. For each galaxy, h_{HI} was calculated for the gravitational potential produced by stars and dark matter (see Sect. 2.2.2 for details), and then h_{H_2} was derived including also the potential of the atomic gas distribution with the flare.² The radial profiles of h_{HI} for our galaxies can be found in Fig. 2.1. A major improvement of this work is that h_{H_2} was calculated using the velocity dispersion measured from CO data (see Sect. 5.4.4). We, however, found that the resulting profiles are compatible within the errors with those obtained in Sect. 2.4.2, where we assumed $\sigma_{\text{H}_2} \approx \sigma_{\text{HI}}/2$ (see Fig. 2.1).

Taking NGC 2403 as an example, Figure 5.1 shows the dramatic effect of including the flaring of the HI when deriving the dissipation timescale as a function of the galactocentric radius (Eq. 5.4). The dashed black line is τ_{d} obtained with $\sigma_{\text{HI}} = 10 \text{ km s}^{-1}$ and $h_{\text{HI}} = 100 \text{ pc}$, which gives a constant dissipation timescale of 20 Myr. The red curve represents $\tau_{\text{d}}(R)$ calculated with the profiles of $h_{\text{HI}}(R)$ and of $\sigma_{\text{HI}}(R)$ from Chapter 2. At large radii, the dissipation timescale is prolonged by one order of magnitude with respect to the constant τ_{d} . In other words, the observed turbulent energy is easier to maintain in thick discs, even with few SN explosions. We note that the timescale shown in Fig. 5.1 should be considered a lower limit in the framework of Kolmogorov's theory, as the observed velocity dispersion used in this example still includes the contribution of thermal motions.

The rate of kinetic energy injected per unit area and per unit time by multiple SN explosions is (e.g. Tamburro et al., 2009; Utomo et al., 2019)

$$\dot{E}_{\text{turb,SNe}} = \eta \mathcal{R}_{\text{cc}} E_{\text{SN}}, \quad (5.6)$$

where η is the dimensionless efficiency of SNe in transferring kinetic energy to the ISM, \mathcal{R}_{cc} is the rate of core-collapse SNe per unit area, and $E_{\text{SN}} = 10^{51} \text{ erg}$ is the total energy released by a single SN. The SN rate per unit area can be obtained from the SFR surface density as

$$\mathcal{R}_{\text{cc}} = \Sigma_{\text{SFR}} f_{\text{cc}}, \quad (5.7)$$

where f_{cc} is the number of core-collapse SNe that explode for unit of stellar mass formed. This latter is $f_{\text{cc}} \approx 1.3 \times 10^{-2} \text{ M}_{\odot}^{-1}$ for a Kroupa initial mass

¹<https://github.com/iogiul/galpynamics>

²This choice implies that the atomic gas distribution is not influenced by the molecular gas distribution. We expect that including this latter does not significantly affect h_{HI} , as the molecular gas is concentrated in the inner regions of the galaxies, where stars are the dominant mass component.

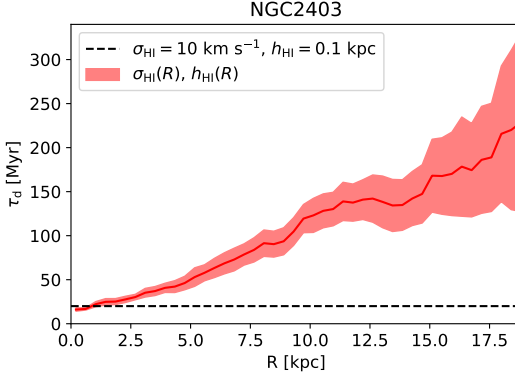


Figure 5.1 – Dissipation timescale of HI turbulence as a function of the galactocentric radius calculated with Eq. 5.4 for NGC 2403. The dashed black line is $\tau_d = 20$ Myr obtained with a constant velocity dispersion of 10 km s^{-1} and a constant scale height of 0.1 kpc (i.e. no flaring). The red curve and band are $\tau_d(R)$ and its uncertainty adopting the radially-decreasing $\sigma_{\text{HI}}(R)$ and the increasing $h_{\text{HI}}(R)$ from Chapter 2.

function (Kroupa, 2002). In Sect. 5.5.4, we discuss the effect of including type Ia SNe and different parameters for the initial mass function.

The turbulent energy per unit area from SN feedback is obtained from Eq. 5.4 using Eq. 5.5, Eq. 5.6, and Eq. 5.7,

$$E_{\text{turb,SNe}} = \eta \Sigma_{\text{SFR}} f_{\text{cc}} E_{\text{SN}} \frac{2h}{v_{\text{turb}}} \simeq \eta (2.6 \times 10^{46} \text{ erg pc}^{-2}) \left(\frac{\Sigma_{\text{SFR}}}{10^{-4} \text{ M}_{\odot} \text{ yr}^{-1} \text{ kpc}^{-2}} \right) \left(\frac{h}{100 \text{ pc}} \right) \left(\frac{v_{\text{turb}}}{10 \text{ km s}^{-1}} \right)^{-1}, \quad (5.8)$$

which gives the turbulent energy component in Eq. 5.2. In Sect. 5.3.2, we describe how we estimated η for our galaxies using the observational constraints obtained in Sect. 5.2.

Thermal energy

The thermal velocity in Eq. 5.3 mainly depends on the temperature of the gas T

$$v_{\text{th}} = \sqrt{\frac{k_{\text{B}} T}{\mu m_{\text{p}}}} \simeq (9.1 \text{ km s}^{-1}) \left(\frac{T}{10^4 \text{ K}} \right)^{\frac{1}{2}} \mu^{-\frac{1}{2}}, \quad (5.9)$$

where μ is the mean particle weight in units of the proton mass m_{p} and k_{B} is the Boltzmann constant. The mean particle weight varies with the chemical composition of the emitting particles: it is $\mu = 1$ for HI, and $\mu \simeq 28$ for CO. The thermal energy per unit area in Eq. 5.2 is

$$E_{\text{th}}(R) = \frac{3}{2} \Sigma(R) \frac{k_{\text{B}} T}{\mu m_{\text{p}}} \simeq (2.5 \times 10^{46} \text{ erg pc}^{-2}) \left[\frac{\Sigma(R)}{10 \text{ M}_{\odot} \text{ pc}^{-2}} \right] \left(\frac{T}{10^4 \text{ K}} \right) \mu^{-1}, \quad (5.10)$$

where $\Sigma(R)$ is the surface density of the gas (atomic or molecular), $\mu \approx 1.36$ for the atomic gas, and $\mu \approx 2.3$ for the molecular gas. Thanks to observations and physical models of the ISM, we have useful constraints on the temperature distribution of the atomic gas and the molecular gas in galaxies (see §4.2 and §D.2.2 in Cimatti, Fraternali, & Nipoti, 2019) and we can estimate the contribution of thermal motions to the observed velocity dispersion.

Atomic gas

The atomic (neutral) gas is distributed in two phases, CNM and WNM (e.g. Wolfire et al., 1995, 2003; Heiles & Troland, 2003), whose contribution to the total thermal velocity depends on their abundance. Let us define f_w as the mass fraction of warm atomic gas and label the rest as CNM (with mass fraction $1 - f_w$). The thermal energy in Eq. 5.2 is then

$$E_{\text{th}} = E_{\text{th,c}} + E_{\text{th,w}} = \frac{3}{2} \Sigma_{\text{atom}} [(1 - f_w) v_{\text{th,c}}^2 + f_w v_{\text{th,w}}^2], \quad (5.11)$$

where $E_{\text{th,c}}$ and $E_{\text{th,w}}$ are the thermal energy of the CNM and the WNM respectively, which can be calculated using Eq. 5.10 if their temperatures are known. In Eq. 5.3, we have then

$$v_{\text{th}} = \sqrt{f_w v_{\text{th,w}}^2 + (1 - f_w) v_{\text{th,c}}^2}, \quad (5.12)$$

where $v_{\text{th,c}}$ and $v_{\text{th,w}}$ are given by Eq. 5.9.

We take as references the average temperatures of the atomic gas resulting from the model by Wolfire et al. (2003) (see their Table 3), which are distributed between $T \approx 40$ K and $T \approx 190$ K for the CNM, and $T \approx 7000$ K and $T \approx 8830$ K for the WNM. These temperature ranges correspond to $0.6 \text{ km s}^{-1} \lesssim v_{\text{th,c}} \lesssim 1.3 \text{ km s}^{-1}$ for the cold HI and $7.6 \text{ km s}^{-1} \lesssim v_{\text{th,w}} \lesssim 8.6 \text{ km s}^{-1}$ for the warm HI, respectively. This approach implicitly assumes that the HI is thermally stable, while there are observational indications that ≈ 50 % of the HI in our Galaxy is in the thermally unstable state with $T \approx 500$ – 5000 K (Heiles & Troland, 2003; Kalberla & Haud, 2018; Murray et al., 2018). Given these uncertainties, we decided to consider two extreme cases, the first with $f_w = 0$ and the second with $f_w = 1$, which are analysed in Sect. 5.4.1 and Sect. 5.4.2. Clearly, in these two particular cases, we can directly use Eq. 5.9 and Eq. 5.10. This choice allows us to test whether SN feedback can maintain turbulence even with the minimum possible contribution from thermal motions (i.e. CNM case, $f_w = 0$) and to quantify the dependence of our results on the HI temperature distribution. In Sect. 5.4.3, we investigate the two-phase scenario with $0 < f_w < 1$ and using Eq. 5.11 and Eq. 5.12.

Molecular gas

Molecular gas is mostly observed in giant molecular clouds, where the temperatures are typically very low ($T \approx 10 - 15$ K). This gas can be slightly warmer close to young stars (e.g. Redaelli et al., 2017), but the coldest fraction is undoubtedly dominant in mass. We chose $10 \text{ K} \lesssim T \lesssim 15 \text{ K}$, which for CO roughly corresponds to $v_{\text{th}} \approx 0.06 \pm 0.005 \text{ km s}^{-1}$. Hence, thermal motions do not significantly contribute to the observed velocity dispersion (i.e. $5\text{--}15 \text{ km s}^{-1}$) for the typical temperatures in molecular clouds.

5.3.2 Comparison of the model with the observations

In this section, we summarise the method used to infer the SN feedback efficiency required to maintain the turbulent energy in our galaxies. Further details on the formalism of this method can be found in Appendix 5.B. A different, complementary approach is described in Appendix 5.C.

The algorithm works in the same way for the four cases under consideration: *i*) cold atomic gas, *ii*) warm atomic gas, *iii*) two-phase atomic gas, and *iv*) molecular gas (for seven galaxies). We note that the third case involves two free parameters, namely the SN efficiency and the fraction of WNM f_w , while the other only η . We assume that the observed velocity dispersion of the gas includes the contribution of thermal and turbulent motions (i.e. Eq. 5.3), and that turbulence is entirely driven by SNe, implying $0 < \eta < 1$ in Eq. 5.8. The efficiency is assumed to be constant with the galactocentric radius, but it is allowed to vary from one galaxy to another. We assume the same for f_w in the case of a two-phase atomic gas. We adopted a hierarchical Bayesian approach (e.g. Delgado et al., 2019; Cannarozzo et al., 2020; Lamperti et al., 2019) to compare a model for the energy components to the observed profiles.

Bayesian inference is based on Bayes' theorem

$$p(\Theta|\mathcal{D}) \propto p(\mathcal{D}|\Theta)p(\Theta), \quad (5.13)$$

where $p(\Theta|\mathcal{D})$ is the probability distribution of a model depending on a set of parameters Θ given the data \mathcal{D} , $p(\mathcal{D}|\Theta)$ is the probability distribution of the data given a set of parameters (i.e. the likelihood), and $p(\Theta)$ is the prior distribution of the parameters, which includes our a-priori knowledge about their value. The Bayesian approach allows us to take into account the uncertainties on the observed quantities (including the upper limits on Σ_{SFR}), the priors, and the correlation between the model parameters (see for example the case of the two-phase atomic gas in Sect. 5.4.3). Thus, we obtain a posterior distribution on η which is marginalised over all the other parameters (when present) of the model.

Hierarchical methods allow a further level of variability, as the priors on the model parameters depend on an additional set of parameters, the hyper-priors. In other words, the parameters of the priors (Φ) are sampled as the

other parameters of the model, assigning them hyper-prior distributions $p(\Phi)$. Thus, Bayes' rule is written as

$$p(\Theta|\mathcal{D}) \propto p(\mathcal{D}|\Theta)p(\Theta|\Phi)p(\Phi), \quad (5.14)$$

where $p(\Theta|\Phi)$ is the probability distributions of the priors given the hyper-priors. This allows us to parametrise the uncertainty on the priors and use it to obtain robust errors on the final value of η .

In practice, the observed Σ_{SFR} and h are considered as realisations of normal distributions centered on unknown true values (i.e. Σ_{SFR}^T and h^T) and with standard deviation given by the uncertainty on the measurements (i.e. $\Delta\Sigma_{\text{SFR}}$ and Δh).³ The true values are assumed to have a log-normal distribution, which depends on priors and hyper-priors (see Appendix 5.B). For any given galaxy, Σ_{SFR}^T and h^T are compared with the observed values Σ_{SFR} and h in order to obtain the probability of the observed values given the true values (i.e. the likelihood). For four galaxies in the sample (i.e. DDO 154, NGC 2403, NGC 3198, and NGC 6946), the values of the observed SFR surface density at large radii are upper limits, hence Σ_{SFR}^T is assumed to be a uniform distribution from 0 to the upper limit (see Sect. 5.2.3).

Similarly, the observed velocity dispersion σ is compared to the distribution of a true velocity dispersion σ^T to calculate the likelihood probability. In particular, σ^T is obtained through Eq. 5.3, which requires to model the thermal and the turbulent velocity components. We have seen in Sect. 5.3.1 that the thermal equilibrium models of the ISM provide useful constraints on the temperature ranges of the gas and the contribution of thermal motions. Hence, we assume that the center and the standard deviation of the thermal velocity distribution are different for the three single-phase cases under consideration: *i*) 1 km s^{-1} and 0.4 km s^{-1} for the cold atomic gas, *ii*) 8.1 km s^{-1} and 0.5 km s^{-1} for the warm atomic gas, and *iv*) 0.06 km s^{-1} and 0.005 km s^{-1} for the molecular gas. For the two-phase case, the thermal velocity is modelled as a uniform distribution between 1 km s^{-1} and 8.1 km s^{-1} . Our a priori knowledge about the turbulent motions is instead very limited, hence we define v_{turb}^T as a log-normal distribution characterised by weakly informative priors and hyper-priors on its centroid velocity and standard deviation (see Appendix 5.B).

A fourth observed quantity, namely the gas surface density Σ , is available to constrain the parameters of our model for the theoretical energy of the gas. We can use v_{turb}^T to calculate two useful distributions: *a*) the turbulent energy per unit mass $3/2(v_{\text{turb}}^T)^2$, and *b*) the energy from SNe $E_{\text{turb,SNe}}$ (Eq. 5.8). This latter is derived using a uniform prior for η , whose value is between 0 and 1 (see Appendix 5.B). By dividing $E_{\text{turb,SNe}}$ by the density-normalised turbulent energy, we obtain a 'prediction' for the gas surface density that can be compared with the observed one, which is modelled as a normal distribution centered on Σ

³We implicitly consider the scale height h as observed data, even if it is derived assuming the hydrostatic equilibrium (see Sect. 2.2).

and with standard deviation $\Delta\Sigma$. From this comparison, we infer the posterior probability of the observed values given this prediction for the surface density.

Finally, we obtain the posterior distribution of η by marginalising over all the other parameters (including those of priors and hyper-priors) of the model and calculate its median value, whose uncertainty is given by the 16th and the 84th percentiles of the posterior distribution. Henceforth, we refer to this median value as the ‘best efficiency’. In the case of the two-phase atomic gas, we derive the posterior distribution of f_w and its median (i.e. best) value as well. These best values characterise the ‘best model’ in each case under consideration. For each best model, we extract the posterior distributions of $E_{\text{th},c}(R)$, $E_{\text{th},w}(R)$, $E_{\text{th}}(R)$, $E_{\text{turb,SNe}}(R)$, and $E_{\text{mod}}(R)$ shown in Sect. 5.4 (see Appendix 5.B), and of $v_{\text{turb}}^T(R)$, which is used in Sect. 5.4.2 to analyse the Mach number in the case of warm atomic gas. The errors on these quantities are calculated as the 16th and the 84th percentile of the posterior distributions. The parameter space is explored with the Hamiltonian Monte Carlo sampler implemented in the Python routine PyMC3 (Hoffman & Gelman, 2011; Salvatier et al., 2016).

5.4 Results

In this section, we present the results of our analysis and focus on the best values of the SN feedback efficiency required to sustain turbulence in the atomic gas and the molecular gas of our sample of galaxies. As already mentioned, we first explore two extreme single-phase cases for the atomic gas, one with CNM only and the other with WNM only, aiming to derive a robust range of values for η . Second, we analyse the more realistic two-phase atomic gas, in which we attempt to derive not only the SN efficiency for each galaxy but also the fraction of WNM. Lastly, we consider the case of the molecular gas. We expect to find different values of η according to the case under consideration, hence we adopt a different nomenclature in each situation: $\eta_{\text{atom},c}$ for the CNM, $\eta_{\text{atom},w}$ for the WNM, $\eta_{\text{atom},2\text{ph}}$ for the two-phase atomic gas, and η_{mol} for the molecular gas.

5.4.1 Cold atomic gas

In the case of all atomic gas in the CNM phase (i.e. $f_w = 0$), thermal motions give the least possible contribution to the total energy and the turbulent energy is dominant. Hence, the efficiency $\eta_{\text{atom},c}$ can be seen as an upper limit.

Figure 5.2 shows, for the galaxies in our sample, the observed energy E_{obs} (black points, Eq. 5.1) and the total kinetic energy E_{mod} of the best model (green area, Eq. 5.2) using the SFR surface density from Leroy et al. (2008) and Bigiel et al. (2010). E_{mod} is the sum of the thermal energy $E_{\text{th},c}$ (blue area, Eq. 5.10) and the turbulent energy injected by SNe $E_{\text{turb,SNe}}$ (red area, Eq. 5.8). We note that the turbulent energy is typically two orders of magnitude higher than thermal energy of the CNM at all radii, hence the areas representing $E_{\text{mod}}(R)$

and $E_{\text{turb,SNe}}(R)$ tend to overlap. The dotted grey vertical line indicates, for DDO 154, NGC 2403, NGC 3198 and NGC 7793, the outermost radius with measured Σ_{SFR} , hence the upper limit is used for the radii beyond.

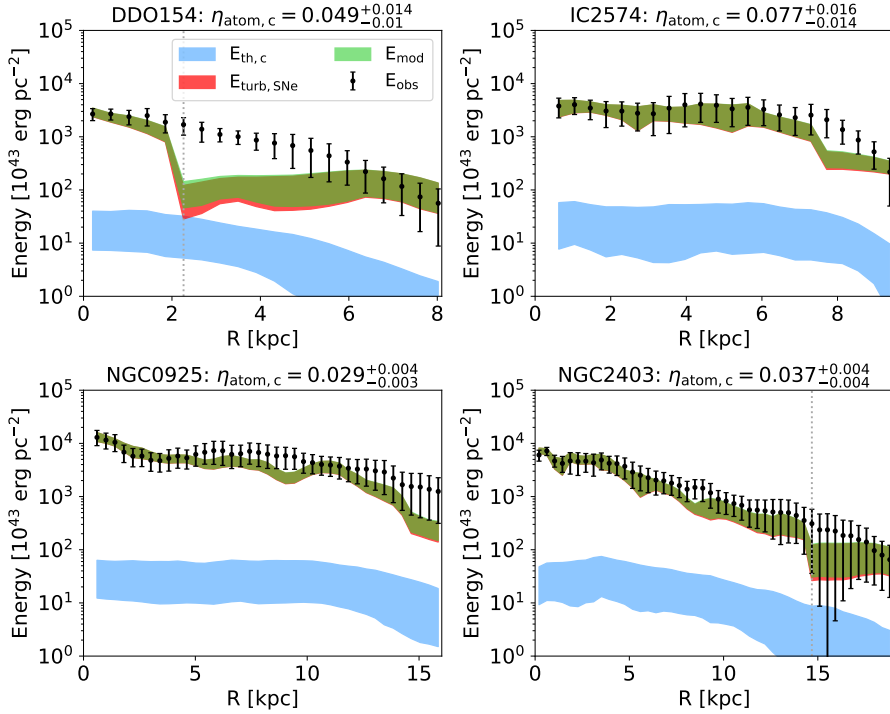


Figure 5.2 – Observed kinetic energy per unit area of the atomic gas (black points) for our sample of galaxies (the errors are calculated with the uncertainty propagation rules applied to Eq. 5.1). The blue area shows the thermal energy ($E_{\text{th,c}}$) of atomic gas if it is assumed to be only CNM. The red area is the turbulent energy injected by SNe ($E_{\text{turb,SNe}}$) with the efficiency $\eta_{\text{atom,c}}$ reported on top of each panel. The green area represents the total energy (E_{mod}) calculated as the sum of $E_{\text{th,c}}$ and $E_{\text{turb,SNe}}$ (see Sect. 5.3.2 and Appendix 5.B). The observed profiles are well reproduced by the theoretical energy for almost all the galaxies. The grey dotted vertical line, when present, indicates the outermost radius with measured Σ_{SFR} , hence the upper limit is used for larger radii. Figure continued on page 161.

The profiles of the observed energy are well reproduced by the theoretical total energy for almost all the galaxies. The efficiencies are $\lesssim 0.08$ and their median value is $\langle \eta_{\text{atom,c}} \rangle \approx 0.035$ (see Table 5.1), showing that SNe with low efficiency can sustain turbulence. However, our model cannot fully reproduce the observed energy in the region $2 \text{ kpc} \lesssim R \lesssim 5 \text{ kpc}$ of DDO 154 and in the outskirts of IC 2574 and NGC 6946, indicating that some contribution from the thermal energy of the WNM may be required. We stress that the assumption that all the atomic gas is in the form of CNM is extreme and unrealistic, so

in this case we are underestimating the thermal contribution. Using the SFR surface density from Muñoz-Mateos et al. (2009), we obtain efficiencies that are, on average, a factor of ~ 2 lower than the values found using the profiles from Leroy et al. (2008) and the median is indeed $\langle \eta_{\text{atom},c} \rangle \approx 0.015$ (see Table 5.1).

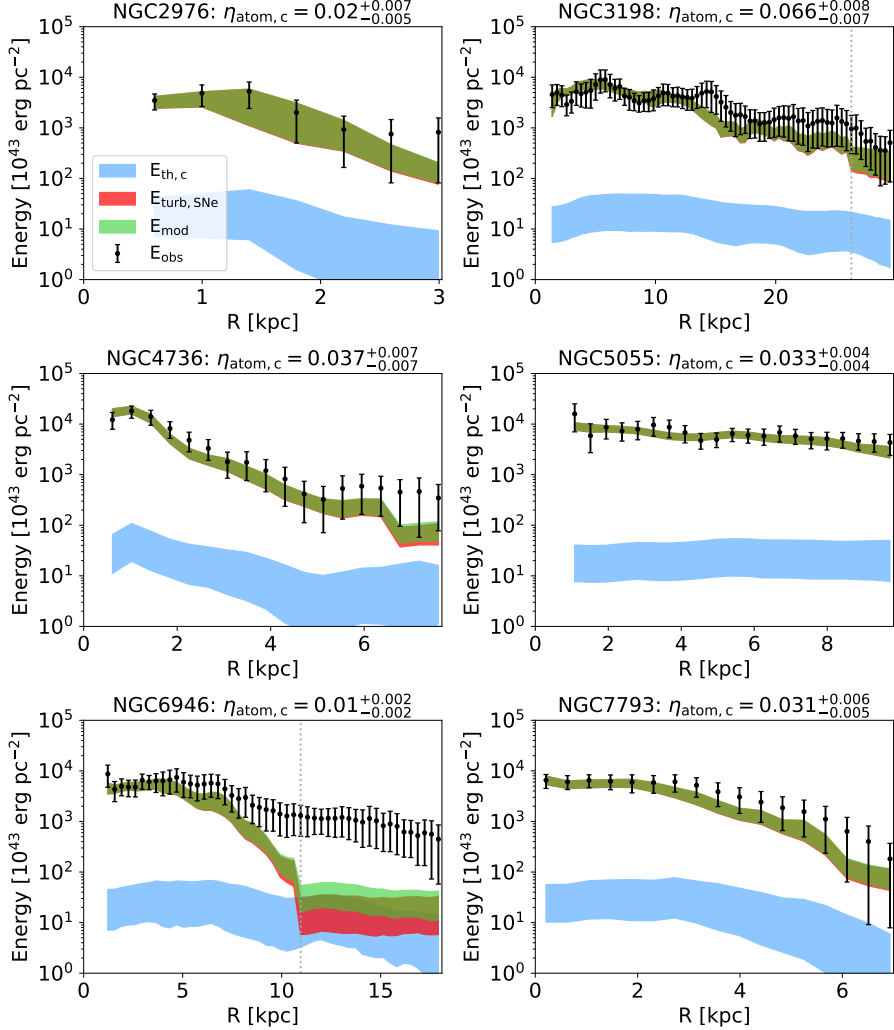


Figure 5.2 – Continued.

We note that turbulent motions are supersonic in the case of cold atomic gas (i.e. $v_{\text{turb}} \gg v_{\text{th},c}$). Since the ISM is compressible, supersonic turbulence produces shocks that transform kinetic energy into internal energy, which may also be lost radiatively (see e.g. Tielens, 2005, § 11). This would invalidate

the energy conservation in the inertial range of the cascade assumed in our model, which is based on the implicit assumption of gas incompressibility in order to apply the Kolmogorov's theory. In the supersonic regime, our model may be suitable to describe the solenoidal motions, which are incompressible and conserve the energy (Elmegreen & Scalo, 2004). The solenoidal motions are expected to be dominant with respect to the compressible ones (see Sect. 5.4.4 for further discussion). We stress moreover that the case of cold atomic gas is unrealistic, hence we may expect that strong shocks have a more limited impact.

5.4.2 Warm atomic gas

We now consider the case of atomic gas in the warm phase (i.e. WNM), thus the thermal motions give the maximum possible contribution to the total energy. Hence, the efficiency of SN feedback $\eta_{\text{atom,w}}$ can be considered a lower limit. In Fig. 5.3, we show the observed energy and the total energy of the best model using the SFR surface density from Leroy et al. (2008).

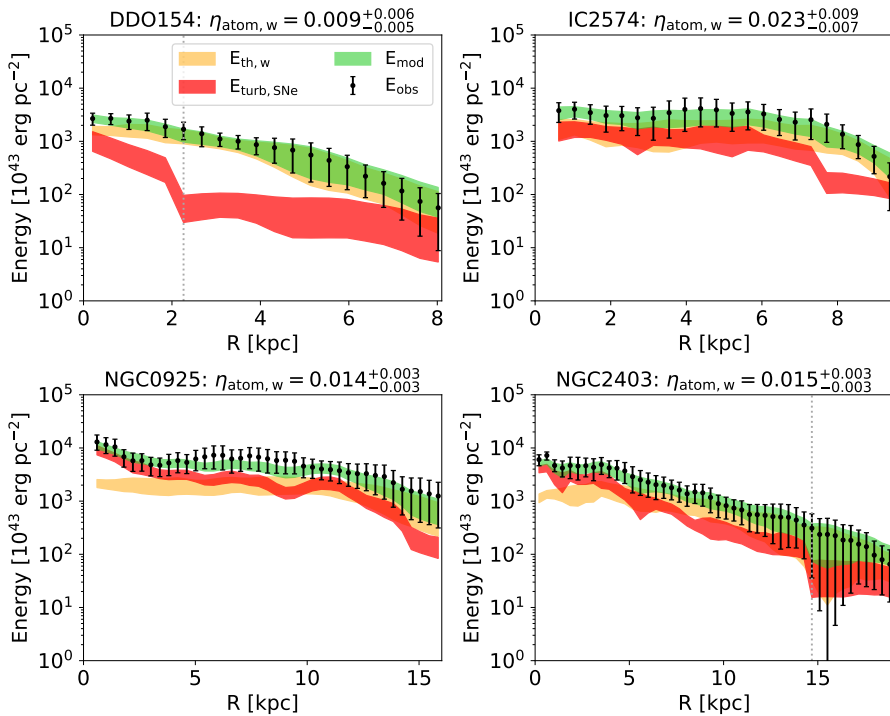


Figure 5.3 – Same as Fig. 5.2, but the atomic gas is assumed to be only WNM in this case. The orange band shows the thermal energy ($E_{\text{th,w}}$) and the best efficiency is indicated as $\eta_{\text{atom,w}}$. Figure continued on page 163.

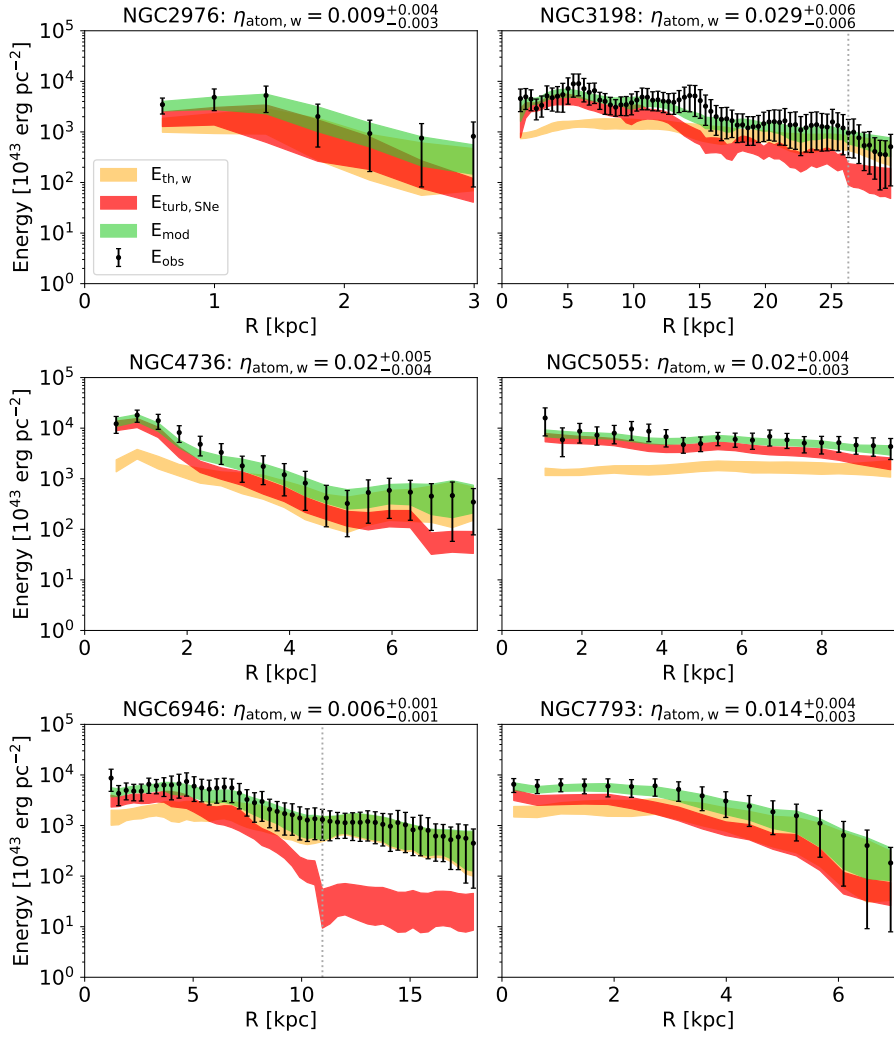


Figure 5.3 – Continued.

The profiles of the observed energy are very well reproduced, better than in the previous case for the CNM. The main difference with respect to Fig. 5.2 is that $E_{\text{turb,SNe}}$ typically dominates only in the inner regions of galaxies, while it is comparable to or lower than $E_{\text{th,w}}$ (orange area) in the other parts. The efficiencies are generally a factor of ≈ 2 lower than in the case of cold atomic gas and the median value is $\langle \eta_{\text{atom,w}} \rangle \approx 0.015$ (Table 5.1). This indicates that SN feedback with low efficiency can maintain turbulence in the warm atomic gas and that no additional source is required. Using the SFR surface density

from Muñoz-Mateos et al. (2009), the resulting efficiencies are lower than those obtained with the other profiles, the median is indeed $\langle \eta_{\text{atom,w}} \rangle \approx 0.006$.

In the case of warm atomic gas, it is interesting to analyse the profile of the turbulent velocity in our galaxies to see whether turbulence is supersonic or subsonic. For our sample of galaxies, we calculated the Mach number ($\mathcal{M} \equiv v_{\text{turb}}/v_{\text{th,w}}$) as a function of the galactocentric radius using the posterior distribution of $v_{\text{turb}}^T(R)$ obtained from the method described in Sect. 5.3.2 and the thermal velocity $v_{\text{th,w}} \approx 8.1 \text{ km s}^{-1}$. We found that turbulent motions are generally weakly supersonic (i.e. transonic regime): the Mach number typically reaches values of about 2–2.5 only in the innermost regions of spiral galaxies, while it is $\mathcal{M} \lesssim 1$ in their outskirts and for dwarf galaxies. The median value is indeed $\langle \mathcal{M} \rangle \approx 1$. This suggests that, at least in the transonic regions, adopting Kolmogorov’s theory for incompressible fluids may be acceptable in the case of warm atomic gas.

5.4.3 Two-phase atomic gas

As already mentioned, both observations and theoretical models of the ISM indicate that the atomic gas is distributed in two phases, CNM and WNM (e.g. Heiles & Troland, 2003; Wolfire et al., 2003). Hence, it is interesting to investigate this scenario, as it is more realistic than the single-phase cases seen in Sect. 5.4.1 and Sect. 5.4.2. We used the same method explained in Sect. 5.3.2, but the thermal speed and thermal energy are calculated using Eq. 5.11 and Eq. 5.12. The thermal speed is the second free parameter in the model and it is used to obtain the WNM fraction f_w together with the SN efficiency $\eta_{\text{atom,2ph}}$. This experiment has two possible outcomes: *i*) if the observed velocity dispersion is lower than the thermal velocity of the WNM, the posterior distributions for $\eta_{\text{atom,2ph}}$ and v_{th} (and therefore f_w) will be well-constrained and we will calculate the median and the 1σ uncertainty on the best parameters; *ii*) if the observed velocity dispersion is higher than the WNM thermal velocity, the best model will tend to be WNM-dominated and equivalent to the case seen in Sect. 5.4.2. NGC 2403 and NGC 4736, which we discuss below, fall into the former case, while the rest of the galaxies in the sample is compatible with having $f_w \approx 1$, hence the resulting efficiencies are equivalent to those in Table 5.1 for the warm atomic gas.

The left panels in Fig. 5.4 show the result of this analysis for NGC 2403 and NGC 4736: the profiles of the observed energy are remarkably well reproduced by the two-phase best model, for both galaxies. We note that the SN energy is the dominant component in the inner regions, while the total thermal energy (dashed area) tends to become equally significant at large radii, as in the case of warm atomic gas (see Fig. 5.3). The right panels in Fig. 5.4 show the corner plots for the $\eta_{\text{atom,2ph}}$ and f_w , which are obtained from the posterior distribution of v_{th} through Eq. 5.12. From the 1D and the 2D posterior distributions, we can see that both parameters are well-constrained, despite the expected degeneracy.

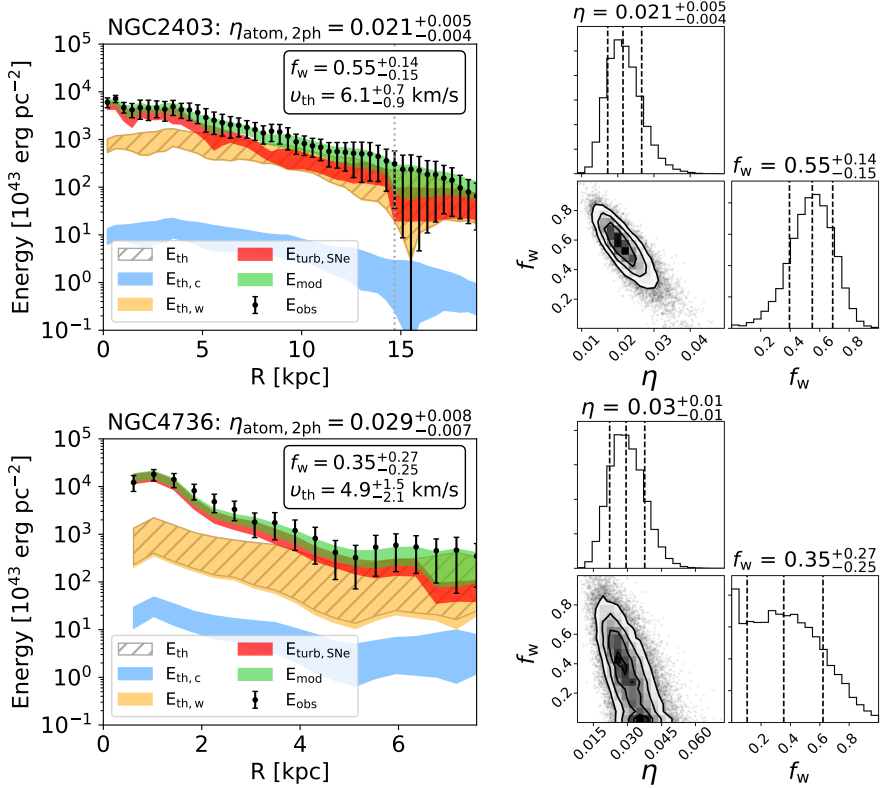


Figure 5.4 – *Left panels:* Observed kinetic energy per unit area of the atomic gas (black points; E_{obs} from Eq. 5.1) for NGC 2403 (upper panel) and NGC 4736 (lower panel). The blue and the orange bands show respectively the thermal energy of the cold ($E_{\text{th,c}}$) and the warm ($E_{\text{th,w}}$) atomic gas. The green area is the total kinetic energy predicted by our best model (E_{mod} ; see also Appendix 5.B), which includes the total thermal energy (grey dashed area; i.e. E_{th} from Eq. 5.11) and the turbulent energy injected by SN feedback (red area; $E_{\text{turb,SNe}}$ from Eq. 5.8) with the best efficiency reported on top of the panel. The grey dotted vertical line indicates the outermost radius of NGC 2403 with measured Σ_{SFR} , the upper limit is used for larger radii. The best fraction of WNM (f_w) is reported in the top-right box, together with the corresponding thermal velocity of the atomic gas (Eq. 5.12). The observed profile is very well reproduced by the theoretical energy of the best model. *Right panels:* Corner plot showing the marginalised posterior distributions of the SN efficiency and the fraction of WNM f_w . The best values with 1σ uncertainties are reported on top of each panel of the 1D posterior distribution.

We obtain that the best model is given by $\eta_{\text{atom,2ph}} \simeq 0.021$ and $f_w \simeq 0.55$ (or $v_{\text{th}} \simeq 6.1 \text{ km s}^{-1}$) for NGC 2403, and $\eta_{\text{atom,2ph}} \simeq 0.029$ and $f_w \simeq 0.35$ (or $v_{\text{th}} \simeq 4.9 \text{ km s}^{-1}$) for NGC 4736. It is surprising that, despite the unavoidable limitations of our approach, the estimates of the fraction of WNM are compatible with those obtained using different methods for the solar neighborhood (e.g. Heiles & Troland, 2003), the Milky Way outskirts (Pineda et al., 2013), and the Magellanic Clouds (Marx-Zimmer et al., 2000; Dickey et al., 2000). We note that the best efficiency is compatible within the uncertainties with the value obtained in the WNM-only case. Indeed, we expect that the thermal broadening is dominated by the WNM, even with a fraction of WNM of about 40–60%. It is worth to point out that the uncertainties on $\eta_{\text{atom,2ph}}$ should be more reliable than those obtained in the single-phase cases, as the best efficiencies is also marginalised on the thermal speed in this case (as this model takes into account the possible presence of CNM).

We must keep in mind two possible caveats of this analysis. First, we did not include any radial gradient of the fraction of WNM, which may not be a realistic assumption for some galaxies (e.g. the Milky Way; Pineda et al. 2013, but see Murray et al. 2018 for a different conclusion). We could assume some functional form for f_w , linear or exponential trends with radius for instance, but this choice would introduce at least two additional free parameters in the model. The second possible caveat is the assumption that the atomic gas is thermally stable and distributed in CNM and WNM, although there are observational indications that a fraction of the atomic gas may be in the thermally unstable region (e.g. Heiles & Troland, 2003; Kalberla & Haud, 2018; Murray et al., 2018). If we do not assume thermal equilibrium, we can use Eq. 5.9 and the best v_{th} mentioned above to estimate the temperature of the atomic gas distributed in a single phase. For NGC 2403 and NGC 4736, respectively, we obtain $T \approx 5800 \text{ K}$ and $T \approx 3800 \text{ K}$, which both correspond to the thermally unstable regime (Wolfire et al., 2003; Tamburro et al., 2009).

5.4.4 Molecular gas

Based on the kinematic analysis of CO data cubes (see Appendix 5.A), we know that the velocity dispersion of CO is much higher than the thermal velocity expected for gas with $T \approx 10 - 15 \text{ K}$ (i.e. $0.05\text{--}0.07 \text{ km s}^{-1}$), indicating strong turbulent motions (e.g. Rosolowsky & Blitz, 2005; Sun et al., 2018). This fact allows us to find a very robust estimate for the SN efficiency η_{mol} .

In Fig. 5.5, we show the example of NGC 6946, which has an extended molecular gas disc. The profile of the observed energy (black squares) is well reproduced by the theoretical profile E_{mod} with a SN efficiency of about 0.003, except for the points at $R \approx 1.2 \text{ kpc}$ and $R \approx 6.4 \text{ kpc}$, which are however uncertain because of the non-circular motions in the innermost regions (see Appendix 5.A) and the low S/N at large radii. As expected, the turbulent energy is fully dominant with respect to the thermal energy (blue area). For

the rest of our the sample, E_{obs} is also very well reproduced by models with $\eta_{\text{mol}} \lesssim 0.016$, and the median value of the efficiency is ≈ 0.004 (see Table 5.1). In Table 5.1, the shaded rows report the best efficiency values obtained using the SFR surface density from Muñoz-Mateos et al. (2009). In general, the values are lower with respect to those found with the Σ_{SFR} from Leroy et al. (2008), but the two estimates are compatible within the errors.

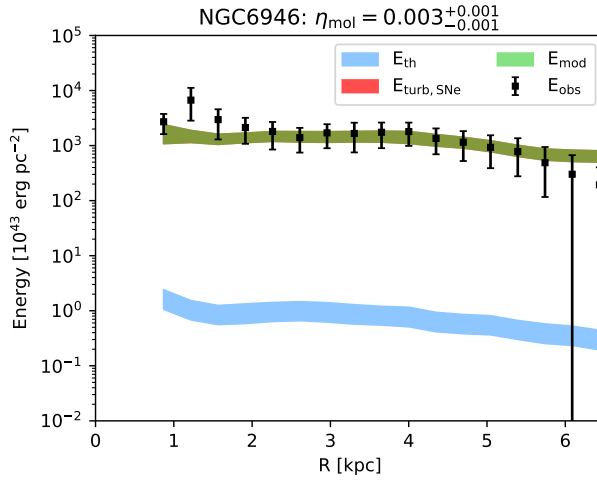


Figure 5.5 – Observed kinetic energy per unit area of the molecular gas (black squares) for NGC 6946. The green area represents the total theoretical energy (E_{mod} ; see also Appendix 5.B) calculated as the sum of the thermal energy (blue band; E_{th}) and the turbulent energy injected by SNe (red band; $E_{\text{turb,SNe}}$) with the efficiency η_{mol} reported on top of the panel. $E_{\text{turb,SNe}}$ is indistinguishable from E_{mod} , as the thermal energy contribution is negligible.

In the case of molecular gas, turbulent motions are strongly supersonic. As mentioned in Sect. 5.4.1, our model is not suitable to describe this regime, as the energy is not conserved in the turbulent cascade and Kolmogorov’s theory cannot be applied (e.g. Elmegreen & Scalo, 2004). Recent numerical simulations of SN-driven supersonic turbulence in molecular clouds suggest that the ratio between compressible and solenoidal motions is about $1/3 - 1/2$ (Padoan et al. 2016; Pan et al. 2016; see also Orkisz et al. 2017 for an observational study). We could speculate that, if solenoidal and compressible motions are separable, the SN efficiency obtained with our model should be multiplied by a factor of the order of unity to take into account the kinetic energy dissipated through shocks.

Table 5.1 – SN feedback efficiency required to sustain turbulence in the neutral gas of our sample of galaxies. The values in the white rows are obtained with the SFR surface density from Leroy et al. (2008) and Bigiel et al. (2010), while those in the shaded rows are derived with the profiles from Muñoz-Mateos et al. (2009), whose sample does not include DDO 154 (indicated with –). The last two rows show the median values obtain from the posteriors of all the galaxies in the sample. The three columns report the best values in different cases: (1) all atomic gas is CNM; (2) all atomic gas is WNM; (3) molecular gas (– indicates that no molecular gas emission is detected).

Galaxy	SN efficiency		
	$\eta_{\text{atom,c}}$ (1)	$\eta_{\text{atom,w}}$ (2)	η_{mol} (3)
DDO 154	$0.049^{+0.014}_{-0.010}$	$0.009^{+0.006}_{-0.005}$	–
	–	–	–
IC 2574	$0.077^{+0.016}_{-0.014}$	$0.023^{+0.009}_{-0.007}$	–
	$0.021^{+0.003}_{-0.003}$	$0.007^{+0.002}_{-0.002}$	–
NGC 0925	$0.029^{+0.004}_{-0.003}$	$0.014^{+0.003}_{-0.003}$	$0.0004^{+0.0002}_{-0.0001}$
	$0.020^{+0.002}_{-0.002}$	$0.010^{+0.002}_{-0.002}$	$0.0004^{+0.0002}_{-0.0001}$
NGC 2403	$0.037^{+0.004}_{-0.004}$	$0.015^{+0.003}_{-0.003}$	$0.004^{+0.002}_{-0.002}$
	$0.013^{+0.001}_{-0.001}$	$0.006^{+0.001}_{-0.001}$	$0.002^{+0.001}_{-0.001}$
NGC 2976	$0.020^{+0.007}_{-0.005}$	$0.009^{+0.004}_{-0.003}$	$0.0013^{+0.008}_{-0.007}$
	$0.012^{+0.003}_{-0.003}$	$0.005^{+0.002}_{-0.002}$	$0.0010^{+0.0006}_{-0.0006}$
NGC 3198	$0.066^{+0.008}_{-0.007}$	$0.029^{+0.006}_{-0.006}$	$0.016^{+0.008}_{-0.006}$
	$0.018^{+0.002}_{-0.002}$	$0.010^{+0.002}_{-0.002}$	$0.007^{+0.004}_{-0.003}$
NGC 4736	$0.037^{+0.007}_{-0.007}$	$0.020^{+0.005}_{-0.004}$	$0.006^{+0.002}_{-0.002}$
	$0.012^{+0.002}_{-0.002}$	$0.006^{+0.002}_{-0.001}$	$0.003^{+0.001}_{-0.001}$
NGC 5055	$0.033^{+0.004}_{-0.004}$	$0.020^{+0.004}_{-0.003}$	$0.010^{+0.003}_{-0.002}$
	$0.027^{+0.004}_{-0.003}$	$0.016^{+0.003}_{-0.003}$	$0.009^{+0.002}_{-0.002}$
NGC 6946	$0.010^{+0.002}_{-0.002}$	$0.006^{+0.001}_{-0.001}$	$0.003^{+0.001}_{-0.001}$
	$0.008^{+0.001}_{-0.001}$	$0.003^{+0.001}_{-0.001}$	$0.0024^{+0.0005}_{-0.0004}$
NGC 7793	$0.031^{+0.006}_{-0.005}$	$0.014^{+0.004}_{-0.003}$	–
	$0.013^{+0.002}_{-0.002}$	$0.006^{+0.002}_{-0.001}$	–
All	$0.035^{+0.029}_{-0.014}$	$0.015^{+0.009}_{-0.008}$	$0.0042^{+0.0075}_{-0.0035}$
	$0.015^{+0.008}_{-0.005}$	$0.006^{+0.005}_{-0.002}$	$0.0024^{+0.0056}_{-0.0018}$

5.5 Discussion

Our results show that SN feedback can maintain turbulence in the atomic gas of nearby disc galaxies with injection efficiency between 0.003 and 0.077. To drive molecular gas turbulence, the required efficiencies are also low ($\eta_{\text{mol}} \lesssim 0.016$). Hence, turbulence can be sustained by SNe alone and no other energy sources are required.

5.5.1 A ‘global’ SN efficiency for nearby galaxies?

We have seen that the values of the best efficiency depend on the choice of the SFR surface density. In the case of the atomic gas, the efficiency depends on the assumed temperature distribution as well. However, finding a single value for the efficiencies may be useful, for example, to include a recipe for SN feedback in numerical simulations and analytical models of galaxy evolution. We can use the posterior distributions of $\eta_{\text{atom,c}}$ and $\eta_{\text{atom,w}}$ to obtain this value in the case of the atomic gas (i.e. $\langle \eta_{\text{atom}} \rangle$) and those of η_{mol} for the molecular gas (i.e. $\langle \eta_{\text{mol}} \rangle$). For each galaxy, we extracted a random sub-sample of one thousand values from the posterior distributions of the efficiency in each of the cases explored in Sect. 5.4. For the atomic gas, we have four cases to consider: *i*) CNM and *ii*) WNM with Σ_{SFR} from Leroy et al. (2008) and Bigiel et al. (2010), and *iii*) CNM and *iv*) WNM with Σ_{SFR} from Muñoz-Mateos et al. (2009). For the molecular gas, we have only two cases, each with a different Σ_{SFR} . We calculated the median and the 1σ uncertainty using the sub-samples of the posterior distributions, finding $\langle \eta_{\text{atom}} \rangle = 0.015_{-0.008}^{+0.018}$ for the atomic gas and $\langle \eta_{\text{mol}} \rangle = 0.003_{-0.002}^{+0.006}$ for the molecular gas.

Figure 5.6 aims to summarise our findings. The left-hand side concerns the atomic gas and the right-hand side is for the molecular gas. The panels in the top row show the maximum SN energy (i.e. Eq. 5.8 with $\eta = 1$) on the x -axis and the turbulent component of the observed energy ($E_{\text{obs,turb}}$, i.e. Eq. 5.1 with the thermal energy subtracted) on the y -axis. To make all the points visible, we do not display the uncertainties and the symbols for the CNM cases are shaded (given that this scenario is also not fully realistic for the atomic gas). The red and the dark red lines show the relations $E_{\text{obs,turb}} = \langle \eta_{\text{atom}} \rangle E_{\text{turb,SNe}}$ and $E_{\text{obs,turb}} = \langle \eta_{\text{mol}} \rangle E_{\text{turb,SNe}}$ for the atomic gas and the molecular gas, respectively. The panels in the bottom row show the best efficiencies, as derived with the method described in Sect. 5.3.2, in comparison with the averages $\langle \eta_{\text{atom}} \rangle$ and $\langle \eta_{\text{mol}} \rangle$. We can clearly see that, for the atomic gas, efficiencies above 0.1 are not required to sustain the observed turbulent energy. The majority of the points in the top left panel follow the relation with slope $\langle \eta_{\text{atom}} \rangle$, indicating that an efficiency of about 0.015 may be a ‘global’ value for the galaxies in our sample. Only a few points belong to the region where $\eta > 0.1$, but they correspond to the CNM cases, which are not very realistic. Similarly, the top right panel shows that the efficiencies for the molecular gas are lower than ~ 0.01

for our galaxies and that a possible ‘global’ value is $\langle\eta_{\text{mol}}\rangle \approx 0.003$. This may suggest that most of the SN energy is transferred to the atomic gas, which is typically the dominant gas phase across the galactic disc.

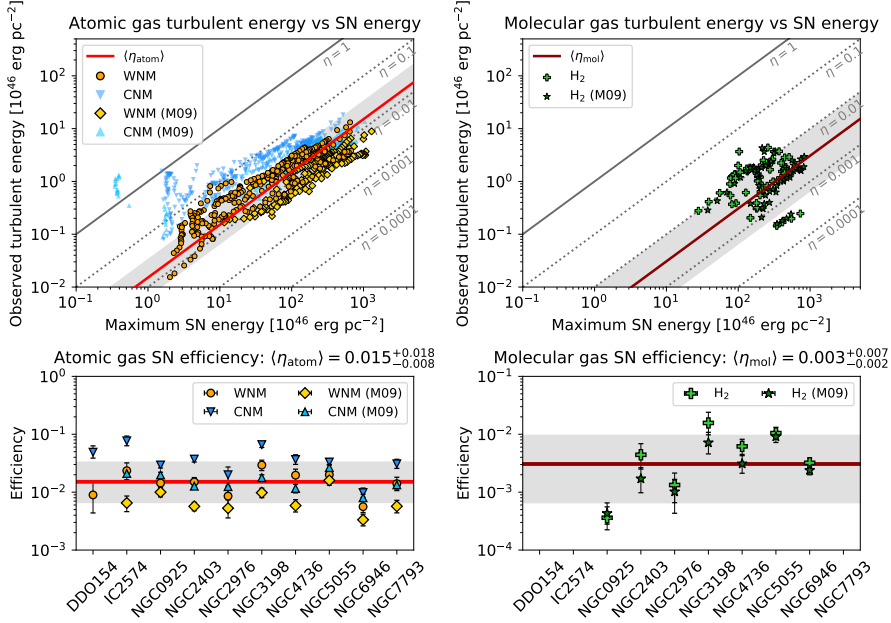


Figure 5.6 – *Top row*: Maximum energy provided by SNe in a dissipation timescale versus the turbulent component of the observed energy, both for the atomic gas (left) and the molecular gas (right). In the left panel, the orange points and the blue triangles are respectively for the cases of CNM and of WNM with Σ_{SFR} from Leroy et al. (2008) and Bigiel et al. (2010), while the yellow diamonds and the light blue triangles show the corresponding cases with Σ_{SFR} from Muñoz-Mateos et al. (2009). Each point is for a single galaxy and for a single radius. In the right panel, the light green crosses and the green stars are the same quantities for the molecular gas obtained with the two Σ_{SFR} . The red and the dark red lines show the relations built with the ‘global’ efficiencies for the atomic gas $\langle\eta_{\text{atom}}\rangle$ and the molecular gas $\langle\eta_{\text{mol}}\rangle$ respectively (see text), with grey areas indicating the uncertainty. The solid grey lines show the same relation with efficiencies of 1, while the dotted lines are obtained, from top to bottom, with efficiencies of 0.1, 0.01, 0.001, and 0.0001. *Bottom row*: Summary of the best efficiency for our sample of galaxies, in the case of the atomic (left) and molecular (right) gas. The symbols are the same as in the top row. The red and dark red horizontal lines are the median $\langle\eta_{\text{atom}}\rangle$ and $\langle\eta_{\text{mol}}\rangle$ (also indicated above each panel) with 1σ error (grey area). Overall, the results of this ‘global’ analysis are consistent with those obtained with the ‘spatially-resolved’ approach, showing that low-efficiency SN feedback can sustain the gas turbulence.

Theoretical and numerical models of SN explosions in the ISM tend to predict that about 10% of the SN energy is available to feed turbulence (e.g. Chevalier, 1974; Thornton et al., 1998; Martizzi et al., 2016; Fierlinger et al., 2016; Ohlin

et al., 2019) and some authors have found even higher values (e.g. $\lesssim 25\%$; Dib et al., 2006). A natural question that may arise from our findings considers how the remaining kinetic energy is used. This residual SN energy could be spent to drive large-scale gas motions outside the disc (i.e. galactic fountain, galactic winds, outflows). For example, Fraternali & Binney (2006, 2008) showed that the HI halo of extra-planar gas in NGC 891 and NGC 2403 could be explained with the galactic fountain cycle: a continuous flow of gas launched out of the disc by super-bubble blow-outs. They calculated that this cycle can be sustained with only a small fraction ($< 4\%$) of the SN energy. Marasco et al. (2012) extended these studies to our Galaxy by reproducing the extra-planar HI emission with only $\approx 0.7\%$ of the kinetic energy from SNe. The remaining SN energy could be spent to drive galactic winds (e.g. Fraternali et al., 2004; Veilleux et al., 2005; Rubin et al., 2014; Cresci et al., 2017; Di Teodoro et al., 2018b; Armillotta et al., 2019).

5.5.2 Empirical evidence for the self-regulating cycle of star formation?

Taken at face value, the results presented in this work can be interpreted in a broader context, in which SN feedback and star-formation are key elements of the same self-regulating cycle (see for example Dopita, 1985; Ostriker & Shetty, 2011). In the previous Chapters, we showed that the SFR volume density correlates with the total gas volume density, following a tight power-law with index ≈ 2 , the volumetric star formation (VSF) law, which is valid for nearby galaxies (both dwarfs and spirals) and the Milky Way. The observed surface densities of the gas and the SFR were converted into volume densities by dividing by the scale height derived under the assumption of hydrostatic equilibrium (same as here). The existence of the VSF law indicates that star formation is regulated by the distribution of the gas, which depends on its velocity dispersion. In this Chapter, we conclude that the turbulent component of the gas velocity dispersion is driven by SN feedback. The energy injected into the ISM by SNe is proportional to the SFR, we can therefore imagine a cycle as follows. If the SFR (per unit volume) increases, the gas becomes more turbulent, implying that the gas disc thickness grows. The gas volume density then decreases and, according to the VSF law, the SFR consequently declines. This can eventually cause the support against the gravitational pull to weaken and the gas volume density to grow again, bringing to a new phase of high SFR. Exploring this self-regulating cycle of star formation and its role in galaxy evolution is of primary interest and we leave it to future work.

5.5.3 Comparison with previous works on SN feedback

The origin of ISM turbulence has been widely investigated in the literature (see also Sect. 5.5.5) using different approaches. In this section, we focus on two works that share some similarities with ours.

Tamburro et al. (2009) selected a sample of 11 galaxies (five of them are in our sample as well) and calculated the HI kinetic energy by measuring the surface density and the velocity dispersion using moment maps obtained from the THINGS data cubes. Then, they compared the observed energy with the expected turbulent energy provided by SN feedback (Eq. 5.8) and MRI (see discussion in Sect. 5.5.5). In particular, they assumed a constant dissipation timescale of $\tau_d = 9.8$ Myr (Mac Low, 1999) for all the galaxies and constant with radius. They concluded that SN feedback with $\eta \lesssim 0.1$ can account for the observed kinetic energy in inner parts of the star-forming disc where $\Sigma_{\text{SFR}} > 10^{-3} \text{ M}_{\odot} \text{ yr}^{-1} \text{ kpc}^{-2}$. In these regions, neither MRI nor thermal motions could explain the observed velocity dispersion of atomic gas. At larger radii instead, they found that unphysical values for the SN efficiency $\eta \gtrsim 1$ are required to maintain the observed line broadening and kinetic energy, given the low SFR (i.e. $\Sigma_{\text{SFR}} < 10^{-3} \text{ M}_{\odot} \text{ yr}^{-1} \text{ kpc}^{-2}$) (see also Stilp et al., 2013). Hence, Tamburro et al. concluded that the HI velocity dispersion could be driven by the MRI or due to the thermal broadening associated with a warm medium with $T \approx 5000$ K. Our results are partially in agreement with Tamburro et al. (2009) concerning the high-SFR regions of galaxies. However, despite we used the same data cubes as Tamburro et al. (2009), we can reproduce the radial profiles of the observed energy per unit area with SN efficiencies $\lesssim 0.1$ constant with radius (and no crucial help from thermal motions for most galaxies) not only in the high-SFR regions, but also in the low-SFR ones. The most fundamental difference with respect to this previous work is that we use the scale height of the gas disc to calculate τ_d , which affects the dissipation timescales (see Fig. 5.1). Moreover, an important improvement in our work is that we measured the velocity dispersion using a 3D approach, which is more robust than the 2D method based on moment maps adopted by Tamburro et al. (2009). 2D methods perform a Gaussian fit to the line profile in each pixel to measure the line broadening, but this approach can easily fail in pixels with low S/N typical of the outskirts of galaxies. ^{3D}BAROLO, after dividing the galaxy in rings, simultaneously fits the rotation velocity and the azimuthally averaged velocity dispersion in order to minimise the residuals between the data and the model (for each ring). This dramatically improves the velocity dispersion measurement with respect to the pixel-by-pixel fitting of the line profile, even for data with S/N as low as ≈ 2 (Di Teodoro & Fraternali, 2015).

Recently, Utomo et al. (2019) investigated the origin of turbulence in M33, considering SNe, MRI, and accretion as possible drivers. Using 21-cm and CO(2–1) emission-line data cubes, they studied the kinematic properties and the distribution of atomic gas and clouds of molecular gas. They calculated the

dissipation timescale in two ways, first using a constant value (i.e. $\tau_d = 4.3$ Myr) and second as $\tau_d = h_{\text{HI}}/\sigma_{\text{HI}}$, where σ_{HI} is the HI velocity dispersion and h_{HI} is the HI scale height calculated assuming the vertical hydrostatic equilibrium (see Ostriker et al., 2010). In the former case, they found that both SN feedback and MRI with efficiencies of 1 are required to maintain turbulence up to $R \approx 8$ kpc. In the latter case, the observed turbulence could instead be sustained by SNe and MRI with the efficiency of about 0.1 in the inner regions and 0.6–0.8 beyond $R = 6$ kpc. Concerning molecular clouds, these authors obtained that the observed turbulent energy could be maintained by SN feedback with $0.001 < \eta < 0.1$. In agreement with Utomo et al. (2019), our results show the importance of calculating the timescale of turbulence dissipation taking into account the increase of the scale height and the radial decrease of the velocity dispersion. The main discrepancy between this previous work and ours is that we conclude that SN feedback alone can maintain turbulence of the atomic gas with efficiencies $\lesssim 0.1$ (see Fig. 5.6). There are several differences between this work and ours that may all jointly explain this discrepancy. We discuss below only the two issues with a primary impact on the SN efficiency, as we expect the others to give a secondary contribution (e.g. method to measure σ_{HI} , components of the mass model for M33, thermal energy subtraction). First, Utomo et al. (2019) assumed that the energy injected in the ISM by a single SN is $\approx 3.6 \times 10^{50}$ erg based on the prescription for the momentum injection by a SN explosion given by Kim & Ostriker (2015b), who performed numerical simulations of SN explosions in a two-phase medium. Hence, their efficiencies should be multiplied by 0.36 to be compared with ours, reducing the discrepancy. Second, these authors assumed $L_D = h_{\text{HI}}$ instead of $L_D = 2h_{\text{HI}}$, meaning that their efficiencies should be re-scaled by a factor of 0.5 when compared to ours. As a result of these different assumptions, the efficiencies found by Utomo et al. (2019) are about 5.6 times higher than those obtained with our approach.

Overall, the main improvement in our work with respect to the literature is that we can explain the observed turbulence with SN feedback only and with a constant efficiency across the galactic discs. The primary reason for our success is that we include the scale height in the calculation of the dissipation timescale. Hence, in contrast with previous authors, we find no indication that other mechanisms are compulsorily required (see Sect. 5.5.5 for further discussions).

5.5.4 Possible caveats on the analysis and stability of the results

A possible caveat on this work may be that we considered only the neutral gas components of the ISM, while the ionised gas is also highly turbulent (e.g. Poggianti et al., 2019; Melnick et al., 2019). Within the disc, the ionised gas is typically subdominant in mass with respect to the neutral gas, thus we do not expect that including it would significantly change our conclusions. Some

authors investigated the possible sources of the turbulent energy in the ionised gas using the velocity dispersion of H α emission lines (e.g. Lehnert et al., 2009; Zhou et al., 2017; Yu et al., 2019; Varidel et al., 2020), but it remains unclear whether SN feedback models can reproduce these observations. Taking into account the gas disc flaring probably helps to solve this conundrum, but it is beyond the scope of this work.

The assumption $L_D = 2h$ (Eq. 5.5) might be questionable. We note however that even adopting $L_D = h$, for instance, our conclusions would not change as the efficiencies would be increased by a factor of 2 only, still being $\lesssim 0.1$. Our choice is supported by observational as well as theoretical arguments. Analytical and numerical models of the evolution of a SN remnant predict that the shell radius reaches about 100 pc for the typical conditions of the ISM, namely $n \approx 1 - 0.1 \text{ cm}^{-3}$ and $\sigma \approx 6 - 10 \text{ km s}^{-1}$ (Cox 1972; Chevalier 1974; Chevalier & Gardner 1974; Cioffi et al. 1988; Martizzi et al. 2015, and §8.7 in Cimatti, Fraternali, & Nipoti 2019). However, massive stars are typically found in associations and evolve simultaneously in a small region. These stars produce powerful winds that sweep the ISM from the surroundings, facilitating the expansion of SN shells and generating a super-bubble, that can easily reach the size of the disc thickness and even blow out (Mac Low et al., 1989). Observations of HI holes with diameter of ≈ 1 kpc in nearby galaxies corroborates this scenario (e.g. Kamphuis et al., 1991; Puche et al., 1992; Boomsma et al., 2008). Given that h_{HI} ranges from ~ 100 pc to ~ 1 kpc (see e.g. Fig. 2.4 and Fig. 4.2), our choice of $L_D = 2h_{\text{HI}}$ is perfectly reasonable. Moreover, in the Small Magellanic Cloud, the velocity power spectrum of atomic gas suggests that $L_D \simeq 2.3$ kpc (Chepurnov et al., 2015), which is consistent with our assumption $L_D \approx 2h_{\text{HI}}$ if we adopt $h_{\text{HI}} \sim 1$ kpc, as indicated by Di Teodoro et al. (2019). The comparison of the observed HI morphology to simulations of dwarf galaxies seems to suggest even higher values ($L_D \approx 6$ kpc, see Dib & Burkert 2005).

We derived the turbulent energy provided by SNe adopting the prescription for the energy injection rate $\dot{E}_{\text{turb,SNe}}$ (Eq. 5.6) given by Tamburro et al. (2009), which depends on the SN rate (Eq. 5.7). This latter takes into account only core-collapse SNe, as they can be directly related to the recent star formation traced by FUV emission from massive stars younger than 100 Myr (e.g. Kennicutt & Evans, 2012). The fraction of SNe Ia is expected to be less than or equal to the fraction of core-collapse SNe depending on the galaxy morphological type (Mannucci et al., 2005; Li et al., 2011). Therefore, considering also SN Ia would not significantly change our results, but just decrease the best values of the efficiencies by a factor $\lesssim 2$, strengthening our conclusions. The fraction of core-collapse SNe in Eq. 5.7 also depends on the index and the upper limit on the stellar mass of the initial mass function. We adopted an index of -1.3 for the stars in the mass range between $0.1 M_{\odot}$ and $0.5 M_{\odot}$, and of -2.3 for those with mass up to $120 M_{\odot}$ (Kroupa, 2002), which gives $f_{\text{cc}} \approx 1.3 \times 10^{-2} M_{\odot}^{-1}$. By decreasing the index or the upper limit on the stellar mass, we would obtain

less massive stars and a lower f_{cc} . However, the effect of these variations on the SN efficiency is not straightforward, also the conversion of far-ultraviolet and infrared emission to SFR is affected, but in the opposite direction (i.e. higher SFR for decreasing number of massive stars; see e.g. Tamburro et al. 2009), suggesting that our results are weakly influenced by the initial mass function parameters.

We verified that the general conclusions of this work do not depend on the method used to obtain the best efficiencies that reproduce the observed kinetic energy. In particular, we performed the analysis adopting two additional approaches. The first was used to carry out preliminary tests aiming to assess whether η is constant with or a function of the galactocentric radius. This method avoids any fitting procedure and does not involve any assumption on the efficiency (see Appendix 5.C for details). For each galaxy, we simply subtracted, at each galactocentric radius, the expected thermal velocity from the observed velocity dispersion (Eq. 5.3) in order to disentangle the turbulent velocity $v_{\text{turb}}(R)$. This latter was used to estimate the turbulent energy component, which was then divided by the energy produced by SNe in one turbulent crossing time (i.e. Eq. 5.8 with $\eta = 1$). Thus, we obtained the radial profile of the SN efficiency, $\eta(R)$, without assuming $0 < \eta < 1$, hence the cases with $\eta > 1$ were possible. For most of the galaxies, $\eta(R)$ had large uncertainties ($\gtrsim 50\%$), in particular at large radii, as the uncertainties on the observable quantities involved in this calculation (e.g. Σ_{SFR}) are larger at large radii than in the inner regions of galaxies (see also Utomo et al., 2019). This indicates that, using this approach, it is not possible to obtain fully satisfactory constraints on the efficiency in the outskirts of galaxies and that η can be assumed to be constant with the galactocentric radius.⁴ For each galaxy, we used $\eta(R)$ to calculate the median and the 1σ uncertainty and found that these are, albeit very uncertain, grossly compatible with those obtained with the hierarchical method and a constant efficiency. The median values for the whole sample of galaxies are (using Σ_{SFR} from Leroy et al. 2008 and Bigiel et al. 2010) $\langle \eta_{\text{atom,c}} \rangle = 0.053^{+0.060}_{-0.027}$ for the cold atomic gas, $\langle \eta_{\text{atom,w}} \rangle = 0.025^{+0.030}_{-0.012}$ for the warm atomic gas, and $\langle \eta_{\text{mol}} \rangle = 0.004^{+0.011}_{-0.002}$ for the molecular gas.

The second approach that we explored is based on the (non-hierarchical) Bayesian framework and consists in fitting Eq. 5.2 to the observed kinetic energy through the algorithm implemented in the Python module `emcee` (Foreman-Mackey et al., 2013). We took an efficiency constant with radius as a free parameter with a uniform prior between 0 and 1. The resulting best-fit

⁴In Fig. 5.3, the black points (E_{obs}) are sometimes systematically above the green band (E_{mod}) at large radii. This suggests that the best value of the efficiency is slightly more constrained by the inner points, which are less uncertain (i.e. have narrower priors), than those at large radii. However, this is a very minor effect and the model perfectly reproduces E_{obs} within the uncertainties; even forcing the outer parts to have more weight than the inner ones, the best efficiency would never increase by more than a factor $\lesssim 2$. Thus, our results strongly point to an efficiency nearly constant with radius.

efficiencies are generally compatible within the errors with those obtained with the hierarchical method. In particular, the median values for the whole sample of galaxies are (using Σ_{SFR} from Leroy et al. 2008 and Bigiel et al. 2010) $\langle \eta_{\text{atom,c}} \rangle = 0.042_{-0.012}^{+0.024}$ for the cold atomic gas, $\langle \eta_{\text{atom,w}} \rangle = 0.024_{-0.009}^{+0.009}$ for the warm atomic gas, and $\langle \eta_{\text{mol}} \rangle = 0.007_{-0.005}^{+0.004}$ for the molecular gas. We conclude that our results do not depend on the adopted statistical method. The fiducial approach described in Sect. 5.3.2 is preferable with respect to others, as it offers a rigorous treatment of the uncertainties.

5.5.5 Other turbulence sources

In this study, we found that SNe are sufficient to maintain the observed turbulence, hence we did not explore in detail other possible sources of energy. Moreover, as we motivate in this section, the contribution from the other drivers is likely of secondary importance and more uncertain than SN feedback.

Other forms of stellar feedback

SNe are not the only form of stellar feedback that can transfer kinetic energy to the ISM (see Mac Low & Klessen, 2004; Elmegreen & Scalo, 2004, and references therein). Proto-stellar outflows (i.e. jets and winds) can be quite powerful, but they inject energy on scales equal to or smaller than that of molecular cloud complexes. Hence, it seems unlikely that they could feed turbulence on the scale of galactic discs.

O–B and Wolf-Rayet stars also produce strong winds, but only those with the highest masses carry a significant amount of kinetic energy into the ISM. For class O and Wolf-Rayet stars (lifetime ~ 4 Myr), the most extreme winds have outflow rates $\dot{M}_{\text{wind}} \sim 10^{-4} M_{\odot} \text{yr}^{-1}$ and velocities $V_{\text{wind}} \approx 3000 \text{ km s}^{-1}$ (e.g. Puls et al., 1996; Nugis & Lamers, 2000; Gatto et al., 2017). Winds from less massive stars are typically characterised by $\dot{M}_{\text{wind}} \sim 10^{-6} M_{\odot} \text{yr}^{-1}$ and $V_{\text{wind}} \approx 2000 \text{ km s}^{-1}$ (Puls et al., 1996; Nugis & Lamers, 2000), hence their contribution to the ISM turbulence is likely lower, despite the longer lifetimes and higher number of these stars. Gatto et al. (2017) used 3D hydro-dynamic simulations to study the influence of winds and SNe from massive stars on the ISM. They compared the cumulative energy of winds and SN explosions and found that, in the whole wind phase, the most massive stars ($\approx 85 M_{\odot}$) produce as much as or more energy than in the SN phase. On the other hand, less massive stars (9–20 M_{\odot}) release in the wind phase about 10^2 – 10^4 times less energy than in the SN phase. These less massive stars are much more numerous than the massive ones, thus SN explosions likely dominate over stellar winds after the first few Myr of the stellar population lifetime (Mac Low & Klessen, 2004).

A further stellar source of energy is the ionising radiation from massive stars. Most of this energy ionises the diffuse medium around the stars, shaping

HII regions and heating the surrounding gas. Ionised gas cools radiatively by emitting non-ionising photons and it contracts due to the thermal instability, possibly driving turbulent motions (Mac Low & Klessen, 2004). For example, Kritsuk & Norman (2002a,b) estimated that $\lesssim 7\%$ of the thermal energy may be converted into kinetic energy through this mechanism. However, as shown by Mac Low & Klessen (2004), the kinetic energy injected into the ISM by ionising radiation is about two to three orders of magnitude lower than produced by SN explosions.

In addition, ionising radiation can transfer kinetic energy to the ISM also through the expansion of HII regions (e.g. Menon et al., 2020). Walch et al. (2012) used 3D SPH simulations to study the effect of the ionising radiation from a single O7 star on a surrounding molecular cloud. They found that $\lesssim 0.1\%$ of the ionising energy is converted into kinetic energy and that this form of stellar feedback can sustain turbulent motions of about 2–4 km s⁻¹ (see also Mellema et al., 2006). Overall, these results suggest that, if compared to SNe, the turbulent energy from ionising radiation is of secondary importance.

Magneto-rotational instability and shear

Several authors have proposed that the MRI (Velikhov, 1959; Chandrasekhar, 1960; Balbus & Hawley, 1991) may be the main source of turbulent energy in the outskirts of galaxies, as it generates Maxwell stresses that transfer kinetic energy from shear to the ISM turbulence (e.g. Hawley et al., 1995; Sellwood & Balbus, 1999; Piontek & Ostriker, 2007). The energy per unit area provided by MRI is (e.g. Mac Low & Klessen, 2004; Tamburro et al., 2009; Utomo et al., 2019)

$$E_{\text{turb,MRI}} \simeq (5 \times 10^{43} \text{ erg pc}^{-2}) \eta_{\text{MRI}} \left(\frac{h}{100 \text{ pc}} \right)^2 \left(\frac{v_{\text{turb}}}{10 \text{ km s}^{-1}} \right)^{-1} \left(\frac{B}{6 \mu\text{G}} \right)^2 \left(\frac{S}{\text{Gyr}^{-1}} \right), \quad (5.15)$$

where η_{MRI} is the MRI efficiency, B is the magnetic field intensity and $S \equiv \left| \frac{d\Omega}{d \ln R} \right| = \left| \frac{dV_{\text{rot}}}{dR} - \frac{V_{\text{rot}}}{R} \right|$ is the shear rate in Gyr⁻¹, which depends on the angular frequency $\Omega \equiv V_{\text{rot}}/R$ given the rotational velocity of the galaxy V_{rot} . The energy provided by the MRI can become significant at large radii, hence it has been advocated to explain turbulence in the outskirts of galaxies, in addition to SNe (e.g. Sellwood & Balbus, 1999; Tamburro et al., 2009; Utomo et al., 2019). Let us take, for example, NGC 6946, which requires a significant contribution from the thermal energy of the warm atomic gas to explain the observed energy per unit area for $R \gtrsim 10$ kpc (see Fig. 5.3). The ordered magnetic field is $B \approx 5 - 10 \mu\text{G}$ (Beck, 2007), the HI scale height increases from $h_{\text{HI}} \approx 150$ pc at $R \approx 10$ kpc to $h_{\text{HI}} \approx 180$ pc at $R \approx 17$ kpc (see Fig. 2.4), the rotation curve is approximately constant at about 200 km s⁻¹ for $R \gtrsim 10$ kpc (see Boomsma et al.,

2008), and the turbulent velocity in these regions is also constant at about $5 - 7 \text{ km s}^{-1}$ (see Fig. 2.2). Using these values in Eq. 5.15 and assuming $\eta_{\text{MRI}} = 1$, we obtain that the MRI can provide $E_{\text{turb,MRI}} \approx 7 - 12 \times 10^{45} \text{ erg pc}^{-2}$ in the regions beyond $R \sim 10 \text{ kpc}$. This estimate of $E_{\text{turb,MRI}}$ is compatible with the observed energy of NGC 6946 (see Fig. 5.3), but we required that 100% of the MRI energy is transferred to the ISM. For example, non-ideal MHD effects (i.e. Ohmic diffusion, ambipolar diffusion, and Hall effect) can suppress the MRI instability (e.g. Wardle, 1999; Kunz & Balbus, 2004; Korpi et al., 2010; Riols & Latter, 2019). In addition, there are indications that SN driven-turbulence can counteract the MRI in the star-forming regions (e.g. Gressel et al., 2013). We also note that $E_{\text{turb,MRI}}$ calculated with Eq. 5.15 can be very uncertain. Indeed, the magnetic field intensity is difficult to measure precisely and there are indications that it varies between different regions of a galaxy (e.g. Beck et al., 1996; Beck, 2007; Chyży & Buta, 2008).

More in general, shear from galactic rotation can transfer kinetic energy to the ISM. It is however not straightforwardly understood how to couple the large scales of galactic rotation to smaller scales and whether the energy input from shear is significant if compared to SN feedback (see e.g. Mac Low & Klessen 2004 and references therein). We conclude that the role of MRI and shear in sustaining the ISM turbulence is still unclear and, given our success in reproducing the observed energy with SNe only, we do not find evidence for the need of these contributions.

Gravitational energy

It has been proposed that turbulence in star-forming galaxies may be driven by gravity through gas accretion (e.g. Klessen & Hennebelle, 2010; Elmegreen & Burkert, 2010). Klessen & Hennebelle (2010) investigated this mechanism for a sample including the MW and 11 nearby galaxies from the THINGS sample (IC 2547, NGC 4736, NGC 6946, and NGC 7793 are also in our sample). They estimated that the energy input rate from the accreted material (over the whole galaxy) is

$$\dot{E}_{\text{turb,infall}} \simeq (1.3 \times 10^{40} \text{ erg s}^{-1}) \left(\frac{\dot{M}_{\text{infall}}}{1 \text{ M}_{\odot} \text{ yr}^{-1}} \right) \left(\frac{V_{\text{infall}}}{200 \text{ km s}^{-1}} \right)^2, \quad (5.16)$$

where \dot{M}_{infall} and V_{infall} are the mass inflow rate and the infall speed. For each galaxy, they assumed that \dot{M}_{infall} is equal to the observed SFR of the galaxy, based on the idea that gas accretion should sustain star formation. For V_{infall} , they used the rotation velocity as an approximation of the impact velocity of the accretion gas onto the galactic disc. Klessen & Hennebelle (2010) calculated the dissipation timescale of turbulence assuming $L_{\text{D}} = 2h_{\text{HI}}$ and with a equation analogous to Eq. 5.4. They found that less than 10% of the kinetic energy from accretion is required to sustain turbulence in spiral galaxies (roughly similar

with the values in Table 5.1). On the other hand, they concluded that other energy sources should dominate in dwarf galaxies (e.g. IC 2547), as the expected accretion rate was too low to explain the observed energy.

It is interesting to compare the energy per unit area provided by SN feedback (Eq. 5.8) and by accretion ($E_{\text{turb,infall}}$). This latter can be obtained from Eq. 5.16 by replacing \dot{M}_{infall} with $\dot{\Sigma}_{\text{infall}}$, and multiplying by the dissipation timescale (Eq. 5.4) and the infall efficiency η_{infall} (i.e. the fraction of the infall energy that goes into feeding turbulence). Assuming $L_{\text{D}} = 2h_{\text{HI}}$, the ratio between the SNe and the infall energies is

$$\frac{E_{\text{turb,infall}}}{E_{\text{turb,SNe}}} \simeq (3.1 \times 10^{-2}) \frac{\eta_{\text{infall}}}{\eta_{\text{SNe}}} \left(\frac{V_{\text{infall}}}{200 \text{ km s}^{-1}} \right)^2 \left(\frac{\dot{\Sigma}_{\text{infall}}}{10^{-4} \text{ M}_{\odot} \text{ yr}^{-1} \text{ kpc}^{-2}} \right) \left(\frac{\Sigma_{\text{SFR}}}{10^{-4} \text{ M}_{\odot} \text{ yr}^{-1} \text{ kpc}^{-2}} \right)^{-1}, \quad (5.17)$$

where the SN efficiency is defined as η_{SNe} to distinguish it from the infall efficiency η_{infall} . If we take $\dot{\Sigma}_{\text{infall}} = \Sigma_{\text{SFR}}$ as suggested by Klessen & Hennebelle (2010), the infall energy is about two orders of magnitude lower than the SN energy when $\eta_{\text{infall}} \approx \eta_{\text{SNe}}$. The velocity term in Eq. 5.17 is unlikely to go in the direction of increasing $E_{\text{turb,infall}}/E_{\text{turb,SNe}}$. For example, high-velocity clouds, which are among the candidates for accreting gas on to galaxies (e.g. Putman et al., 2012), have velocities between $\approx 50 \text{ km s}^{-1}$ and $\approx 150 \text{ km s}^{-1}$ (e.g. Boomsma, 2007; Marasco et al., 2013). The galactic fountain cycle is another possible channel for gas accretion, as fountain clouds can trigger gas condensation from the hot corona and fall back onto the disc, bringing new material (see Fraternali 2017 and references therein).⁵ However, fountain clouds have velocities below 100 km s^{-1} (e.g. Fraternali & Binney, 2006, 2008; Marasco et al., 2012, 2019), hence it is very unlikely that they could transfer a significant amount of energy to the ISM. We also note that $\dot{\Sigma}_{\text{infall}}/\Sigma_{\text{SFR}}$ might vary with the galactocentric radius of galaxies. Marasco et al. (2012) found that the peak in the accretion rate of the galactic fountain lies well beyond the peak of the SFR in the Milky Way. Pezzulli & Fraternali (2016) showed that, in general, this mismatch between the radial profiles of $\dot{\Sigma}_{\text{infall}}$ and Σ_{SFR} is related to the deficit of angular momentum of the accreted gas with respect to the gas in the disc. Hence, estimating E_{infall} is not straightforward and requires a careful modelling of the accretion channel under consideration.

⁵Fountain clouds return into the disc at approximately the same radius where they were launched in orbit, but with an angular momentum mismatch with respect to the gas in the disc, as they accreted low-angular momentum coronal gas. Therefore, this material is expected to move radially towards the inner and lower-angular momentum regions of the galaxy. In principle, these radial flows could contribute to feeding turbulence. However, Pezzulli & Fraternali (2016) have shown that the radial velocity of this gas is of the order of 1 km s^{-1} , which is negligible with respect to the observed velocity dispersion. Thus, we do not expect radial motions to significantly contribute to turbulence.

Another gravity-driven mechanism that may sustain turbulence is the gravitational instability of the galactic disc, which is usually studied using the Toomre parameter (Toomre, 1964). For example, Krumholz & Burkhardt (2016) tested two models of turbulence, one based on feedback from star formation and the other on gravitational instability (see e.g. Bournaud et al. 2010 for a different approach). They compared both models to measurements of the velocity dispersion of HI and H α lines in both local and distant galaxies, finding that the gravity-driven mode is favoured only in star-forming galaxies with high velocity dispersion ($\gtrsim 50 \text{ km s}^{-1}$) and high SFR ($\gtrsim 10 \text{ M}_{\odot}\text{yr}^{-1}$). This is not the case of our galaxies, which have standard velocity dispersions (about 6–15 km s^{-1}) and star formation rates (i.e. from $\text{SFR} \approx 0.005 \text{ M}_{\odot}\text{yr}^{-1}$ for DDO 154 to $\text{SFR} \approx 3.2 \text{ M}_{\odot}\text{yr}^{-1}$ for NGC 6946; Leroy et al. 2008). Moreover, whether these high velocity dispersions are real or affected by observational biases is debated. Several authors have shown indeed that, if the effect of beam smearing is properly taken into account, the velocity dispersions in distant galaxies are comparable to or only slightly larger than in local galaxies (e.g. Di Teodoro et al., 2016, 2018a; Lelli et al., 2018).

In this Chapter, we have shown that the radial profile of the observed energy can be perfectly reproduced by our simple model of energy injection by SN feedback with constant efficiency. We find no indication that any additional source of energy is required to sustain turbulence in our sample of galaxies. Moreover, the estimates of the energy injected by SNe is the least uncertain considering all the issues related to the other possible driving mechanisms. We conclude that SN feedback is likely the most important driver of turbulence in the ISM of nearby galaxies.

5.6 Summary and conclusions

The aim of this Chapter was understanding whether SN feedback can sustain turbulence in the atomic gas and the molecular gas of star-forming galaxies. The distribution and kinematics of HI (see Chapter 2) and CO were derived using emission line data cubes for a sample of ten nearby galaxies, allowing us to calculate the kinetic energy per unit area as a function of the galactocentric radius. We adopted a simple model based on the idea that the gas is in hydrostatic equilibrium and its kinetic energy is given by the sum of two components, namely the turbulent energy and the thermal energy. Relying on Kolmogorov’s framework, we assumed that the turbulent energy is entirely supplied by SN feedback with efficiency η , corresponding to the fraction of the total energy that is transferred to the ISM as kinetic energy. The rate of SN explosions per unit area is derived from the observed SFR surface density. We also assumed that the driving scale of SN feedback is $L_D = 2h$, where h is the scale height of the gas in hydrostatic equilibrium. The increase of the scale height with the galactocentric radius has a crucial impact on the timescale of

turbulence dissipation, which we estimated to be one order of magnitude longer at larger radii than in the inner regions of the disc. For the atomic gas in particular, we explored two extreme scenarios with either all CNM or all WNM, in which the thermal motions give respectively the minimum and the maximum possible contribution to the total energy of the gas, and a more realistic case with a mixture of the two phases. We used a Bayesian method to compare our model to a set of observations, aiming to estimate the SN efficiency required to maintain turbulence. We found that the radial profiles of the observed energy per unit area in our sample of galaxies are reproduced by the SN feedback model with η constant with the galactocentric radius at values always below 0.1.

Our main conclusions are the following.

1. At most a few percent of the energy from SN feedback is required to sustain the gas turbulence in our galaxies. We estimate that the median SN efficiency is $\langle \eta_{\text{atom}} \rangle \approx 0.015$ for the atomic gas and $\langle \eta_{\text{mol}} \rangle \approx 0.003$ for the molecular gas. Therefore, no additional sources of turbulent energy are needed.
2. Thermal motions significantly contribute to the observed kinetic energy and velocity dispersion of the atomic gas, especially in the outer and low-SFR regions of galaxies.

These findings show that low-efficiency SN feedback is sufficiently energetic to be the sole driver of turbulence in local star-forming galaxies.

The results presented in this and previous Chapters provide empirical indications that SN feedback and star formation are part of the same self-regulating cycle (e.g. Dopita, 1985; Ostriker & Shetty, 2011; Sun et al., 2020). In this scenario, the SFR per unit volume of a galaxy depends on the volume density of the gas as $\rho_{\text{SFR}} \propto \rho_{\text{gas}}^2$. The balance between gravity and gas pressure is set by the velocity dispersion of the gas, which includes both thermal and turbulent motions. These latter are sustained by SN feedback and therefore depends on the SFR itself. In future works, we plan to study this self-regulating cycle and its role in galaxy formation and evolution.

Acknowledgements

CB is grateful to E. M. Di Teodoro for the help and the advice in the analysis of the THINGS data cubes. This work was carried out using the publicly available data cubes from HERACLES (Leroy et al., 2005), THINGS (Walter et al., 2008), and HALOGAS (Heald et al., 2011).

Appendix 5.A Detailed molecular gas kinematics

The kinematics of molecular gas was analysed using ^{3D}BAROLO on HERACLES CO(2-1) data cubes (see Sect. 5.2.2), which have a channel separation of 5.2 km s⁻¹ and a spatial resolution of about 13". We smoothed the data cubes of NGC 2403 to 27", NGC 2976 to 23", and NGC 4736 to 18", in order to match with the working resolution adopted in Chapter 2 (see Table 2.B.2), and to increase the S/N. The inclination and the position angle were taken from Table 2.1. Small corrections of 2°–3° were applied to NGC 5055 and NGC 6946 after an exploratory fit of the data cube. Indeed, the values reported in Table 2.1 were derived from the HI emission, which is more extended than the CO emission, and the inclination and position angle of the outer regions of the HI disc may not be the best choice for the CO disc in the presence of a warp. The systemic velocities are the same as in Table 2.B.2 except for three galaxies, which required a small correction to obtain a better fit the CO data cube: NGC 4736 (+13.3 km s⁻¹), NGC 5055 (+8.3 km s⁻¹), and NGC 6946 (+14.3 km s⁻¹). The panels in Figs. 5.A.1–5.A.7 provide the main information about the data cubes and the best-fit model of each galaxy.⁶ The description of each panel follows below.

- Panel A: 0th moment map of CO emission. The white cross indicates the galaxy center and the white ellipse corresponds to the outermost fitted ring.
- Panel B: velocity field or 1st moment map of the data cube. The thick contour shows the systemic velocity and the black circle in the bottom right corner represents the beam of the telescope or the adopted beam after smoothing, as explained above.
- Panel C: velocity dispersion map obtained as the 2nd moment map of the data cube. The black bar in the bottom right corner shows the physical scale of the observations.
- Panel D: molecular gas surface density as a function of the galactocentric radius R from Frank et al. (2016) (see Sect. 5.2.2 for details).
- Panel E: rotation velocity of CO as a function of R .
- Panel F: CO velocity dispersion radial profile. This is not obtained from the 2nd moment map but through the 3D modelling. The dotted horizontal line shows the velocity resolution limit, which is $\approx 0.85\Delta v_{\text{ch}} \approx 4.4 \text{ km s}^{-1}$ for Hanning-smoothed data cubes with channel separation

⁶In all the fits, we used the following set of ^{3D}BAROLO parameters: `ftype=1, wfunc=2, ltype=1, norm=local, mask=smooth, side=B`.

$\Delta v_{\text{ch}} = 5.2 \text{ km s}^{-1}$. The points marked with the red cross (when present) were excluded from this study.

- Panel G: inclination of the rings, which was kept constant with R (the dashed grey line shows this constant value).
- Panel H: position angle of the rings. The dashed grey line shows the mean value and the red curve (when present) indicates the regularised profile used to obtain the final model (see Di Teodoro & Fraternali 2015 for details).
- Panel I: position–velocity diagram along the major axis of the CO disc. The black and the red contours are the iso-density contours of the galaxy and the best-fit model, respectively. The horizontal black dashed line shows the systemic velocity.
- Panel J: position–velocity diagram along the minor axis.

From panels F in Figs 5.A.1–5.A.7, we can see that the CO velocity dispersion decreases with increasing R , going from 10–20 km s^{-1} in the inner regions to 4–8 km s^{-1} at the largest radii, very similar to the HI velocity dispersion profiles obtained by many authors (e.g. Fraternali et al. 2002; Boomsma et al. 2008; Tamburro et al. 2009; Iorio et al. 2017, and Chapter 2). However, the distribution of CO in NGC 0925 and NGC 2976 extends only at $R \approx 2 \text{ kpc}$, hence the decline is not appreciable.

We excluded some points from the analysis, which are indicated with red crosses in the panel F of each galaxy. In particular, the velocity dispersion measured at the outermost radii of most galaxies (i.e. NGC 0925, NGC 3198, NGC 4736, NGC 5055, and NGC 6946) is excluded, as it is lower than the data cubes velocity resolution. From the position-velocity diagrams of NGC 4736 (Fig. 5.A.5) and NGC 6946 (Fig. 5.A.7), we can see that the red contours of ^3D BAROLO model are thinner than the black ones of the galaxy emission in the regions within about 1 kpc from the center. This is due to the presence of a bar, which drives strong non-circular motions and produces wiggles in the velocity field (see also Moellenhoff et al., 1995; Boomsma et al., 2008). These kinematic feature cannot be reproduced by the tilted-ring model, as it assumes circular motions. NGC 0925 is also barred galaxy (e.g. Pisano et al., 1998), but in this case the feature is not evident from the position-velocity diagram (Fig. 5.A.1) due to the low S/N of the data. However, the odd shape of the rotation curve suggests that there could be non-circular motions in the region within $R \approx 1 \text{ kpc}$, which cannot be caught by the tilted-ring model. We note that the position angle of NGC 4736 (see panel B in Fig. 5.A.5) is appropriate for the outer disc, while the velocity field in inner regions suggests a lower value. In the case of NGC 6946, we adopted an ‘ad hoc’ approach to improve the model. We first ran ^3D BAROLO setting the velocity dispersion at 4 km s^{-1} , in order to retrieve a good-quality rotation curve. Then, we performed a second run fixing

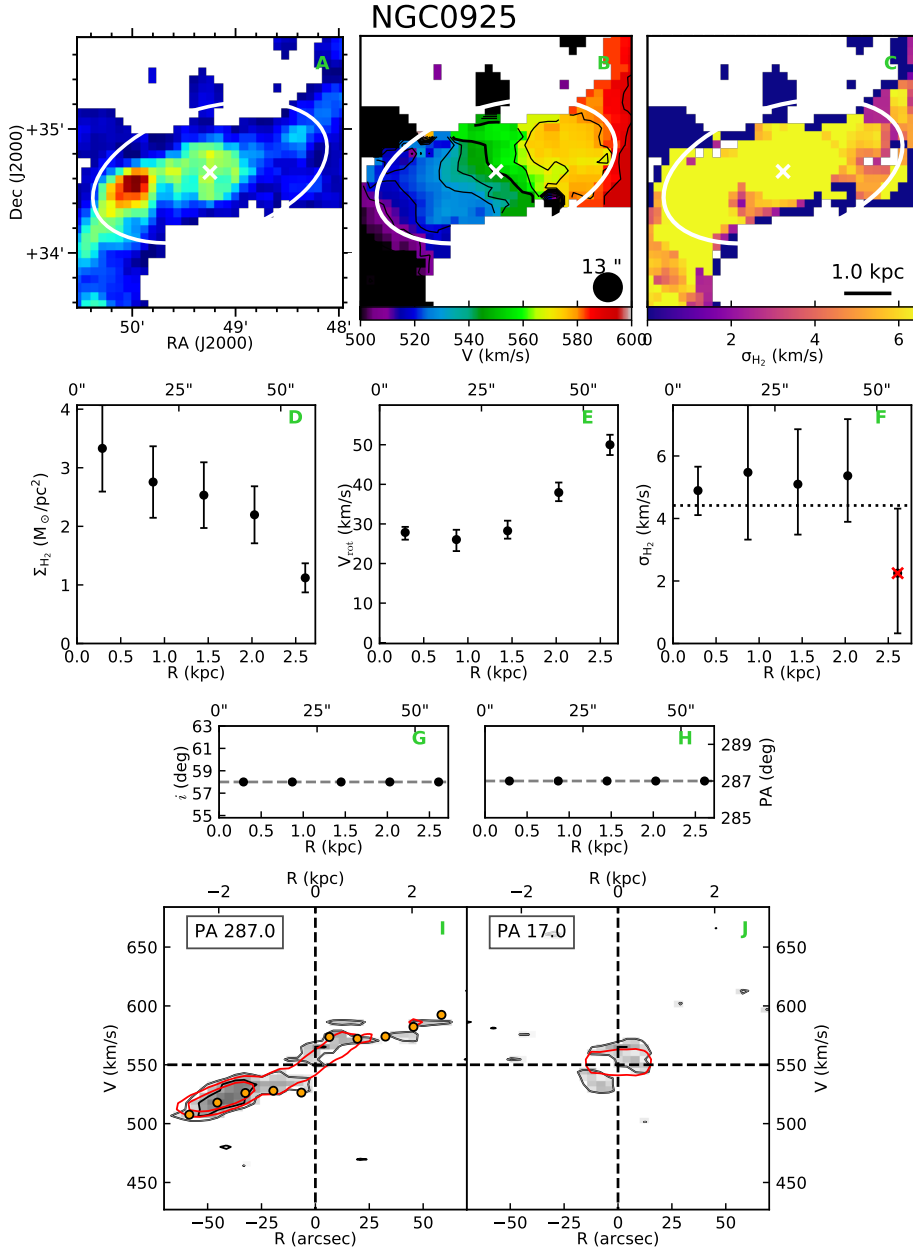


Figure 5.A.1 – See description in Appendix 5.A.

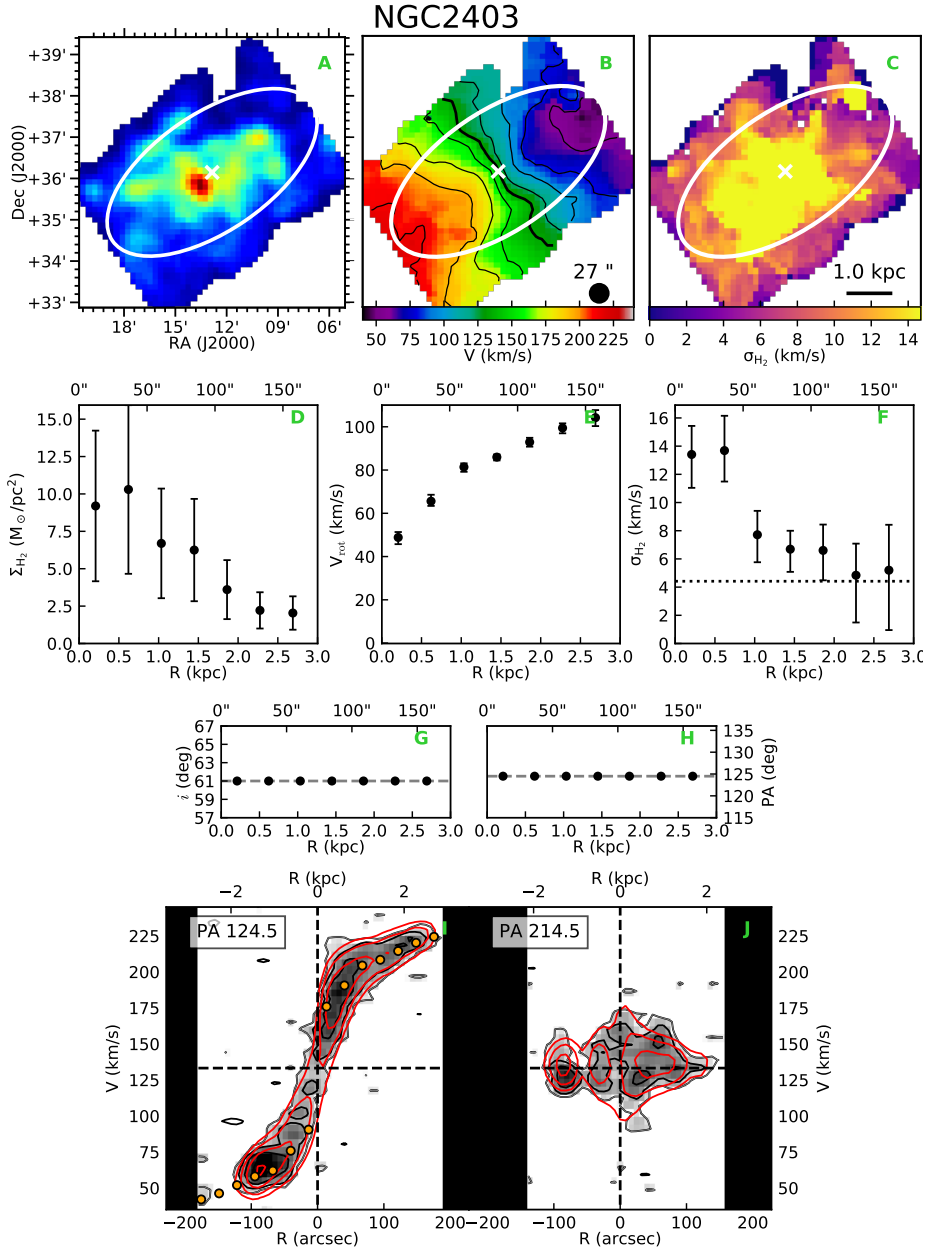


Figure 5.A.2 – Same as Fig. 5.A.1.

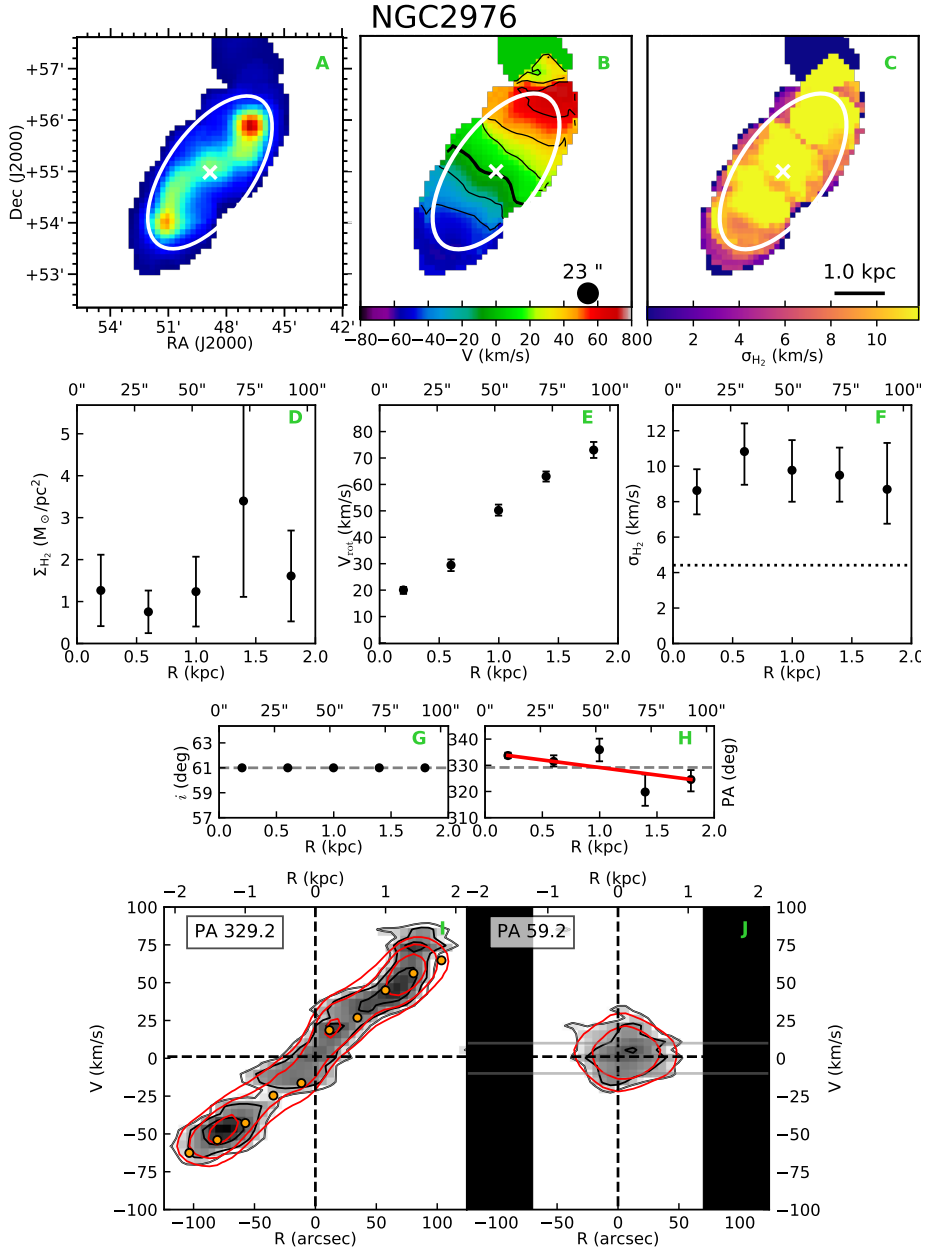


Figure 5.A.3 – Same as Fig. 5.A.1.

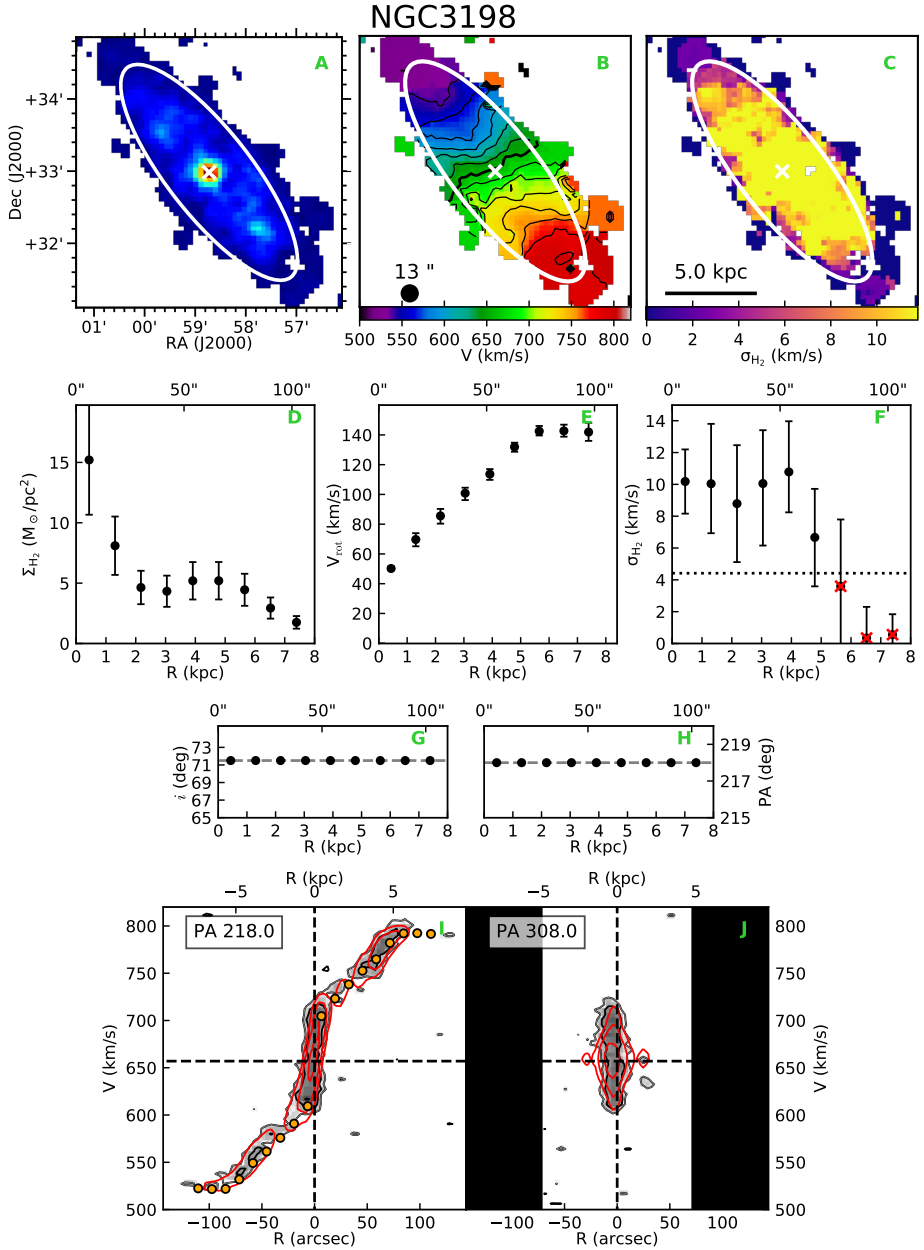


Figure 5.A.4 – Same as Fig. 5.A.1.

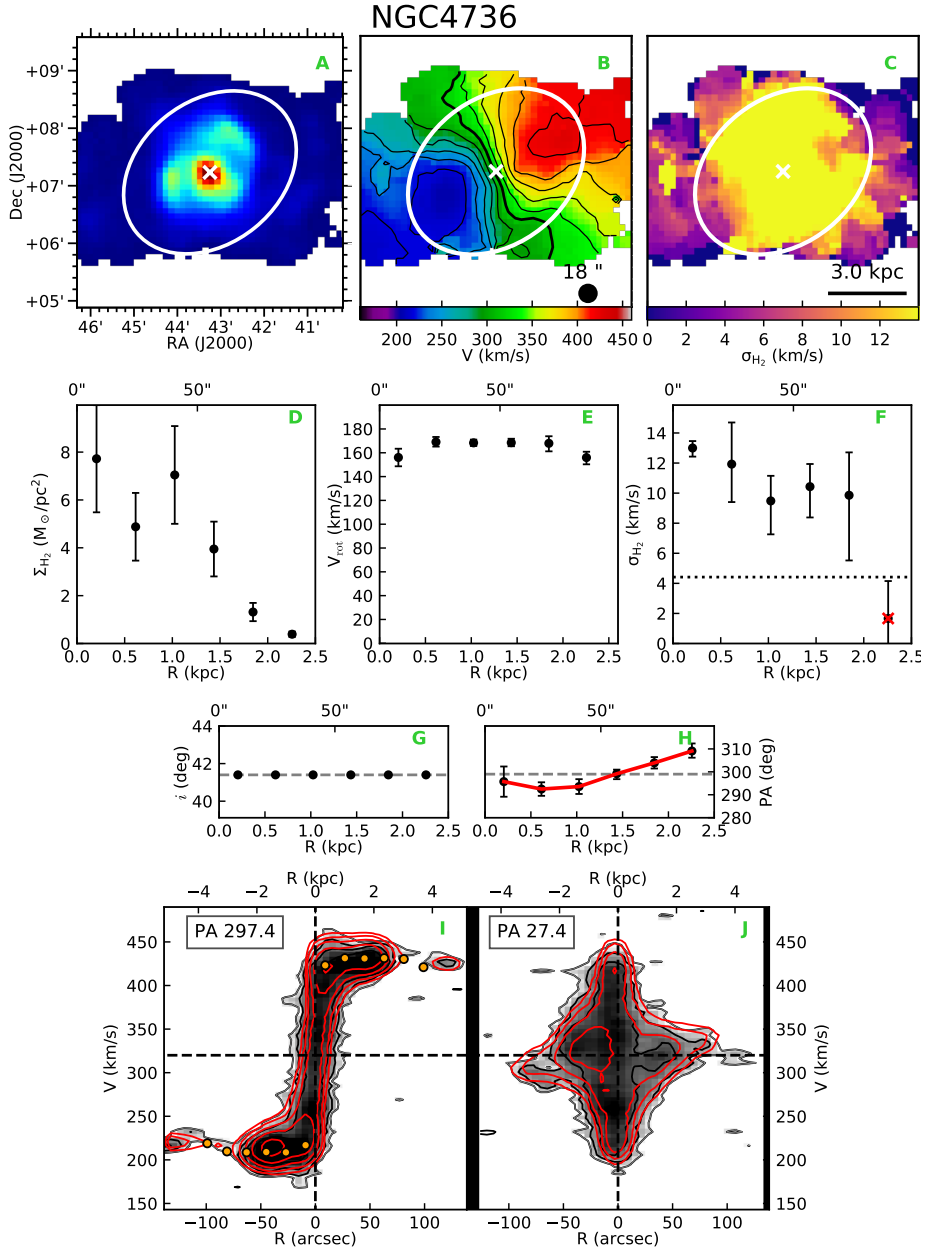


Figure 5.A.5 – Same as Fig. 5.A.1.

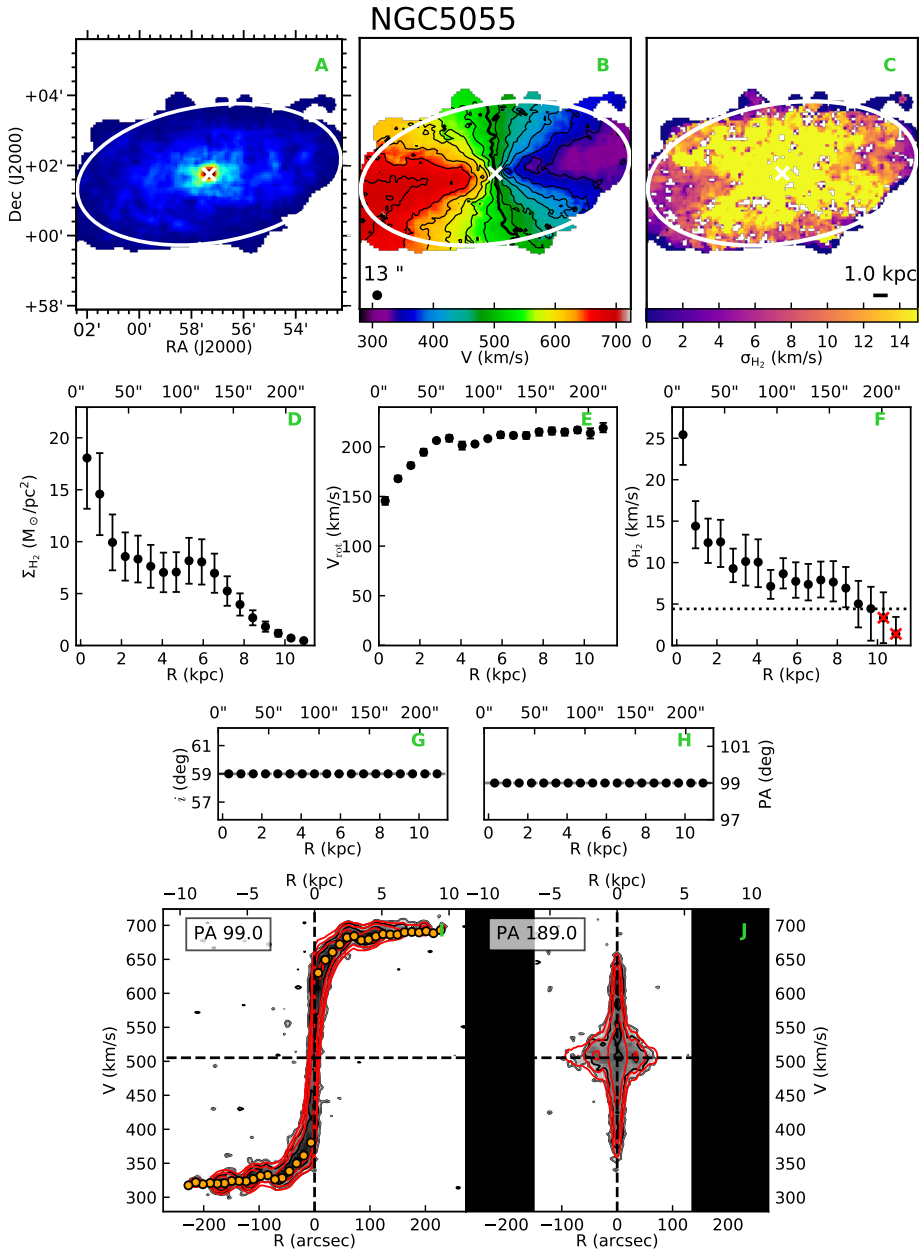


Figure 5.A.6 – Same as Fig. 5.A.1.

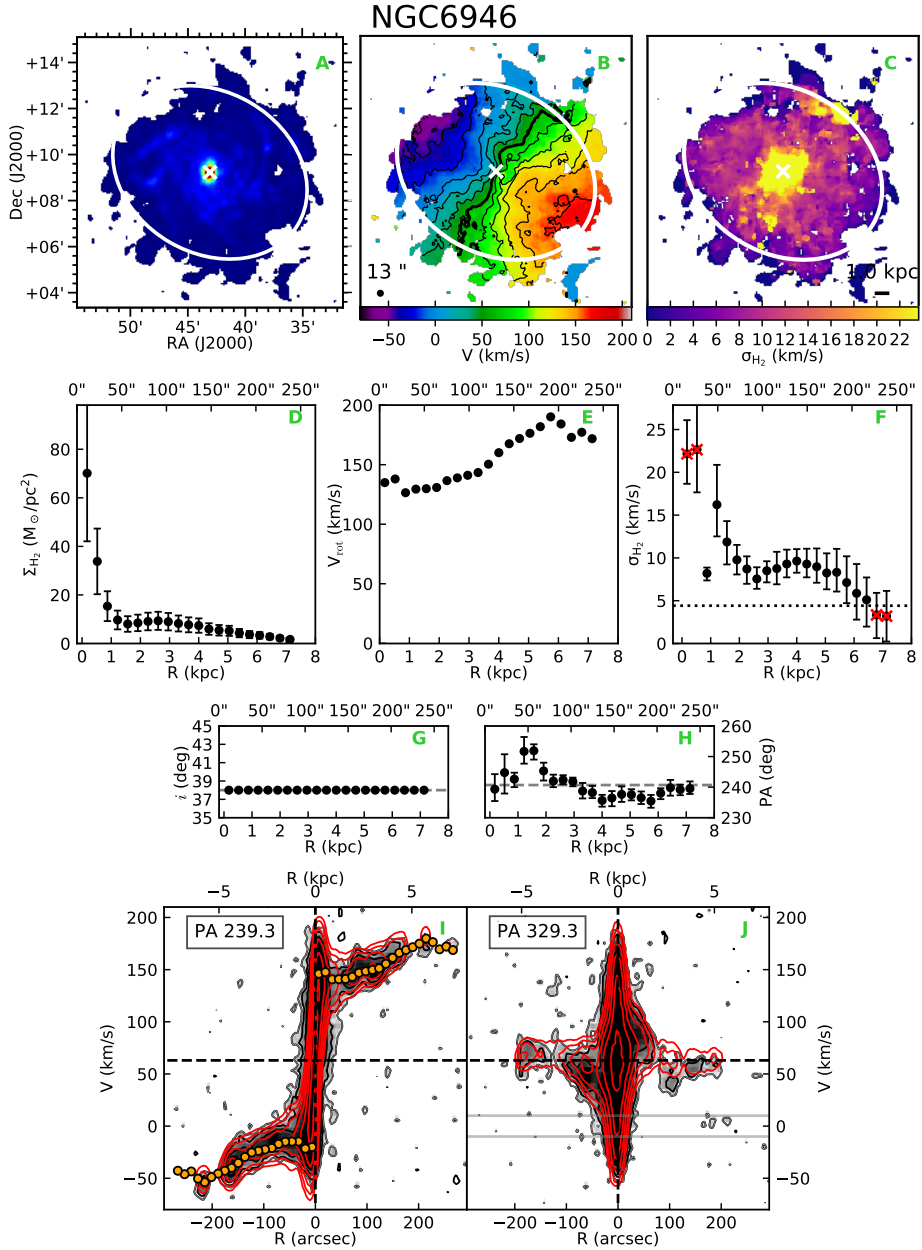


Figure 5.A.7 – Same as Fig. 5.A.1.

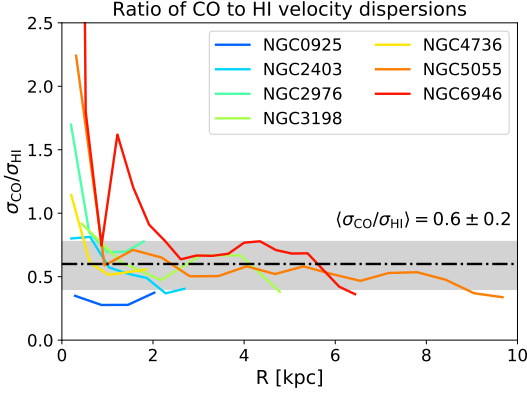


Figure 5.A.8 – Ratio of the CO-to-HI velocity dispersion as a function of the galactocentric radius for the galaxies in our sample with CO detected. The median and the 84th and the 16th percentiles are represented by the dot-dashed black line and the grey area, respectively, and their values are reported above.

the rotation velocities of the rings to those obtained previously, and fitting the velocity dispersion. After inspecting the position-velocity diagram of NGC 6946 (Fig. 5.A.7), we decided however to remove the first two inner points, as the velocity dispersion is clearly overestimated.

Figure 5.A.8 shows, for each galaxy in the sample, the radial profile of the ratio of σ_{CO} to σ_{HI} . The grey area represents the 84th and the 16th percentiles of all the points, which enclose also the median value indicated by the black dash-dotted line $\langle \sigma_{\text{CO}}/\sigma_{\text{HI}} \rangle = 0.6 \pm 0.2$. This value is in agreement with previous works (e.g. Mogotsi et al., 2016; Marasco et al., 2017; Koch et al., 2019) and additionally confirms the assumption made in Chapter 2 (see Sect. 2.4.2). We note however that the velocity resolution of HERACLES data cubes is not optimal to study the molecular gas velocity dispersion, which may be even lower than 4.4 km s^{-1} at large radii. Hence, the median value that we found could be slightly overestimated.

Appendix 5.B Hierarchical Bayesian inference

In this section, we describe the formalism of the Bayesian method presented in Sect. 5.3.2. We estimate, for each galaxy in our sample, the posterior distribution of η , assuming that it is constant with the galactocentric radius R . For a single galaxy divided in N annuli, the data are $\mathcal{D} = \{\mathbf{d}_i\}_{i=1}^N$. Let us define R_{SFR} as the outermost radius where the SFR surface density is measured. Hence, we have the upper limit on Σ_{SFR} where $R_i > R_{\text{SFR}}$, which is the case of DDO 154, NGC 2403, NGC 3198, and NGC 6946. For the other galaxies instead, $R_i \leq R_{\text{SFR}}$ at any radius. The observed quantities at a certain radius R_i are therefore

$$\mathbf{d}_i = (\Sigma_{\text{SFR}_i}, \sigma_i, h_{\text{HI}_i}, \Sigma_{\text{HI}_i}) \text{ where } R_i \leq R_{\text{SFR}}, \quad (5.B.1)$$

and

$$\mathbf{d}_i = (\sigma_i, h_{\text{HI}_i}, \Sigma_{\text{HI}_i}) \text{ where } R_i > R_{\text{SFR}}. \quad (5.B.2)$$

The associated uncertainties are

$$\Delta \mathbf{d}_i = (\Delta \Sigma_{\text{SFR}_i}, \Delta \sigma_i, \Delta h_{\text{HI}_i}, \Delta \Sigma_{\text{HI}_i}) \text{ where } R_i \leq R_{\text{SFR}}, \quad (5.B.3)$$

and

$$\Delta \mathbf{d}_i = (\Delta \sigma_i, \Delta h_{\text{HI}_i}, \Delta \Sigma_{\text{HI}_i}) \text{ where } R_i > R_{\text{SFR}}. \quad (5.B.4)$$

As a preliminary step, the observed quantities for each galaxy were normalised to their median value. The elements of \mathbf{d}_i are considered realisation of normal distributions centered on true values (indicated with the apex T) and with standard deviation given by the uncertainties in $\Delta \mathbf{d}_i$. In order to avoid negative true values, we used log-normal distributions as priors (i.e. $v_{\text{turb}_i}^T$, $\Sigma_{\text{SFR}_i}^T$, and $h_{\text{HI}_i}^T$). Each log-normal distribution is defined by two parameters: the central value ($\alpha_{v_{\text{turb}_i}}$, $\alpha_{\Sigma_{\text{SFR}_i}}$, and $\alpha_{h_{\text{HI}_i}}$) and the standard deviation ($\beta_{v_{\text{turb}_i}}$, $\beta_{\Sigma_{\text{SFR}_i}}$, and $\beta_{h_{\text{HI}_i}}$), whose hyper-priors are a normal distribution and a Gamma distribution, respectively (see Table 5.B.1). The thermal velocity is a normal distribution with centroid $\mu_{v_{\text{th}}}$ and standard deviation $\sigma_{v_{\text{th}}}$ of 0.06 km s⁻¹ and 0.005 km s⁻¹ for CO, 1 km s⁻¹ and 0.4 km s⁻¹ for the cold HI, and 8.1 km s⁻¹ and 0.5 km s⁻¹ for the warm HI. The true velocity dispersion is calculated with Eq. 5.3. Following §5 in Gelman et al. (2013), the prior on η is defined by a beta-distribution with exponents $\gamma_\eta = \epsilon\zeta$ and $\delta_\eta = \zeta(1 - \epsilon)$, whose hyper-parameters ϵ and ζ are distributed as reported in Table 5.B.1. Hence, the prior on η is a continuous distribution between 0 and 1, which is equivalent to a uniform distribution in the particular case $\gamma_\eta = \delta_\eta = 1$. In addition, this prior of η allows us to explore, at the same time, other distributions than the uniform one, adding a further level of generalisation.

Where $R_i \leq R_{\text{SFR}}$, the likelihood in Eq. 5.14 is written as

$$\begin{aligned} p(\mathcal{D}|\Theta) &= \prod_{i=1}^N p(\mathbf{d}_i|\Theta) = \prod_{i=1}^N p(\Sigma_{\text{SFR}_i} | \Sigma_{\text{SFR}_i}^T, \Delta \Sigma_{\text{SFR}_i}) \\ & p(h_{\text{HI}_i} | h_{\text{HI}_i}^T, \Delta h_{\text{HI}_i}) p(\sigma_i | \Delta \sigma_i, v_{\text{turb}_i}^T, v_{\text{th}}) \\ & p(\Sigma_{\text{HI}_i} | \Delta \Sigma_{\text{HI}_i}, v_{\text{turb}_i}^T, \Sigma_{\text{SFR}_i}^T, h_{\text{HI}_i}^T), \end{aligned} \quad (5.B.5)$$

while, where $R_i > R_{\text{SFR}}$, it is

$$\begin{aligned} p(\mathcal{D}|\Theta) &= \prod_{i=1}^N p(\mathbf{d}_i|\Theta) = \prod_{i=1}^N p(h_{\text{HI}_i} | h_{\text{HI}_i}^T, \Delta h_{\text{HI}_i}) \\ & p(\sigma_i | \Delta \sigma_i, v_{\text{turb}_i}^T, v_{\text{th}}) p(\Sigma_{\text{HI}_i} | \Delta \Sigma_{\text{HI}_i}, v_{\text{turb}_i}^T, \Sigma_{\text{SFR}_i}^T, h_{\text{HI}_i}^T). \end{aligned} \quad (5.B.6)$$

Table 5.B.1 – Hyper-priors probability distributions: **Normal** indicates a normal distribution with central value μ_α and standard deviation σ_α ; **Exp** is an exponential distribution with scale λ_β ; **Uniform** is a continuous uniform distribution between a minimum l_ϵ and a maximum u_ϵ ; **Gamma** is a gamma distribution with shape parameter γ_ζ and rate parameter δ_ζ (see Gelman et al., 2013).

Hyper-priors	Probability distribution
$\alpha_{v_{\text{turb}_i}}, \alpha_{\Sigma_{\text{SFR}_i}}, \alpha_{h_{\text{HI}_i}}$	Normal($\mu_\alpha = 0, \sigma_\alpha = 2$)
$\beta_{v_{\text{turb}_i}}, \beta_{\Sigma_{\text{SFR}_i}}, \beta_{h_{\text{HI}_i}}$	Exp($\lambda_\beta = 1$)
ϵ	Uniform($l_\epsilon = 0, u_\epsilon = 1$)
ζ	Gamma($\gamma_\zeta = 1, \delta_\zeta = 1/20$)

In Eq. 5.B.5 and Eq. 5.B.6, the probability distributions of Σ_{SFR_i} , σ_i , h_{HI_i} , and Σ_{HI_i} are normal distributions. Then, the probability distribution of the priors in Eq. 5.14, where $R_i \leq R_{\text{SFR}}$, is

$$\begin{aligned} \pi(\Theta|\Phi) &= \pi(\eta|\gamma_\eta, \delta_\eta) \prod_{i=1}^N \pi\left(v_{\text{turb}_i}^T | \alpha_{v_{\text{turb}_i}}, \beta_{v_{\text{turb}_i}}\right) \\ &\pi\left(\Sigma_{\text{SFR}_i}^T | \alpha_{\Sigma_{\text{SFR}_i}}, \beta_{\Sigma_{\text{SFR}_i}}\right) \pi\left(h_{\text{HI}_i}^T | \alpha_{h_{\text{HI}_i}}, \beta_{h_{\text{HI}_i}}\right) \\ &\pi\left(\sigma_i^T | v_{\text{turb}_i}^T, v_{\text{th}}\right), \end{aligned} \quad (5.B.7)$$

where the probability distributions of $\Sigma_{\text{SFR}_i}^T$, σ_i^T , $h_{\text{HI}_i}^T$, and $\Sigma_{\text{HI}_i}^T$ are log-normal distributions. Where $R_i > R_{\text{SFR}}$, we have instead

$$\begin{aligned} \pi(\Theta|\Phi) &= \pi(\eta|\gamma_\eta, \delta_\eta) \prod_{i=1}^N \pi\left(v_{\text{turb}_i}^T | \alpha_{v_{\text{turb}_i}}, \beta_{v_{\text{turb}_i}}\right) \\ &\pi\left(\Sigma_{\text{SFR}_i}^T | 0, u_{\Sigma_{\text{SFR}}}\right) \pi\left(h_{\text{HI}_i}^T | \alpha_{h_{\text{HI}_i}}, \beta_{h_{\text{HI}_i}}\right) \\ &\pi\left(\sigma_i^T | v_{\text{turb}_i}^T, v_{\text{th}}\right), \end{aligned} \quad (5.B.8)$$

and the probability distributions of $\Sigma_{\text{SFR}_i}^T$ is a uniform distribution between 0 and the upper limit $u_{\Sigma_{\text{SFR}}}$.

In the case of the two-phase HI, the probability distribution of the thermal velocity is a uniform distribution between $l_{v_{\text{th}}} = v_{\text{th,c}} = 1 \text{ km s}^{-1}$, which is the value for the CNM, and $u_{v_{\text{th}}} = v_{\text{th,w}} = 8.1 \text{ km s}^{-1}$, which is the value for the WNM.

We note that our best models (green bands in Figs. 5.2-5.5) are not directly obtained from E_{obs} (black points in Figs. 5.2-5.5), which is derived through Eq. 5.1 using the observed velocity dispersion and surface density (the error bars are calculated with the uncertainty propagation rules). As explained in this

section and in Sect. 5.3.2, our procedure is based on the priors on the observable quantities (Eq. 5.B.7 and Eq. 5.B.8). We can define a ‘true’ observed energy (E_{obs}^T) and derive its posterior distribution through Eq. 5.1 using the priors on Σ and σ^T . The median and 1σ error of E_{obs}^T are not necessarily the same as the value and the error bar of E_{obs} . This latter is directly derived from the observed quantities, while E_{obs}^T is ‘theoretical’. Hence, it is formally correct to compare E_{mod} with E_{obs} . This applies to all the figures shown in Sect. 5.4.

Appendix 5.C SN efficiency radial gradient

In this section we derive the efficiency of SN feedback using a different approach with respect to the hierarchical Bayesian method described in Sect. 5.3.2 and Appendix 5.B. This exercise was done as a preliminary test aiming to explore the case of a SN efficiency which can vary with the galactocentric radius. We simply chose the value and the uncertainty of the thermal velocity to be $v_{\text{th,c}} = 1 \pm 0.4 \text{ km s}^{-1}$ for the CNM, $v_{\text{th,w}} = 8.1 \pm 0.5 \text{ km s}^{-1}$ for the WNM, and $v_{\text{th,H}_2} = 0.06 \pm 0.005 \text{ km s}^{-1}$ for the molecular gas. In each case, we applied the following procedure at each galactocentric radius and for each galaxy. We subtracted the contribution of thermal motions from the observed velocity dispersion in order to estimate the turbulent velocity $v_{\text{turb}}(R)$ (Eq. 5.3), which was then used to calculate the SN energy assuming $\eta = 1$, $E_{\text{turb,SNe}}^{\text{max}}(R)$, through Eq. 5.8. We obtained the turbulent (i.e. non-thermal) component of the observed energy, $E_{\text{obs,turb}}(R)$, by subtracting the thermal energy (Eq. 5.9 and Eq. 5.10) from the observed energy and finally we derived the efficiency as $\eta(R) \equiv E_{\text{obs,turb}}(R)/E_{\text{turb,SNe}}^{\text{max}}(R)$. The errors on all the quantities were calculated using the rules of the uncertainty propagation.

Figures 5.C.9, 5.C.10 and 5.C.11, respectively, show the result of this analysis for all the galaxies in our sample in the case of the CNM, the WNM, and the molecular gas. In particular, the panels in the first and the third rows compare the radial profiles of the observed energy (black points) with the model energy (grey curve), which is the sum of the thermal energy (either blue or orange band) and the turbulence energy from SNe obtained with $\eta(R)$ (red curve). Clearly, the observed profiles are, by construction, perfectly reproduced by the model. The panels in the second and forth rows show the radial profiles of the SN efficiency $\eta(R)$ (grey points) and the median values $\langle \eta \rangle$ (dashed black line) with the 16th and the 84th percentile indicating the error (magenta band). First of all, we note that the efficiencies are always below unity, which is in agreement with the results obtained using the Bayesian approach and assuming η constant with the galactocentric radius. The values of $\langle \eta \rangle$ are also compatible within the uncertainties with those in Table 5.1. Moreover, $\eta(R)$ is generally compatible within the errors with its median, meaning that a flat profile can also reproduce the observation. In fact, the model energy obtained with $\langle \eta \rangle$ (magenta band) typically reproduces the observed energy as well as the profile obtained with

$\eta(R)$. This might indicate that the SN efficiency does not strongly depend on the ISM conditions (i.e. gas volume density, ISM speed) and, consequently, on the galactocentric radius, as expected from analytical model of SN remnant expansion (see §8.7 in Cimatti, Fraternali, & Nipoti, 2019). However, because of the large error on the efficiency, this interpretation remains uncertain (see discussion in Sect. 5.5.4). In the light of these results, we decided to assume η constant with the galactocentric radius in our fiducial model.

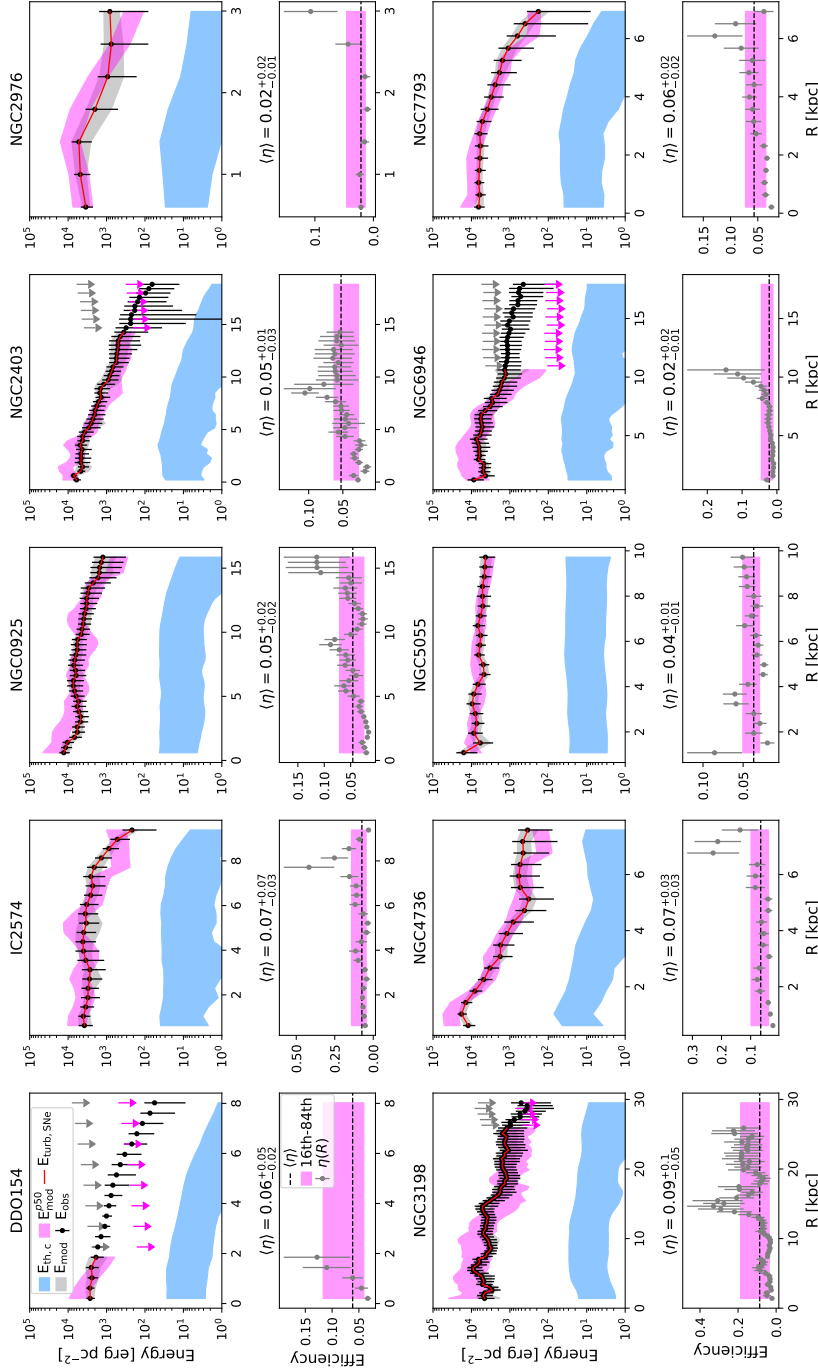


Figure 5.C.9 – *1st* & *3rd* rows: Observed energy per unit area of the atomic gas (black points) for our galaxy sample. The blue area shows the thermal energy ($E_{\text{th},c}$) of atomic gas for the CNM case. The red curve is the turbulent energy injected by SNe ($E_{\text{turb,SNe}}$) obtained with $\eta(R)$ (see panels below). The grey and magenta bands are the total energy obtained with $\eta(R)$ and with $\langle \eta \rangle$ (see panels below), respectively. Arrows indicate upper limits. *2nd* & *4th* rows: The grey points show the radial profile of the SN efficiency, whose median is indicated by the dashed black line. The magenta band corresponds to the 16th and 84th percentiles.

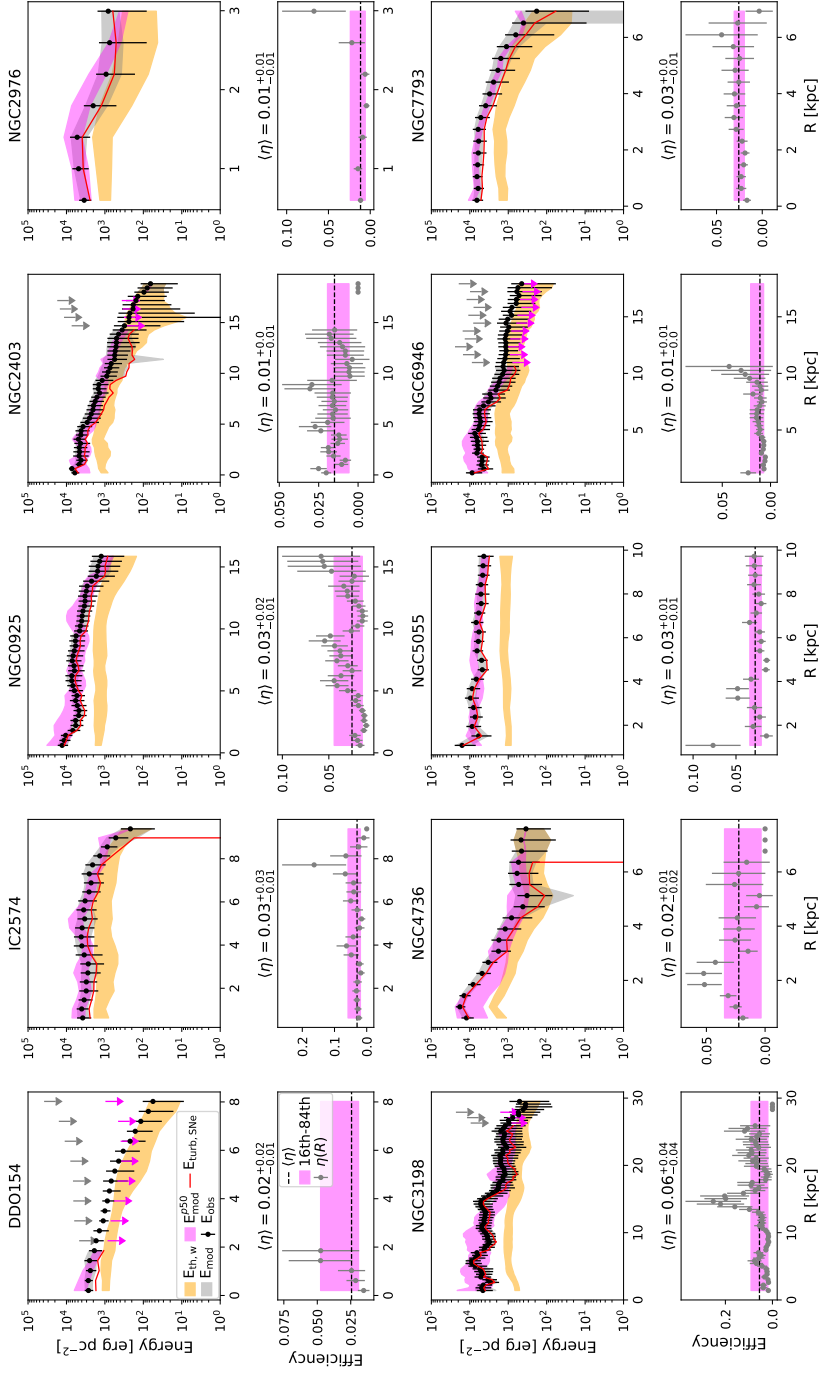


Figure 5.C.10 – Same as Fig. 5.C.9 but for the WNM case. The orange area shows the thermal energy ($E_{\text{th,w}}$) of atomic gas.

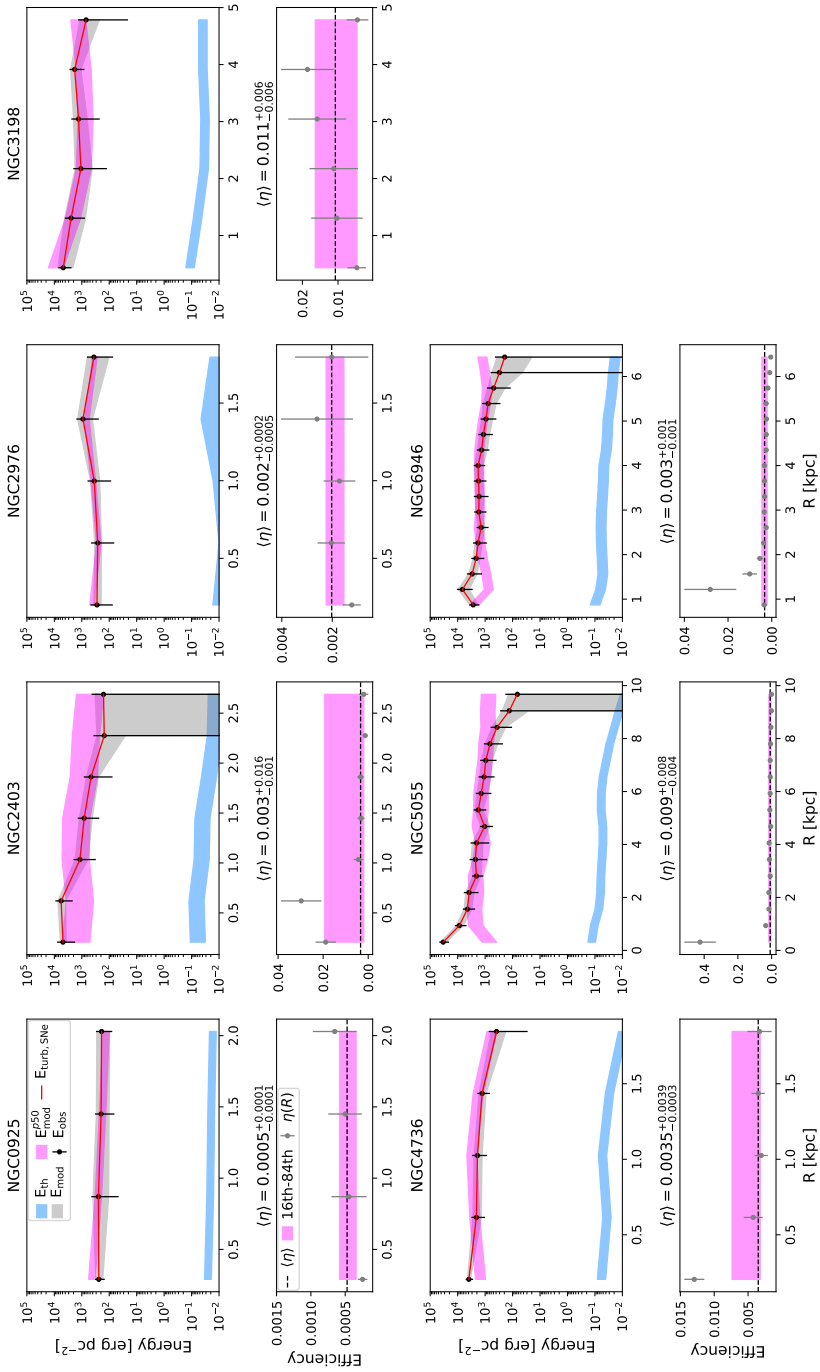


Figure 5.C.11 – Same as Fig. 5.C.9 but for the molecular gas.

CHAPTER 6

**Conclusions and future
prospects**

6.1 Summary and highlights

In this Ph.D. thesis, two crucial aspects of galaxy formation and evolution were investigated: star formation laws and the origin of turbulence in the interstellar medium (ISM). The key improvement with respect to previous studies consists in taking into account that gas discs in galaxies are thick and, most importantly, their scale height flares with the galactocentric radius.

In Chapters 2, 3 and 4, we used the scale height of gas discs in hydrostatic equilibrium to convert the observed surface densities of the gas (both HI and H₂) and the SFR to the corresponding volume densities for a sample of 22 nearby galaxies, including ten spiral and 12 dwarf galaxies, and for the Milky Way (MW). We thus derived the volumetric star formation (VSF) law involving the total gas (HI+H₂) and the SFR volume densities.

In Chapter 5, we used the gas scale height to accurately calculate the dissipation timescale of the turbulent energy of the neutral gas in the disc of ten nearby star-forming galaxies. We found that this timescale is longer and turbulent motions are therefore easier to sustain in flaring discs with respect to thin discs. We concluded that supernova (SN) explosions can effectively feed gas turbulence employing only a few percent of their total energy.

6.1.1 The flaring of gas discs in galaxies

The scale height of gas discs in spiral (Chapters 2 and 3) and dwarf (Chapter 4) galaxies grows with the distance from the galactic centre (i.e. flaring), both for the atomic and the molecular gas. This is expected from the assumption of hydrostatic equilibrium (see also Narayan & Jog, 2002; Banerjee et al., 2011; Iorio, 2018; Patra, 2018, 2020, for example) but also corroborated by observational measurements of the gas flaring in our Galaxy (e.g. Lockman, 1984; Wouterloot et al., 1990; Nakanishi & Sofue, 2003, 2006; Marasco et al., 2017), as well as by tentative estimates of the gas scale height in highly inclined and edge-on galaxies in the nearby Universe (e.g. Olling, 1996; Kregel et al., 2004; O'Brien et al., 2010; Peters et al., 2017b; Yim et al., 2020). The flaring is most prominent in the disc outskirts, where the gas scale height is from a few times to one order of magnitude larger than in the inner regions of the disc. As a consequence of the flaring, assuming that gas discs in galaxies are thin or have a constant thickness is not a realistic approximation and should be avoided when the gas distribution in spatially resolved galaxies is studied. The observed distribution of the gas in galaxies is indeed subject to significant projection effects and the same values of surface density can be measured where the volume density is low and the gas disc is thick, or vice versa. Therefore, it is of primary interest to properly measure the thickness of gaseous discs from observations (see Sect. 6.2.1).

To calculate the scale height of the gas in hydrostatic equilibrium, a robust analysis of the gas kinematics is fundamental for two important tasks. The

first is to accurately measure the gas velocity dispersion as a function of the galactocentric radius. To this aim, we analysed 21-cm and CO(2-1) emission line data cubes using the software ^{3D}BAROLO (Di Teodoro & Fraternali, 2015). The second critical task to derive the scale height is taking into account the main components of the gravitational potential (and mass distribution) of a galaxy. These components can be obtained through the rotation curve decomposition and consist in the stellar disc (or discs), the stellar bulge (when present), the gas itself, and the dark matter halo. If this latter is not considered, the resulting scale height is significantly overestimated in the outskirts (Fig. 2.3).

In Chapter 3, we have shown that the SFR vertical distribution in the MW also flares, closely following the same scale height as the gas in hydrostatic equilibrium. This suggests that the newborn stars preserve (at least for a few hundreds of Myr) the vertical distribution and velocity dispersion of the parent gas, perhaps indicating that the gas which is converted into stars is indeed in hydrostatic equilibrium. Interestingly, we found that the scale height of the atomic gas measured from observations in our Galaxy appears to be about 1.5 times larger than the ‘theoretical’ expectation based on the assumption of hydrostatic equilibrium, despite the latter is derived using the observed HI velocity dispersion. On the contrary, the observed and the ‘theoretical’ scale heights are in agreement in the case of the molecular gas. These findings may suggest that most of the molecular gas is in hydrostatic equilibrium and participating in star formation, while the atomic gas consists in two components, one in hydrostatic equilibrium and tracing the star-forming CO-dark gas, and the other (representing a relatively small fraction of the total atomic gas) which is neither in equilibrium nor star-forming. The origin of this second component is not clear, but it might be related to the extra-planar gas component, which has higher velocity dispersion than the gas in the disc (e.g. Marasco et al., 2017, 2019).

6.1.2 The volumetric star formation law

The VSF law is an empirical relation linking the total gas (HI+H₂) and the SFR volume densities as $\rho_{\text{SFR}} \propto \rho_{\text{gas}}^\alpha$. In Chapter 2, we derived the VSF law for twelve nearby galaxies, but we could only bracket the index of the VSF between $\alpha \simeq 1.3$ and $\alpha \simeq 1.9$ depending on whether a flare in the SFR scale height is taken into account or not. This uncertainty was due to the dearth of information on the vertical distribution of the SFR in nearby galaxies (but see Yim et al. 2020 and Elmegreen & Elmegreen 2020 for recent studies). In Chapter 3, we could overcome this issue by showing that the SFR scale height in our Galaxy flares in a very similar fashion to the gas. We also demonstrated that the VSF law is valid in the MW no matter whether the hydrostatic equilibrium is assumed or the volume densities are measured from the observations (Fig. 3.6). In Chapter 4, the VSF law was assessed in the regimes of dwarf galaxies as well as the outermost star-forming regions of spiral galaxies.

The index of the VSF law is $\alpha \simeq 2$ and this relation holds unbroken from low-density (HI-dominated) to high-density (H_2 -rich) environments. The absence of a break disfavors the existence of a density threshold for star formation. On the contrary, our results indicate that the break seen in surface-based star formation laws is a consequence of projection effects due to the disc flaring rather than to a drop in the star formation efficiency. The VSF law is remarkably tight and its intrinsic scatter ($\sigma_{\perp} \sim 0.1$ dex) is lower than that of surface-based star formation laws. This may indicate that the VSF law is the fundamental star formation law, also considering that the intrinsic volume densities are more physically meaningful than surface densities, which depend on projection effects. The quadratic index of the VSF law is consistent with the idea that, on kiloparsec scale, radiative cooling might be the primary process which sets the conversion of gas into stars, beforehand the gravitational instability is at play on the scales of molecular clouds. In this scenario, the cooling time ($\tau_{\text{cool}} \propto \rho_{\text{gas}}^{-1}$) regulates star formation on kiloparsec scale, while the free-fall time ($\tau_{\text{ff}} \propto \rho_{\text{gas}}^{-1/2}$) becomes important on cloud scale. In fact, the SFR per unit volume is given by the gas mass (per unit volume) which is converted into stars per unit timescale τ_{sf} , hence $\rho_{\text{SFR}} \propto \rho_{\text{gas}}/\tau_{\text{sf}}$. If radiative cooling is the main regulator of star formation (and $\tau_{\text{ff}} \ll \tau_{\text{cool}}$), we have then $\tau_{\text{sf}} \simeq \tau_{\text{cool}}$ and $\rho_{\text{SFR}} \propto \rho_{\text{gas}}/\tau_{\text{cool}} \propto \rho_{\text{gas}}^2$, in agreement with our empirical VSF law.

A surprising outcome of Chapters 2, 3 and 4 is the re-evaluation of the atomic gas as a tracer of the star-formation gas. We have shown that the volume densities of the atomic gas and the SFR correlate, following a power-law relation which is steeper than the VSF law with the total gas, but it is almost equally tight in terms of intrinsic scatter. However, the scatter of the relation with the atomic gas only tends to increase in H_2 -rich regions, suggesting that the total gas is a good tracer of the star-forming gas in the inner regions of discs, while the atomic gas does better where the gas density is low. This might be due to the presence, in the outskirts of galaxies, of a significant amount of CO-dark gas which is participating in star formation but is not accessible to observations (see also Elmegreen & Hunter, 2015; Hu et al., 2016). Alternatively, the relation involving the atomic gas may suggest that star formation can directly occur in the atomic gas in extreme ISM conditions (e.g. Glover & Clark, 2012). This scenario may seem controversial but is possible if the timescale of molecule formation is longer than both the cooling time and the free-fall time, as might happen in low-density and metal-poor environments (see e.g. Krumholz, 2012, 2013).

We also investigated the relation between the molecular gas and the SFR volume densities. Unsurprisingly, these two quantities correlate, but the intrinsic scatter of the relation (~ 0.4 dex) is comparable to that of the molecular star formation laws based on the surface densities. This indicates that, in the case of the molecular gas, the correction for the flaring is not as fundamental as for the atomic gas. However, (empirical) star formation laws involving the

molecular gas are available only the inner regions of spiral galaxies, where the emission of molecular gas tracers is observed. A interesting consequence of these considerations might be that, despite newborn stars are observed inside molecular clouds, it is advisable to adopt star formation laws based on the volume densities of the total gas (or the atomic gas) when one aims to study star-forming discs on kiloparsec scale (see Sect. 6.2.3).

6.1.3 Supernova-driven turbulence

Chapter 5 aimed to identify the physical mechanism which can energetically maintain the ISM turbulence in nearby star-forming galaxies. Previous works in the literature concluded that supernova (SN) feedback, which is expected to be the primary driver of turbulence, is insufficient to supply this energy. We showed that this is not the case if the flaring of the gas disc is taken into account, as the dissipation timescale is longer at large radii than in the inner regions of galaxies. We applied this model to a sample of eight spiral and two dwarf galaxies, for which we analysed the atomic and molecular gas distributions and kinematics. We found that a small fraction ($\lesssim 3\%$) of the SN energy estimated from the current SFR is required to maintain the observed turbulent motions of the gas in the disc, meaning that the other energy sources are essentially not needed or have a very minor role. We showed that thermal motions, together with turbulence, also give a significant contribution to the observed velocity dispersion of the atomic gas, especially in the outer and low-SFR regions of galaxies.

The results of this thesis are consistent with a scenario in which SN feedback and star formation are key elements of the same self-regulating cycle (see also e.g. Dopita, 1985; Ostriker & Shetty, 2011), which can be sketched as follows. When the SFR per unit volume increases, more SNe explode and transfer energy to the ISM, implying that the gas becomes more turbulent and its scale height grows. This makes the gas volume density in the midplane decrease and the SFR decline, accordingly to the VSF law. The gas then becomes less turbulent, weakening the support against gravity. This increases the gas volume density again, bringing to a new phase of high SFR. This self-regulating cycle can be valid locally in a star-forming region but does not necessarily occur to the whole disc. Exploring this scenario is of primary importance in the context of galaxy formation and evolution and requires dedicated studies (see Sect. 6.2.3).

6.2 Future developments

6.2.1 Measuring the thickness of discs

We mentioned already that the assumption of hydrostatic equilibrium for gas discs has not been extensively tested in the literature. To this aim, one should

measure the gas scale height from the observations and compare it with that of the gas in hydrostatic equilibrium (similarly to what we have done in Chapter 3). This task is however very challenging: while the rotation curve (necessary to estimate the galactic potential) is relatively easy to derive for edge-on discs, the velocity dispersion and the scale height are dramatically affected by projection effects (e.g. warps along the line of sight, non-circular motions, extra-planar gas). Therefore, it is necessary to develop a novel method to simultaneously measure the gas kinematics and vertical distribution in galaxies with relatively high inclination.

A possible approach might be based on a parametric model for the gas rotating in the disc in which its kinematics and structural properties (including the scale height) are described by functional forms depending on the galactocentric radius and a set of free parameters (e.g. Bouché et al., 2015; Peters et al., 2017a; Rizzo et al., 2018; Marasco et al., 2019). These parameters could then be fit in order to reproduce the observations of nearby disc galaxies using emission-line data cubes with suitable spatial resolution (see e.g. Peters et al., 2017a). Thus, the gas scale height and kinematics (i.e. velocity dispersion and rotation curve) could be derived in a self-consistent way.

A different method to estimate the gas scale height consists in measuring the physical scale at which the power spectrum of turbulence breaks as a consequence of the transition from 3D small-scale motions to 2D turbulence on scales larger than the disc scale height (e.g. Elmegreen et al., 2001; Padoan et al., 2001; Dutta et al., 2009). Hence, for a nearby disc with low inclination, it may be possible to obtain the observed scale height of the gas and, independently, the velocity dispersion through the ‘standard’ tilted-ring modelling.

6.2.2 Where star formation laws dare: taking the VSF law to extremes

Throughout this thesis, we stressed many times that the VSF law might be the fundamental star formation law for nearby galaxies. However, the validity of this relation is still limited to ‘normal’ disc galaxies and has not been tested in ‘extreme’ environments, such as starbursts and early-type galaxies (ETGs) with ongoing star formation.

In the high-density and H₂-dominated regime, starburst are an important test-case for star formation laws (see e.g. Kennicutt, 1998; Daddi et al., 2010; Genzel et al., 2010; Wilson et al., 2019). So far, we have partially studied this kind of environment in the innermost regions of a few massive spiral galaxies. We can guess that most of the gas in starburst is strongly turbulent as a consequence of the high SFR. Hence, this type of galaxies may host very thick gas discs, meaning that their gas distribution is subject to significant projection effects and making starburst an interesting case of study.

ETGs occasionally host rotating discs of atomic gas (e.g. Oosterloo et al., 2007b; Serra et al., 2014) and molecular gas in the inner regions (e.g. Young

et al., 2011; Davis et al., 2013). Moreover, these ‘active’ ETGs show indeed UV emission from recent star formation (e.g. Salim et al., 2012; Moffett et al., 2012; Yıldız et al., 2017), which is typically inefficient in this regime (e.g. Martig et al., 2013; Davis et al., 2014). To our knowledge, the gas scale height has never been investigated in this type of galaxies, but estimating the thickness of the gas discs and the potential flaring (likely present in the HI disc) is of primary interest to understand whether this inefficiency is due to projection effects and if the VSF law is valid also for ETGs.

6.2.3 Gas cycles in star-forming discs

The results presented in this thesis open to the analytical or semi-empirical studies of galaxy evolution based on the VSF law. As mentioned in Sect. 6.1.3, we found empirical indications of a self-regulating cycle in which SN-driven turbulence regulates the volume density of the star-forming gas in hydrostatic equilibrium, which determined the SFR per unit volume according to the VSF law. During the lifetime of a galaxy, this cycle is expected to interact with the cycle of gas accretion. In fact, the VSF law (Eq. 4.15) can be re-written to obtain the gas depletion time $\tau_{\text{dep}} \equiv \rho_{\text{gas}}/\rho_{\text{SFR}}$, which is the time required to convert all the available gas into stars. Assuming $\log A = 1$ and $\alpha = 2$ (see Table 4.2), we find $\tau_{\text{dep}} \simeq 0.1(\rho_{\text{gas}}/(\text{M}_{\odot}\text{pc}^{-3}))^{-1}$ Gyr. Therefore, the depletion time is $\tau_{\text{dep}} \sim 0.1 - 1$ Gyr for $\rho_{\text{gas}} \sim 0.1 - 1 \text{ M}_{\odot} \text{ pc}^{-3}$ and $\tau_{\text{dep}} \sim 100$ Gyr for $\rho_{\text{gas}} \sim 10^{-3} \text{ M}_{\odot} \text{ pc}^{-3}$, meaning that new gas needs to be accreted onto the inner regions of the disc in order to sustain star formation throughout the galaxy lifetime (assuming a SFR nearly constant in time). Hence, we need an accretion mechanism which is more efficient in the high- and medium-density regions of galaxies than in the outskirts. A possible candidate is galactic fountain accretion (see e.g. Fraternali, 2017). In this scenario, gas clouds are launched above the star-forming disc by super-bubble blowouts, accrete coronal material along their orbit, and finally fall back into the disc feeding the gas reservoir (e.g. Marinacci et al., 2011; Marasco et al., 2012; Armillotta et al., 2016). Before becoming available for star formation, the accreted gas has to move inward because its angular momentum is lower than that of the gas in disc at the impact radius (e.g. Pezzulli & Fraternali, 2016). The timescale of fountain accretion is ~ 100 Myr, which is typically shorter than the depletion time, hence this mechanism is likely able to sustain star formation even in this case of moderate accretion rates. Alternatively, accretion might occur in the outer disc and be transported through radial flows to the inner regions (e.g. Bouché et al., 2013; Krumholz et al., 2018). Future research will aim to distinguish between these two scenarios.

In addition, the VSF law might have interesting applications in the study of the inside-out growth of discs, as star formation laws are among the key ingredients of analytical and semi-analytical models of disc evolution (e.g. Dopita, 1985; Lilly et al., 2013; Pezzulli & Fraternali, 2016). Adopting a different relation may have an important impact on the predictions of theoretical models

(e.g. chemical abundances, galaxy scaling relations), in particular in the disc outskirts where surface-based star formation laws break down.

Bibliography

- Abramova, O. V. & Zasov, A. V. 2008, *Astronomy Reports*, 52, 257
- Agertz, O., Kravtsov, A. V., Leitner, S. N., & Gnedin, N. Y. 2013, *ApJ*, 770, 25
- Alves, J., Lombardi, M., & Lada, C. J. 2007, *A&A*, 462, L17
- Amorín, R., Muñoz-Tuñón, C., Aguerri, J. A. L., & Planesas, P. 2016, *A&A*, 588, A23
- Armillotta, L., Fraternali, F., & Marinacci, F. 2016, *MNRAS*, 462, 4157
- Armillotta, L., Krumholz, M. R., Di Teodoro, E. M., & McClure-Griffiths, N. M. 2019, *MNRAS*, 490, 4401
- Bahcall, J. N. 1984, *ApJ*, 276, 156
- Bahcall, J. N. & Casertano, S. 1984, *ApJ*, 284, L35
- Baillard, A., Bertin, E., de Lapparent, V., et al. 2011, *A&A*, 532, A74
- Balbus, S. A. & Hawley, J. F. 1991, *ApJ*, 376, 214
- Banerjee, A., Jog, C. J., Brinks, E., & Bagetakos, I. 2011, *MNRAS*, 415, 687
- Barnes, K. L., van Zee, L., Côté, S., & Schade, D. 2012, *ApJ*, 757, 64
- Battaglia, G., Fraternali, F., Oosterloo, T., & Sancisi, R. 2006, *A&A*, 447, 49
- Beck, R. 2007, *A&A*, 470, 539
- Beck, R., Brandenburg, A., Moss, D., Shukurov, A., & Sokoloff, D. 1996, *ARA&A*, 34, 155
- Begeman, K. G. 1987, PhD thesis, -
- Bigiél, F., Leroy, A., Walter, F., et al. 2010, *AJ*, 140, 1194
- Bigiél, F., Leroy, A., Walter, F., et al. 2008, *AJ*, 136, 2846
- Binney, J., Gerhard, O. E., Stark, A. A., Bally, J., & Uchida, K. I. 1991, *MNRAS*, 252, 210
- Binney, J. & Merrifield, M. 1998, *Galactic Astronomy* (Princeton University Press)
- Binney, J. & Tremaine, S. 2008, *Galactic Dynamics: Second Edition* (Princeton

- University Press)
- Bland-Hawthorn, J. & Gerhard, O. 2016, *ARA&A*, 54, 529
- Blitz, L. & Rosolowsky, E. 2006, *ApJ*, 650, 933
- Boissier, S., Gil de Paz, A., Boselli, A., et al. 2007, *ApJS*, 173, 524
- Boissier, S., Prantzos, N., Boselli, A., & Gavazzi, G. 2003, *MNRAS*, 346, 1215
- Bolatto, A. D., Leroy, A. K., Jameson, K., et al. 2011, *ApJ*, 741, 12
- Bolatto, A. D., Wolfire, M., & Leroy, A. K. 2013, *ARA&A*, 51, 207
- Bolatto, A. D., Wong, T., Utomo, D., et al. 2017, *ApJ*, 846, 159
- Bono, G., Marconi, M., Cassisi, S., et al. 2005, *ApJ*, 621, 966
- Boomsma, R. 2007, PhD thesis, Kapteyn Astronomical Institute, University of Groningen
- Boomsma, R., Oosterloo, T. A., Fraternali, F., van der Hulst, J. M., & Sancisi, R. 2008, *A&A*, 490, 555
- Bosma, A. 1981, *AJ*, 86, 1825
- Bouché, N., Carfantan, H., Schroetter, I., Michel-Dansac, L., & Contini, T. 2015, *The Astronomical Journal*, 150, 92
- Bouché, N., Murphy, M. T., Kacprzak, G. G., et al. 2013, *Science*, 341, 50
- Bournaud, F., Elmegreen, B. G., Teyssier, R., Block, D. L., & Puerari, I. 2010, *MNRAS*, 409, 1088
- Bregman, J. N. 1980, *ApJ*, 236, 577
- Bronfman, L., Casassus, S., May, J., & Nyman, L.-Å. 2000, *A&A*, 358, 521
- Bronfman, L., Cohen, R. S., Alvarez, H., May, J., & Thaddeus, P. 1988, *ApJ*, 324, 248
- Burke, B. F. 1957, *AJ*, 62, 90
- Burton, W. B. 1974, in *IAU Symposium, Vol. 60, Galactic Radio Astronomy*, ed. F. J. Kerr & S. C. Simonson, 551
- Burton, W. B. & Gordon, M. A. 1978, *A&A*, 63, 7
- Calabrò, A., Daddi, E., Cassata, P., et al. 2018, *ApJ*, 862, L22
- Caldú-Primo, A., Schrubba, A., Walter, F., et al. 2013, *AJ*, 146, 150
- Cannarozzo, C., Sonnenfeld, A., & Nipoti, C. 2020, *MNRAS*[[arXiv:1910.06987](https://arxiv.org/abs/1910.06987)]
- Caputo, F., Marconi, M., & Musella, I. 2000, *A&A*, 354, 610
- Cardelli, J. A., Clayton, G. C., & Mathis, J. S. 1989, *ApJ*, 345, 245
- Case, G. L. & Bhattacharya, D. 1998, *ApJ*, 504, 761
- Catinella, B., Saintonge, A., Janowiecki, S., et al. 2018, *MNRAS*, 476, 875
- Chandrasekhar, S. 1960, *Proceedings of the National Academy of Science*, 46, 253
- Chen, X., Wang, S., Deng, L., et al. 2019, *Nature Astronomy*, 3, 320
- Chen, X., Wang, S., Deng, L., de Grijs, R., & Yang, M. 2018, *ApJS*, 237, 28
- Chepurnov, A., Burkhardt, B., Lazarian, A., & Stanimirovic, S. 2015, *ApJ*, 810, 33
- Chevalier, R. A. 1974, *ApJ*, 188, 501

- Chevalier, R. A. & Gardner, J. 1974, *ApJ*, 192, 457
- Chomiuk, L. & Povich, M. S. 2011, *AJ*, 142, 197
- Chyży, K. T. & Buta, R. J. 2008, *ApJ*, 677, L17
- Cimatti, A., Fraternali, F., & Nipoti, C. 2019, *Introduction to Galaxy Formation and Evolution: From Primordial Gas to Present-Day Galaxies* (Cambridge University Press)
- Cioffi, D. F., McKee, C. F., & Bertschinger, E. 1988, *ApJ*, 334, 252
- Ciotti, L. & Ostriker, J. P. 2007, *ApJ*, 665, 1038
- Clemens, D. P., Sanders, D. B., & Scoville, N. Z. 1988, *ApJ*, 327, 139
- Cook, D. O., Dale, D. A., Johnson, B. D., et al. 2014, *MNRAS*, 445, 881
- Cormier, D., Bendo, G. J., Hony, S., et al. 2017, *MNRAS*, 468, L87
- Cormier, D., Madden, S. C., Lebouteiller, V., et al. 2015, *A&A*, 578, A53
- Cormier, D., Madden, S. C., Lebouteiller, V., et al. 2014, *A&A*, 564, A121
- Cortese, L., Boselli, A., Franzetti, P., et al. 2008, *MNRAS*, 386, 1157
- Cox, D. P. 1972, *ApJ*, 178, 159
- Cresci, G., Vanzi, L., Telles, E., et al. 2017, *A&A*, 604, A101
- Daddi, E., Elbaz, D., Walter, F., et al. 2010, *ApJ*, 714, L118
- Dale, D. A., Cohen, S. A., Johnson, L. C., et al. 2009, *ApJ*, 703, 517
- Dame, T. M., Hartmann, D., & Thaddeus, P. 2001, *ApJ*, 547, 792
- Dame, T. M., Ungerechts, H., Cohen, R. S., et al. 1987, *ApJ*, 322, 706
- Davis, T. A., Alatalo, K., Bureau, M., et al. 2013, *MNRAS*, 429, 534
- Davis, T. A., Young, L. M., Crocker, A. F., et al. 2014, *MNRAS*, 444, 3427
- de Blok, W. J. G. & Bosma, A. 2002, *A&A*, 385, 816
- de Blok, W. J. G., Keating, K. M., Pisano, D. J., et al. 2014, *A&A*, 569, A68
- de Blok, W. J. G., Walter, F., Brinks, E., et al. 2008, *AJ*, 136, 2648
- de los Reyes, M. A. C. & Kennicutt, Jr., R. C. 2019, *ApJ*, 872, 16
- Dehnen, W. & Binney, J. 1998, *MNRAS*, 294, 429
- Dékány, I., Hajdu, G., Grebel, E. K., & Catelan, M. 2019, *ApJ*, 883, 58
- Delgado, H. E., Sarro, L. M., Clementini, G., Muraveva, T., & Garofalo, A. 2019, *A&A*, 623, A156
- Dessauges-Zavadsky, M., Verdugo, C., Combes, F., & Pfenniger, D. 2014, *A&A*, 566, A147
- Di Teodoro, E. M. & Fraternali, F. 2015, *MNRAS*, 451, 3021
- Di Teodoro, E. M., Fraternali, F., & Miller, S. H. 2016, *A&A*, 594, A77
- Di Teodoro, E. M., Grillo, C., Fraternali, F., et al. 2018a, *MNRAS*, 476, 804
- Di Teodoro, E. M., McClure-Griffiths, N. M., Jameson, K. E., et al. 2019, *MNRAS*, 483, 392
- Di Teodoro, E. M., McClure-Griffiths, N. M., Lockman, F. J., et al. 2018b, *ApJ*, 855, 33

- Dib, S., Bell, E., & Burkert, A. 2006, *ApJ*, 638, 797
- Dib, S. & Burkert, A. 2005, *ApJ*, 630, 238
- Dickey, J. M. & Brinks, E. 1993, *ApJ*, 405, 153
- Dickey, J. M. & Lockman, F. J. 1990, *ARA&A*, 28, 215
- Dickey, J. M., Mebold, U., Stanimirovic, S., & Staveley-Smith, L. 2000, *ApJ*, 536, 756
- Digel, S. W. 1991, PhD thesis, Harvard University, Cambridge, MA.
- Donovan, J. L., Serra, P., van Gorkom, J. H., et al. 2009, *AJ*, 137, 5037
- Dopita, M. A. 1985, *ApJ*, 295, L5
- Dopita, M. A. & Ryder, S. D. 1994, *ApJ*, 430, 163
- Dutta, P., Begum, A., Bharadwaj, S., & Chengalur, J. N. 2009, *MNRAS*, 397, L60
- Elmegreen, B. G. 1997, in *Revista Mexicana de Astronomia y Astrofisica Conference Series*, Vol. 6, *Revista Mexicana de Astronomia y Astrofisica Conference Series*, ed. J. Franco, R. Terlevich, & A. Serrano, 165
- Elmegreen, B. G. 2000, *ApJ*, 530, 277
- Elmegreen, B. G. 2015, *ApJ*, 814, L30
- Elmegreen, B. G. 2018, *ApJ*, 854, 16
- Elmegreen, B. G. & Burkert, A. 2010, *ApJ*, 712, 294
- Elmegreen, B. G. & Elmegreen, D. M. 2020, *ApJ*, 895, 71
- Elmegreen, B. G. & Hunter, D. A. 2015, *ApJ*, 805, 145
- Elmegreen, B. G., Kim, S., & Staveley-Smith, L. 2001, *ApJ*, 548, 749
- Elmegreen, B. G., Rubio, M., Hunter, D. A., et al. 2013, *Nature*, 495, 487
- Elmegreen, B. G. & Scalo, J. 2004, *ARA&A*, 42, 211
- Ewen, H. I. & Purcell, E. M. 1951, *Nature*, 168, 356
- Ferguson, A. M. N., Wyse, R. F. G., Gallagher, J. S., & Hunter, D. A. 1998, *ApJ*, 506, L19
- Field, G. B. 1965, *ApJ*, 142, 531
- Fielding, D., Quataert, E., & Martizzi, D. 2018, *MNRAS*, 481, 3325
- Fierlinger, K. M., Burkert, A., Ntormousi, E., et al. 2016, *MNRAS*, 456, 710
- Foreman-Mackey, D., Hogg, D. W., Lang, D., & Goodman, J. 2013, *PASP*, 125, 306
- Frank, B. S., de Blok, W. J. G., Walter, F., Leroy, A., & Carignan, C. 2016, *AJ*, 151, 94
- Fraternali, F. 2017, in *Astrophysics and Space Science Library*, Vol. 430, *Gas Accretion onto Galaxies*, ed. A. Fox & R. Davé, 323
- Fraternali, F. & Binney, J. J. 2006, *MNRAS*, 366, 449
- Fraternali, F. & Binney, J. J. 2008, *MNRAS*, 386, 935
- Fraternali, F., Oosterloo, T., & Sancisi, R. 2004, *A&A*, 424, 485
- Fraternali, F., Oosterloo, T., Sancisi, R., & van Moorsel, G. 2001, *ApJ*, 562, L47
- Fraternali, F. & Tomassetti, M. 2012, *MNRAS*, 426, 2166
- Fraternali, F., van Moorsel, G., Sancisi, R., & Oosterloo, T. 2002, *AJ*, 123, 3124

- Freedman, D. & Diaconis, P. 1981, On the Histogram as a Density Estimator: L 2 Theory
- Gaia Collaboration, Brown, A. G. A., Vallenari, A., et al. 2018, *A&A*, 616, A1
- Gao, Y. & Solomon, P. M. 2004, *ApJ*, 606, 271
- Gatto, A., Fraternali, F., Read, J. I., et al. 2013, *MNRAS*, 433, 2749
- Gatto, A., Walch, S., Naab, T., et al. 2017, *MNRAS*, 466, 1903
- Gelman, A., Carlin, J. B., Stern, H. S., & Rubin, D. B. 2013, *Bayesian Data Analysis*, 3rd edn. (Chapman and Hall/CRC)
- Gentile, G., Fraternali, F., Klein, U., & Salucci, P. 2003, *A&A*, 405, 969
- Gentile, G., Józsa, G. I. G., Serra, P., et al. 2013, *A&A*, 554, A125
- Genzel, R., Tacconi, L. J., Gracia-Carpio, J., et al. 2010, *MNRAS*, 407, 2091
- Gil de Paz, A., Boissier, S., Madore, B. F., et al. 2007, *ApJS*, 173, 185
- Glover, S. C. O. & Clark, P. C. 2012, *MNRAS*, 421, 9
- Grabelsky, D. A., Cohen, R. S., Bronfman, L., Thaddeus, P., & May, J. 1987, *ApJ*, 315, 122
- Green, D. A. 2015, *MNRAS*, 454, 1517
- Gressel, O., Elstner, D., & Ziegler, U. 2013, *A&A*, 560, A93
- Hao, C.-N., Kennicutt, R. C., Johnson, B. D., et al. 2011, *ApJ*, 741, 124
- Hawley, J. F., Gammie, C. F., & Balbus, S. A. 1995, *ApJ*, 440, 742
- Heald, G., Józsa, G., Serra, P., et al. 2011, *A&A*, 526, A118
- Heiles, C. & Troland, T. H. 2003, *ApJ*, 586, 1067
- Helfer, T. T., Thornley, M. D., Regan, M. W., et al. 2003, *ApJS*, 145, 259
- Helmholtz, H. 1896, *Theorie der Luftschwingungen in Roehren MIT offenen Enden* (1859)
- Helmi, A. 2020, arXiv e-prints, arXiv:2002.04340
- Henshaw, J. D., Kruijssen, J. M. D., Longmore, S. N., et al. 2020, *Nature Astronomy* [arXiv:2007.01877]
- Herrera, C. N., Pety, J., Hughes, A., et al. 2020, *A&A*, 634, A121
- Heyer, M. H., Corbelli, E., Schneider, S. E., & Young, J. S. 2004, *ApJ*, 602, 723
- Hoffman, M. D. & Gelman, A. 2011, arXiv e-prints, arXiv:1111.4246
- Hollenbach, D. & McKee, C. F. 1979, *ApJS*, 41, 555
- Hu, C.-Y., Naab, T., Walch, S., Glover, S. C. O., & Clark, P. C. 2016, *MNRAS*, 458, 3528
- Hunt, L. K., García-Burillo, S., Casasola, V., et al. 2015, *A&A*, 583, A114
- Hunt, L. K., Testi, L., Casasola, V., et al. 2014, *A&A*, 561, A49
- Hunter, D. A., Elmegreen, B. G., & Baker, A. L. 1998a, *ApJ*, 493, 595
- Hunter, D. A., Elmegreen, B. G., & Baker, A. L. 1998b, *ApJ*, 493, 595
- Hunter, D. A., Elmegreen, B. G., & Berger, C. L. 2019, *AJ*, 157, 241
- Hunter, D. A., Elmegreen, B. G., & Ludka, B. C. 2010, *AJ*, 139, 447

- Hunter, D. A., Ficut-Vicas, D., Ashley, T., et al. 2012, *AJ*, 144, 134
- Ianjamasimanana, R., de Blok, W. J. G., & Heald, G. H. 2017, *AJ*, 153, 213
- Iorio, G. 2014, Master of Science Thesis, Bologna University, 1, 185
- Iorio, G. 2018, PhD thesis, PhD Thesis, University of Bologna, (2018)
- Iorio, G., Fraternali, F., Nipoti, C., et al. 2017, *MNRAS*, 466, 4159
- Jameson, K. E., McClure-Griffiths, N. M., Liu, B., et al. 2019, *ApJS*, 244, 7
- Jiménez-Donaire, M. J., Bigiel, F., Leroy, A. K., et al. 2019, *ApJ*, 880, 127
- Jones, E., Oliphant, T., Peterson, P., et al. 2001, *SciPy: Open source scientific tools for Python*
- Kalberla, P. M. W., Burton, W. B., Hartmann, D., et al. 2005, *A&A*, 440, 775
- Kalberla, P. M. W. & Dedes, L. 2008, *A&A*, 487, 951
- Kalberla, P. M. W., Dedes, L., Kerp, J., & Haud, U. 2007, *A&A*, 469, 511
- Kalberla, P. M. W. & Haud, U. 2018, *A&A*, 619, A58
- Kalberla, P. M. W. & Kerp, J. 1998, *A&A*, 339, 745
- Kamphuis, J., Sancisi, R., & van der Hulst, T. 1991, *A&A*, 244, L29
- Keller, B. W., Wadsley, J., Benincasa, S. M., & Couchman, H. M. P. 2014, *MNRAS*, 442, 3013
- Kennicutt, R. C., J. 1983, *ApJ*, 272, 54
- Kennicutt, R. C. & Evans, N. J. 2012, *ARA&A*, 50, 531
- Kennicutt, Jr., R. C. 1989, *ApJ*, 344, 685
- Kennicutt, Jr., R. C. 1998, *ApJ*, 498, 541
- Kennicutt, Jr., R. C., Armus, L., Bendo, G., et al. 2003, *PASP*, 115, 928
- Kennicutt, Jr., R. C., Calzetti, D., Walter, F., et al. 2007, *ApJ*, 671, 333
- Kerr, F. J., Hindman, J. V., & Carpenter, M. S. 1957, *Nature*, 180, 677
- Kim, C.-G. & Ostriker, E. C. 2015a, *ApJ*, 802, 99
- Kim, C.-G. & Ostriker, E. C. 2015b, *ApJ*, 802, 99
- Klessen, R. S. & Hennebelle, P. 2010, *A&A*, 520, A17
- Knapen, J. H., Lee, J. C., & Gil de Paz, A. 2017, *Outskirts of Galaxies: Astrophysics and Space Science Library*, Vol. 434 (Springer International Publishing)
- Koch, E. W., Rosolowsky, E. W., Schrubba, A., et al. 2019, *MNRAS*, 485, 2324
- Koda, J. 2008, in *Astronomical Society of the Pacific Conference Series*, Vol. 396, *Formation and Evolution of Galaxy Disks*, ed. J. G. Funes & E. M. Corsini, 97
- Kolmogorov, A. 1941, *Akademiia Nauk SSSR Doklady*, 30, 301
- Koo, B.-C. & McKee, C. F. 1992, *ApJ*, 388, 93
- Korpi, M. J., K p yl , P. J., & V is l , M. S. 2010, *Astronomische Nachrichten*, 331, 34
- Koyama, H. & Ostriker, E. C. 2009, *ApJ*, 693, 1346
- Kramer, E. D. & Randall, L. 2016, *ApJ*, 829, 126
- Kregel, M., van der Kruit, P. C., & de Blok, W. J. G. 2004, *MNRAS*, 352, 768

- Kritsuk, A. G. & Norman, M. L. 2002a, *ApJ*, 580, L51
- Kritsuk, A. G. & Norman, M. L. 2002b, *ApJ*, 569, L127
- Kroupa, P. 2002, *Science*, 295, 82
- Kroupa, P. & Weidner, C. 2003, *ApJ*, 598, 1076
- Krumholz, M. & Burkert, A. 2010, *ApJ*, 724, 895
- Krumholz, M. R. 2012, *ApJ*, 759, 9
- Krumholz, M. R. 2013, *MNRAS*, 436, 2747
- Krumholz, M. R. 2014, *Phys. Rep.*, 539, 49
- Krumholz, M. R. & Burkert, B. 2016, *MNRAS*, 458, 1671
- Krumholz, M. R., Burkert, B., Forbes, J. C., & Crocker, R. M. 2018, *MNRAS*, 477, 2716
- Krumholz, M. R., Dekel, A., & McKee, C. F. 2012, *ApJ*, 745, 69
- Krumholz, M. R. & Thompson, T. A. 2007, *ApJ*, 669, 289
- Kumari, N., Irwin, M. J., & James, B. L. 2020, *A&A*, 634, A24
- Kunz, M. W. & Balbus, S. A. 2004, *MNRAS*, 348, 355
- Lada, C. J., Lombardi, M., & Alves, J. F. 2010, *ApJ*, 724, 687
- Lada, C. J., Lombardi, M., Roman-Zuniga, C., Forbrich, J., & Alves, J. F. 2013, *ApJ*, 778, 133
- Lamperti, I., Saintonge, A., De Looze, I., et al. 2019, *MNRAS*, 489, 4389
- Larson, R. B. 1981, *MNRAS*, 194, 809
- Leavitt, H. S. & Pickering, E. C. 1912, *Harvard College Observatory Circular*, 173, 1
- Lee, J. C., Gil de Paz, A., Tremonti, C., et al. 2009, *ApJ*, 706, 599
- Lehnert, M. D., Nesvadba, N. P. H., Le Tiran, L., et al. 2009, *ApJ*, 699, 1660
- Lelli, F., De Breuck, C., Falkendal, T., et al. 2018, *MNRAS*, 479, 5440
- Lelli, F., McGaugh, S. S., & Schombert, J. M. 2016, *AJ*, 152, 157
- Lelli, F., Verheijen, M., & Fraternali, F. 2014a, *A&A*, 566, A71
- Lelli, F., Verheijen, M., & Fraternali, F. 2014b, *MNRAS*, 445, 1694
- Lelli, F., Verheijen, M., Fraternali, F., & Sancisi, R. 2012, *A&A*, 544, A145
- Leroy, A., Bolatto, A. D., Simon, J. D., & Blitz, L. 2005, *ApJ*, 625, 763
- Leroy, A. K., Walter, F., Bigiel, F., et al. 2009, *AJ*, 137, 4670
- Leroy, A. K., Walter, F., Brinks, E., et al. 2008, *AJ*, 136, 2782
- Leroy, A. K., Walter, F., Sandstrom, K., et al. 2013, *AJ*, 146, 19
- Levine, E. S., Blitz, L., & Heiles, C. 2006, *ApJ*, 643, 881
- Li, C., Zhao, G., Jia, Y., et al. 2019, *ApJ*, 871, 208
- Li, P., Lelli, F., McGaugh, S., & Schombert, J. 2020, *ApJS*, 247, 31
- Li, W., Chornock, R., Leaman, J., et al. 2011, *MNRAS*, 412, 1473
- Li, Y., Mac Low, M.-M., & Klessen, R. S. 2006, *ApJ*, 639, 879
- Licquia, T. C. & Newman, J. A. 2015, *ApJ*, 806, 96

- Lilly, S. J., Carollo, C. M., Pipino, A., Renzini, A., & Peng, Y. 2013, *ApJ*, 772, 119
- Liszt, H. S. 1992, in *Astrophysics and Space Science Library*, Vol. 180, The Center, Bulge, and Disk of the Milky Way, ed. L. Blitz, 111–130
- Liu, G., Koda, J., Calzetti, D., Fukuhara, M., & Momose, R. 2011, *ApJ*, 735, 63
- Lockman, F. J. 1984, *ApJ*, 283, 90
- Luna, A., Bronfman, L., Carrasco, L., & May, J. 2006, *ApJ*, 641, 938
- Lyne, A. G., Manchester, R. N., & Taylor, J. H. 1985, *MNRAS*, 213, 613
- Mac Low, M.-M. 1999, *ApJ*, 524, 169
- Mac Low, M.-M. & Klessen, R. S. 2004, *Reviews of Modern Physics*, 76, 125
- Mac Low, M.-M., Klessen, R. S., Burkert, A., & Smith, M. D. 1998, *Phys. Rev. Lett.*, 80, 2754
- Mac Low, M.-M. & McCray, R. 1988, *ApJ*, 324, 776
- Mac Low, M.-M., McCray, R., & Norman, M. L. 1989, *ApJ*, 337, 141
- Mackereth, J. T., Bovy, J., Schiavon, R. P., et al. 2017, *MNRAS*, 471, 3057
- Madau, P. & Dickinson, M. 2014, *ARA&A*, 52, 415
- Madden, S. C. & Cormier, D. 2019, in *IAU Symposium*, Vol. 344, Dwarf Galaxies: From the Deep Universe to the Present, ed. K. B. W. McQuinn & S. Stierwalt, 240–254
- Madore, B. F. 1977, *MNRAS*, 178, 1
- Madore, B. F., van den Bergh, S., & Rogstad, D. H. 1974, *ApJ*, 191, 317
- Mannucci, F., Della Valle, M., Panagia, N., et al. 2005, *A&A*, 433, 807
- Marasco, A. & Fraternali, F. 2011, *A&A*, 525, A134
- Marasco, A., Fraternali, F., & Binney, J. J. 2012, *MNRAS*, 419, 1107
- Marasco, A., Fraternali, F., Heald, G., et al. 2019, *A&A*, 631, A50
- Marasco, A., Fraternali, F., van der Hulst, J. M., & Oosterloo, T. 2017, *A&A*, 607, A106
- Marasco, A., Marinacci, F., & Fraternali, F. 2013, *MNRAS*, 433, 1634
- Marinacci, F., Fraternali, F., Nipoti, C., et al. 2011, *MNRAS*, 415, 1534
- Martig, M., Crocker, A. F., Bournaud, F., et al. 2013, *MNRAS*, 432, 1914
- Martin, C. L. & Kennicutt, Jr., R. C. 2001, *ApJ*, 555, 301
- Martin, D. C., Fanson, J., Schiminovich, D., et al. 2005, *ApJ*, 619, L1
- Martinsson, T. P. K., Verheijen, M. A. W., Bershady, M. A., et al. 2016, *A&A*, 585, A99
- Martizzi, D., Faucher-Giguère, C.-A., & Quataert, E. 2015, *MNRAS*, 450, 504
- Martizzi, D., Fielding, D., Faucher-Giguère, C.-A., & Quataert, E. 2016, *MNRAS*, 459, 2311
- Marx-Zimmer, M., Herbstmeier, U., Dickey, J. M., et al. 2000, *A&A*, 354, 787
- McKee, C. F. & Ostriker, E. C. 2007, *ARA&A*, 45, 565
- McKee, C. F. & Ostriker, J. P. 1977, *ApJ*, 218, 148

- McKee, C. F. & Williams, J. P. 1997, *ApJ*, 476, 144
- McMillan, P. J. 2011, *MNRAS*, 414, 2446
- McMillan, P. J. 2017, *MNRAS*, 465, 76
- McQuinn, K. B. W., Skillman, E. D., Dolphin, A. E., & Mitchell, N. P. 2015, *ApJ*, 808, 109
- McQuinn, K. B. W., Skillman, E. D., Heilman, T. N., Mitchell, N. P., & Kelley, T. 2018, *MNRAS*, 477, 3164
- Melioli, C., Brighenti, F., & D’Ercole, A. 2015, *MNRAS*, 446, 299
- Melioli, C., Brighenti, F., D’Ercole, A., & de Gouveia Dal Pino, E. M. 2008, *MNRAS*, 388, 573
- Melioli, C., Brighenti, F., D’Ercole, A., & de Gouveia Dal Pino, E. M. 2009, *MNRAS*, 399, 1089
- Mellema, G., Arthur, S. J., Henney, W. J., Iliev, I. T., & Shapiro, P. R. 2006, *ApJ*, 647, 397
- Melnick, J., Terlevich, R., Tenorio-Tagle, G., Telles, E., & Terlevich, E. 2019, arXiv e-prints, arXiv:1912.03543
- Menon, S. H., Federrath, C., & Kuiper, R. 2020, *MNRAS*, 493, 4643
- Misiriotis, A., Xilouris, E. M., Papamastorakis, J., Boumis, P., & Goudis, C. D. 2006, *A&A*, 459, 113
- Moellenhoff, C., Matthias, M., & Gerhard, O. E. 1995, *A&A*, 301, 359
- Moffett, A. J., Kannappan, S. J., Baker, A. J., & Laine, S. 2012, *ApJ*, 745, 34
- Mogotsi, K. M., de Blok, W. J. G., Caldú-Primo, A., et al. 2016, *AJ*, 151, 15
- Mondal, C., Subramaniam, A., & George, K. 2018, *AJ*, 156, 109
- Mróz, P., Udalski, A., Skowron, D. M., et al. 2019, *ApJ*, 870, L10
- Muñoz-Mateos, J. C., Gil de Paz, A., Boissier, S., et al. 2009, *ApJ*, 701, 1965
- Muñoz-Mateos, J. C., Boissier, S., de Paz, A. G., et al. 2011, *The Astrophysical Journal*, 731, 10
- Murray, C. E., Stanimirović, S., Goss, W. M., et al. 2018, *ApJS*, 238, 14
- Nakai, N. & Sofue, Y. 1982, *PASJ*, 34, 199
- Nakanishi, H. & Sofue, Y. 2003, *PASJ*, 55, 191
- Nakanishi, H. & Sofue, Y. 2006, *PASJ*, 58, 847
- Narayan, C. A. & Jog, C. J. 2002, *A&A*, 394, 89
- Narayanan, D., Krumholz, M. R., Ostriker, E. C., & Hernquist, L. 2012, *MNRAS*, 421, 3127
- Navarro, J. F., Frenk, C. S., & White, S. D. M. 1996, *ApJ*, 462, 563
- Nipoti, C. & Binney, J. 2015, *MNRAS*, 446, 1820
- Nugis, T. & Lamers, H. J. G. L. M. 2000, *A&A*, 360, 227
- O’Brien, J. C., Freeman, K. C., & van der Kruit, P. C. 2010, *A&A*, 515, A62
- Obukhov, A. M. 1962, *J. Geophys. Res.*, 67, 3011
- Oh, S.-H., Brook, C., Governato, F., et al. 2011, *AJ*, 142, 24

- Oh, S.-H., de Blok, W. J. G., Walter, F., Brinks, E., & Kennicutt, Jr., R. C. 2008, *AJ*, 136, 2761
- Ohlin, L., Renaud, F., & Agertz, O. 2019, *MNRAS*, 485, 3887
- Ohnishi, T. 1975, *Progress of Theoretical Physics*, 53, 1042
- Olling, R. P. 1995, *AJ*, 110, 591
- Olling, R. P. 1996, *AJ*, 112, 457
- Oosterloo, T., Fraternali, F., & Sancisi, R. 2007a, *AJ*, 134, 1019
- Oosterloo, T. A., Morganti, R., Sadler, E. M., van der Hulst, T., & Serra, P. 2007b, *A&A*, 465, 787
- Orkisz, J. H., Pety, J., Gerin, M., et al. 2017, *A&A*, 599, A99
- Ostriker, E. C., McKee, C. F., & Leroy, A. K. 2010, *ApJ*, 721, 975
- Ostriker, E. C. & Shetty, R. 2011, *ApJ*, 731, 41
- Padoan, P., Kim, S., Goodman, A., & Staveley-Smith, L. 2001, *ApJ*, 555, L33
- Padoan, P. & Nordlund, Å. 1999, *ApJ*, 526, 279
- Padoan, P., Pan, L., Haugbølle, T., & Nordlund, Å. 2016, *ApJ*, 822, 11
- Paladini, R., Davies, R. D., & De Zotti, G. 2004, *MNRAS*, 347, 237
- Pan, L., Padoan, P., Haugbølle, T., & Nordlund, Å. 2016, *ApJ*, 825, 30
- Patra, N. N. 2018, *MNRAS*, 478, 4931
- Patra, N. N. 2020, *MNRAS*
- Pellegrini, S. 2011, *ApJ*, 738, 57
- Peters, S. P. C., van der Kruit, P. C., Allen, R. J., & Freeman, K. C. 2017a, *MNRAS*, 464, 2
- Peters, S. P. C., van der Kruit, P. C., Allen, R. J., & Freeman, K. C. 2017b, *MNRAS*, 464, 32
- Pezzulli, G. & Fraternali, F. 2016, *MNRAS*, 455, 2308
- Pezzulli, G., Fraternali, F., Boissier, S., & Muñoz-Mateos, J. C. 2015, *MNRAS*, 451, 2324
- Pfrommer, C., Pakmor, R., Schaal, K., Simpson, C. M., & Springel, V. 2017, *MNRAS*, 465, 4500
- Pickering, T. E., Impey, C. D., van Gorkom, J. H., & Bothun, G. D. 1997, *AJ*, 114, 1858
- Pickering, T. E., van Gorkom, J. H., Impey, C. D., & Quillen, A. C. 1999, *AJ*, 118, 765
- Piffi, T., Binney, J., McMillan, P. J., et al. 2014, *MNRAS*, 445, 3133
- Pineda, J. L., Langer, W. D., Velusamy, T., & Goldsmith, P. F. 2013, *A&A*, 554, A103
- Piontek, R. A. & Ostriker, E. C. 2007, *ApJ*, 663, 183
- Pisano, D. J., Wilcots, E. M., & Elmegreen, B. G. 1998, *AJ*, 115, 975
- Poggianti, B. M., Gullieuszik, M., Tonnesen, S., et al. 2019, *MNRAS*, 482, 4466
- Ponomareva, A. A., Verheijen, M. A. W., Peletier, R. F., & Bosma, A. 2017, *MNRAS*, 469, 2387

- Pontzen, A. & Governato, F. 2014, *Nature*, 506, 171
- Posti, L., Fraternali, F., Di Teodoro, E. M., & Pezzulli, G. 2018, *A&A*, 612, L6
- Posti, L. & Helmi, A. 2019, *A&A*, 621, A56
- Puche, D., Westpfahl, D., Brinks, E., & Roy, J.-R. 1992, *AJ*, 103, 1841
- Puls, J., Kudritzki, R. P., Herrero, A., et al. 1996, *A&A*, 305, 171
- Putman, M. E., Peek, J. E. G., & Jounge, M. R. 2012, *ARA&A*, 50, 491
- Read, J. I., Agertz, O., & Collins, M. L. M. 2016a, *MNRAS*, 459, 2573
- Read, J. I. & Gilmore, G. 2005, *MNRAS*, 356, 107
- Read, J. I., Iorio, G., Agertz, O., & Fraternali, F. 2016b, *MNRAS*, 462, 3628
- Read, J. I., Iorio, G., Agertz, O., & Fraternali, F. 2017, *MNRAS*, 467, 2019
- Redaelli, E., Alves, F. O., Caselli, P., et al. 2017, *ApJ*, 850, 202
- Redaelli, E., Alves, F. O., Santos, F. P., & Caselli, P. 2019, *A&A*, 631, A154
- Riols, A. & Latter, H. 2019, *MNRAS*, 482, 3989
- Ripepi, V., Molinaro, R., Musella, I., et al. 2019, *A&A*, 625, A14
- Rizzo, F., Vegetti, S., Fraternali, F., & Di Teodoro, E. 2018, *MNRAS*, 481, 5606
- Robitaille, T. P. & Whitney, B. A. 2010, *ApJ*, 710, L11
- Rogstad, D. H., Lockhart, I. A., & Wright, M. C. H. 1974, *ApJ*, 193, 309
- Romeo, A. B. 1990, PhD thesis, PhD thesis, SISSA, Trieste, Italy, (1990)
- Romeo, A. B. 1992, *MNRAS*, 256, 307
- Romeo, A. B. & Falstad, N. 2013, *MNRAS*, 433, 1389
- Romeo, A. B. & Mogotsi, K. M. 2017, *MNRAS*, 469, 286
- Rosolowsky, E. & Blitz, L. 2005, *ApJ*, 623, 826
- Roychowdhury, S., Chengalur, J. N., Begum, A., & Karachentsev, I. D. 2010, *MNRAS*, 404, L60
- Roychowdhury, S., Chengalur, J. N., & Shi, Y. 2017, *A&A*, 608, A24
- Roychowdhury, S., Huang, M.-L., Kauffmann, G., Wang, J., & Chengalur, J. N. 2015, *MNRAS*, 449, 3700
- Rubin, K. H. R., Prochaska, J. X., Koo, D. C., et al. 2014, *ApJ*, 794, 156
- Rubin, V. C., Ford, W. K., J., & Thonnard, N. 1978, *ApJ*, 225, L107
- Saintonge, A., Catinella, B., Tacconi, L. J., et al. 2017, *ApJS*, 233, 22
- Salim, S., Fang, J. J., Rich, R. M., Faber, S. M., & Thilker, D. A. 2012, *ApJ*, 755, 105
- Salim, S., Rich, R. M., Charlot, S., et al. 2007, *ApJS*, 173, 267
- Salvatier, J., Wiecki, T., & Fonnesbeck, C. 2016, *PeerJ Computer Science* 2:e55
- Sancisi, R. & Allen, R. J. 1979, *A&A*, 74, 73
- Sancisi, R., Fraternali, F., Oosterloo, T., & van der Hulst, T. 2008, *A&A Rev.*, 15, 189
- Sanders, D. B., Solomon, P. M., & Scoville, N. Z. 1984, *ApJ*, 276, 182
- Sandstrom, K. M., Leroy, A. K., Walter, F., et al. 2013, *ApJ*, 777, 5

- Sanduleak, N. 1969, *AJ*, 74, 47
- Sarkar, S. & Jog, C. J. 2018, *A&A*, 617, A142
- Schaye, J. 2004, *ApJ*, 609, 667
- Schinnerer, E., Hughes, A., Leroy, A., et al. 2019, *ApJ*, 887, 49
- Schmidt, M. 1959, *ApJ*, 129, 243
- Schruba, A., Leroy, A. K., Walter, F., et al. 2011, *AJ*, 142, 37
- Schruba, A., Leroy, A. K., Walter, F., et al. 2012, *AJ*, 143, 138
- Schuster, K. F., Kramer, C., Hitschfeld, M., Garcia-Burillo, S., & Mookerjia, B. 2007, *A&A*, 461, 143
- Seifried, D., Walch, S., Girichidis, P., et al. 2017, *MNRAS*, 472, 4797
- Sellwood, J. A. 2014, *Reviews of Modern Physics*, 86, 1
- Sellwood, J. A. & Balbus, S. A. 1999, *ApJ*, 511, 660
- Serra, P., Oser, L., Krajnović, D., et al. 2014, *MNRAS*, 444, 3388
- Sérsic, J. L. 1963, *Boletín de la Asociación Argentina de Astronomía La Plata Argentina*, 6, 41
- Shapiro, P. R. & Field, G. B. 1976, *ApJ*, 205, 762
- Shi, Y., Helou, G., Yan, L., et al. 2011, *ApJ*, 733, 87
- Shi, Y., Yan, L., Armus, L., et al. 2018, *ApJ*, 853, 149
- Shu, F. H. 1977, *ApJ*, 214, 488
- Shu, F. H., Allen, R. J., Lizano, S., & Galli, D. 2007, *ApJ*, 662, L75
- Sicking, F. J. 1997, PhD thesis, PhD Thesis, University of Groningen, (1997)
- Silk, J. 1997, *ApJ*, 481, 703
- Simpson, C. M., Pakmor, R., Marinacci, F., et al. 2016, *ApJ*, 827, L29
- Skillman, E. D., Bothun, G. D., Murray, M. A., & Warmels, R. H. 1987, *A&A*, 185, 61
- Skowron, D. M., Skowron, J., Mróz, P., et al. 2019, *Science*, 365, 478
- Sofue, Y. 2017, *MNRAS*, 469, 1647
- Sofue, Y. & Nakanishi, H. 2017, *PASJ*, 69, 19
- Sormani, M. C., Binney, J., & Magorrian, J. 2015, *MNRAS*, 454, 1818
- Sormani, M. C. & Magorrian, J. 2015, *MNRAS*, 446, 4186
- Stilp, A. M., Dalcanton, J. J., Skillman, E., et al. 2013, *ApJ*, 773, 88
- Stone, J. M., Ostriker, E. C., & Gammie, C. F. 1998, *ApJ*, 508, L99
- Sun, J., Leroy, A. K., Ostriker, E. C., et al. 2020, *ApJ*, 892, 148
- Sun, J., Leroy, A. K., Schruba, A., et al. 2018, *ApJ*, 860, 172
- Swaters, R. A. 1999, PhD thesis, , Rijksuniversiteit Groningen, (1999)
- Swaters, R. A., Madore, B. F., van den Bosch, F. C., & Balcells, M. 2003, *ApJ*, 583, 732
- Swaters, R. A., Sancisi, R., & van der Hulst, J. M. 1997, *ApJ*, 491, 140
- Tacconi, L. J. & Young, J. S. 1987, *ApJ*, 322, 681

- Talbot, R. J., J. & Arnett, W. D. 1975, *ApJ*, 197, 551
- Tamburro, D., Rix, H.-W., Leroy, A. K., et al. 2009, *AJ*, 137, 4424
- Teich, Y. G., McNichols, A. T., Nims, E., et al. 2016, *ApJ*, 832, 85
- Tenjes, P. & Haud, U. 1991, *A&A*, 251, 11
- Thilker, D. A., Bianchi, L., Meurer, G., et al. 2007a, *ApJS*, 173, 538
- Thilker, D. A., Boissier, S., Bianchi, L., et al. 2007b, *ApJS*, 173, 572
- Thornton, K., Gaudlitz, M., Janka, H. T., & Steinmetz, M. 1998, *ApJ*, 500, 95
- Tielens, A. G. G. M. 2005, *The Physics and Chemistry of the Interstellar Medium*
- Tolstoy, E., Hill, V., & Tosi, M. 2009, *ARA&A*, 47, 371
- Toomre, A. 1964, *ApJ*, 139, 1217
- Utomo, D., Blitz, L., & Falgarone, E. 2019, *ApJ*, 871, 17
- van Albada, T. S., Bahcall, J. N., Begeman, K., & Sancisi, R. 1985, *ApJ*, 295, 305
- van de Hulst, H. C. 1946, PhD thesis, -
- van den Bosch, F. C. & Swaters, R. A. 2001, *MNRAS*, 325, 1017
- van der Kruit, P. C. & Freeman, K. C. 2011, *Annual Review of Astronomy and Astrophysics*, 49, 301
- van der Kruit, P. C. & Searle, L. 1981a, *A&A*, 95, 105
- van der Kruit, P. C. & Searle, L. 1981b, *A&A*, 95, 105
- Varidel, M. R., Croom, S. M., Lewis, G. F., et al. 2020, *MNRAS*, 495, 2265
- Veilleux, S., Cecil, G., & Bland-Hawthorn, J. 2005, *ARA&A*, 43, 769
- Velikhov, E. 1959, *Sov. Phys. JETP*, 36, 995
- Wada, K., Meurer, G., & Norman, C. A. 2002, *ApJ*, 577, 197
- Walch, S. K., Whitworth, A. P., Bisbas, T., Wünsch, R., & Hubber, D. 2012, *MNRAS*, 427, 625
- Walter, F. & Brinks, E. 1999, *AJ*, 118, 273
- Walter, F., Brinks, E., de Blok, W. J. G., et al. 2008, *AJ*, 136, 2563
- Walter, F., Cannon, J. M., Roussel, H., et al. 2007, *ApJ*, 661, 102
- Wang, B. & Silk, J. 1994a, *ApJ*, 427, 759
- Wang, B. & Silk, J. 1994b, *ApJ*, 427, 759
- Wang, H.-F., Liu, C., Xu, Y., Wan, J.-C., & Deng, L. 2018, *MNRAS*, 478, 3367
- Wang, J., Kauffmann, G., Józsa, G. I. G., et al. 2013, *MNRAS*, 433, 270
- Wardle, M. 1999, *MNRAS*, 307, 849
- Warren, S. R., Skillman, E. D., Stilp, A. M., et al. 2012, *ApJ*, 757, 84
- Weaver, R., McCray, R., Castor, J., Shapiro, P., & Moore, R. 1977, *ApJ*, 218, 377
- Weisz, D. R., Johnson, B. D., Johnson, L. C., et al. 2012, *ApJ*, 744, 44
- Westerhout, G. 1957, *Bulletin of the Astronomical Institutes of the Netherlands*, 13, 201
- Wilson, C. D., Elmegreen, B. G., Bemis, A., & Brunetti, N. 2019, *ApJ*, 882, 5

- Wilson, C. D., Warren, B. E., Irwin, J., et al. 2011, MNRAS, 410, 1409
- Wolfire, M. G., Hollenbach, D., & McKee, C. F. 2010, ApJ, 716, 1191
- Wolfire, M. G., Hollenbach, D., McKee, C. F., Tielens, A. G. G. M., & Bakes, E. L. O. 1995, ApJ, 443, 152
- Wolfire, M. G., McKee, C. F., Hollenbach, D., & Tielens, A. G. G. M. 2003, ApJ, 587, 278
- Wong, T. & Blitz, L. 2002, ApJ, 569, 157
- Wouterloot, J. G. A., Brand, J., Burton, W. B., & Kwee, K. K. 1990, A&A, 230, 21
- Wyder, T. K., Martin, D. C., Barlow, T. A., et al. 2009, ApJ, 696, 1834
- Wyse, R. F. G. 1986, ApJ, 311, L41
- Xiang, M., Shi, J., Liu, X., et al. 2018, ApJS, 237, 33
- Yıldız, M. K., Serra, P., Peletier, R. F., Oosterloo, T. A., & Duc, P.-A. 2017, MNRAS, 464, 329
- Yim, K. & van der Hulst, J. M. 2016, MNRAS, 463, 2092
- Yim, K., Wong, T., Howk, J. C., & van der Hulst, J. M. 2011, AJ, 141, 48
- Yim, K., Wong, T., Rand, R. J., & Schinnerer, E. 2020, MNRAS, 494, 4558
- Yim, K., Wong, T., Xue, R., et al. 2014, AJ, 148, 127
- Young, L. M., Bureau, M., Davis, T. A., et al. 2011, MNRAS, 414, 940
- Yu, X., Shi, Y., Chen, Y., et al. 2019, MNRAS, 486, 4463
- Yusifov, I. & Küçük, I. 2004a, A&A, 422, 545
- Yusifov, I. & Küçük, I. 2004b, A&A, 422, 545
- Zhang, H.-X., Hunter, D. A., Elmegreen, B. G., Gao, Y., & Schrupa, A. 2012, AJ, 143, 47
- Zhou, L., Federrath, C., Yuan, T., et al. 2017, MNRAS, 470, 4573
- Zschaechner, L. K., Rand, R. J., Heald, G. H., Gentile, G., & Kamphuis, P. 2011, ApJ, 740, 35

Summary

Quiescent and star-forming galaxies

Galaxies, systems of stars bound by gravity, are the building elements of the Universe. For example, the Sun and our Solar System are located in the Milky Way, a galaxy containing hundreds of billions of other stars which has a total mass of about 50 billion times the mass of the Sun. The Universe has evolved since the Big Bang for nearly 14 billion years, producing a wide diversity of galaxies with various shapes, sizes and masses (see Figure I). However, it is possible to divide galaxies in two groups simply according to their star formation activity. The formation of new stars is indeed a key property of galaxies used to distinguish between *quiescent galaxies* with very moderate or absent star formation activity, and *star-forming galaxies*, in which the birth of new stars is ongoing and sometimes vigorous (the so-called ‘starbursts’; Fig. Id).

Among quiescent systems one finds, in order of decreasing content of stars, giant elliptical galaxies (Fig. Ia), massive lenticular galaxies (Fig. Ib) and small dwarf spheroidal galaxies. Quiescent systems are mostly made of old stars with red-yellow colors.¹ In the star-forming group, there are spiral galaxies and dwarf irregular galaxies, the main object of study of this thesis. Most of the stars in star-forming systems are old, but part of the newborn population is very bright, hence the galaxies are characterised by blue colors. Spiral galaxies, such as the Milky Way, have their stars mostly distributed in a disc with

¹The color of stars mainly depends on the temperature of their atmosphere. The electromagnetic radiation (i.e. light) emitted by a star is composed of a wide range of frequencies and is called *continuum emission*. The coldest stars have temperatures of a few thousand degrees and yellow-red colors; they emit most radiation in the infrared wavelengths. The hottest stars have temperatures of a few 10 thousand degrees and blue colors; most of their radiation is emitted in the ultraviolet wavelengths.

‘arms’ starting from the galactic center, where a bulge of stars is often present (Fig. **Ic**). Spiral galaxies also contain a large amount of interstellar dust and gas at different temperatures. Stars, gas and dust rotate around the galactic centre along circular orbits. Dwarf irregular galaxies (Fig. **Ie**) have typically smaller sizes and masses than spiral ones and host, in proportion, much more gas and very little dust. Stars and dust (when present) are located in the inner regions of star-forming galaxies and their density decreases with increasing distance from the galactic centre, called galactocentric radius. The light emitted by stars heats the surrounding interstellar medium up to about 10 thousand degrees, hence the majority of this hot gas is typically found in the inner regions of the disc, where stars are numerous. Instead, the discs of ‘cold’ gas with temperatures from a few thousand to a hundred degrees tend to reach larger sizes and extends much further from the galactic centre than the stellar disc.

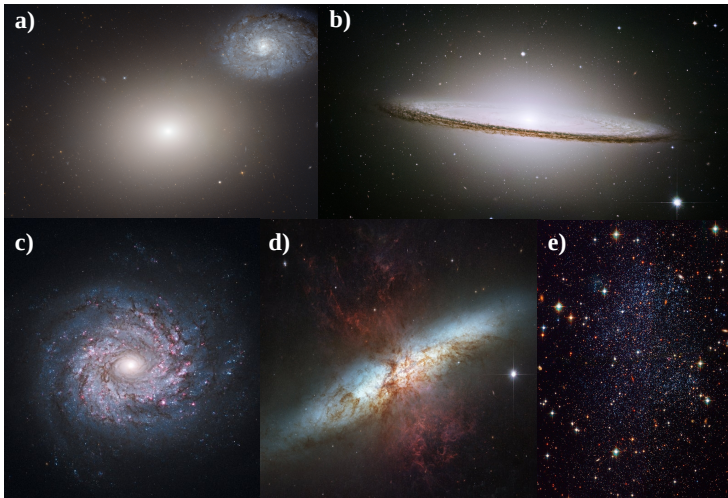


Figure I – Different galaxy types (not on the same scale) seen with the Hubble Space Telescope. *Panels a) and b)*: two quiescent galaxies, one with a star-forming companion. The left image shows a giant elliptical galaxy (M60) and a faint bluish spiral galaxy (NGC 4647). M60 has a mass of about one trillion times the Sun mass, while NGC 4647 mass is about one hundred times smaller. The right panel shows the lenticular galaxy NGC 4594, or Sombrero galaxy, which has a mass of about 200 billion times that of the Sun. Its stellar disc is seen almost edge-on, highlighting the central bulge of stars and the dark lane produced by dust absorbing the stellar light. *Panels c), d) and e)*: three star-forming galaxies. The left image shows NGC 3982, a face-on spiral galaxy with a bulge in the centre. The spiral arms hosts star-forming regions (pink), newborn star clusters (blue), and dust (dark lanes). The central image shows a starburst galaxy (M82) forming stars in its centre at a rate 10 times faster than the whole Milky Way. The red plumes trace the galactic wind, gas ejected by the explosions of young and massive stars (called *supernovae*). The image on the right shows a dwarf irregular galaxy in the constellation of Sagittarius and its blue and bright newborn stars.

The fuel for star formation

Linked to the star formation activity, an important difference between quiescent and star-forming galaxies is the reservoir of cold interstellar gas, the ‘raw material’ for new stars. Quiescent galaxies are poor or devoid of cold gas, their gas reservoir mainly consists of a gaseous halo at temperatures of several million degrees. Cold gas is instead abundant in star-forming galaxies and mainly consists of hydrogen, the most abundant element in the Universe, in the form of atomic and molecular hydrogen.

The cold gas can be observed and studied thanks to the radiation emitted by the gas particles. In particular, one of the most important radiation emitted by cold gas is the atomic hydrogen emission line, which can be measured in the radio band at the wavelength of about 21 cm (corresponding to a frequency of 1.42 billion hertz).² The 21-cm emission line was theoretically predicted by the Dutch astronomer and mathematician H. C. van de Hulst in 1944 and then observed in 1951 by H. I. Ewen and E. M. Purcell at Harvard University and confirmed by C. A. Muller and J. H. Oort at Leiden Observatory.

The cold gas in a galactic disc is not distributed smoothly, but it is structured in giant clouds and filaments. The inner and denser parts of these interstellar structures, which are typically made of molecular gas, are the loci of star formation (see Fig. II). Gravity drives the contraction and collapse of these dense cores, bringing to the formation of stars. The physical mechanisms that regulate this process are not completely understood and are among the most important topics of ongoing astrophysical research.



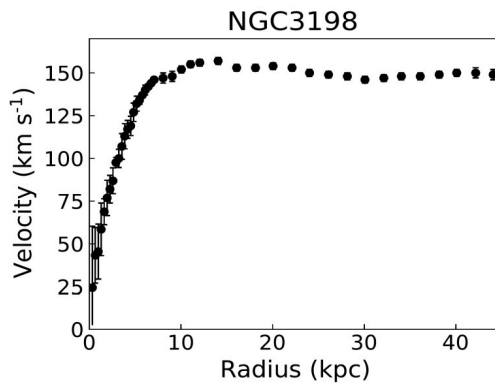
Figure II – A group of young and massive stars (R136) only a few million years old located in the Tarantula Nebula (or 30 Doradus), an extremely prolific star-forming regions in the Milky Way satellite galaxy named Large Magellanic Cloud. The blue stars in this image are among the most massive stars known and several of them are 100 times more massive than the Sun. These stars emit strong radiation and winds made of their atmospheric material, thus heating and carving the surrounding interstellar medium (green and red). Image obtained with the Hubble Space Telescope.

²*Emission line* means that the electromagnetic radiation emitted by a particle is characterised by a single frequency (or wavelength).

Between order and chaos

The gas in the disc of star-forming galaxies rotates in circular orbits around the galactic centre. This ordered rotation is the dominant motion of the gas. The rotation speed ranges from a few tens of kilometers per second in the case of small dwarf galaxies with stellar mass of about 100 thousand times the Sun mass, to a few hundreds of kilometers per second for the most massive spiral galaxies with stellar masses of a few 10 billion times the solar mass. The most common method used by astronomers to measure this rotation is based on the Doppler shift of the 21-cm emission line.³ Indeed, when one observes a rotating disc in projection in the sky plane, the emission from the two opposite sides of the disc is received at wavelengths shifted in different directions with respect to the emission from a non-rotating disc. Since the Doppler shift depends on the velocity of the emitting material, it is possible to measure the rotation speed of the gas as a function of the galactocentric radius, the so-called *rotation curve* (see Fig. III).

Figure III – Rotation curve of the spiral galaxy NGC 3198 obtained using observations of the emission line of atomic hydrogen at 21 cm. The galactocentric radius is expressed in kiloparsec (kpc; one kpc is equal to about 30,000 billion kilometers). The velocity increases in the inner regions of the disc, where most of the stellar mass is located, and it remains flat further out. Adapted from Cimatti, Fraternali & Nipoti (2019, Cambridge University Press).



The rotation speed of the gas at a given position in the disc depends on the mass contained in the region between this point and the galaxy center. Indeed, the stability of the gas disc is bound to the balance between the gravitational force, which attracts the gas toward the galactic centre, and the centrifugal force generated by rotation, which sustains the disc structure against gravitational collapse. For this reason, the rotation curve is a powerful tool to measure the mass distribution in galaxies. In the seventies, the study of rotation curves in nearby galaxies, mostly carried out in Groningen, led to the discovery of the dark matter. It was found that the visible mass in galaxies is not sufficient to

³The Doppler effect, or shift, is the change of the wavelength of a wave (the electromagnetic radiation in this case) caused by the motion of the emitting source with respect to the receiver. When the source moves away from the receiver, the wave is stretched, meaning the wavelength increases and the frequency decreases. Vice versa, if the source approaches the receiver, the wave is compressed, the wavelength decrease and the frequency increases.

explain the observed rotation velocity (see Fig. III), implying the presence of invisible matter. Later research highlighted that the Universe is dominated by dark matter, whose nature remains one of the biggest open questions in modern science.

The ordered rotation of the gas disc coexists with disordered motions, similarly to water swirls in the flow of a river. These random motions are of the order of a few kilometers per second and partially due to the temperature of the gas particles, but their dominant component, called *turbulence*, has a different nature. Turbulence can be visualised as chaotic motions between macroscopic portions of interstellar gas with various sizes, or eddies, which interact with each other. The viscosity of the gas tends to dissipate the energy of these eddies. Hence, a continuous source of energy is needed in order to sustain turbulence in the interstellar gas.

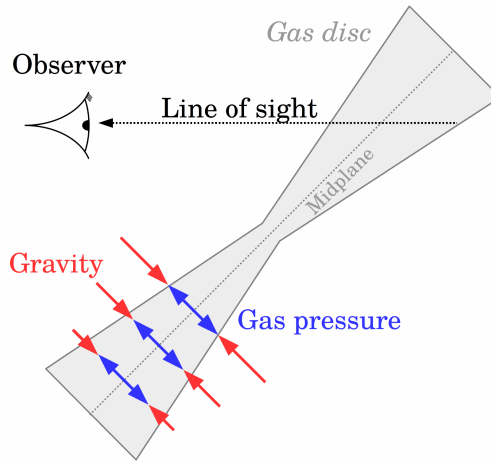
Disordered motions can be measured through the broadening of the emission lines of the gas. For instance, that at 21-cm has been extensively used for this purpose. Due to turbulence, the gas particles along an observer's line of sight move randomly both in the receding and the approaching directions with a wide range of different speeds. Hence, the emitted radiation is Doppler-shifted at various wavelengths. The observer, who receives the sum of all this emission, measures therefore a broad emission line covering different wavelengths. The line broadening is a direct measurement of the strength of the chaotic motions in the gas and can be used to study the nature of turbulence.

More than flat discs

In galaxies, the gas random motions generate a form of pressure, which contributes to the equilibrium of the gas disc by opposing the gravitational pull along either the direction of the galactocentric radius and the vertical direction. Along the galactocentric radius, this pressure helps rotation in balancing gravity; its contribution is negligible in the case of the disc of spiral galaxies, which are largely dominated by rotation, but it can become significant for dwarf galaxies with slowly rotating discs. The gas pressure is instead the main form of support against gravity along the vertical direction above and below the midplane of the disc (see Fig. IV). In other words, pressure 'puffs up' the gas disc, while gravity tends to flatten it. In galaxies, the vertical structure of the gas is established by the balance between pressure and gravity; this condition is called *vertical hydrostatic equilibrium*. With increasing height above the disc and distance from the galaxy centre, the density of matter (stars, gas and dark matter) decreases and, consequently, the gravitational pull along the vertical direction weakens. As a result, a gas disc in hydrostatic equilibrium becomes thicker and thicker with increasing galactocentric distance.

Galaxies are seen in projection in the sky plane by an external observer. Their line of sight pierces the galactic disc at a certain galactocentric distance,

Figure IV – Sketch of a galactic gas disc in vertical hydrostatic equilibrium. Above and below the disc midplane (grey dotted line), the gas pressure (blue arrows) tends to ‘inflate’ the gas disc by opposing gravity (red arrows), which pulls the gas in the opposite direction. Since the gravitational force weakens with increasing distance from the galaxy centre and height above the midplane, the thickness of the gas disc grows. An external observer sees the sum of the emission of all the material along the line of sight and the further one looks from the galaxy centre, the thicker is the gas layer crossed by the line of sight.



collecting the light emitted by all the material along it. Since the disc thickness increases with the disc radius, the line of sight meets a larger column of gas in the outer regions of a galaxy than in the inner ones. Hence, one can observe bright emission from the gas either where the disc is thin and the gas is dense, as in inner parts of galaxies, or where the disc is thick and the gas is diffuse, which is typically the case of the outer regions. Therefore, the projection effect due to the disc thickness must be taken into account in the study of the density and distribution of gas in galaxies.

This thesis

The importance of the thickness of gas discs is the ‘fil rouge’ running throughout the chapters of this thesis, which can be divided in two main parts.

The first part focuses on the relation between recent star formation and the amount of cold interstellar gas present in the disc of star-forming galaxies. This idea was originally proposed in 1959 by the Dutch astronomer Maarten Schmidt, born in Groningen and Oort’s Ph.D. student in Leiden. Based on theoretical arguments, he proposed that the rate of star formation in a given volume inside the disc of a galaxy is proportional to density of the cold gas in the same volume. This relation is generally referred to as *star formation law*. Using observations in the Milky Way, Schmidt estimated that the star formation rate increases with the gas density to a power between unity and three, hence the exact formulation of the star formation law remained uncertain.

The star formation law is fundamental in the study of the formation and evolution of galaxies. It is indeed used in theoretical models to calculate the rate of consumption of the gas reservoir of a galaxy, the corresponding rate of star formation across time and the growth of the galaxy stellar mass. Moreover,

the exact dependence (e.g. quadratic or cubic) of the star formation rate on the gas density can give important hints on the physical mechanisms that regulate star formation.

In external galaxies, it is not possible to measure the gas density and the star formation rate *per unit volume*, as galaxies are seen in projection in the sky plane; the observable quantities are instead the gas density and the star formation rate *per unit surface*. These projected quantities have been successfully and extensively used to derive the surface-based star formation law for galaxies with different masses and strength of the star formation activity, from dwarf galaxies to starbursts. However, it is still not clear whether the same star formation law is valid for all star-forming galaxies. Observational evidence also indicates that, while this relation holds in the inner regions of galactic discs, it breaks down in their outskirts where there is little cold gas and the star formation activity is modest. Therefore, different versions of the star formation law have been proposed since Schmidt's pioneering work, but no general consensus is reached on which formulation is correct.

In this respect, the approach and results presented in this thesis represent an important improvement, as the star formation law is obtained using the gas density and the star formation rate per unit volume. These quantities were derived from the observed gas density and the star formation rate per unit surface using the thickness of the gas disc. The thickness was calculated assuming that the gas is in vertical hydrostatic equilibrium. The random motions of the gas were measured from the emission line broadening and the gravitational force was derived from the mass distribution traced by the rotation curve. The star formation rate per unit volume was found to be proportional to the square of the gas density per unit volume, in agreement with Schmidt's results. This volume-based relation, called *volumetric star formation law*, was derived for a sample of dwarf and spiral galaxies and for the Milky Way. Differently from the surface-based relation, the volumetric star formation law is valid for both gas-poor and moderately star-forming environments and for gas-rich and more active regions of galaxies. This is the main result of the first part of this dissertation and indicates that the current theoretical models of star formation adopted in the study of galaxy formation and evolution possibly need revision.

The other section of this thesis aims to investigate the origin of turbulence in cold interstellar gas and its 'engine'. The measurements of random motions of the cold gas in galactic discs show that this medium is highly turbulent. Since turbulence is thought to be dissipated relatively quickly, some physical phenomenon is required to regenerate turbulent motions. In this respect, supernova explosions are the primary suspects, as they release huge amounts of energy in the interstellar medium. However, an empirical confirmation of this scenario has been lacking until now. Furthermore, the number of supernova explosions expected from the population of newborn massive stars in galaxies

was found to be insufficient to maintain turbulence across the whole gas disc, indicating that other feeding mechanisms are needed. By taking into account the disc thickness, a crucial improvement is obtained in this thesis with respect to previous works. Indeed, turbulence dissipation acts more slowly in thick discs than in thin ones. This reduces the energy supply required to sustain turbulent motions, bringing to the conclusion that supernova explosions alone can maintain the turbulence of the cold gas in galaxies.

Overall, the results presented in this dissertation represent a significant progress in the knowledge of the link between the interstellar gas in galaxies and the formation of new stars, and improve our understanding of the impact of supernovae on the gas motions in galactic discs.

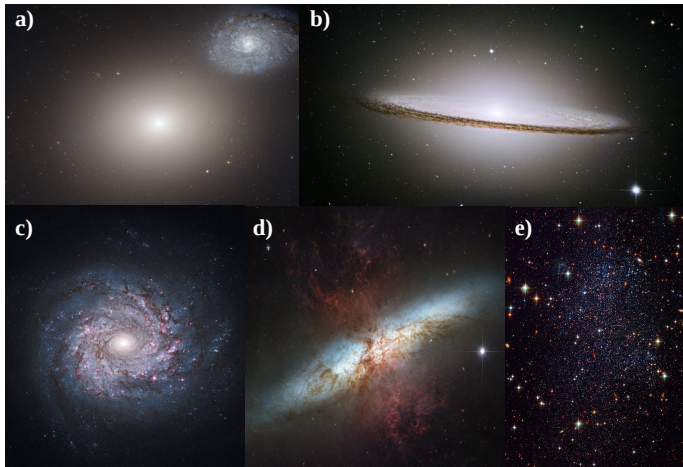
Samenvatting

Rustige en stervormende sterrenstelsels

Sterrenstelsel, systemen van sterren gebonden door zwaartekracht, vormen de bouwstenen van het Universum. Bijvoorbeeld, de zon en ons zonnestelsel bevinden zich in het Melkwegstelsel (of de Melkweg), een sterrenstelsel met honderden miljarden andere sterren die in totaal een massa heeft van ongeveer 50 miljard keer de zonsmassa. Het universum is sinds de Oerknal geëvolueerd over een periode van bijna 14 miljard jaar, hierdoor is er een grote diversiteit aan sterrenstelsels van verschillende vormen, maten en massa's (zie Figuur I). Het is echter mogelijk om sterrenstelsels te verdelen in twee groepen, simpelweg op basis van hun stervormingsactiviteit. De mate van stervorming is een sleuteleigenschap die gebruikt wordt om onderscheid te maken tussen *rustige sterrenstelsels*, dit zijn systemen met een zeer geringe of geen stervorming, en *stervormende sterrenstelsels*, waarin de geboorte van nieuwe sterren continue plaatsvindt en soms zeer krachtig is (de zo zogenaamde 'starbursts'; Fig. Id).

Onder rustige systemen vindt men, in de volgorde van afnemend aantal sterren, gigantische elliptische sterrenstelsels (Fig. Ia), massieve lensvormige sterrenstelsels (Fig. Ib) en kleine bolvormige dwergsterrenstelsels (ook wel dwergstelsels genaamd). Rustige systemen bestaan meestal uit oude sterren met roodgele kleuren.¹ In de stervormende groep bevinden zich spiraalvormige sterrenstelsels (spiraalstelsel) en onregelmatige dwergsterrenstelsels, beide wor-

¹De kleur van sterren wordt voornamelijk bepaald door de temperatuur van hun atmosfeer. De elektromagnetische straling (d.w.z. licht) die door een ster wordt uitgezonden bestaat uit een breed scala aan frequenties en wordt *continuïemissie* genoemd. De koudste sterren hebben temperaturen van een paar duizend graden, zijn geelrood in kleur en zenden de meeste straling uit in het infrarood. De heetste sterren hebben temperaturen van enkele tienduizend graden, kleuren blauw en stralen voornamelijk ultraviolet licht uit.



Figuur I – Verschillende soorten sterrenstelsels (niet weergegeven op dezelfde schaal) gezien door de Hubble Space Telescope. *Panelen a) en b)*: twee rustige sterrenstelsels, één gezien met een stervormende metgezel. De linker afbeelding toont een gigantisch elliptisch sterrenstelsel (M60) en een zwak blauwachtig spiraalstelsel (NGC 4647). M60 heeft een massa van ongeveer een biljoen zonsmassa's, terwijl de massa van NGC 4647 ongeveer een factor honderd keer kleiner is. Het rechterpaneel toont het lenticulaire sterrenstelsel NGC 4594, ook wel genaamd het Sombrestelsel. Dit sterrenstelsel heeft een massa van ongeveer 200 miljard keer die van de zon. De stellaire schijf is bijna van opzij te zien (edge-on) en benadrukt de centrale opeenhoping van sterren en de donkere baan die wordt geproduceerd door het stof dat het stellaire licht absorbeert. *Panelen c), d) en e)*: drie stervormende sterrenstelsels. De linker afbeelding toont NGC 3982, een face-on spiraalstelsel met een uitstulping in het midden. De spiraalarmen herbergen stervormingsgebieden (de roze gebieden), pasgeboren sterclusters (de blauw gebieden) en stof (de donkere streken). De centrale afbeelding toont een starburst sterrenstelsel (M82) dat in het midden sterren vormt met een snelheid die 10 keer hoger ligt dan die van de Melkweg. De rode pluimen volgen de galactische wind: gas dat is uitgestoten door de explosies van jonge en zware sterren (genaamd *supernovae*). De afbeelding rechts toont een onregelmatig dwergsterrenstelsel in het sterrenbeeld van de Boogschutter, dit zijn blauwe heldere sterren die pas geboren zijn.

den bestudeerd in dit proefschrift. De meeste sterren in stervormingssystemen zijn oud, maar een deel van de pasgeboren populatie is erg helder, daarom worden deze sterrenstelsels gekenmerkt door blauwe kleuren. Spiraalstelsels, zoals de Melkweg, hebben hun sterren meestal verdeeld in een schijf met 'armen'. Deze armen beginnen vanuit het galactische centrum, waar vaak een opeenhoping (de 'buldge') van sterren aanwezig is (Fig. 1c), en strekken zich uit naar buiten toe. Spiraalstelsels bevatten ook een grote hoeveelheid interstellair gas en stof van verschillende temperaturen, die tegelijk met de sterren, in cirkelvormige banen rondom het galactische centrum draaien. Onregelmatige dwergsterrenstelsels (Fig. 1e) zijn doorgaans kleiner en bestaan uit minder massa dan spiraalvormige sterrenstelsels, daarnaast is er naar verhouding veel meer gas

en veel meer stof aanwezig. Sterren en stof (mits aanwezig) bevinden zich in de binnenste regio's van stervormende sterrenstelsels en hun dichtheid neemt af als functie van afstand ten opzichte van het galactische centrum, de zogenaamde galactocentrische straal. Het door sterren uitgestraalde licht verwarmt het omringende interstellair medium tot ongeveer tienduizend graden. Het grootste deel van dit hete gas meestal wordt aangetroffen in de binnenste regionen van de schijf, waar sterren talrijk zijn. In tegenstelling tot heet gas, hebben de schijven met 'koud' gas temperaturen van een paar honderd tot duizend graden. Deze schijven hebben de neiging grotere afstanden te bestrijken en strekken zich veel verder uit van het galactische centrum dan de stellaire schijf.

De brandstof voor stervorming

Gekoppeld aan de stervormingsactiviteit, is een belangrijk verschil tussen rustige en stervormende sterrenstelsels het reservoir van koud interstellair gas, de 'brandstof' voor nieuwe sterren. Rustige sterrenstelsels zijn arm of volledig leeg van koud gas, hun gasreservoir bestaat voornamelijk uit een gasvormige halo van enkele miljoenen graden. Koud gas is daarentegen in overvloed aanwezig in stervormende sterrenstelsels en bestaat voornamelijk uit atomaire en moleculair waterstof, het meest voorkomende element in het heelal.

Het koude gas kan worden waargenomen en bestudeerd dankzij de straling van de gasdeeltjes. De belangrijkste straling die wordt uitgezonden door koud gas is dat van de atomaire waterstofemissielijn, deze wordt gemeten in het radio bij een golflengte van ongeveer 21 cm (hetgeen overeenkomt met een frequentie van 1.42 miljard Hertz). De 21 cm-(emissie)lijn ² werd in 1944 voorspeld door de Nederlandse astronoom en wiskundige H. C. van de Hulst. Vervolgens werd de lijn waargenomen in 1951 door H. I. Ewen en E. M. Purcell aan de Harvard University en deze observatie werd later bevestigd door C. A. Muller en J. H. Oort van de Sterrewacht Leiden.

Het koude gas in de galactische schijf is niet gelijkmatig verdeeld, maar is gestructureerd in gigantische wolken en filamenten. De binnenste en dichtere delen van deze interstellair structuren, die typisch bestaan uit moleculair gas, zijn de loci van stervorming (zie Fig. II). De zwaartekracht drijft de samentrekking van deze gaswolken, waardoor sterren ontstaan. De fysische mechanismen die dit proces reguleren zijn nog niet volledig begrepen en vormen een belangrijk onderzoeksveld binnen de astrofysica.

Tussen orde en chaos

Het gas in de schijf van stervormende sterrenstelsels draait in cirkelvormige banen rond het galactische centrum. Deze geordende rotatie is de dominante

²De elektromagnetische straling uitgezonden door een deeltje wordt gekenmerkt door een frequentie (of een golflengte), dit wordt ook een *emissielijn* genoemd.

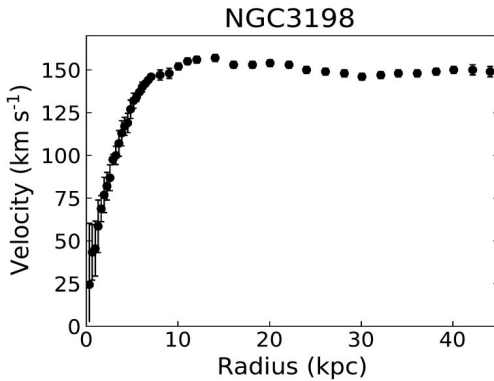
Figuur II – Een groep jonge en zware sterren (R136) in de Tarantula-nevel (of 30 Doradus) van slechts een paar miljoen jaar oud. Dit is een rijk stervormingsgebied in het Melkwegstelsel, genaamd de Grote Magelhaense Wolk. De blauwe sterren op deze afbeelding behoren tot de zwaarste sterren die we kennen, een aantal hiervan zijn honderd keer zwaarder dan de zon. Deze sterren zenden sterke straling en winden (gemaakt van hun atmosferische materiaal) uit. Hierdoor wordt het omringende interstellair medium (groen en rood) verwarmd en opgesneden. De afbeelding verkregen is met de Hubble Space Telescope.



beweging van het gas. De rotatiesnelheid varieert van enkele tientallen kilometers per seconde voor kleine dwergstelsels met een stellaire massa van ongeveer honderdduizend keer de zonsmassa, tot enkele honderden kilometers per seconde voor de meest massieve spiraalstelsels met een stellaire massa van een enkele tien miljard zonsmassa's. De meest gebruikelijke methode voor het meten van deze rotatie is door middel van de Dopplerverschuiving³ van de 21 cm-lijn. Wanneer men een roterende schijf in het observatievlak waarneemt, wordt de emissie van de twee tegenoverliggende zijden van de schijf ontvangen bij golflengtes die in verschillende richtingen, ten opzichte van de emissie van een niet-roterende schijf, zijn verschoven. De mate van Dopplerverschuiving hangt af van de rotatiesnelheid van het materiaal en daarom is het mogelijk om de rotatiesnelheid van het gas te meten als functie van de galactocentrische straal, de zogenaamde *rotatiecurve* (zie Fig. III).

De rotatiesnelheid van het gas voor een gegeven de galactocentrische straal hangt af van de totale massa in het gebied vanaf dit punt tot het centrum van het sterrenstelsel. De stabiliteit van de schijf wordt bepaald door de balans tussen de zwaartekracht, die het gas naar het galactische centrum toetrekt, en de centrifugale kracht (gegenereerd door de rotatie), die de zwaartekracht tegenwerkt. Op deze manier wordt de rotatiecurve gebruikt om de massaverdeling in sterrenstelsels te meten. In de jaren zeventig,

³Het Doppler effect (of de Dopplerverschuiving) is de verandering in golflengte van een golf (in dit geval de elektromagnetische straling) die wordt veroorzaakt door de beweging van de bron ten opzichte van de ontvanger. Wanneer de bron van de ontvanger af beweegt wordt de golf uitgerekt, wat betekent dat de golflengte toeneemt en de frequentie afneemt. Omgekeerd, wanneer de bron de ontvanger nadert, wordt de golf gecompriëerd, dus neemt de golflengte af en de frequentie toe.



Figuur III – Rotatiecurve van het spiraalstelsel NGC 3198 verkregen met behulp van waarnemingen van de emissielijn van atomaire waterstof op 21 cm. De galactocentrische straal wordt uitgedrukt in kiloparsec (kpc; één kpc is gelijk aan ongeveer 30.000 miljard kilometer). De snelheid neemt toe in de binnenste regionen van de schijf, waar het grootste deel van de stellaire massa zich bevindt, en blijft verder plat. Aangepast van Cimatti, Fraternali & Nipoti (2019, Cambridge University Press).

leidde het onderzoek naar rotatiecurven in nabije sterrenstelsels, voornamelijk uitgevoerd in Groningen, tot de ontdekking van donkere materie. Dit onderzoek toonde aan dat de zichtbare massa in sterrenstelsels niet voldoende was om de waargenomen rotatiesnelheid te verklaren (zie Fig. III), hetgeen de aanwezigheid van onzichtbare (of donkere) materie impliceerde. Later onderzoek wees uit dat het heelal wordt gedomineerd door donkere materie. De aard van deze materie vormt nog steeds een van de grootste open vragen in de moderne wetenschap.

De geordende rotatie van de gasschijf bestaat naast een ongeordende bewegingen, welke vergelijkbaar met water dat in de stroming van een rivier wervelt. De willekeurige bewegingen zijn in de orde van enkele kilometers per seconde en zijn gedeeltelijk te wijten aan de temperatuur van de gasdeeltjes, maar hun dominante component, *turbulentie* genaamd, heeft een andere aard. Turbulentie kan worden gezien als de chaotische bewegingen tussen macroscopische delen van interstellair gas van verschillende afmetingen, deze wervelingen of “eddies” staan met elkaar in wisselwerking. De viscositeit van het gas heeft de neiging om de energie van deze eddies af te voeren, daarom is een continue energiebron nodig om turbulentie in het interstellaire gas in stand te houden.

De ongeordende bewegingen van het gas kunnen worden gemeten door de verbreding van de emissielijnen te bepalen. Als gevolg van turbulente bewegingen de gasdeeltjes zich willekeurig langs de gezichtslijn van de waarnemer met een breed scala aan verschillende snelheden. De uitgezonden straling ondergaat hier Dopplerverschuiving of verschillende golflengtes. De waarnemer, die de geïntegreerde emissies ontvangt, meet daarom een bredere emissielijn die meerdere golflengtes bestrijkt. Deze lijnverbreding geeft ene directe maat voor de sterkte van de chaotische bewegingen in het gas en wordt daarom gebruikt om de aard van turbulentie te bestuderen. De 21 cm-lijn is hiervoor op grote schaal gebruikt.

Meer dan platte schijven

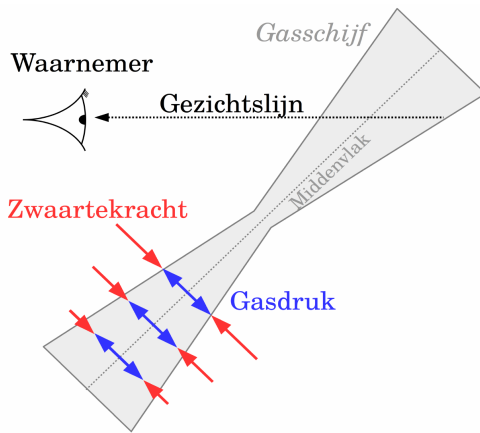
In sterrenstelsels wekken de willekeurige gasbewegingen een druk op. Deze druk draagt bij aan het evenwicht van de gasschijf door de zwaartekracht tegen te werken, langs zowel de galactocentrische straal als in de verticale richting (zie Fig. IV). Voor spiraalstelsel is de willekeurige gasdruk bijdrage langs galactocentrische straal verwaarloosbaar klein, aangezien deze grotendeels gedomineerd worden door rotatie, maar het kan significant worden voor dwergsterrenstelsels met langzamer roterende schijven. In de verticale richting is deze gasdruk de belangrijkste component die de zwaartekracht tegenwerkt, zeker boven en onder het middenvlak van de schijf. De willekeurige gasdruk ‘blaast’ de gasschijf op, terwijl de zwaartekracht de neiging heeft om deze af te vlakken. Op deze manier wordt de verticale structuur van het gas in sterrenstelsel bepaald door de balans tussen de willekeurige gasdruk en de zwaartekracht; deze toestand wordt ook wel *verticaal hydrostatisch evenwicht* genoemd. De dichtheid van materie (sterren, gas en donkere materie) neemt af als functie van toenemende hoogte boven de schijf en galactocentrische straal, met als gevolg dat de zwaartekracht in verticale richting zwakker wordt. Als resultaat wordt een gasschijf in hydrostatisch evenwicht wijder met toenemende galactocentrische afstand.

Sterrenstelsels worden door een externe waarnemer gezien als een projectie in het observatievlak gezien. Hun gezichtslijn doorboort de galactische schijf op een bepaalde galactocentrische afstand en verzamelt het licht dat wordt uitgezonden door het materiaal langs deze lijn. De schijfdikte neemt toe als een functie schijfradius, daarom is de dichtheid langs de gezichtslijn hoger voor de buitenste regionen van het sterrenstelsel dan voor de binnenste. Hierdoor ziet men een sterke emissie van gebieden van waar de schijf dun is en het gas een hoge dichtheid heeft (de binnenste delen) of van waar de schijf dik is en het gas diffuus is (de buitenste delen). Met andere woorden, bij het bestuderen van de dichtheid en verdeling van gas in sterrenstelsels moet men rekening houden met het projectie effect wat ontstaat als gevolg van de schijfdikte.

Dit proefschrift

Het belang van de dikte van gasschijven is de leidraad die door de hoofdstukken van dit proefschrift loopt, en kan ik twee delen worden verdeeld.

Het eerste deel richt zich op de relatie tussen recente stervorming en de hoeveelheid koud interstellair gas aanwezig in de schijf van stervormende sterrenstelsels. Dit idee werd oorspronkelijk in 1959 geopperd door de Nederlandse astronoom Maarten Schmidt, geboren in Groningen en Oort’s promovendus in Leiden. Op basis van theoretische argumenten stelde hij dat de mate van stervorming in een bepaald volume binnen de schijf van een sterrenstelsel een verband heeft met de dichtheid van het koude gas in datzelfde



Figuur IV – Schets van een galactische gasschijf in verticaal hydrostatisch evenwicht. Boven en onder het middenvlak van de schijf (grijze stippellijn) neigt de gasdruk (blauwe pijlen) ertoe om de gasschijf op te blazen en de zwaartekracht (rode pijlen), die het gas in de tegenovergestelde richting trekt, tegen te werken. De zwaartekracht neemt af met galactocentrische straal en de hoogte boven het middenvlak, hierdoor wordt de gasschijf wijder. Een externe waarnemer ziet de som van de emissie van al het materiaal langs de gezichtslijn. Dus, hoe verder men kijkt vanuit het centrum van sterrenstelsel, des te dikker is de gaslaag die wordt doorkruist door de gezichtslijn.

volume. Deze relatie wordt doorgaans de *stervormingswet* genoemd. Met behulp van Melkweg waarnemingen schatte Schmidt dat de stervormingssnelheid toeneemt als de gasdichtheid tot de exponent, waarbij de exponent een waarde van tussen de één en drie heeft. De onzekerheid in de exponent zorgde er echter voor dat een exacte formulering van de stervormingswet uit bleef.

De stervormingswet is fundamenteel voor het bestuderen van de vorming en evolutie van sterrenstelsels. Het wordt in theoretische modellen gebruikt om de verbruik snelheid (wat gedefinieerd is als de mate van stervorming over de groei van de stellaire massa als functie van tijd) van het gasreservoir in sterrenstelsels te berekenen. Bovendien kan de exacte waarde van de exponent (bijvoorbeeld kwadratisch of kubisch) in de stervormingswet belangrijke aanwijzingen geven over de fysische mechanismen die stervorming en gasdichtheid reguleren.

Voor externe sterrenstelsels (alle sterrenstelsels behalve de Melkweg) is het niet mogelijk om de gasdichtheid en de stervormingssnelheid *per volume-eenheid* te meten, aangezien sterrenstelsels in projectie in het observatievlak worden waargenomen. In plaats daarvan, zijn de waarneembare grootheden de gasdichtheid en de stervormingssnelheid *per oppervlakte-eenheid*. Deze geprojecteerde grootheden worden gebruikt om de oppervlakte gebaseerde stervormingswet af te leiden voor verschillende sterrenstelsels, van dwergsterrenstelsels tot starbursts. Het is echter nog niet duidelijk of dezelfde stervormingswet geldt voor alle stervormende sterrenstelsels. Observatieel bewijs geeft aan dat dit verband geldt voor de binnenste regionen van galactische schijven, maar niet voor de buitengebieden, waar er weinig koud gas aanwezig is en de stervormingsactiviteit beperkt is. Daarom zijn er sinds Schmidts pionierswerk verschillende versies van de stervormingswet voorgesteld, maar is er nog geen algemene consensus bereikt over een eenduidige formulering.

In dit opzicht vormen de aanpak en resultaten die in dit proefschrift worden gepresenteerd een belangrijke verbetering, aangezien de stervormingswet

wordt verkregen met behulp van de gasdichtheid en de stervormingssnelheid per volume-eenheid. Deze hoeveelheden zijn afgeleid van de waargenomen gasdichtheid en de stervormingssnelheid per oppervlakte-eenheid met behulp van de dikte van de gasschijf. De dikte werd berekend in de veronderstelling dat het gas zich in verticaal hydrostatisch evenwicht bevindt. De willekeurige bewegingen van het gas werden gemeten door middel van de emissielijnverbreding en de zwaartekracht werd afgeleid gebruikmakend van de rotatiecurve. De stervormingssnelheid per volume-eenheid bleek te schalen met het kwadraat van de gasdichtheid per volume-eenheid, hetgeen in overeenstemming is met de resultaten van Schmidt. Deze op volume gebaseerde relatie, genaamd de *volumetrische stervormingswet*, werd afgeleid voor een set van sterrenstelsels, bestaande uit dwerg- en spiraalstelsels en de Melkweg. Anders dan voor de op oppervlak gebaseerde relatie, is de volumetrische stervormingswet geldig voor zowel gasarme gebieden met beperkte stervorming als voor gasrijke en actievere stervormingsgebieden. Dit is het belangrijkste resultaat van het eerste deel van dit proefschrift en geeft aan dat de huidige theoretische modellen voor stervorming, die worden gebruikt voor het bestuderen van de vorming en evolutie van sterrenstelsels, mogelijk herzien moeten worden.

Het andere deel van dit proefschrift richt zich op de oorsprong van turbulentie in koud interstellair gas en de onderliggende aandrijvende fenomenen. De observaties van willekeurige bewegingen in galactische schijven laten zien dat dit medium zeer turbulent is. Men denkt dat turbulentie relatief snel verdwijnt en dat er een fysisch fenomeen nodig is om turbulente bewegingen te regenereren. Supernova explosies zijn de belangrijkste kandidaten, omdat ze enorme hoeveelheden energie vrijgeven in het interstellaire medium. Een observationele bevestiging van dit scenario ontbrak echter nog. Bovendien bleek dat het aantal voorspelde supernova explosies (op basis van de populatie van pasgeboren massieve sterren in sterrenstelsels) onvoldoende was om turbulentie over de hele gasschijf te behouden, wat aangeeft dat andere regeneratie mechanismen nodig zijn. Door rekening te houden met de schijfdikte, wordt in dit proefschrift een cruciale verbetering bereikt ten opzichte van eerdere werken. Een belangrijk inzicht is dat de dissipatie van turbulentie langzamer gaat voor dikke schijven dan voor dunne schijven. Dit vermindert de benodigde energietoevoer om turbulente draaiende te houden, waardoor het aantal supernova explosies nu wel toereikend is om turbulentie in het koude gas van sterrenstelsels te kunnen handhaven.

De resultaten van dit proefschrift laten een significante vooruitgang zien in het begrip van de relatie tussen het interstellaire gas in sterrenstelsels en de vorming van nieuwe sterren. Daarnaast verbeteren de resultaten de onderschatting van de impact van supernovae op de gasbewegingen in galactische schijven.

Sommario

Galassie quiescenti e galassie che formano stelle

Le galassie, sistemi di stelle legati dalla forza di gravità, sono gli elementi costitutivi dell'Universo. Ad esempio, il Sole e il nostro Sistema Solare si trovano nella Via Lattea, una galassia contenente centinaia di miliardi di altre stelle e che ha una massa totale di circa 50 miliardi di volte più grande di quella del Sole. L'Universo si è evoluto dal Big Bang per quasi 14 miliardi di anni, producendo un'ampia varietà di galassie con forme, dimensioni e masse diverse (si veda Figura I). Tuttavia, è possibile dividere le galassie in due gruppi semplicemente in base alla loro attività di formazione stellare. La capacità di formare nuove stelle è infatti una proprietà chiave delle galassie ed è usata per distinguere tra *galassie quiescenti*, con attività di formazione stellare molto ridotta o assente e *galassie in fase di formazione stellare*, in cui è attualmente in corso la creazione di nuove stelle, a volte con ritmo 'esplosivo' (le cosiddette galassie 'starbursts'; Fig. Id).

Tra i sistemi quiescenti si trovano, in ordine decrescente di contenuto di stelle, galassie ellittiche giganti (Fig. Ia), lenticolari massicce (Fig. Ib) e piccole sferoidali nane. Le galassie quiescenti sono costituite principalmente da stelle vecchie di colore rosso-giallo.¹ I principali oggetti di studio in questa tesi appartengono al gruppo delle galassie in fase di formazione stellare e sono le

¹Il colore delle stelle dipende principalmente dalla temperatura della loro atmosfera. La radiazione elettromagnetica (cioè la luce) emessa da una stella è composta da un'ampia gamma di frequenze ed è chiamata *emissione continua*. Le stelle più fredde hanno temperature di qualche migliaio di gradi, sono di colore giallo-rosso ed emettono la maggior parte della radiazione nelle lunghezze d'onda dell'infrarosso. Le stelle più calde hanno temperature di qualche decina di migliaia di gradi e sono di colore blu; la maggior parte della loro radiazione viene emessa nelle lunghezze d'onda ultraviolette.

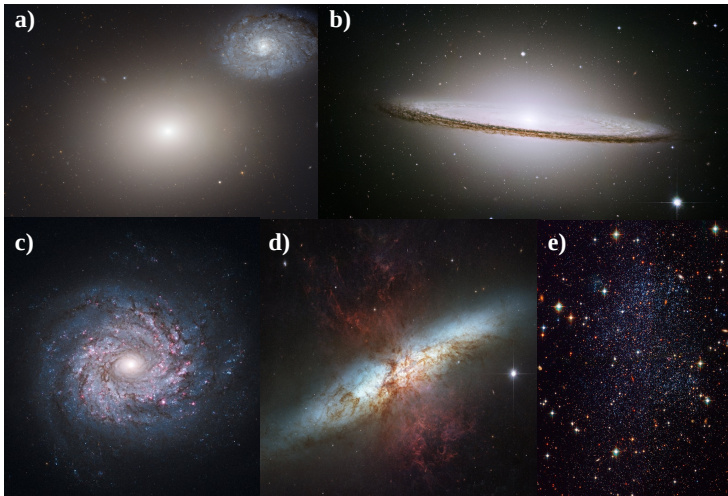


Figura I – Galassie di diverso tipo viste con il telescopio spaziale Hubble Space Telescope (le immagini hanno scale diverse). *Pannelli a) e b)*: due galassie quiescenti, una delle quali ha una compagna in fase di formazione stellare. L'immagine a sinistra mostra una galassia ellittica gigante (M60) e una galassia a spirale bluastra (NGC 4647) poco luminosa. M60 ha una massa di circa un trilione di volte la massa del Sole, mentre la massa di NGC 4647 è circa cento volte più piccola. Il pannello di destra mostra la lenticolare NGC 4594, o galassia Sombbrero, che ha una massa di circa 200 miliardi di volte quella del Sole. Il disco stellare è visto quasi di taglio, evidenziando il rigonfiamento centrale e la banda oscura prodotta dalla polvere che assorbe la luce delle stelle. *Pannelli c), d) ed e)*: tre galassie in fase di formazione stellare. L'immagine a sinistra mostra NGC 3982, una spirale con un 'rigonfiamento' al centro che è vista frontalmente. Nei bracci a spirale si trovano regioni di formazione stellare (in rosa), ammassi di stelle molto giovani (in blu) e polvere (bande scure). L'immagine centrale mostra una galassia *starburst* (M82) che, al proprio centro, forma stelle ad un tasso 10 volte maggiore dell'intera Via Lattea. I pennacchi rossi tracciano il vento galattico, gas espulso dalle esplosioni di stelle giovani e massicce chiamate *supernovae*. L'immagine a destra mostra una galassia nana irregolare nella costellazione del Sagittario e le sue stelle 'neonate', blu e luminose.

spirali e le nane irregolari. La maggior parte delle stelle in queste galassie è vecchia ma una parte della popolazione 'neonata' è molto luminosa, quindi spirali e nane irregolari sono caratterizzate da colori blu. Nelle galassie a spirale, come la Via Lattea, le stelle sono per lo più distribuite in un disco con dei 'bracci' che partono dal centro galattico, dove è spesso presente un 'rigonfiamento' di stelle (Fig. 1c). Le galassie a spirale contengono anche una grande quantità di polvere e gas interstellare a diverse temperature. Le stelle, il gas e la polvere ruotano attorno al centro galattico lungo orbite circolari. Le galassie nane irregolari (Fig. 1e) hanno tipicamente dimensioni e masse minori rispetto alle spirali e contengono, in proporzione, molto più gas e pochissima polvere. Le stelle e la polvere (quando questa è presente) si trovano nelle parti interne delle

galassie in fase di formazione stellare e la loro densità diminuisce con l'aumentare della distanza dal centro galattico, chiamata anche raggio galatto-centrico. La luce emessa dalle stelle riscalda il mezzo interstellare circostante fino a circa 10,000 gradi, perciò la maggior parte del gas caldo si trova solitamente nelle regioni interne del disco, dove le stelle sono numerose. Invece, i dischi di gas 'freddo', con temperature da poche migliaia a cento gradi, hanno tipicamente dimensioni maggiori e si estendono molto più lontano dal centro galattico rispetto al disco stellare.

Il carburante per la formazione stellare

Collegata all'attività di formazione stellare, un'importante differenza tra galassie quiescenti e in fase di formazione stellare è costituita dalla loro riserva di gas interstellare freddo, la materia prima per la creazione di nuove stelle. Le galassie quiescenti sono povere o prive di gas freddo, la loro riserva di gas è costituita principalmente da un alone gassoso a temperatura di diversi milioni di gradi. Il gas freddo è invece abbondante nelle galassie che stanno formando stelle ed è costituito principalmente da idrogeno, l'elemento più abbondante nell'Universo, che si trova in forma atomica e molecolare.

Il gas freddo può essere osservato e studiato grazie alla radiazione emessa dalle particelle di gas. In particolare, uno dei tipi di radiazione più importanti emesse dal gas freddo è la riga di emissione dell'idrogeno atomico, misurabile in banda radio alla lunghezza d'onda di circa 21 cm (corrispondente ad una frequenza di 1.42 miliardi di hertz).² La riga di emissione a 21 cm fu predetta dall'astronomo e matematico olandese H. C. van de Hulst nel 1944, poi osservata nel 1951 da H. I. Ewen e E. M. Purcell dell'Università di Harvard e confermata da C. A. Muller e J. H. Oort dell'Osservatorio di Leiden.

Il gas freddo nei dischi galattici non è distribuito uniformemente ma in nubi massicce e filamenti. La formazione stellare avviene nelle parti interne e più dense di queste strutture interstellari, tipicamente costituite da gas molecolare (si veda Fig. II). La forza di gravità guida la contrazione e il collasso di questi nuclei densi, portando alla formazione di stelle. I meccanismi fisici che regolano questo processo non sono ancora completamente compresi e costituiscono uno dei temi di ricerca più importanti per l'astrofisica.

Tra ordine e caos

Il gas distribuito nel disco delle galassie in fase di formazione stellare ruota seguendo orbite circolari attorno al centro galattico. Questa rotazione ordinata è il moto principale del gas. La velocità di rotazione varia da poche decine di chilometri al secondo nel caso di piccole galassie nane con massa stellare di circa

² *Riga di emissione* significa che la radiazione elettromagnetica emessa da una particella è caratterizzata da una singola frequenza (o lunghezza d'onda).

Figura II – Un gruppo di stelle giovani e massicce (chiamato R136) formatosi solo pochi milioni di anni fa. È situato nella Nebulosa Tarantola (o 30 Doradus), una regione di formazione stellare estremamente prolifica in una galassia satellite della Via Lattea chiamata Grande Nube di Magellano. Le stelle blu in questa immagine sono tra le più massicce conosciute e molte di esse sono 100 volte più grandi del Sole. Queste stelle producono una radiazione molto intensa ed emettono forti venti stellari costituiti da materiale atmosferico, che riscaldando e ‘scavando’ il mezzo interstellare circostante (in verde e rosso). Immagine ottenuta con il telescopio spaziale Hubble Space Telescope.



100,000 volte la massa solare, a qualche centinaio di chilometri al secondo per le spirali più massicce con masse stellari di alcune decine di miliardi di volte la massa dal Sole. Il metodo più comunemente utilizzato dagli astronomi per misurare la rotazione si basa sullo spostamento per effetto Doppler della linea di emissione a 21 cm.³ Infatti, quando si osserva un disco rotante in proiezione nel piano del cielo, l'emissione dai due lati opposti del disco viene ricevuta a lunghezze d'onda traslate in direzioni diverse rispetto all'emissione da un disco che non è in rotazione. Poiché lo spostamento per effetto Doppler dipende dalla velocità del materiale emittente, è possibile misurare la velocità di rotazione del gas in funzione del raggio galatto-centrico, cioè la sua *curva di rotazione* (si veda Fig. III).

La velocità di rotazione del gas in una data posizione nel disco dipende dalla massa contenuta nella regione tra questo punto e il centro della galassia. La stabilità del disco gassoso è infatti legata all'equilibrio tra la forza di gravità, che attira il gas verso il centro galattico, e la forza centrifuga generata dalla rotazione, che sostiene la struttura del disco impedendone il collasso gravitazionale. Per questo motivo, la curva di rotazione è un potente strumento per misurare la distribuzione di massa nelle galassie. Negli anni settanta, diversi studi della curva di rotazione di galassie vicine alla nostra, condotti per lo più a Groningen, ha portato alla scoperta della materia oscura. Fu

³L'effetto Doppler è il cambiamento della lunghezza d'onda della radiazione elettromagnetica, o di una qualsiasi onda, causato dal moto della sorgente emittente rispetto ad un osservatore. L'onda viene 'stirata' quando la sorgente si allontana da quest'ultimo, il che significa che la lunghezza d'onda aumenta e la frequenza diminuisce. Viceversa, l'onda viene compressa quando la sorgente si avvicina all'osservatore, quindi la lunghezza d'onda diminuisce e la frequenza aumenta.

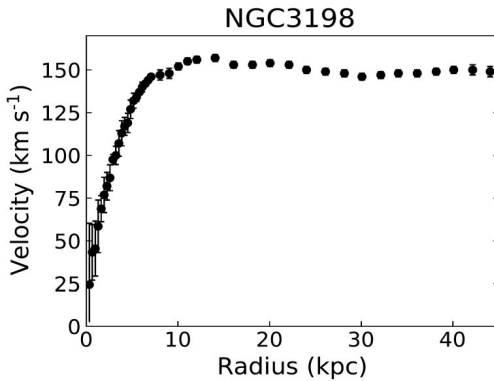


Figura III – Curva di rotazione della galassia a spirale NGC 3198 ottenuta utilizzando le osservazioni della riga di emissione dell'idrogeno atomico a 21 cm. Il raggio galatto-centrico è espresso in kiloparsec (in breve kpc; un kpc è pari a circa 30,000 miliardi di chilometri). La velocità aumenta nelle regioni interne del disco, dove si trova la maggior parte della massa stellare, e rimane costante a distanze maggiori dal centro galattico. Figura adattata da Cimatti, Fraternali & Nipoti (2019, Cambridge University Press).

infatti verificato che la massa visibile nelle galassie non è sufficiente a spiegare la velocità di rotazione osservata (si veda Fig. III), implicando la presenza di materia invisibile. Successive ricerche hanno evidenziato che l'Universo è dominato dalla materia oscura, la cui natura rimane uno dei più grandi misteri della scienza moderna.

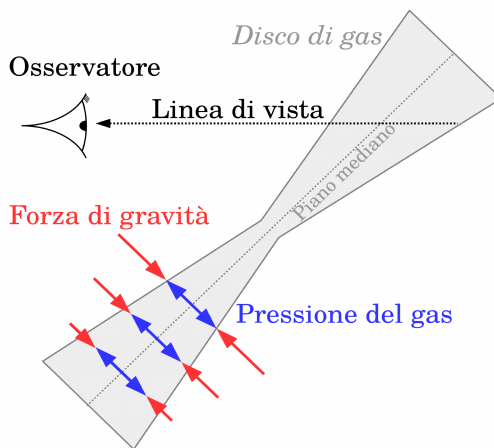
La rotazione ordinata del disco gassoso coesiste con moti disordinati, in modo analogo a vortici d'acqua nel flusso di un fiume. Questi moti casuali hanno velocità dell'ordine di 10 chilometri al secondo e sono in parte dovuti alla temperatura delle particelle di gas. La loro componente dominante, chiamata *turbolenza*, ha però una natura diversa. La turbolenza può essere visualizzata come moti caotici tra porzioni macroscopiche di gas interstellare di varie dimensioni, o vortici, che interagiscono tra loro. La viscosità del gas tende a dissipare l'energia di questi vortici, rendendo necessaria una continua fonte di energia per sostenere la turbolenza nel gas interstellare.

I moti disordinati del gas possono essere misurati attraverso l'allargamento delle righe di emissione. Quella a 21 cm, ad esempio, è stata largamente utilizzata per questo scopo. A causa della turbolenza, le particelle di gas lungo la linea di vista di un osservatore si muovono con diverse velocità sia nella direzione di allontanamento che in quella di avvicinamento ad esso. Quindi, la radiazione emessa viene spostata per effetto Doppler a varie lunghezze d'onda. L'osservatore, che riceve la somma di tutta la radiazione, misura perciò una riga di emissione che copre diverse lunghezze d'onda. Questo allargamento consente di misurare la velocità dei moti caotici nel gas e può essere utilizzato per studiare la natura della turbolenza.

Dischi sottili ma non troppo

I moti disordinati del gas nelle galassie generano una forma di pressione che, opponendosi all'attrazione gravitazionale lungo la direzione del raggio galatto-

Figura IV – Rappresentazione schematica del disco di gas di una galassia che si trova in equilibrio idrostatico verticale. Sopra e sotto il piano mediano del disco (linea tratteggiata grigia), la pressione del gas (frece blu) tende a ‘gonfiare’ il disco opponendosi alla forza di gravità (frece rosse) che attira il gas nella direzione opposta. Poiché la forza gravitazionale si indebolisce con l’aumentare della distanza dal centro della galassia e dell’altezza sopra il piano mediano, lo spessore del disco gassoso aumenta. Un osservatore esterno vede la somma dell’emissione di tutto il materiale lungo la linea di vista e più il suo sguardo si allontana dalla centro della galassia, più diventa spesso lo strato di gas.



centrico e la direzione verticale, contribuisce all’equilibrio del disco gassoso. Lungo il raggio galatto-centrico, la pressione aiuta la rotazione a bilanciare la forza di gravità; il suo contributo è trascurabile nel caso delle galassie a spirale, nelle quali la rotazione è predominante, ma può diventare significativo per le galassie nane che ruotano lentamente. La pressione del gas è invece la principale antagonista alla forza di gravità lungo la direzione verticale, sopra e sotto il piano mediano del disco (si veda Fig. IV). In altre parole, la pressione ‘gonfia’ il disco gassoso, mentre la forza di gravità tende ad appiattirlo. La struttura verticale del gas nelle galassie è stabilita dall’equilibrio tra pressione e gravità, questa condizione è chiamata *equilibrio idrostatico verticale*. Con l’aumentare dell’altezza sopra il disco e della distanza dal centro della galassia, la densità della materia (stelle, gas e materia oscura) diminuisce e, di conseguenza, l’attrazione gravitazionale lungo la direzione verticale si indebolisce. Il disco di gas in equilibrio idrostatico diventa quindi sempre più spesso all’aumentare della distanza galatto-centrica.

Un osservatore esterno vede le galassie in proiezione nel piano del cielo. La sua linea di vista attraversa il disco a un certo raggio galatto-centrico, intercettando la luce emessa da tutto il materiale lungo di essa. Poiché lo spessore del disco aumenta con il raggio, la colonna di gas diventa sempre più alta nelle regioni esterne di una galassia rispetto a quelle interne. È quindi possibile osservare un’emissione molto luminosa sia dove il disco è sottile e il gas è denso, come nelle parti interne delle galassie, sia dove il disco è spesso e il gas è diffuso, che è tipicamente il caso delle regioni esterne. Pertanto, l’effetto di proiezione dovuto allo spessore del disco deve essere preso in considerazione nello studio della densità e della distribuzione del gas nelle galassie.

In questa tesi

L'importanza dello spessore dei dischi di gas è il 'fil rouge' che attraversa i capitoli di questa tesi, organizzata in due parti principali.

La prima parte si concentra sulla relazione tra la formazione stellare recente e la quantità di gas interstellare freddo presente nel disco delle galassie in fase di formazione stellare. Questa idea fu originariamente proposta nel 1959 dall'astronomo olandese Maarten Schmidt, nato a Groningen e dottorando di J. H. Oort a Leiden. Sulla base di argomenti teorici, Schmidt ipotizzò che il tasso di formazione stellare in un dato volume all'interno del disco di una galassia è proporzionale alla densità del gas freddo nello stesso volume. Questa relazione è generalmente chiamata *legge sulla formazione stellare*. Utilizzando alcune osservazioni effettuate nella Via Lattea, Schmidt stimò che il tasso di formazione stellare aumenta in modo proporzionale alla densità del gas elevata ad una potenza compresa tra uno e tre. L'esatta formulazione della legge di formazione stellare è rimasta però incerta dalla sua scoperta fino ad oggi.

La legge di formazione stellare è fondamentale nello studio della formazione e dell'evoluzione delle galassie. Viene infatti utilizzata nei modelli teorici per calcolare il tasso di consumo del gas di una galassia, il corrispondente tasso di formazione stellare e l'aumento della sua massa in stelle. L'esatta dipendenza del tasso di formazione stellare dalla densità del gas, legata all'esponente della legge, può inoltre fornire importanti indicazioni riguardo ai processi fisici che regolano questo fenomeno.

Per un osservatore esterno, non è possibile misurare la densità del gas e il tasso di formazione stellare *per unità di volume*, poiché le galassie sono viste in proiezione nel piano del cielo; le quantità osservabili sono invece la densità del gas e il tasso di formazione stellare *per unità di superficie*. Queste quantità proiettate sono state ampiamente utilizzate con successo per derivare la legge di formazione stellare per galassie con diverse masse e intensità di formazione stellare, dalle nane alle *starburst*. Tuttavia, non è ancora chiaro se la stessa relazione sia valida per tutti i tipi di galassie. Alcune evidenze osservative indicano inoltre che, sebbene questa legge sia confermata nelle regioni interne dei dischi galattici, essa perde validità nelle zone esterne dove c'è poco gas freddo e l'attività di formazione stellare è piuttosto debole. In seguito al pionieristico lavoro di Schmidt, sono state proposte diverse versioni della legge di formazione stellare. Manca tuttavia un consenso generale riguardo a quale tra queste sia la formulazione corretta.

A questo proposito, l'approccio e i risultati presentati in questa tesi rappresentano un importante miglioramento, in quanto la legge di formazione stellare viene ottenuta utilizzando la densità del gas e il tasso di formazione stellare per unità di volume. Queste quantità sono state derivate dalla densità del gas e dal tasso di formazione delle stelle misurate per unità di superficie, utilizzando lo spessore del disco del gas calcolato assumendo l'equilibrio idrostatico verticale. I moti disordinati del gas sono stati misurati

grazie all'allargamento delle righe di emissione, mentre la forza gravitazionale è stata derivata dalla distribuzione di massa delle galassie, tracciata dalla curva di rotazione. Il tasso di formazione stellare per unità di volume è risultato essere proporzionale al quadrato della densità del gas per unità di volume, in accordo con i risultati di Schmidt. Questa relazione, chiamata *legge di formazione stellare volumetrica*, è stata ottenuta per un campione di galassie nane e a spirale e per la nostra Via Lattea. A differenza della relazione basata sulle quantità superficiali, la legge volumetrica è valida sia per le zone del disco galattico che sono povere di gas e formano poche stelle, sia per le regioni ricche di gas e più attive. Questa scoperta è il risultato principale della prima parte della tesi ed indica che i modelli teorici per la formazione stellare comunemente adottati nello studio della formazione e dell'evoluzione delle galassie potrebbero richiedere una revisione.

Lo scopo della seconda parte della tesi è individuare l'origine della turbolenza nel gas interstellare freddo e il 'motore' che la alimenta. Le misurazioni dei moti disordinati del gas freddo nei dischi galattici indicano che questo mezzo è fortemente turbolento. Poiché si ritiene che la turbolenza venga dissipata in tempi relativamente brevi, è necessario che vi sia un fenomeno fisico che la rigeneri. A questo proposito, le esplosioni di supernova sono i principali 'sospettati' poiché rilasciano enormi quantità di energia nel mezzo interstellare. Manca tuttavia una conferma empirica di questo scenario. Il numero di esplosioni di supernova attese dalla popolazione di stelle massicce appena formate è infatti risultato insufficiente per mantenere la turbolenza nell'intero disco delle galassie, rendendo necessarie altre sorgenti di energia. Rispetto ai lavori precedenti, in questa tesi si ottiene un miglioramento decisivo tenendo conto dello spessore del disco di gas, in quanto la dissipazione della turbolenza avviene più lentamente nei dischi spessi che in quelli sottili. Ciò riduce l'approvvigionamento energetico necessario per sostenere i moti turbolenti, portando alla conclusione che le esplosioni di supernova possono, da sole, mantenere la turbolenza del gas freddo nelle galassie.

Nel complesso, i risultati presentati in questa tesi rappresentano un progresso significativo nella conoscenza del legame tra il gas interstellare nelle galassie e la formazione di nuove stelle e, inoltre, migliorano la nostra comprensione dell'impatto delle supernove sui moti dei gas nei dischi galattici.

Acknowledgments

I had the opportunity to spend the past 4 years in two wonderful cities, Bologna and Groningen, where I met so many nice and friendly people that it seems impossible to properly thank everyone, but I will try anyway.

Filippo, you've been an amazing supervisor during the past 5 years, from the Master thesis to the PhD. To properly thank you for everything you did for me, both from the scientific and the personal points of view, I would need tens of pages and, due to my well-known slowness in writing, at least one month! I can say, beyond any doubt, that these years have greatly exceeded expectations (not because I've never started our original PhD project!). Thank you for teaching me so much about astrophysics and research, for your tireless patience and support, and for bringing me to the Kapteyn Institute, where I could learn a lot and meet wonderful people. Last but not least, thanks for giving me the opportunity to see amazing places around the world (Australia in particular!), for the group dinners and the (many!) bottles of excellent wine.

Carlo, you 'adopted' me as your PhD and warmly welcomed me in your group, thank you really very much! I've learned a lot during our meetings and from your constructive feedback. I greatly appreciated that you've always been keen to listen, read and discuss about different topics from your own research, giving your original and interesting point of view.

Antonino, Gabriele and Giuliano, your help and feedback were essential to accomplish this doctorate. Thanks for sharing with me your expertise and wise comments, I've really learned a lot working with you. I also enjoyed very much chatting with you about many things, from science to food. Thanks for everything!

Andrea and Pavel, thank you for being so friendly and for your constant attempts to cheer me up in stressful periods. You really made my months in

Groningen (and, together with Francesca, our days in China) much more funny, despite my antisocial attitude!

I would like to thank Eline for the help with the thesis propositions and, in particular, for her kindness and hospitality.

I'm very grateful to the people at the Kapteyn Institute, I was impressed by the welcoming and lively environment! I would like to thank the amazing group of the PhD students and postdocs and the (super efficient!) administrative staff. In particular, thanks to Lorenzo P., Davide M., Cristiana, Laura (and the other members of the 'Italian group'!), Tirna, Hannah, Giulio, Kostas, Tadeja and Asger. Special thanks to Bram Lap for his help with the samenvatting!

I'm very grateful to Margreet, Henry, Menno and Sanne for giving me a place to stay in Groningen, their hospitality and their kindness.

During the time in Bologna, I had the pleasure to spend my working days and many evenings with wonderful people. Thanks to Matilde & Carlo (without you, all these years in Bologna wouldn't have been so special), Matteo (for all the interesting chats about science and politics), Alessia (for being you!), Mario (I loved all your amazing and perfect cakes!), Bobore (for imposing the coffee breaks), Elena, Silvia, Riccardo, Nadia, Caterina, Cristiano, Federica, Raffaele, Lucia, Sara, Vittorio, Annalisa, Alberto, ... and all the others! Special thanks to the 'Sanremo group' for the online aperitifs during the lock-down.

Ringrazio tutta la mia famiglia per avermi sempre dato supporto e affetto, specialmente nei momenti più difficili. Grazie a Emanuele, Mariella, Costanza, Nicolas, Filippo, Leonardo, Giancarlo, Federica, Maddalena, Giulia, Pietro, Manuel e Antonio per tutte le cene, gli aperitivi, i pranzi, le colazioni, le merende, le degustazioni, le grigliate, i picnic, i banchetti, gli spuntini e, soprattutto, l'ottima compagnia!

Lastly but most importantly, thanks to Lorenzo (better known as Fassa) for his love, patience, understanding, and support during all these years. Always.